Characterisation and Functionalisation of Ultrabithorax Materials for Biosensing

Karol Piotr Szuba-Jablonski

Submitted to Swansea University in fulfilment of the requirements for the Degree of Doctor of Philosophy

Swansea University
Prifysgol Abertawe

Swansea University

2023

Abstract

Ultrabithorax (Ubx) is a Hox transcription factor, which self-assembles into protein films and fibres at the air-water interface. Ubx materials are bio- and cytocompatible, and can be functionalised with DNA, proteins, and growth factors to benefit from functions such as supporting cell proliferation. This thesis investigated the optical, electrical, and mechanical properties of Ubx fusion fibres in conditions relevant to applications in biosensing and tissue engineering. The steady-state and time-resolved spectra of the fibres were measured using an ultrafast laser source. The dityrosine emission peak red-shifted by 50 nm in fibres compared to Ubx fusion solutions, and resonance energy transfer between dityrosine and enhanced green fluorescent protein (EGFP) was observed in the EGFP-Ubx protein fusion. The electrical properties of Ubx fusion fibres were tested, and an increase in their electrical conductivity by 3 orders of magnitude was measured with rising relative humidity. Tensile tests of Ubx fusion fibres revealed that the fibres were less extensible but stronger after prolonged storage and rehydration, which could influence the design of Ubx materials for tissue engineering. Significant binding of DNA aptamers to Ubx in solution and in fibres was observed. A fluorescence-based method to assess binding efficiency of bacteria and the SARS-CoV-2 spike RBD protein was developed. Some indication of increased specific pathogen binding was observed using long oligonucleotide sequences bound to Ubx fusion fibres, and improvements to this system were suggested. Alginate and collagen are biomaterials widely used in tissue engineering. Preliminary experiments were conducted that showed the feasibility of production of composite materials made of Ubx and alginate or collagen, which could be applied to create functional tissue scaffolds. Ubx-based platforms and composite materials could benefit from the intrinsic properties of Ubx, and Ubx functionalisation with proteins, growth factors and DNA aptamers for applications in biosensing and tissue engineering.

Declarations and Statements

This work has not previously been accepted in substance for any degree and is not being concurrently submitted in candidature for any degree.

Signed [redacted]..... (candidate)
Date .....12/01/2024.....

This thesis is the result of my own investigations, except where otherwise stated. Other sources are acknowledged by footnotes giving explicit references. A bibliography is appended.

Signed [redacted]..... (candidate)
Date .....12/01/2024.....

I hereby give consent for my thesis, if accepted, to be available for electronic sharing.

Signed ..[redacted]..... (candidate)
Date .....12/01/2024.....

The University's ethical procedures have been followed and, where appropriate, that ethical approval has been granted.

Signed [redacted]..... (candidate)
Date .....12/01/2024.....

Acknowledgements

I thank my collaborators and colleagues for the discussions, shared work, guidance, and training that supported my work during this project. The guidance and expertise of Prof. Sarah Bondos and Prof. Ken Meissner have been invaluable in driving the development of Ultrabithorax materials, and linking the research communities across the United States and Europe. They created a friendly and collaborative research community, and inspired and supported my research. I want to thank Prof. Ken Meissner for continued support and mentoring during the project, as well as his unbreakable spirit and positive energy. His curiosity and enthusiasm for research have been inspiring and encouraging in the pursuit of new experimental ideas. I want to thank Carolyn Greig, Dr. Almudena Ortiz-Urquiza, and Dr. Valeria Italia for the shared time in the lab and the hard work that established our protein production capacity and the ability to work with aptamers. The support and expertise of Dr. Drew Riley, Dr. Ardalan Armin, Dr. Gregory Burwell, Dr. Bernard Mostert, and other members of the Sêr SAM group, have enabled the exploration of the electrical and optical properties of Ubx. The specialist team at Deben, with a particular mention of John Gilbert, aided the troubleshooting of the resolution problems in the measurements of the mechanical properties of Ubx fibres, and led the training in the related techniques. Thank you to Dr. Christopher Wright, Dr. Jonathan Widdowson, Charlie Fricker, Dr. Matthew Turner, and Dr. Laurence Hill for sharing the samples and the knowledge essential to developing the composite biomaterials including Ubx. I would like to thank the members of the technical and PGR teams who have enabled conducting and sharing my research. The funding from the Swansea University Research Excellence Scholarship and the Welsh Government supported this work and allowed me to pursue my research ideas.

I am hugely grateful to my family and friends who have been supportive and encouraging of my research endeavours. Wiktor, Zuzia, John, Lewis, Emily, Kasper,

Heather, and Drew have accompanied me through the successes and crises. Ola, Aleksander and Agata have been my best friends. To Katya, Lucas, Mohammad and Ricardo, the adventures we have had together have made this journey unbelievable. Thank you.

Contents

List of Figures

List of Tables

Acronyms

BSA bovine serum albumin.

CPE constant phase element.

DNA deoxyribonucleic acid.

dsDNA double stranded DNA.

EGFP enhanced green fluorescent protein.

EYFP enhanced yellow fluorescent protein.

FARP fluorescence recovery after photobleaching.

FLIM fluorescence lifetime imaging.

FRET Förster resonance energy transfer.

FWHM full width at half maximum.

GFP green fluorescent protein.

mACE2 membrane-bound angiotensin-converting enzyme 2.

MNEC meningitis or sepsis associated *E.coli*.

PBS phosphate buffered saline.

RABV rabies virus.

RBD receptor binding domain.

RH relative humidity.

RNA ribonucleic acid.

ROI region of interest.

SELEX systematic evolution of ligands by ex- ponential enrichment.

SPR surface plasmon resonance.

ssDNA single stranded DNA.

STC sequential toggle cell.

TRPL time-resolved photoluminescence.

Ubx Ultrabithorax.

VEGF vascular endothelial growth factor.

w/v weight per volume.

Chapter 1

Introduction

This thesis is an investigation of the mechanical, electrical, and optical properties of self-assembled Ultrabithorax (Ubx) materials, and the subsequent functionalisation of Ubx for applications in biosensing. This introduction outlines the literature on protein materials and the research on Ubx materials to date, which provides the motivation for the use of Ubx for tissue engineering and biosensing. The methods in chapter 2 describe the general experimental techniques related to Ubx protein production and subsequent Ubx material formation. It also details the protein material characterisation and imaging methods used throughout this thesis. Each of the next chapters contains an introduction and description of methods specific to the experiments, and a discussion of the results of these experiments. For this reason, this introductory chapter provides the general context to this work, and specific introductions are included in each of the following chapters. Chapter 3 investigates the electrical and optical properties of Ubx fusion fibres, including the effect of protein fusions on the optical properties of Ubx materials, and the effect of the relative humidity on the electrical properties of fibres. Chapter 4 describes the examination of the effect of storage and sample rehydration on the mechanical properties of Ubx and EGFP-Ubx fibres with the motivation of using Ubx materials in biomedical applications. Chapter 5 details the testing of Ubx-aptamer complexes for analyte capture, which could have applications in biosensing and targeted therapeutics. The preliminary experiments on the formation of composite materials are described in chapter 6. The suggested future work on Ubx materials and the strategies for scaling up Ubx production, nanofunctionalisation, and production of composite materials, were discussed in the summary in chapter 7.

1.1 Protein materials

Proteins are molecules composed of long amino acid sequences with complex three dimensional structures, which perform catalytic and structural functions *in vivo*. In the recent decades, proteins have also been used for controlled building of structural or bioactive materials in bionanotechnology [1]. The applications of protein materials and products span a range of industries, including food, textile, agriculture, biotechnology and medicine. The important considerations regarding the use of proteins include their batch production, the production cost, biodegradability, functionality, and sustainability. Protein materials offer significant benefits particularly in biomedical applications due to their biocompatibility and biodegradability [2–6]. These features mean that protein materials can be a more biocompatible and biodegradable alternative for more easily produced synthetic and metal materials if appropriate material properties and functions can be achieved [3–13]. Biofunctionalisation of protein materials through processes such as protein fusion can be of particular interest because it offers a clean pathway to achieving tissue growth using growth factors [14], enhancing sensing possibilities by attachment of fluorescent proteins, or combining natural properties of several proteins with their unique functions [15–17]. Additional enhancements of functional properties can be provided by using constructs such as the DNA aptamers, which allow for the detection and capture of analytes of interest [18–21]. The study of intrinsic properties of protein materials and the effect of their functionalisation on their properties is crucial to determining and developing applications in vital industries, such as the development of implantable tissue engineering scaffolds or diagnostic systems.

An example of a protein material is silk fibroin derived from *Bombyx mori*, which was characterised in many experiments as having valuable mechanical properties, including large tensile strength and elasticity, and favourable material forming capabilities for tissue engineering [22, 23]. The promotion of cell proliferation or alignment with biomaterials is an important feature of tissue scaffolds. Electrospun silk fibroin fibres supported cell proliferation of both human aortic endothelial (HAEC) and human coronary artery smooth muscle cells (HCASMC), which could make silk fibroin a good scaffold for tissue engineering [23]. Another protein of interest in biomedical applications is collagen, which is abundant in native human tissues [13]. Collagen has been used for bone, skin, tendon, and ligament tissue engineering [4, 6, 10, 12, 13]. Type I collagen is of particular interest because

of its ability to interact with cells and stimulate their proliferation. Expression of type I collagen indicated the formation of extracellular matrix for HCASMCs, which could be used for blood vessel tissue engineering [23]. Various proteins, of which silk fibroin and type I collagen are examples, can and have been used for biomedical applications. Composite materials and protein functionalisation with nanomolecules are two possible pathways to design materials for clinical applications [3, 8, 9, 24].

The creation of functional protein fusions or composites is important for the design of devices applicable to biotechnology and medicine [25]. Gene fusion of peptides or proteins creates covalent bonding and enables the incorporation of the appended molecule into the protein material of choice [15,17,26]. It is preferential for proteins or peptides comparable in size or smaller than the protein [15]. In the case of silk, conjugation of functional protein and silk after purification could be used when sufficient yield could not be achieved using gene fusion, the fold and therefore function of appended protein was lost during self-assembly, or if the appended molecule was much larger than silk protein, which could inhibit self-assembly [15]. Protein conjugation could be achieved by cross-linking using carbodiimides and N-hydroxysuccinimide [3, 15]. The use of protein fusions and cross-linking of biomaterials could be used to create materials with enhanced functionality and physical properties.

1.2 Biomedical applications and functionalisation of protein materials

Crucially, the incorporation of nanomaterials in biomaterial scaffolds increases the scaffold's strength and electrical conductivity. The compressive modulus of cardiac patches is reported to increase threefold within the three-dimensional alginate scaffold with embedded gold nanowires [27]. Presence of gold nanowires or gold nanoparticles in scaffolds for myocardial tissue engineering was also shown to increase the electrical conductivity of scaffolds by several (9 and more) orders of magnitude compared to pristine material [8,27]. The rise in electrical conductivity and surface area was also achieved by growing multiwalled carbon nanotubes within nanopores on anodised titanium surface [28]. It allowed for enhanced redox reaction sensing during osteoblast formation, which could be used to detect bone tissue formation and potential inflammations in the implant area. The increased

mechanical strength of scaffolds reinforced with nanomaterials could allow their stable operation *in vivo*, while increased electrical conductivity within the cardiac patches guides the electrical wave and promotes cell-cell interactions [29], allowing for muscle contraction. Moreover, nanoparticles promote connexin 43 activity and expression within newly formed myocytes [27, 29]. The cells also formed anisotropic structures along the scaffolds to support contraction of the cardiac patch synchronous with the healthy part of heart [29]. The nanofunctionalisation of protein materials offers significant functional enhancements. Protein materials have the favourable intrinsic biocompatibility and ability to interact with cells, and the increases in the mechanical strength and electrical conductivity due to the addition of nanoparticles and nanowires can expand the range of their biomedical applications.

Aptamers are nucleic acid sequences (oligonucleotides) that exhibit high specificity binding to a target molecule [18]. In the past decades, they have been researched as a promising group of molecules for targeted therapeutics, diagnostics and biosensing because of their specificity and high affinity to target molecules [18–21]. The word aptamer originated from two Greek words *aptus* and *merus*, which mean "bound to a particle". In fact, aptamers can bind a range of molecules such as metal ions, peptides, proteins, cells, or even organisms such as bacteria and viruses. The binding occurs due to hydrophobic and electrostatic interactions, hydrogen bonding, or van der Waals forces [18]. The interactions between aptamers and their targets resemble those of antibodies and antigens, which also exhibit high specificity and affinity. However, aptamers are nonimmunogenic, which means that in some applications they are preferred over antibodies [19]. Ribonucleic acid (RNA) aptamers offer a wide range of available three-dimensional structures, but their use is limited because of their susceptibility to cleavage in the presence of RNases [19]. Deoxyribonucleic acid (DNA) aptamers are short oligonucleotides capable of binding targets with high specificity and affinity through their secondary structures that complement the shape of their targets [19]. Oligonucleotides involving DNA aptamers to Ubx, *E. coli* and a coronavirus spike protein (SARS-CoV-2 spike RBD protein) were tested in this work to investigate the possibility of applying Ubx-aptamer systems as biosensing or drug delivery platforms.

1.3 Ultrabithorax

Ubx is a Hox gene transcription factor present in insects such as *Drosophila melanogaster*. In adult *Drosophila*, it is expressed in specified segments of the thorax and the abdomen, and it regulates the growth of wings and limbs. Across different species, different Ubx expression patterns may result in the formation of fangs, legs or maxillipeds, or a complete lack of limb development in a segment of the body [30]. Ubx functions in insects have been studied to understand the influence of gene transcription factors on the morphological developmental mechanisms [31]. The structure of the Ubx protein was investigated, which revealed a DNA-binding homeodomain [32]. Ubx isoform Ia was used in this thesis. It is a monomeric protein with a 380 amino acid structure and a molecular weight of 40 kDa [17,33]. As a homeodomain transcription factor, Ubx belongs to the group of Hox proteins, which are intrinsically disordered [34–36]. The secondary structure of Ubx contains multiple disordered regions with random coils, and a small portion of α-helices [35, 37]. Interestingly, Ubx was produced using the recombinant DNA technology for experiments on its biological properties, which has led to an unexpected discovery, in which Dr Sarah Bondos's group first observed the formation of Ubx fibres *in vitro* because of protein self-assembly [38]. Following this discovery, the Bondos group investigated the Ubx material formation mechanism, and the material properties of the resulting materials. It was found that Ubx self-assembles at the air-water interface [38] by forming dityrosine bonds between the Ubx monomers [39]. Ubx materials have a blue autofluorescence due to the presence of the dityrosine bonds with an emission peak at 438 nm at 305 nm excitation, which is consistent with other protein materials with dityrosine presence [39]. The formation of materials at the air-water interface occurs in several stages. First, nanoscale fibrils form at the air-water interface. Then, the fibrils aggregate to form a thin surface film, from which a thicker sheet can form. The film or sheet can be lifted from the air-water interface and create a thin coating. Alternatively, a fibre can be pulled from the aggregated protein layer, and the length and diameter of fibres depend on the initial concentration of protein [38].

Ubx materials were found to have a range of interesting properties both in terms of the protein structure and the physical properties of fibres. They are elastic, with an average breaking strain of 53%, which is larger than the breaking strain of many silks including natural spider silk (40%), and between the breaking strains of two of the most common proteins in humans, collagen and elastin [17, 38, 39].

Freshly produced Ubx fibres exhibited a considerable breaking strength between 3 and 66 MPa, which decreased rapidly with the fibre diameter [17, 38]. The ability to control the size of fibres, and the reliable self-assembly of Ubx materials led to the exploration of material properties focused on biomedical applications, such as tissue regeneration. Ubx fibres were observed to be biocompatible and nonimmunogenic, which was evidenced in experiments involving injection in mice, culturing with macrophages, and incubation with red blood cells [2]. Moreover, Ubx fibres were cytocompatible when cultured with primary human vascular cells including umbilical vein endothelial cells, brain vascular pericytes, and aortic smooth muscle cells [40]. The bio- and cytocompatiblity of Ubx fibres provided a motivation to study Ubx for biomedical applications. In addition, the structure of Ubx fibres was shown to protect the functions of the fluorescent proteins appended by gene fusion under harsh conditions such as immersion in ethanol or autoclaving [17]. This protective capacity of Ubx materials motivated the further investigation of their physical properties presented in this thesis.

Ubx was functionalised with various proteins and DNA, which did not alter the ability of Ubx protein fusions to assemble into fibres [17, 26]. The protein fusions of Ubx with functional proteins use a flexible linker between the constituents [17]. Ubx is a largely intrinsically disordered protein, while the fusion partners used in this work consist of α-coils (myoglobin) or a combination of α-helices and β-sheets (EGFP and mCherry). The protein unfolding could result in the loss of function during material assembly. However, Ubx fusions used in this work do not exhibit a function loss upon material formation, which indicates that the fusion partners maintain their native fold. Ubx functionalised with fluorescent dyes retained the fluorescent properties of the dyes, particularly the shapes of spectra and fluorescence intensity [26]. The fibres made using one of the protein fusions with the enhanced green fluorescent protein (EGFP-Ubx) had lower breaking strain and higher breaking stress than pristine Ubx fibres [17]. It indicated that Ubx fusions with other proteins created materials with different mechanical properties, which enabled tuning these properties. Because of these properties of Ubx materials, an opportunity was recognised to functionalise Ubx with proteins, DNA, nanoparticles or antibodies to use such systems in biosensing or tissue engineering.

The choice of fusion partners was dictated by their potential use as reporters, the ease of identification of Ubx fusions with fluorescent protein, and the intrinsic properties of the fusion partners, which could affect the material properties of

the resulting materials. EGFP and mCherry are fluorescent proteins that have been used as fluorescent reporters. Their molecular weights are 27.1 kDa and 26.9 kDa, respectively. Myoglobin is a protein that facilitates oxygen transport in tissues. It has a molecular weight of 17.6 kDa. It can exhibit electronic transfer behaviours such as the single electron transistor effect during electron tunnelling through the heme group [41]. We proposed to study the effect of this fusion partner on the electrical properties of resulting materials. The secondary structure of both EGFP and mCherry is dominated by α helices and β sheets. The secondary structure of myoglobin is dominated by α helices [17]. These proteins had a molecular weight comparable to that of Ubx, and a monomeric quaternary structure, both of which were key factors to ensure the protein yield and subsequent material formation [17]. Therefore, the fusions of EGFP-Ubx, mCherry-Ubx, and myoglobin-Ubx were selected as suitable materials to explore the effect of protein fusions on the electrical and optical properties of Ubx materials.

Several research questions were posed based on the previous work on Ubx materials. The characterisation of the optical properties of Ubx materials had been limited to fluorescence microscopy and measurements of steady-state fluorescence spectra of Ubx fibres [17, 26]. No fluorescence lifetime data was available. The experiments presented here provided information about both the steady-state spectra and fluorescence lifetimes of several Ubx fusion fibres, which had not previously been measured. The measurements of the electrical properties of Ubx fibres were limited to the DC electrical conductivity of one fusion of EGFP-Ubx [42]. Because of the significant effect of humidity on the electrical properties of biomaterials [43], an investigation into the effect of relative humidity on the electrical properties of Ubx fusion fibres was conducted in this thesis. Previous measurements of the mechanical properties of Ubx fusion fibres concentrated on freshly pulled fibres [17, 38]. Oxidation of Ultrabithorax and the resulting formation of intermolecular dityrosine bonds was suggested to be responsible for the strength of Ubx materials [39], and the prolonged storage was implied to cause stiffening of Ubx fibres [38]. Therefore, this work considered the effect of prolonged storage on the mechanical properties of Ubx fibres, which is important in the prospect of applying Ubx materials in tissue engineering, where device storage is likely to be required.

The second part of this thesis focused on the functionalisation of Ubx materials with DNA aptamers (chapter 5) to examine the feasibility of using this system as a biosensing or therapeutic device, and preparation of composite materials

with a potential for tissue engineering applications (chapter 6). Because of the importance of aptamers in biomedical applications and their specific binding to proteins, the binding of long oligonucleotides (designed within the research group) including Ubx aptamers to Ubx fibres was tested. These oligonucleotides also included aptamers against analytes such as bacteria and the SARS-CoV-2 spike RBD protein. The binding efficiency between Ubx fibres functionalised with DNA aptamers and these pathogens was measured in this thesis. Finally, chapter 6 explored the preliminary work on the production of composite materials made of Ubx and alginate or collagen, which are biomaterials routinely used in tissue engineering.

In summary, this thesis investigates the intrinsic physical properties of Ubx fusions, including the effect of storage and environmental conditions on their electrical, optical (chapter 3), and mechanical properties (chapter 4). A particular focus is placed on the effect of storage time, relative humidity, and sample hydration on the physical properties of fibres. In chapter 5, the functionalisation strategies for Ubx materials are tested. The binding capacity of DNA-based aptamers to Ubx in solution and in fibres is measured. Subsequently, the capability of the Ubx fibre-aptamer complex to bind pathogens such as bacteria (*E. coli*) and viruses (indirectly through a DNA-binding SARS-CoV-2 spike protein) is trialled. Finally, chapter 6 details the creation and evaluation of optical and structural properties of composite materials composed of EGFP-Ubx and collagen or sodium alginate, both of which are biomaterials used to produce tissue scaffolds for tissue engineering and regeneration. The thesis summary in chapter 7 outlines suggested future work on Ubx materials, which would enable the production of Ubx protein on a larger scale, and the formation of larger structures made of Ubx fusions. Moreover, nanofunctionalisation methods and strategies to create functional composite materials are discussed to enable applications of Ubx in biosensing and tissue engineering.

Chapter 2

General materials and methods

In this chapter, the materials and methods used throughout the thesis will be described. The production of Ubx protein fusions was undertaken using the recombinant technology in the host *E. coli* cells. The description of the growth of the bacterial culture and the protein purification will be given in section 2.1. The pulling of Ubx fusion fibres is enabled by self-assembly of the protein film at the surface of an aqueous buffer. The parameters of this process and a graphical depiction will be presented in section 2.2. Section 2.3 will describe the fluorescence and confocal microscopy. The equipment used in spectrophotometry and measuring the steady-state photoluminescence spectra will be described in section 2.3.1. The image processing and the quantitative analysis of the fluorescence microscopy data will be described in section 2.3.2.

2.1 Batch production of Ultrabithorax

Ubx was produced and purified using Rosetta strain of *E. coli* using the procedure described in [44]. The genes encoding Ubx fusion proteins were incorporated in a pET-19b plasmid and the expressed protein contained the His tag to enable protein purification using a chromatography column. The *E. coli* Rosetta(DE3) pLysS competent cells (Invitrogen) were transformed with the plasmid incorporating the ampicillin and chloramphenicol resistance genes (plasmids kindly provided by Professor Sarah Bondos). The transformation occurred through a heat shock at 42 °C for 45 s. Following the transformation, all of the LB media, including LB-agar, contained 30 µg L^{-1} chloramphenicol (Sigma Aldrich) and 200 µg L^{-1} ampicillin (Formedium). The transformed cells were placed in 500 µL

of LB-Lennox media with antibiotics, and incubated for 45 min at 37 °C with shaking at 200 rpm. Then, the bacteria were grown overnight at 37 °C on an LB-agar (Miller, purchased from Thermo Scientific) plate with antibiotics. A single colony was transferred into a flask with 50 mL of LB-Lennox media and incubated overnight at 37 °C with shaking at 200 rpm. 7 mL of the culture was added to 1 L of LB-Lennox media with antibiotics, and grown at 37 °C with shaking at 200 rpm for approximately 6 h until the optical density of culture at 600 nm was between 0.6 and 0.7. The Ubx fusion protein expression in the transformed cells was induced from the T7 promoter in mid-log phase by the addition of isopropyl $\beta - \mathrm{d} - 1 -$ thiogalactopyranoside (IPTG) to an effective concentration of 1 mM. The incubation temperature of the culture was decreased to 26 °C, and the culture was grown for 3 h with shaking at 200 rpm. Subsequently, the flasks containing the bacterial culture were placed on ice and the cells were harvested by centrifugation at 3500 rpm and 4 °C for 30 min. The supernatant was decanted, and the cell pellet from a 1 L culture was resuspended in 5 mL of phosphate buffered saline (PBS) and stored at −20 °C until the protein purification.

The base buffer used in cell purification was a "G0 buffer", which contained 50 mM sodium phosphate monobasic, 500 mM sodium chloride, and 5% w/v glucose. The lysis, wash and elution buffers contained the same ingredients as the G0 buffer with added imidazole in a varying concentration between 20 mM and 300 mM. These buffers were referred to as G20, G40, G80, and G300, where the number referred to the concentration of imidazole in mM. The cell pellet was lysed in 40 mL of G20 buffer at pH 8.0 with added: two protease inhibitor cocktail tablets (Roche), 12.5 mM dithiothreitol (Roche), 100 mg lysozyme (Sigma Aldrich), 300 µL of 200 mM $4 - (2 -$ aminoethyl)benzenesulfonylfluoridehydrochloride (Sigma Aldrich), and 320 µL DNase I (Roche). The cell lysate was centrifuged for 30 min at 14 000 rpm at 4 °C. The supernatant was mixed with 5 mL of Pure 100 INDIGO Ni-agarose resin (Cube Biotech) and incubated on a rocking shaker for 1 h to enable the protein binding to the resin. The protein lysate with resin was added to the C 10/20 chromatography column (Cytiva) and the flow of the lysate through the column was controlled by the P-1 peristaltic pump (Cytiva). The resin containing protein bound by the nickel settled at the bottom of the column. It was washed using 50 mL of G0, G20 and G40 buffers, and then 15 mL of G80 buffer. Then, 30 mL of G300 buffer at pH 7.0 was added and the protein elution was collected in approximately 3 mL aliquots. The protein concentration was evaluated with the Bradford assay using the protein assay dye reagent

(Bio-Rad).

2.2 Production of Ultrabithorax fibres through self-assembly

A shallow polytetrafluoroethylene-coated tray with surface area of 450 cm^2 was filled with 1.3 L of the G0 buffer containing 5% w/v glucose, 500 mM NaCl, and 50 mM NaH_2PO_4 in deionised water (G0 buffer) at pH 7.0 when working with pure Ubx and pH 8.0 for Ubx fusions. Between 1.5 and 10 mL of Ubx protein solution containing approximately 20 nmol of Ubx was pipetted onto the surface of the buffer and left undisturbed for 16 h to allow for Ubx film formation [38], after which the surface film was gathered in a smaller area of 90 cm^2 using a polypropylene barrier. A diagram of this process is shown in figure 2.2.1a. The fibres were pulled from the surface film by immersing a 2 cm wide U-shaped aluminium loop, lifting the loop and wrapping the fibre around its edges (figures 2.2.1b and 2.2.1c). The fibres were either stored on the aluminium loops, or fixed onto polysine adhesion slides (Thermo Fisher Scientific) using ethyl 2-cyanoacrylate (Loctite).

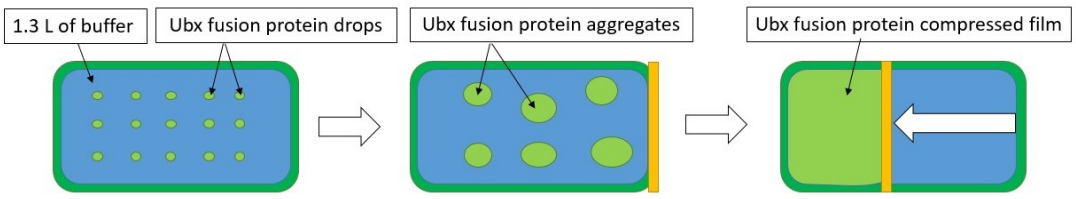

(a)

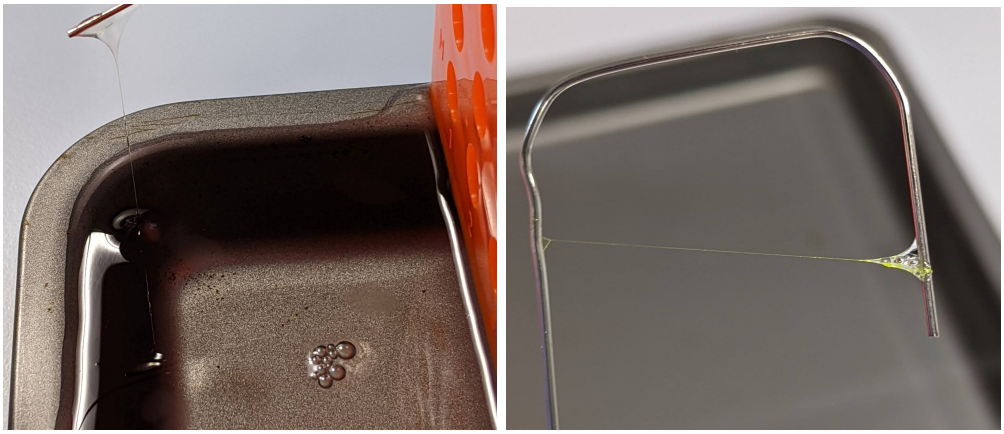

(b) (c)

Figure 2.2.1: (a) The self-assembly of a Ubx protein fusion film and the gathering of the surface film. (b) The fibre pulling process from a self-assembled Ubx fusion protein film. (c) A pulled fibre on the U-shaped aluminium loop.

2.3 Fluorescence and confocal microscopy

Luminescence is the spontaneous emission of radiation due to an electronic or vibrational excitation of a molecule [45]. Fluorescence is a type of photoluminescence (spontaneous emission of visible radiation), which results from the decay of an excited singlet state, a state in which the excited electron has an opposite spin to the highest energy electron in the ground state [46]. Fluorescence often results from the excitation of the sample using light. Single- and multiple-photon excitation can be used, and the emitted photon can have an energy equal to or lower than the combined energy of the photons used to excite the specimen, subject to vibrational and rotational relaxation to the lowest energy vibrational excited state. The return to the ground state is rapid and the fluorescence lifetime is the measure of the average time between the excitation and photon emission. For small molecules, the energies of transitions between the excited and ground states are discrete because of the well defined electronic states. For larger molecules, the electronic levels of different states overlap and continuous fluorescence excitation and emission spectra are observed, which can be measured using fluorescence spectroscopy. The fluorescence spectra of samples contain information about the molecular composition of specimens.

The two main types of light sources used in fluorescence microscopy and spectroscopy are white light sources, the output of which is passed through optical filters before illuminating a sample, and laser sources with a specified wavelength of the output, which can be used to directly illuminate a specimen [47]. While the use of white light provides more freedom in the choice of the range of excitation wavelengths, laser excitation can be used to generate more powerful illumination, and therefore can be preferred for high resolution measurements of small samples or samples with weak fluorescence. The size of the smallest feature distinguishable by a fluorescence microscope in the imaging plane is limited by the Abbe formula:

$$d = \frac{0.61\lambda}{n \sin \alpha}, \tag{2.3.1}$$

where λ is the wavelength, n is the index of refraction and α is the half-angle of the lens aperture. The resolution in the axial plane is lower and is described by the equation:

$$d_z = \frac{1.77\lambda}{n \sin^2 \alpha}. \tag{2.3.2}$$

The poor resolution in the axial direction can be improved with the laser scanning

confocal microscopy, in which the light emitted away from the focal plane is blocked by the addition of pinholes, which generate a diffraction limited spot size of the laser illumination and limit the detection of out-of-focus light by spatially filtering the radiation from the specimen [48]. The corresponding resolution in the focal plane is:

$$d = \frac{0.4\lambda}{n \sin \alpha}, \tag{2.3.3}$$

and in the axial plane the increased resolution is:

$$d_z = \frac{1.28\lambda}{n \sin^2 \alpha}. \tag{2.3.4}$$

The enhanced contrast between focused and out-of-focus light detection in confocal microscopy enables sectioning of the samples in the axial direction and generating Z-stacks, which refer to the stacked images in the direction orthogonal to the focal plane. Z-stacks provide valuable information about the spatial distribution of fluorescent molecules within the samples. Because of its enhanced resolution and the capability for optical sectioning, confocal microscopy was used to quantitatively analyse the binding of fluorescently labelled aptamers and analytes in the experiments described in chapter 5.

In this thesis, the fluorescence microscopy was performed using an inverted Zeiss fluorescence microscope (figure 2.3.1 with a white light source and appropriate wavelength filters applied for both illumination and detection. The confocal microscopy was conducted with a Zeiss LSM 710 laser scanning confocal microscope. The fluorescence and confocal microscopy images were processed and analysed using the open-source ImageJ software [49].

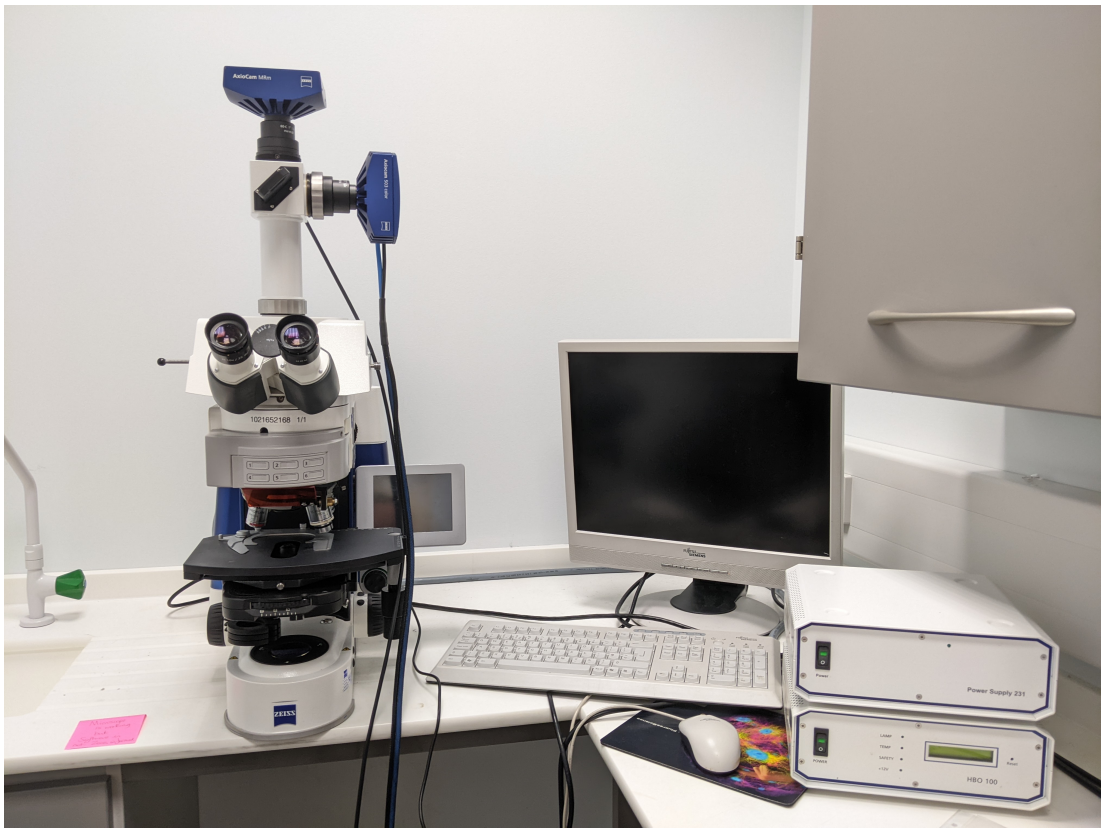

Figure 2.3.1: The Zeiss fluorescence microscope used to collect fluorescence images.

2.3.1 The photoluminescence spectra of Ubx and composite materials

Spectrophotometer measurements of absorbance and fluorescence spectra

200 µL of specified protein or polymer solutions was pipetted into a transparent 96-well plate. The samples were placed in the SpectraMax iD3 Multi-Mode Microplate Reader (Molecular Devices LLC, San Jose, California, United States) and mixed for 5 minutes using the orbital mixing function. A photograph of the spectrophotometer is shown in figure 2.3.2. Absorbance, excitation or fluorescence measurements at appropriate wavelengths were conducted using the 'high precision' setting. The light source was a high power xenon flash lamp and the detectors were a photodiode and a photomultiplier tube. The wavelength resolution available with the plate reader was 1 nm, which is achieved using a monochromator. The available range of wavelengths was: 230 nm to 1000 nm for absorption measurements, 250 nm to 830 nm for fluorescence excitation, and 270 nm to 850 nm for fluorescence emission. For spectral measurements, a separation of 40 nm between the excitation and emission wavelength was recommended, which restricted the available range of wavelengths for excitation of fluorophores.

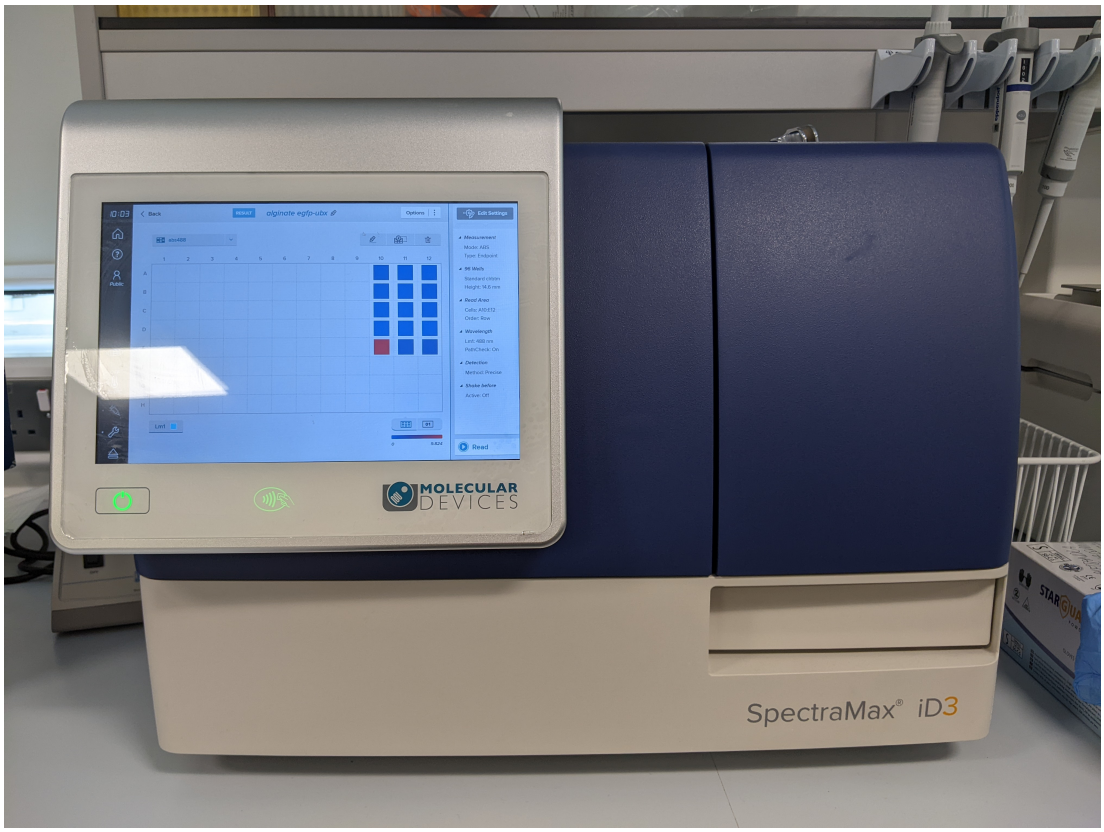

Figure 2.3.2: The SpectraMax iD3 Multi-Mode Microplate Reader used to measure the optical excitation and emission spectra of protein and biomaterial solutions.

Steady-state photoluminescence spectra

The steady-state and time-resolved photoluminescence (PL) spectra provide useful information about the sample composition and intrinsic optical and structural properties. Steady-state measurements are conducted with constant sample illumination, while time-resolved measurements require an excitation light pulse shorter (normally on the picosecond scale) than the decay time of the sample, and a detection system capable of capturing photons with a matching time resolution [46]. Steady-state measurements provide averaged spectral photoluminescence data, while time-resolved spectroscopy yields detailed information about fluorescence lifetimes of the specimens.

The steady-state PL spectra were measured on solid samples (fibres and films) fixed to a polysine glass slide. An ultrafast laser light source (Pharos PHM02-2H-3H) with a pulse duration of 300 fs, repetition rate of 25 kHz, and 50 µm spot size was used for optical excitation of Ubx fusion fibres and composite films at 343 nm. A photograph of the light source is shown in figure 2.3.3. The collimated sample photoluminescence was filtered to remove scattered light and focused into the Photonic Multichannel Analyzer (Hamamatsu C10027-02). The only two laser wavelengths available for sample excitation were 343 nm and 515 nm, which restricted the range of possible spectral measurements. 343 nm was chosen as the primary excitation wavelength due to its ability to excite both dityrosine and the appended fluorescent proteins in Ubx fusions, EGFP and mCherry. However, this choice limited the excitation efficiency of both the fluorescent proteins (see figure 3.1.1 for their excitation spectra). These measurements were conducted with the help of Dr Drew Riley at Swansea University.

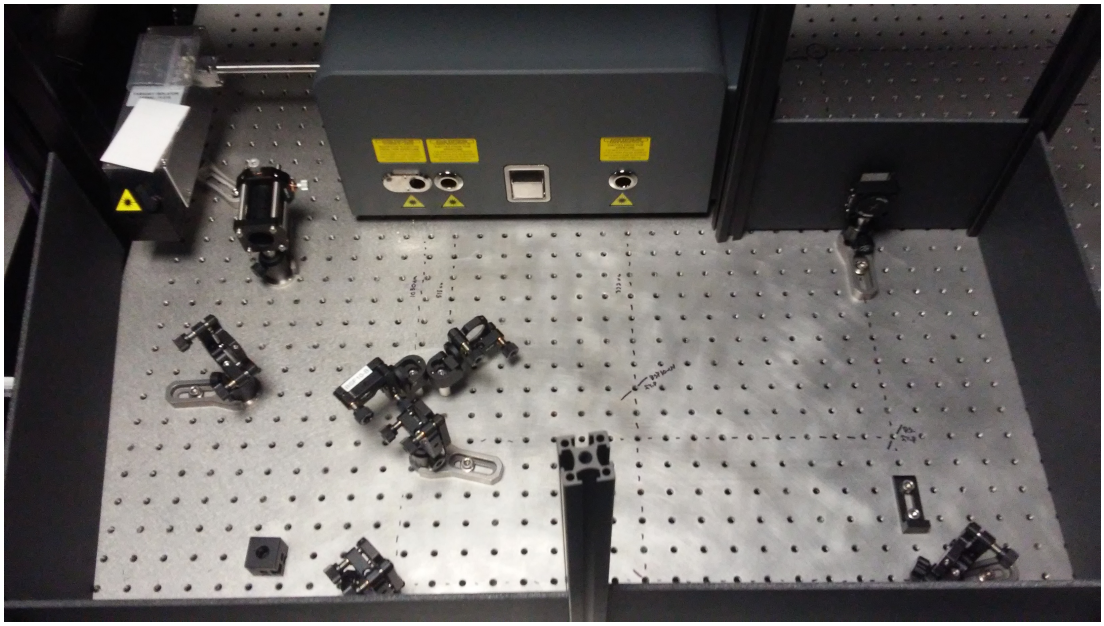

Figure 2.3.3: The Pharos PHM02-2H-3H ultrafast laser light source and the optical setup for photoluminescence excitation. Image courtesy of Dr Drew Riley at Swansea University.

2.3.2 The image processing and measurements of fluorescence intensities using ImageJ software

The images were processed using the selection, thresholding, masking, measurement, and analyse particles functions of the ImageJ software (FIJI version). These functions were used to measure the size of fibres, their average fluorescence intensity in the different measurement channels, and the fluorescence intensity and percentage area occupied by bright fluorescence regions within the fibre region of interest (ROI). The processing methods will be described and illustrated in this section.

Fibre size measurement

Following fibre production using the process described in section 2.2, the fibres were imaged under the fluorescence microscope. The fibre diameters were measured using the FIJI version of the ImageJ open-source image processing software by selecting the Straight-line segment stretched across the fibre. Then, measurements of the length and fluorescence intensity of the straight-line segments were taken. An illustration of a measurement of the fibre diameter is shown in figure 2.3.4.

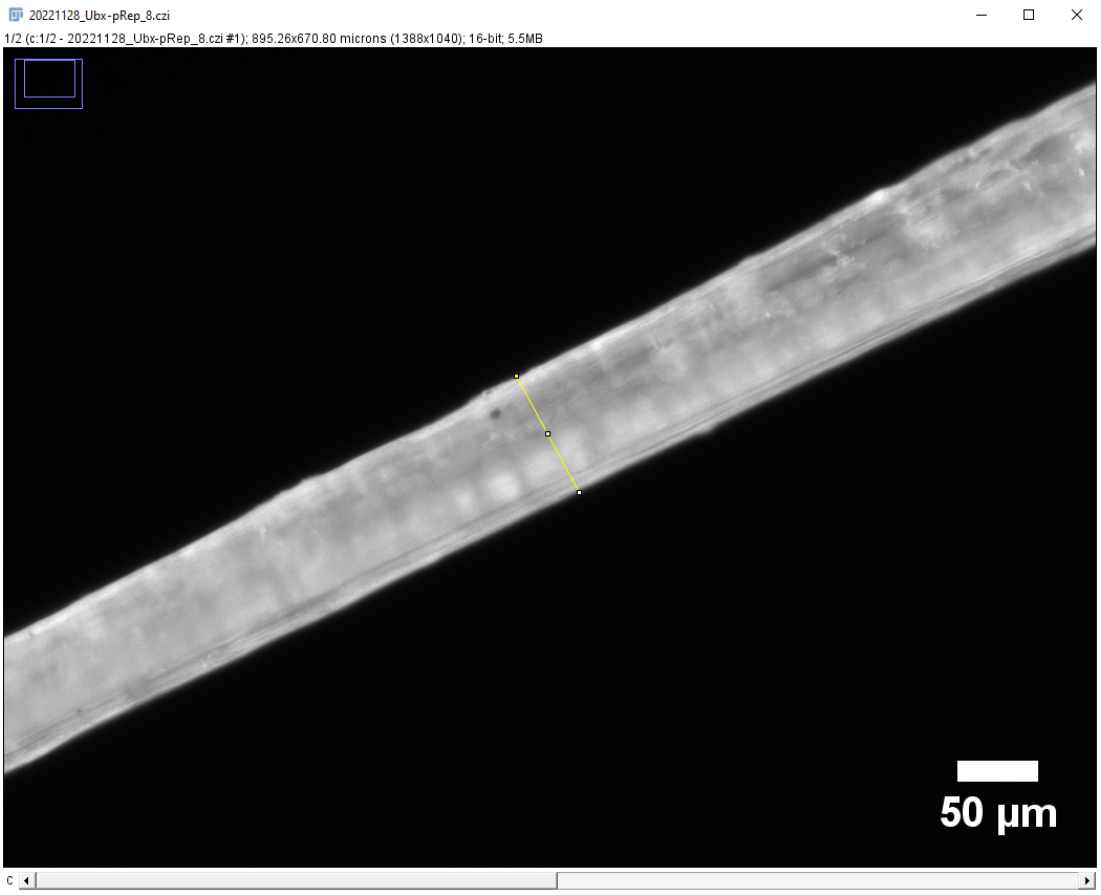

Figure 2.3.4: A measurement of the fibre diameter using ImageJ software. Measurements were taken in at least three parts of the fibre and the average of the measurements was used for analysis.

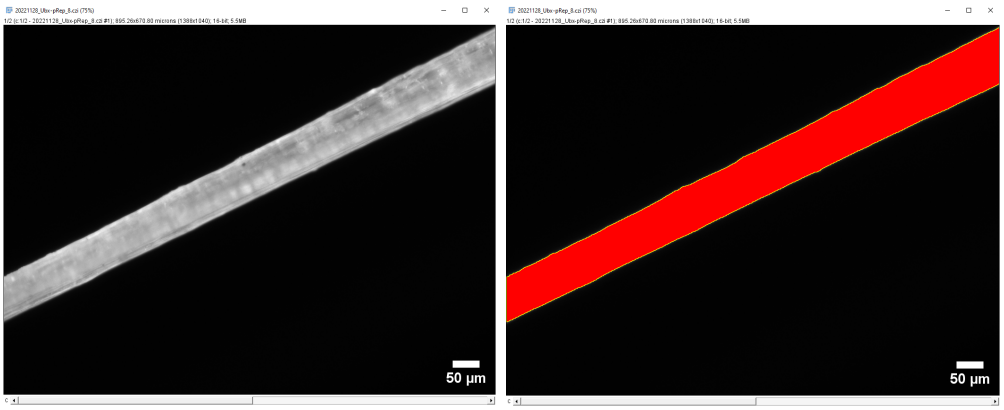

(a) (b)

Figure 2.3.5: A measurement of the average fluorescence intensity across the fibre using ImageJ software. (a) Fluorescence micrograph of a fibre before thresholding and selection of the region of interest. (b) A mask created using thresholding of the fluorescence intensity and the 'Create selection' function in the ImageJ software.

Measurements of average fluorescence intensity across the fibre

The measurements of average fluorescence intensity of fibres were used for selection of fibres with similar size and fluorescence intensity. These measurements also enabled a quantitative comparison of the fluorescence intensity in different fluorescence channels with or without treatment with separate reagents, which was used extensively in the experiments involving binding DNA aptamers in chapter 5. This measurement required the thresholding of the fluorescence intensity and the creation of a mask, which were performed using the 'Threshold' and 'Create Selection' functions in the ImageJ software. An example of a fibre and the respective mask is shown in figure 2.3.5. The Threshold function selected the pixels in the micrograph with the fluorescence intensity above the threshold determined by the MaxEntropy algorithm, which uses the entropy of a grayscale image to establish the threshold [50]. This function was found empirically to highlight the pixels within the micrograph that corresponded to the fibre fluorescence. An empirical testing of the thresholding methods also revealed that this method allowed the detection of bound analytes in the aptamer binding experiments (chapter 5). The function Create Selection produced a selection of the pixels picked in the thresholding process.

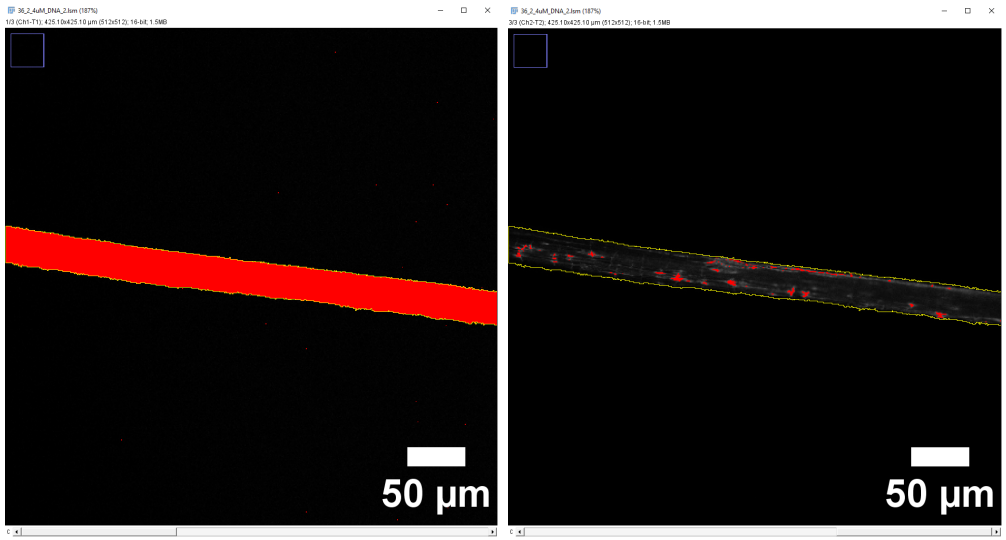

(a) (b)

Figure 2.3.6: A measurement of the fluorescence intensity and percentage area occupied by bright regions within the masked fibre using ImageJ software. (a) A mask created using thresholding of the fluorescence intensity and the 'Create selection' function in the ImageJ software. (b) The bright regions within the fibre ROI selected using a thresholding of fluorescence in the channel of interest.

Measurements of the fluorescence intensity and percentage area occupied by bright fluorescence regions within the fibre ROI

In order to quantify binding of fluorescently labelled aptamers and analytes, the fluorescence intensity and the fraction of fibre area occupied by the bright regions in the channel corresponding to the attached fluorescent label were measured. This process included selecting the fibre ROI as described in section 2.3.2. Subsequently, thresholding of the fluorescence within the masked ROI was performed in the relevant fluorescence channel (normally, the channel corresponding to the fluorescent label of analytes bound to fibres). Then, the measurement of the fluorescence intensity and the percentage area of ROI above the threshold was performed using the 'Analyze Particles' function of FIJI [49], which created outlines of the objects with brightness above the threshold, and then performed individual and group size and intensity measurements on these objects. An illustration of this process is shown in figure 2.3.6.

Chapter 3

Electrical conductivity and optical properties of Ultrabithorax fibres

3.1 Introduction

This chapter will describe the measurements of steady-state and time-resolved photoluminescence spectra of Ubx fusion materials. The spectra were measured for Ubx fusions with an iron- and oxygen-binding protein myoglobin, and fluorescent proteins EGFP and mCherry. The spectral properties, fluorescence lifetimes, and energy transfer were investigated in this chapter. Then, the electrical conductivity of Ubx, EGFP-Ubx, and myoglobin-Ubx was measured both in ambient conditions, and with changing relative humidity. Probe station measurements and impedance spectroscopy were used to test the electrical properties of Ubx materials. This section will describe the optical biosensing methods and review the optical properties of proteins used in this work and relevant literature. Then, the electrical properties of protein materials will be reviewed along with aspects of impedance spectroscopy relevant for this work. Finally, literature on properties of Ubx materials will be discussed, and the experiments will be outlined.

3.1.1 Optical properties of protein materials and biosensing

Protein materials are an important group of biomaterials with ubiquitous applications in biosensing and tissue engineering. The range of methods of protein material formation, along with their intrinsic biocompatibility, make them functional in biological environments. Monitoring the functions of protein materials, and the ability to monitor other cellular and molecular processes, requires the use of biosensing techniques and the prior knowledge of the physical properties of protein materials. The basic properties of interest in biosensing include optical properties such as the fluorescence lifetime, light absorption profile, and photoluminescence excitation and emission spectra. Electrical properties such as the electrical conductivity are also of interest. There are a range of optical biosensing techniques that make use of these properties. Spectroscopy provides useful information about the molecular constituents of protein materials and the environment, in which the molecule is located. Fluorescence quenching is a phenomenon of the fluorophore activity decreasing due to the presence of a quencher, which decreases the intensity of emission. A similar technique is fluorescence recovery after photobleaching (FARP), which removes the fluorescence of the probe by a photochemical reaction, and then monitors the molecular dynamics and replenishing of the molecular species responsible for fluorescence. This technique is used in monitoring diffusion and protein binding. Fluorescence quenching can be used to detect protein or membrane binding. Förster resonance energy transfer (FRET) is another technique that can be used to detect molecular binding of molecules such as proteins. Its basis is the energy transfer due to dipole-dipole interactions between molecules with a large overlap between the emission spectrum of the donor and the excitation spectrum of the acceptor molecule. This energy transfer only occurs at small distances up to approximately 6 nm, which makes FRET highly sensitive to bound molecules. Fluorescence lifetime imaging microscopy (FLIM) is a technique sometimes combined with FRET. FLIM measures the fluorescence lifetime in different parts of the sample, which enables the distinction between the molecular species present in these parts of the sample where the fluorescence intensity data from regular fluorescence microscopy would be insufficient to distinguish between them [46].

Since their discovery, fluorescent proteins have been widely used in studies of intercellular interactions and cell activity. The genetic mutants of wild type fluo-

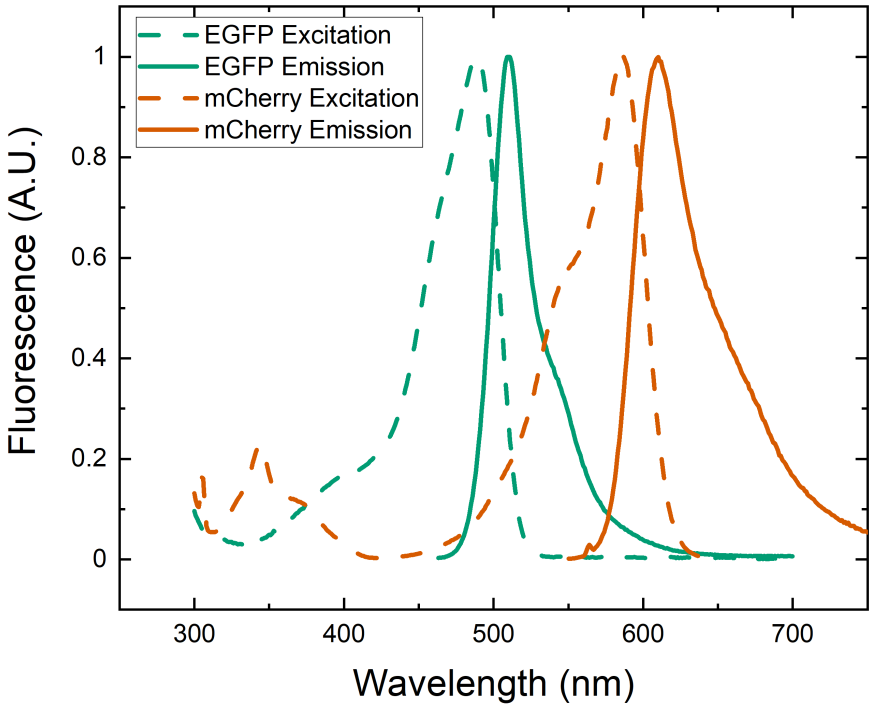

Figure 3.1.1: The fluorescence excitation and emission spectra of EGFP and mCherry in solution (reproduced from [51, 52, 57]).

rescent proteins exhibit more desirable optical properties such as higher quantum yield, and narrower or shifted fluorescence excitation and emission spectra. Examples of such modifications to fluorescent proteins include the enhanced green fluorescent protein EGFP [51] and the red fluorescent protein variant mCherry [52], whose fluorescence spectra were shown in figure 3.1.1. The fluorescence decay of EGFP and mCherry observed in time-resolved measurements was either bi- or tri-exponential for single- and two-photon excitation [53, 54]. The fluorescence lifetimes of EGFP with 405 nm excitation wavelength were strongly dependent on the emission wavelength, with reported values of 40 ps, 210 ps and 500 ps at 440 nm, and significantly increased lifetimes of 120 ps, 600 ps and 2.8 ns at 510 nm [53]. Meanwhile, the fluorescence decay of mCherry was biexponential when measured at 543 nm excitation and 610 nm emission, with measured lifetimes of 0.7 ns (10%) and 1.6 ns (90%) [55]. Dominating longer component in the biexponential decay of mCherry was confirmed, but with higher lifetimes of (0.90 ± 0.08) ns and (1.94 ± 0.07) ns [56].

Dityrosine was previously used to study the oxidation of protein materials. Its intrinsic fluorescence is a useful indicator of the progress of oxidation in processes such as cross-linking and other material formation methods. The properties of dityrosine fluorescence were reviewed [58]. Absorption spectra of free dityrosine changed with the pH and the constitution of the buffer, however the emission spectra had a maximum at 409 nm regardless of the buffer. The reported excited state lifetime for free dityrosine was 4.3 ns. Another study of dityrosine samples indicated a fluorescence emission peak at 400 nm whose position was also independent of the buffer pH [59]. However, this study reported two components of the fluorescence decay. In the emission range between 350 and 430 nm, the shorter lifetime component dominated at shorter wavelengths while the longer lifetime component prevailed at longer wavelengths. The two decay constants of dityrosine ranged between 0.06 and 1 ns, and 4.0 to 4.4 ns. The properties of dityrosine fluorescence in biological materials differ from those of free dityrosine. The dityrosine chromophores present in outer walls of yeast spores underwent a bimodal fluorescence decay with a 404 nm emission peak when excited at 323 nm [60]. The measured lifetimes were 0.5 ns and 2.6 ns. When both the excitation and emission wavelengths were increased to 350 nm and 430 nm, a broader lifetime distribution centred at 2.1 ns was observed. These measurements provide valuable reference for the determination of the fluorescence properties of Ubx materials investigated in this study. The dityrosine fluorescence excitation and emission spectra are shown in figure 3.1.2.

Myoglobin is another protein of interest both due to its biological function as an iron and oxygen transporting protein, and its applications in biosensing. The fluorescence activity of myoglobin was attributed to the presence of tryptophans, which exhibited a tri-exponential fluorescence decay in the time-resolved fluorescence studies (decay components: 14 ps, 106 ps, and 2.68 ns) [62]. The study of the apo and met states of myoglobin revealed a triexponential fluorescence decay with longer lifetimes of 135-342 ps, 1.16-1.75 ns and 3.16-5.19 ns for apomyoglobin, and 16-28 ps, 790-823 ps and 2.90-3.34 ns for metmyoglobin [63]. The myoglobin fluorescence activity occurred predominantly in the UV region, with emission peaks between 320 and 335 nm at 265 nm excitation [62]. Interestingly, myoglobin absorbance was also reported at approximately 550 nm (figure 3.1.3) [64].

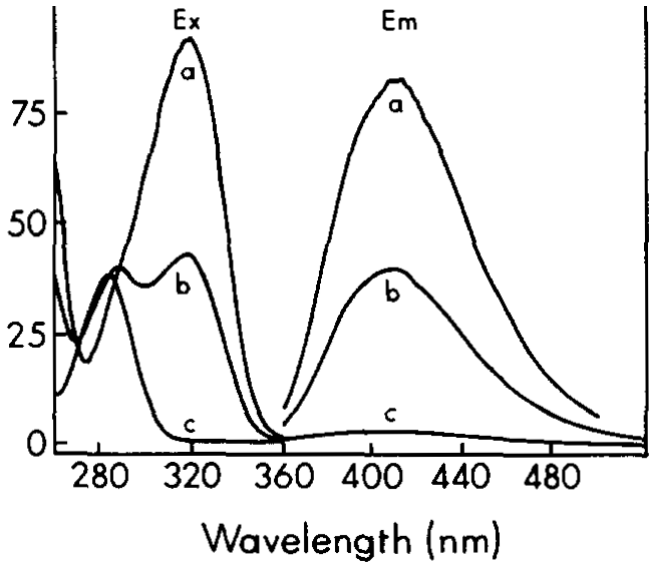

Figure 3.1.2: The fluorescence excitation and emission spectra of dityrosine in solution at a concentration of 3 µM at pH (a) 9.3, (b) 7.0, and (c) 3.7 (reproduced from [61]).

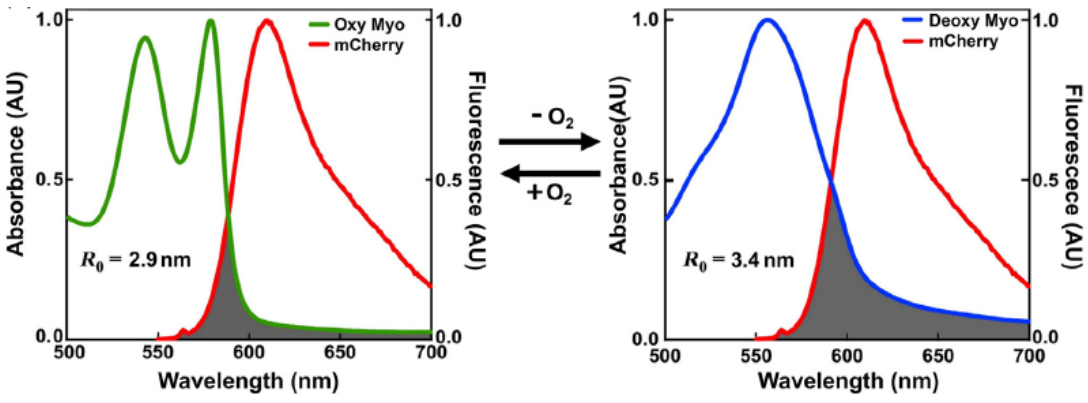

Figure 3.1.3: The absorption spectrum of oxygenated and deoxygenated myoglobin (reproduced from [64]).

3.1.2 Protein fusions and their applications in biosensing

Protein fusions have a variety of applications in biosensing, diagnostics, and biomedical materials. FLIM is a technique widely used to study cellular dynamics and interactions [64, 65]. The intracellular mitochondrial oxygenation level was measured using a FRET probe with mCherry acting as the donor, and the non-fluorescent myoglobin as an acceptor [64]. The myoglobin absorption spectrum shifted after oxygenation, which reduced its spectral overlap with mCherry emission, consequently reducing the fluorescence intensity and lifetime of mCherry in the probe. A consistent increase in both components of the fluorescence lifetime of mCherry was observed in the oxygenated cells compared to no change for a probe containing only mCherry, which implied the detection of intracellular oxygenation. More recently, measurements of the fluorescence lifetime of EYFP in a double fusion of EYFP-myoglobin-mCherry were used to selectively detect metmyoglobin production [65], while the ratio of the EYFP to mCherry fluorescence intensity was used to measure the intracellular oxygenation. The use of this modified probe provides a pathway to detect the presence of nitric oxide and reactive oxygen species, which are important markers of oxidative stress involved in the development of cardiovascular disease and cancer [66]. FLIM was used to study protein-protein interactions in cells and the role of proteins in cell apoptosis [67] and DNA repair following laser-induced damage [68]. Therefore, fluorescent protein-based systems have been used in conjunction with FLIM to elucidate a range of live cell properties, which paves the way to sensing applications *in vivo*.

Fluorescent protein biosensing can be used to monitor cell activity and track the cell cycle using FLIM. FLIM shows how the fluorescence lifetime of GFP and tdTomato reporter proteins decreases rapidly following cell division [69]. Fluorescent proteins have also been used as reporters of cellular toxicity [70]. Toxicity detection can be realised with several approaches including fluorescence labelling, membrane integrity testing and inducible protein expression. Monitoring toxicity and cytocompatibility characteristics of biomaterials would allow the application of composite or protein fusion materials *in vivo*. Protein fusions incorporating fluorescent proteins can be used to monitor biomaterial-tissue interactions with already existing techniques, while other constituents of the protein fusions can serve their respective functions. FLIM measurements revealed that cytosolic and membrane-bound GFP acts as a refractive index sensor for intracellular environments, which means that the fluorescent probes can be used as either protein

localisation or intracellular condition sensors [71].

3.1.3 Electrical properties of protein materials

Impedance spectroscopy measurements were conducted in this thesis. Impedance spectroscopy is used to describe the charge transfer properties both in biomaterials and electronics [43,72]. The impedance model commonly used to fit impedance spectroscopy data is the Randles equivalent circuit [73] shown in figure 3.1.4. This circuit has been used to describe the impedance spectra of electrochemical cells and impedimetric sensors [72]. Its characteristic parameters are the presence of the double-layer capacitance C, the contact resistance R_u, the charge-transfer resistance R_{ct} within the sample, and a diffusive element called the Warburg element Z_w. This circuit is commonly used in the analysis of impedance spectra, and a modified version of the Randles circuit with the Warburg element exchanged for a more general constant phase element was used to analyse impedance spectra in this thesis.

The intrinsic electrical conductivity of biomaterials is strongly dependent on environmental factors such as temperature and relative humidity. A comprehensive review of hydration strategies and their effect on the electrical conductivity of biomaterials showed that the control of relative humidity enabled the determination of charge transfer properties [43]. Humidity-dependent measurements were particularly important in distinguishing between electrical conductivity of the electronic or ionic nature, which are due to the transfer of charged electrons or ions, respectively. Samples with electronic charge transfer mechanism exhibited small changes in the electronic conductivity with rising humidity. However, biomaterials exhibiting ionic conductivity experienced a large increase in electrical conductivity (up to 8 orders of magnitude) with sample hydration. This review stressed the importance of controlling the relative humidity in measurements of electrical properties.

The electrical conductivity of protein materials is relatively low compared to widely used synthetic and inorganic materials. This section will give an overview of the measured values of electrical conductivity of protein materials and the functionalisation strategies that enable enhancing the conductivity. A range of functionalisation methods, including nanofunctionalisation with carbon nanotubes, Au and Ag nanowires and nanoparticles, were used to enhance the electrical properties of materials made with proteins such as silk, collagen and hyaluronic acid.

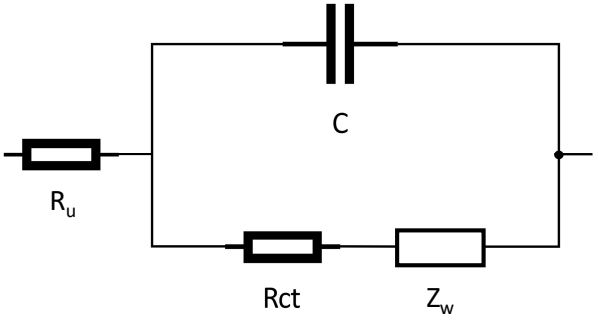

Figure 3.1.4: The Randles equivalent circuit [73] commonly used in the analysis of the impedance spectroscopy data, particularly in application to electrochemical cells and impedimetric biosensors [72].

The low electrical conductivity of protein materials was measured for hyaluronic acid and collagen films with maximum values at $0.1\,\mathrm{mS\,m^{-1}}$ and $1\,\mathrm{pS\,m^{-1}}$, respectively [74]. The electrical conductivity of both hyaluronic acid and collagen films also exhibited a strong temperature dependence between -50 and 40 °C [74].

A coagulated protein composite of silk and cellulose was shown to have an ionic electrical conductivity increasing with the β-sheet content in the material. The electrical conductivity ranged from approximately $0.1\,\mathrm{\mu S\,m^{-1}}$ to $0.1\,\mathrm{S\,m^{-1}}$, depending on the coagulation agent [75]. Other studies used carbon nanotube functionalisation to achieve the electrical conductivity of silk nanofibroin sheets of up to $2\,\mathrm{kS\,m^{-1}}$, and silk and cotton yarns of $11\,\mathrm{S\,m^{-1}}$ and $0.4\,\mathrm{S\,m^{-1}}$, respectively [76, 77]. A modest increase of electrical conductivity from $0.3\,\mathrm{S\,m^{-1}}$ to $0.7\,\mathrm{S\,m^{-1}}$ with added carbon nanotube content was also observed for collagen hydrogels [78].

Silk microfibres with diameters of the order of 10 µm were shown to have low electrical conductivity that rapidly increased with relative humidity up to about $0.1\,\mathrm{mS\,m^{-1}}$ at 70% relative humidity [79]. The functionalisation of silk microfibre-based textiles with Ag nanowires can reduce their surface electrical resistance by multiple orders of magnitude down to $1\,\mathrm{k\Omega}$, while also lending the material enhanced antimicrobial properties [80].

More widely, biopolymers such as alginate can be used to create tissue scaffolds that have the desirable biocompatibility and porosity for clinical applications.

These scaffolds are functionalisable by nanomaterials such as Au nanowires to facilitate muscle contraction for cardiac tissue engineering [27]. The nanofunctionalisation significantly increased the electrical conductivity and decreased the impedance across a range of frequencies, which addressed the electrical conductivity issues encountered with other collagen and biopolymer scaffolds [27].

3.1.4 Electrical and optical properties of Ubx materials

Ubx materials exhibit autofluorescence with an emission peak at 438 nm due to the dityrosine bonds when excited with a light source at 305 nm. This peak is red-shifted compared to the dityrosine fluorescence in solution, which has a peak at 400 nm [81]. The red-shift for dityrosine bonds might be caused by the positively charged amino acids located nearby the bonds [82]. Previous fluorescence studies revealed that functional proteins, such as the fluorescent proteins EGFP and mCherry, retain their functionality in materials created using EGFP-Ubx and mCherry-Ubx protein fusions [17, 26]. The same studies also showed that EGFP and mCherry had their characteristic fluorescence peaks in EGFP-Ubx and mCherry-Ubx fibres at 507 nm and 610 nm, respectively. However, the electrical properties of Ubx materials, including their electrical conductivity, had not previously been studied in detail. Therefore, the present work addresses the need to measure the basic electrical and optical properties of Ubx materials to explore their range of potential applications. It also explores some of the environmental parameters associated with strong changes in optical and electrical properties, such as the effect of relative humidity on the electrical conductivity of fibres, which could be important in biomedical applications. Herein, a strong increase of the electrical conductivity with rising relative humidity was found. Additionally, the functional stability of the fluorescence of protein fusions of Ubx with fluorescent proteins, EGFP and mCherry, was confirmed. The optical properties of Ubx fusions were measured in a range of conditions and the spectral characteristics and the energy transfer were investigated. These measurements, along with the summary of protein and biopolymer properties, inform potential applications and functionalisation strategies for biosensing and tissue regeneration. The lifetime measurements and humidity-dependent impedance spectroscopy could be of particular importance for biosensing because of the availability of techniques such as FLIM, FRET, and impedimetric biosensing.

3.2 Experimental section

3.2.1 The optical properties

Fluorescence spectra measurements of Ubx fusions in solution

The fluorescence emission spectra of Ubx, EGFP-Ubx, mCherry-Ubx, and myoglobin-Ubx solutions were measured using 343 nm excitation wavelength using the spectrophotometer described in 2.3.1. The Ubx fusion solutions were prepared in the G0 buffer in a 1:20 ratio. The concentrations of the protein fusions before dilution were: 5.45 µM for Ubx, 16.53 µM for EGFP-Ubx, 21.25 µM for mCherry-Ubx, and 2.13 µM for myoglobin-Ubx.

Time-resolved photoluminescence spectra

These measurements were conducted on fibres or sheets fixed to a polysine glass microscope slide. An ultrafast light source (Pharos PHM02-2H-3H) with a pulse duration of 300 fs, repetition rate of 25 kHz, and 50 µm spot size was used for optical excitation of Ubx fusion fibres at 343 nm. The collimated sample photoluminescence was filtered to remove scattered light and focused into the Hamamatsu C14831 Streak Camera for the temporal and spectral photon integration measurements that yielded the time-resolved photoluminescence spectra (TRPL). The optics used in collecting the sample photoluminescence are shown in figure 3.2.1. The temporal resolution of the measurements increased with the time scale measured, and was 13.2 ps for a measurement with a 2 ns time window and 77.6 ps for a measurement with a 10 ns time window. The spectral resolution of the instrument was approximately 0.05 nm/pixel. The low repetition rate ensured that the full fluorescence decay of the sample could occur in the time between the excitation pulses. As mentioned previously in section 2.3.1, the only available laser excitation wavelengths were 343 nm and 515 nm. The former wavelength was chosen as the primary excitation source to ensure that both dityrosine autofluorescence and the fluorescence of appended proteins EGFP and mCherry could be measured. However, this put a constraint on the excitation efficiency of mCherry and, to a lesser extent, EGFP. These measurements were taken with the help of Dr Drew Riley of Swansea University.

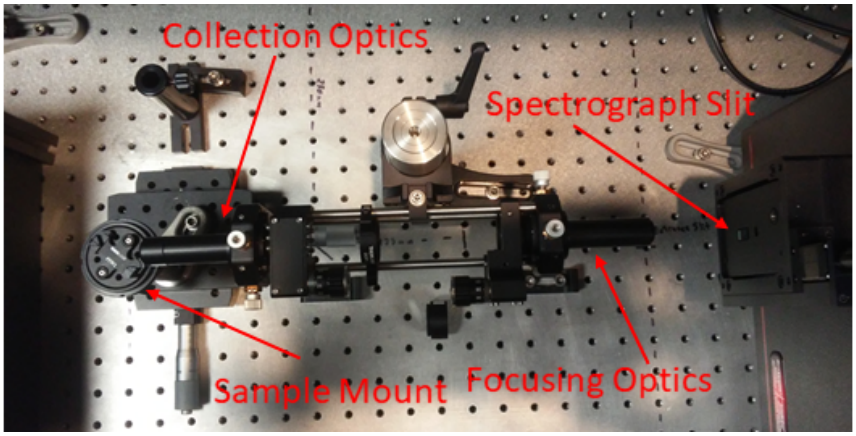

Figure 3.2.1: The optics used to collect the sample photoluminescence in the time-resolved photoluminescence spectra. Image courtesy of Dr Drew Riley of Swansea University.

3.2.2 Data analysis of the optical properties

The full width at half maximum of photoluminescence spectra

The measurements of the full width at half maximum (FWHM) of the emission spectra of Ubx fusion fibres were conducted using the Origin software (version 2020b, OriginLab Corporation, Northampton, MA, USA). The 'Peak Analyzer' function was used. The data was smoothed using a 10-point smoothing filter, and the peaks were identified in the Find Peaks section. The Peak Integration function allowed the measurements the following measurements for each individual peak: the peak centre, the FWHM, and both the beginning and ending wavelength. Figure 3.2.2 shows an example of the use of the Peak Analyzer and the identified peaks and boundaries in an emission spectrum of an EGFP-Ubx fibre.

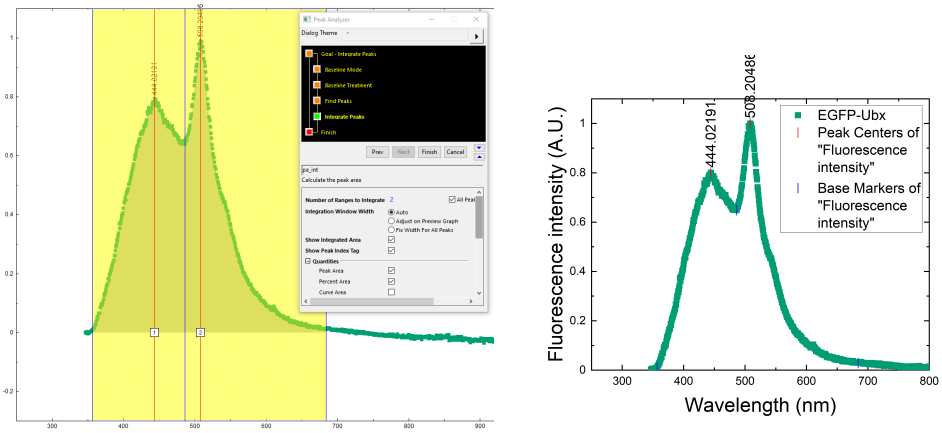

(a) (b)

Figure 3.2.2: (a) An example showing Peak Analyzer function used to identify peak wavelength and FWHM in an EGFP-Ubx fibre photoluminescence emission spectrum. (b) The identified peak and boundaries on the emission spectrum.

The analysis of the time-resolved photoluminescence spectra

The time-resolved photoluminescence spectra were imported into the Origin software and the horizontal profile was plotted to analyse the fluorescence decay in the selected wavelength range. Multiexponential fits were chosen from the 'Exponential fit' function to determine the fluorescence lifetime decay, and the time constants were extracted using the Exponential Decay ('ExpDec') function with up to three time constant parameters. The fit was performed with the logarithmic y-scale to highlight the differences between the multiexponential fits and enable the choice of the best fit for the sample using the R-square characteristic. An example of the fitting process is shown in figure 3.2.3.

After the calculation of the Ubx protein fusions lifetimes, the average decay times τ were calculated using the formula $\tau = \sum A_i \tau_i$, where A_i is the pre-exponential coefficient corresponding to an exponential decay with a time constant τ_i. Then, the FRET efficiency E could be calculated using equation 3.2.1 [46]:

$$E = 1 - \frac{\tau_{DA}}{\tau_D}, \tag{3.2.1}$$

where τ_{DA} is the fluorescence lifetime of the donor in the presence of the acceptor and τ_D is the lifetime in the absence of the acceptor. The energy transfer between dityrosine as the donor and EGFP or mCherry as acceptors was estimated using

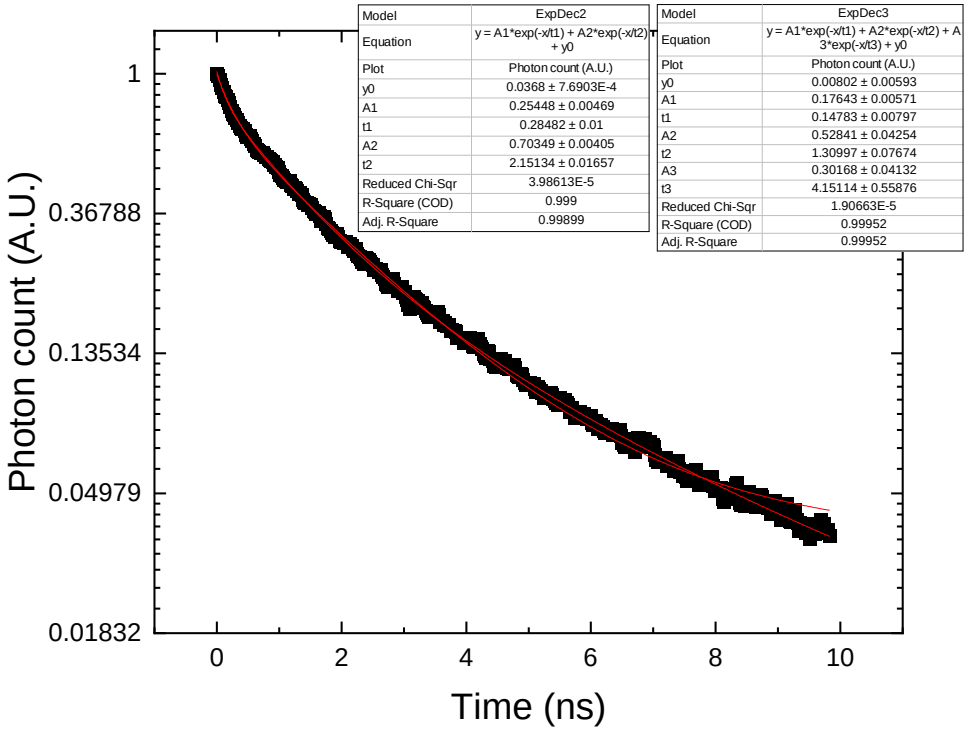

Figure 3.2.3: A sample fluorescence time decay for an mCherry-Ubx fibre. Multiexponential fits were performed to the data and the fit with the best R-square characteristic was chosen.

this method.

3.2.3 The electrical properties

Probe station DC electrical current measurements

An Everbeing probe station shown in figure 3.2.4 was used for direct current (DC) measurements. 2-probe measurements were performed using two high resolution probes and a Keysight B1500A semiconductor device parameter analyser with a 2 fA and 2 mV resolution. The current-voltage (I-V) dependence was measured with a voltage sweep, which included both negative and positive applied potential differences. The potential difference was applied to one of the probes, and the resulting current was measured at the second probe. The electrical contact between the probes and the sample was achieved by directly lowering the probes onto the fibres. The Dino-Lite USB microscope ensured contact and photographed the fibre-probe system. Then, the probe separation along the fibre was measured with the segmented line function in the ImageJ (FIJI) software [49]. The probe separation was approximately 300 µm for these measurements.

Electrical properties measurements with changing relative humidity

Preliminary tests to measure the effect of varying humidity and sample hydration were performed using two methods. The first method involved storing the fibres in a polystyrene box with warm water for 30 minutes prior to the measurements. The second method included measuring the electrical conductivity in ambient conditions, followed by a measurement directly after a rapid deposition of water vapour onto the sample without strict humidity control.

Following the preliminary tests, a more rigorous examination of the effect of the relative humidity on the electrical conductivity of fibres was performed. Ubx protein fusion fibres fixed to the polysine adhesion slides were placed inside the vacuum chamber of a FWPX cryogenic probe station (Lake Shore). Multiple fibres were placed on a single slide to allow for the direct comparison of data at a given relative humidity. Vacuum pumps were used to achieve a sub-1 mbar absolute measured pressure. Water vapour was injected into the system to increase the relative humidity before the samples were allowed to equilibriate for 1 hour. The probes were lowered directly onto the fibre to establish electrical contact. The probe separation and the contact were monitored and measured using a USB microscope. The AC impedance measurements, in the frequency range between 0.1 Hz and 1 MHz, with 0.5 V amplitude, were performed using the Autolab device (Metrohm). The DC current was measured as a function of

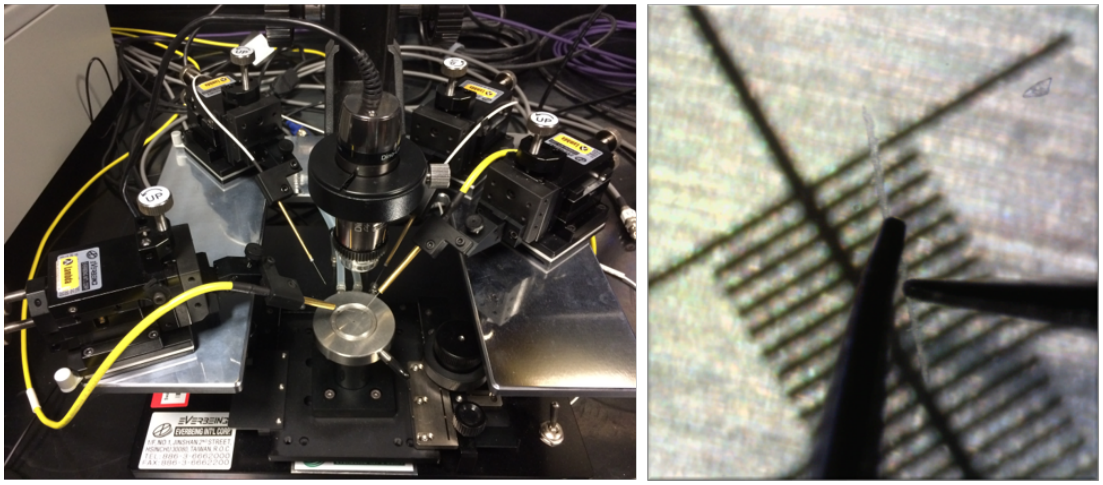

Figure 3.2.4: An Everbeing probe station (left) with high resolution probes used for the measurements of the DC current-voltage characteristics of Ubx fusion fibres. A micrograph of a fibre (right) with the probes forming an electrical contact.

voltage between $-1\,\mathrm{V}$ and $1\,\mathrm{V}$ using a Keysight B2962A source meter unit. A photograph of the cryogenic probe station and a micrograph of a fibre and the probes forming an electrical contact are shown in figure 3.2.5. The typical probe separations at low relative humidity were between $50\,\mu\mathrm{m}$ and $100\,\mu\mathrm{m}$, and at high relative humidity they were up to $1.5\,\mathrm{mm}$.

The saturation vapour pressure P_s of water at the ambient temperature T was calculated using the formula [83], given by equation 3.2.2:

$$P_s = 6.112121 \exp\left\{\frac{17.502T}{240.97 + T}\right\}. \tag{3.2.2}$$

The relative humidity (RH) at a given vapour pressure P was calculated with $RH = \frac{P}{P_s}$.

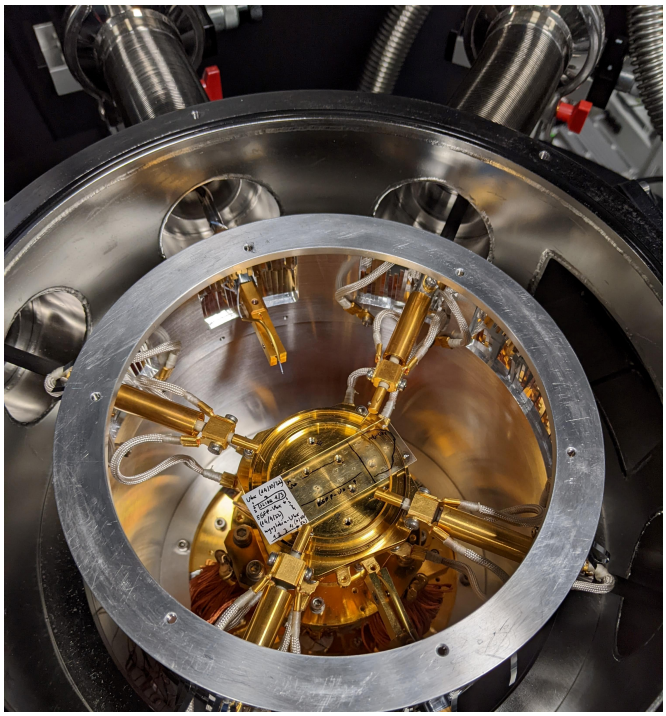

(a)

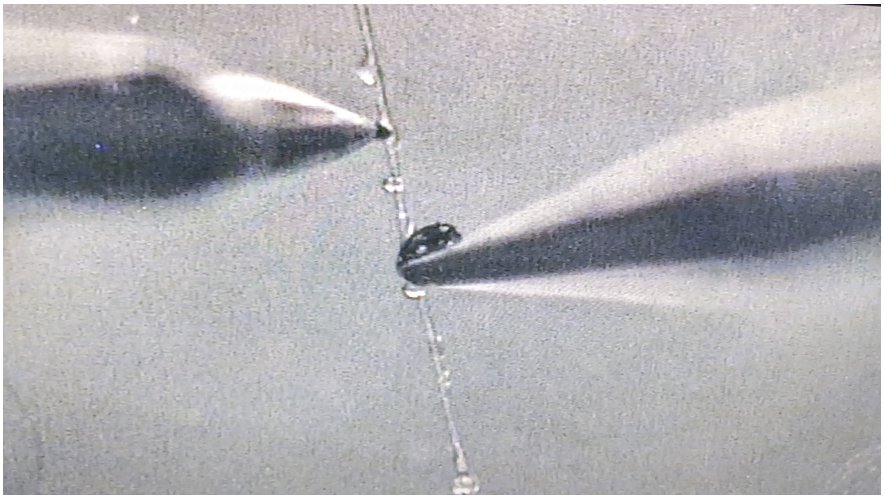

(b)

Figure 3.2.5: (a) The vacuum chamber of the cryogenic probe station with the fibres mounted on the microscope slide. (b) A USB micrograph of a fibre and the probe forming an electrical contact. Condensation of the water vapour on the fibre is visible due to the high relative humidity.

3.2.4 Data analysis of the electrical properties

The electrical conductivity in DC probe station measurements

After the measurement of a current-voltage characteristic using the method described in section 3.2.3, the I-V curve was created and a linear fit was performed using the function *fitlm* in MATLAB [84]. A sample current-voltage curve and the straight line fit to the data for a Ubx fusion fibre is shown in figure 3.2.6. The Ohm's law $I = \frac{V}{R}$ was used to calculate the resistance of the fibre, and subsequently the electrical conductivity σ of the fibre was calculated using equation 3.2.3:

$$\sigma = \frac{1}{R}\frac{l}{A}, \tag{3.2.3}$$

where R is the electrical resistance of the fibre, l is the probe separation, and A is the cross-sectional area of the fibre, where a circular cross-section with the diameter equal to the diameter of the fibre was assumed.

Data fitting to the impedance model based on the Randles circuit

The impedance spectroscopy data collected for Ubx fusion fibres displayed features similar to those of the Randles circuit [72, 73]. The main difference was the slope of the diffusion tail in the Nyquist plot, which in the Randles circuit results from the presence of Warburg impedance, which results from the difficulty in mass transport to the electrode. In the Randles circuit, the diffusion tail is semi-infinite and has a slope of 1 in the Nyquist plot.

For Ubx fusions, the slope of the diffusion tail took a range of values lower than 1 at low humidity, and larger than 1 when the humidity was increased. This behaviour could be modelled by introducing a constant phase element (CPE), which replaced the Warburg element. The impedance Z of the CPE is described by equation 3.2.4.

$$Z_{CPE} = Y_0^{-1}(j\omega)^{-n} \tag{3.2.4}$$

where Y_0 is a parameter related to the capacitance of the CPE, ω is the angular frequency, and n is a parameter related to the phase of the impedance. The power n can range between 0 for an ideal resistor, 0.5 for a Warburg element, and 1 for an ideal capacitor. Therefore, it describes whether a resistive or capacitive behaviour is dominant in the CPE. An equivalent circuit that closely describes

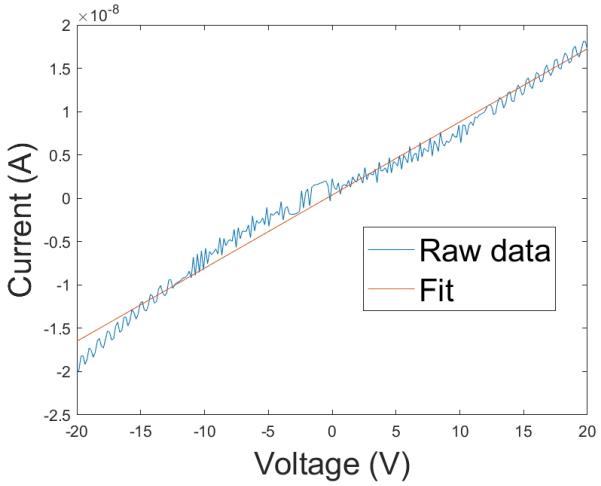

Figure 3.2.6: A sample current-voltage plot for an EGFP-Ubx fibre. The curve was approximately linear and a straight line was fitted to the data to extract the electrical conductivity of the fibre.

the behaviour of Ubx fibres in impedance spectroscopy measurement was shown in figure 3.2.7.

The real part of the impedance Z as a function of angular frequency ω is expressed by equation 3.2.5:

$$Z^{'} = R_u + \frac{R_{ct} + Y_0^{-1}\omega^{-n}\cos\frac{n\pi}{2}}{\omega^2 C_{dl}^2(R_{ct} + Y_0^{-1}\omega^{-n}\cos\frac{n\pi}{2})^2 + (Y_0^{-1}\omega^{1-n}C_{dl}\sin\frac{n\pi}{2} + 1)^2}. \quad (3.2.5)$$

The imaginary part of the impedance Z as a function of angular frequency ω is expressed by equation 3.2.6:

$$Z^{''} = R_u + \frac{Y_0^{-1}\omega^{-n}\sin\frac{n\pi}{2} + C_{dl}\omega(R_{ct} + Y_0^{-1}\omega^{-n})^2 - 2(1-\cos\frac{n\pi}{2})R_{ct}C_{dl}Y_0^{-1}\omega^{1-n}}{\omega^2 C_{dl}^2(R_{ct} + Y_0^{-1}\omega^{-n}\cos\frac{n\pi}{2})^2 + (Y_0^{-1}\omega^{1-n}C_{dl}\sin\frac{n\pi}{2} + 1)^2}. \quad (3.2.6)$$

The magnitude of the impedance was calculated using equation 3.2.7:

$$Z = \sqrt{(Z')^2 + (Z'')^2} \quad (3.2.7)$$

The sample Bode and Nyquist plots of the impedance with frequency ranging between 0.1 Hz and 1 MHz were shown in figure 3.2.8.

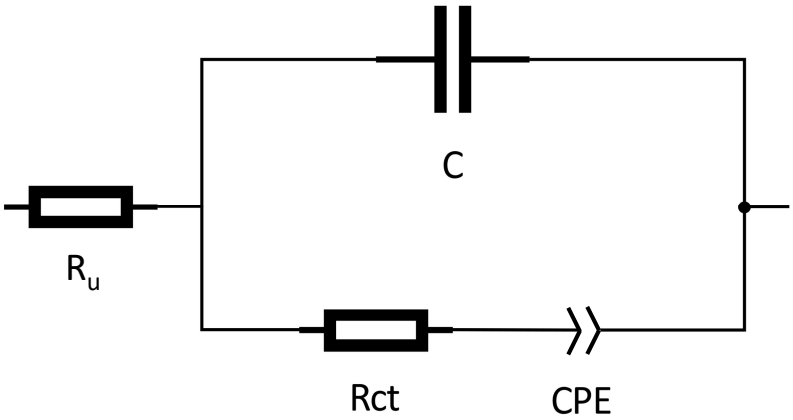

Figure 3.2.7: The diagram of the equivalent circuit used to model the impedance spectroscopy data on Ubx fusion fibres.

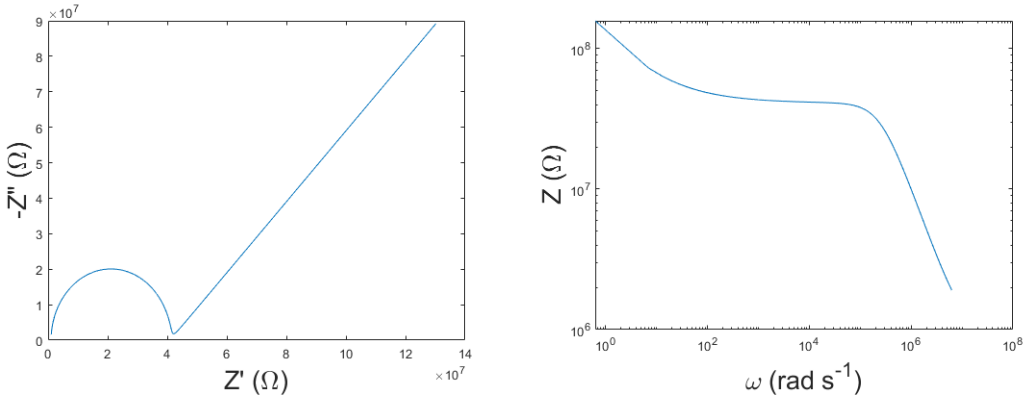

(a) (b)

Figure 3.2.8: The sample (a) Nyquist and (b) Bode plots of the impedance of the equivalent circuit shown in figure 3.2.7. The frequency range was 0.1 Hz to 1 MHz, and the parameters of the model were: $R_u = 1\,\mathrm{M\Omega}$, $R_{ct} = 40\,\mathrm{M\Omega}$, $C_{dl} = 0.1\,\mathrm{pF}$, $Y_0 = 10\,\mathrm{nFs^{n-1}}$, and $N = 0.5$.

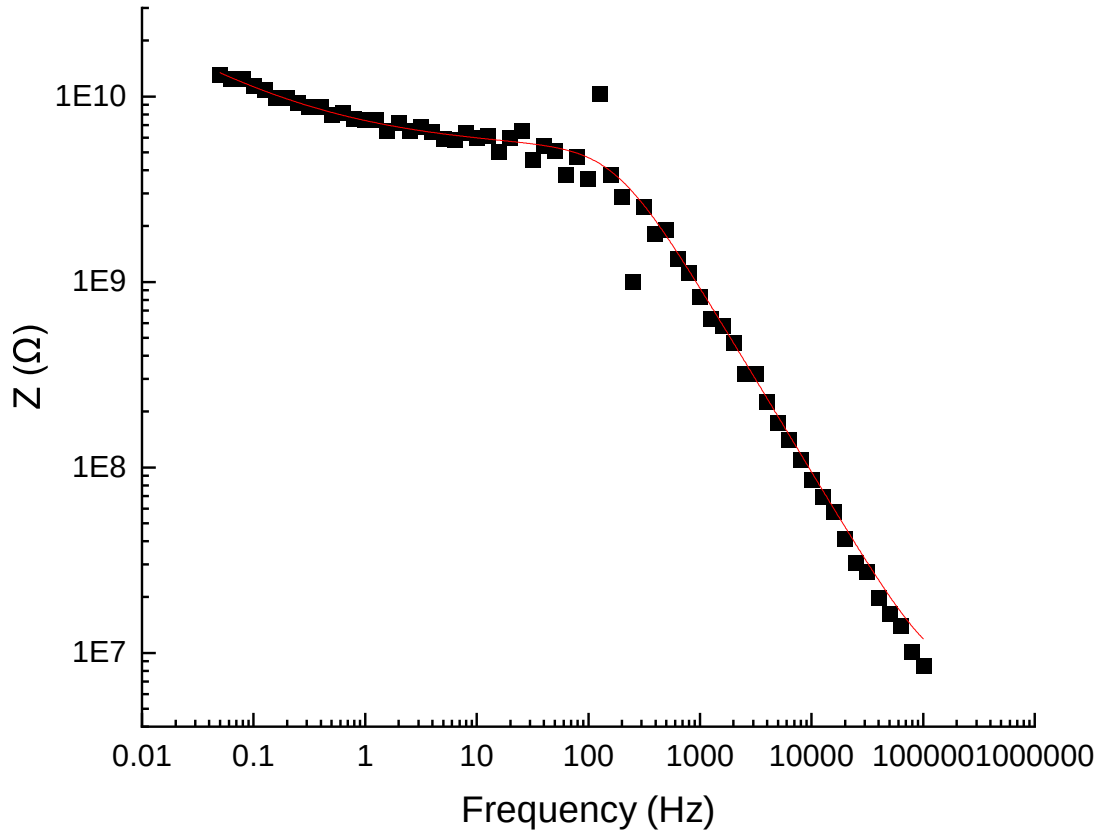

Figure 3.2.9: A sample Bode plot of the measurement of a Ubx fibre impedance in a range of frequencies between 0.05 Hz and 1 MHz. The corresponding fit was plotted using Origin software (version 2020b, OriginLab Corporation, Northampton, MA, USA).

The data of impedance spectroscopy was fitted to the model described in this section using Origin software (version 2020b, OriginLab Corporation, Northampton, MA, USA). Figure 3.2.9 shows an example of a Bode plot and the fit to the model. The parameters of the model were extracted using non-linear fitting to the model described by equation 3.2.7.

3.3 Results and discussion

3.3.1 The optical properties of Ubx fusions

Fluorescence spectra of Ubx fusions in solution

The fluorescence emission spectra of Ubx, EGFP-Ubx, mCherry-Ubx, and myoglobin-Ubx solutions were measured using 343 nm excitation wavelength, as shown in figure 3.3.1. These measurements complement the measurements previously per-

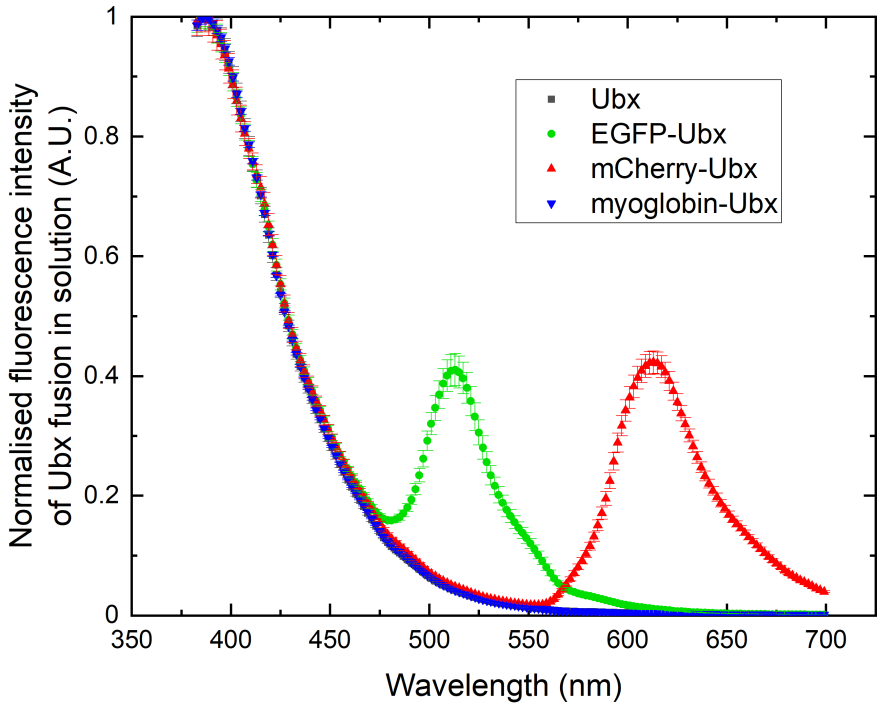

Figure 3.3.1: The emission spectrograph of Ubx, EGFP-Ubx, mCherry-Ubx, and myoglobin-Ubx protein solutions with a 343 nm excitation wavelength.

formed by the Bondos group [26] and provide a baseline for the subsequent measurements of the optical spectra of Ubx materials. Ubx fusion solutions all displayed an emission peak at 387 nm with the emission intensity sharply decaying with the increase in wavelength. The EGFP-Ubx and mCherry-Ubx solutions both displayed an additional emission peak corresponding to the active fluorescent protein at 513 nm and 613 nm, both of which are red-shifted by 6 and 3 nm relative to the literature values [51, 85].

Optical properties of Ubx fusion fibres

The emission of Ubx fusion fibres was measured by a laser source with excitation at 343 nm. The results are shown in figure 3.3.2. The excitation wavelength was selected to ensure that both the autofluorescence of Ubx and fluorescence of the functional proteins were measured. These measurements indicated the peak intensity of autofluorescence of Ubx due to the dityrosine bonds at 442-447 nm, which was significantly red-shifted from the 390 nm peak in solution. This result meant that the fluorescence properties of dityrosine in Ubx fusion fibres differ from those in solution, which had been observed previously [60]. In addition to the Ubx autofluorescence peak, the EGFP-Ubx fibre had an intense emission

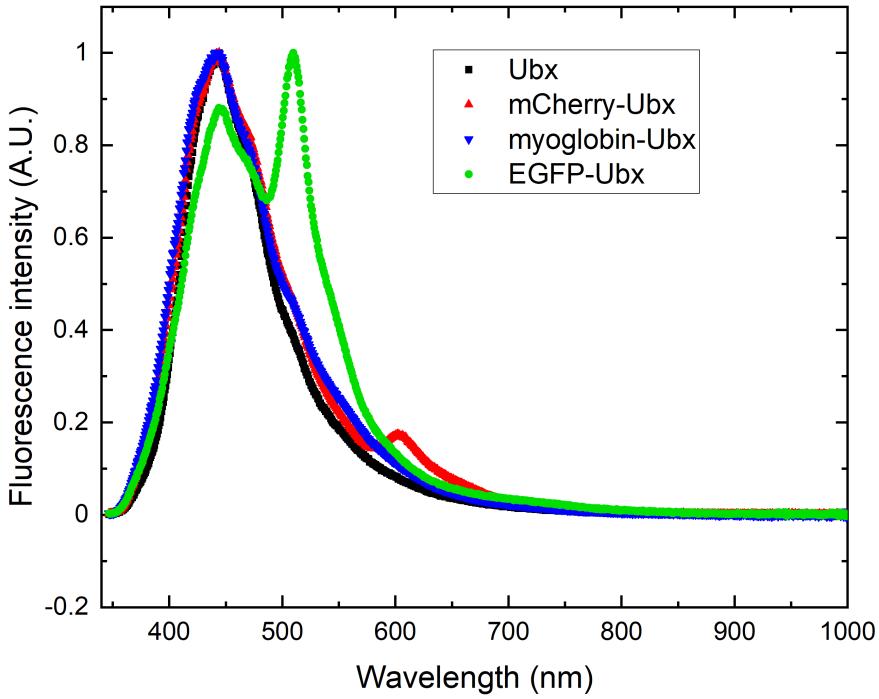

Figure 3.3.2: The emission spectrographs of Ubx, EGFP-Ubx, mCherry-Ubx, and myoglobin-Ubx protein fibres with 343 nm excitation wavelength.

peak at 510 nm, which was 14% stronger than the dityrosine peak. Meanwhile, the mCherry fluorescence emission peak at 602 nm in the mCherry-Ubx fibre was relatively weaker than the dityrosine emission peak at 17% of its maximum value. These results point at a difference in the fluorescence behaviour of EGFP-Ubx and mCherry-Ubx in solution (see section 3.3.1) and when incorporated into fibres. The corresponding EGFP and mCherry peaks in solution were at 41% and 42% of the Ubx peak. These differences could be explained by the stronger dityrosine fluorescence in mCherry-Ubx fibres compared to the protein solution, which might be due to the formation of intermolecular dityrosine bonds during the material formation, and the spectral shift of dityrosine, both of which could increase the relative height of the dityrosine peak compared to the mCherry emission. In the case of EGFP, because of a larger spectral overlap between dityrosine emission and EGFP excitation after the dityrosine emission red-shift, energy transfer (FRET) between the two processes could cause the additional EGFP emission, which caused the larger relative intensity of the EGFP peak in fibres. This is the first indication of FRET occurring in the Ubx protein fusions.

The summary of the FWHM of the peaks in the emission spectra of Ubx fusions is shown in table 3.3.1. Interestingly, there was a difference between the

FWHM of the dityrosine emission peak in Ubx fibres compared to myoglobin-Ubx or mCherry-Ubx fibres, with the measured FWHM of 85.06 nm for Ubx and approximately 100 nm for both myoglobin-Ubx and mCherry-Ubx. The FWHM of the dityrosine peak in EGFP-Ubx increased to only 87.74 nm. Both of the emission peaks of the appended fluorescent proteins were narrower, which means that they have sharper emission peaks.

Table 3.3.1: The FWHM measurements of the fluorescence emission peaks of Ubx fusion fibres.

Fusion	Peak centre (nm)	FWHM (nm)	Peak centre (nm)	FWHM (nm)
Ubx	444.02 ± 0.38	85.1 ± 1.1		
myoglobin-Ubx	441.75 ± 0.33	99.6 ± 1.1		
EGFP-Ubx	444.0 ± 1.5	87.7 ± 1.5	508.2 ± 1.5	47.9 ± 0.8
mCherry-Ubx	444.0 ± 0.8	100.8 ± 1.5	602.0 ± 1.5	61.1 ± 3.0

Further, the power dependence of the fluorescence intensity was measured for an EGFP-Ubx fibre at three power levels (figure 3.3.3). With the increase in illumination power from 10 µW to 100 µW, the maximum intensity rose 9.22-fold, and the subsequent change in power to 1 mW further increased the maximum fluorescence intensity by a factor of 9.07. Therefore, the relationship is nearly linear, suggesting a possible weak power dependence of the fibre's fluorescence intensity. Moreover, the shape of the photoluminescence (PL) spectra is maintained across the power range, with the dityrosine emission peak at 73-74% of the EGFP emission maximum. These results suggest that major photobleaching of Ubx autofluorescence and the fluorescence of functional proteins does not occur, which could allow the utilisation of fluorescence as a sensing tool for material degradation and distribution in composite materials.

Fluorescence lifetimes studies using the time-resolved photoluminescence data.

Dityrosine fluorescence had been shown to undergo a biexponential decay with $\lambda_{em} = 400\,\text{nm}to410\,\text{nm}$ with the shorter component (lifetime between 0.06 and 1 ns) dominating at shorter wavelengths, and the longer decay (2.6 to 4.4 ns) prevailing at longer wavelengths in the 350 and 430 nm region [59]. Ubx fibre autofluorescence was caused by the presence of dityrosine, with the emission peak at 438 nm [39]. However, the time-resolved fluorescence characteristics have not previously been investigated for Ubx materials. The lifetime measurements of

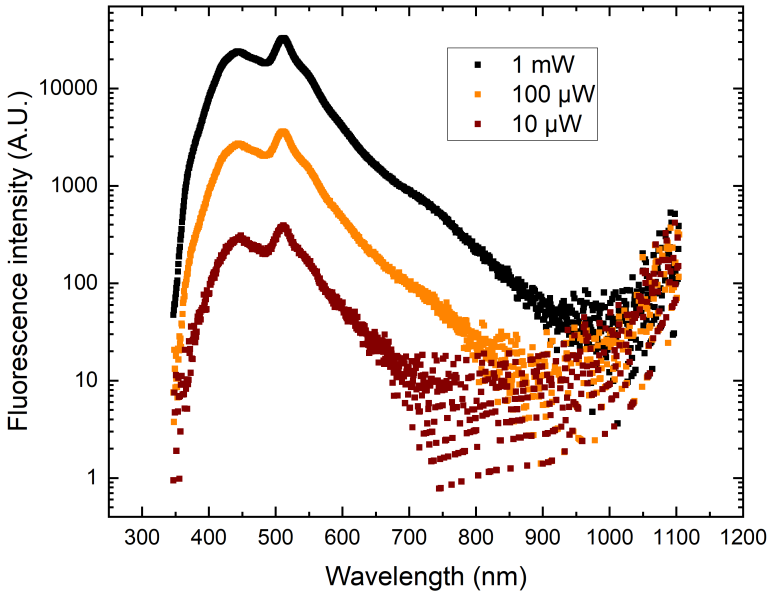

Figure 3.3.3: The emission spectrographs of EGFP-Ubx fibres with 343 nm excitation wavelength and 600 ms integration time.

dityrosine in yeast spores showed a bimodal distribution of fluorescent lifetimes with centres at 0.5 ns and 2.6 ns when measured at the maximum intensity of 404 nm with excitation at 326 nm, which was attributed to the presence of two or more species of dityrosine chromophores [60]. Two main dityrosine residues are present in Ubx fibres [39], which suggests that the Ubx fibre fluorescence may also undergo a multiexponential decay.

That prediction was tested in the TRPL measurements of fluorescence of Ubx fusion fibres using a Streak Camera (method described in section 3.2.1). The fluorescence lifetimes were measured for Ubx in two time ranges in a 40 nm wavelength frame centred around the dityrosine peak at 440 nm. The high resolution measurement in the 2 ns range presented in table 3.3.2 indicated a biexponential decay with a dominating (1.01 ± 0.02) ns component, and a shorter (115 ± 4) ps component. The measurement in the longer range of 10 ns shown in table 3.3.3 showed a triexponential decay with similar components of (190 ± 4) ps ($A_1 = 0.24 \pm 0.01$), (0.83 ± 0.02) ns ($A_2 = 0.34 \pm 0.01$), and an additional component of (2.72 ± 0.04) ns ($A_3 = 0.41 \pm 0.01$).

Similar measurements for the mCherry-Ubx fusion fibres, presented in tables 3.3.2 and 3.3.3 confirmed a biexponential fluorescence decay in the 2 ns time range with the time constants (110 ± 10) ps and the dominating longer component of (1.81 ± 0.18) ns. In the 10 ns range, a triexponential decay was observed. The

short component was maintained at (150 ± 10) ps, and the long component was split into the prevalent (1.31 ± 0.08) ns, and a longer (4.2 ± 0.6) ns component.

The time-resolved measurement of fluorescence of the myoglobin-Ubx fibre shown in table 3.3.3 indicated a biexponential decay with time constants close to those of the Ubx fibre, with the dominant (0.855 ± 0.003) ns decay and the faster (240 ± 1) ps component. Interestingly, in this case the long lifetime component was not present, making myoglobin-Ubx the only Ubx fusion with biexponential fluorescence decay.

An EGFP-Ubx fibre also exhibited a triexponential fluorescence decay measured at the 440 nm dityrosine peak. However, in contrast to the other fusions, the faster decay of (110 ± 4) ps was prevalent, with smaller contributions from the (0.54 ± 0.07) ns and (2.1 ± 0.3) ns components. The prevalence of the fast decay for EGFP-Ubx reflects the experimentally evaluated lifetimes for EGFP in solution [53, 54].

The final set of time-resolved measurements was centred around the respective emission peaks of EGFP-Ubx (510 nm) and mCherry-Ubx (602 nm) (table 3.3.4). The measurements for EGFP-Ubx showed a similar behaviour to those at 440 nm. In addition, the fluorescence lifetimes were consistent with literature values [53]. The lifetimes were increased compared to the measurement at 440 nm with a dominant component of (143 ± 5) ps, and slightly increased contributions from the (0.64 ± 0.06) ns and (2.56 ± 0.30) ns components. Interestingly, the longest decay is equal to the reported average EGFP lifetime [54].

For the mCherry-Ubx measurement centred at the 610 nm fluorescence peak, the lifetimes shown in table 3.3.4 were significantly different from those measured at 440 nm. In the 10 ns measurement, two sub-nanosecond lifetimes were recorded, the more prevalent (250 ± 20) ps and the less pronounced (630 ± 260) ps. A longer decay of (2.25 ± 0.13) ns was also measured. These measurements add an additional fast decay component compared to literature values [55, 56], which is consistent with the measurements for all other Ubx fusion fibres. The remaining decay components follow the previously reported trends for mCherry, with the longest lifetime being more prevalent than the intermediate (630 ± 260) ps decay.

The measurements of the fluorescence lifetimes with emission centred at 440 nm were used to estimate the potential FRET efficiency (equation 3.2.1) between Ubx (donor) and EGFP or mCherry (acceptors). The lifetime of a Ubx fibre

in the absence of fluorescent labels was used as the reference. The respective average lifetimes of Ubx, mCherry-Ubx, and EGFP-Ubx were (1.455 ± 0.019) ns, (1.96 ± 0.17) ns, and (0.42 ± 0.04) ns. Using these values, the estimated FRET efficiency between Ubx and mCherry was negative with $E = -0.35 \pm 0.12$. However, the FRET efficiency between Ubx and EGFP was $E = 0.711 \pm 0.024$, which indicated a significant resonance energy transfer between these two fluorophores. The large calculated FRET efficiency suggested that the observed increase in the relative height of the EGFP emission peak in the steady-state spectra (figure 3.3.1) was due to energy transfer between dityrosine and EGFP. The FRET efficiency calculated here might not be accurate because both mCherry and EGFP could be excited at 343 nm. However, the low excitation efficiency at this wavelength (see figure 3.1.1) allowed for an estimation of FRET efficiency. Interestingly, mCherry exhibited a larger excitation efficiency at 343 nm, which could have affected the measurement of the fluorescence lifetime, and subsequently resulted in the negative FRET efficiency.

Table 3.3.2: The fluorescence lifetimes and pre-exponential components of Ubx fusions fibres measured in the 2 ns time range.

Fusion	λ_{peak} (nm)	A_1 **(A.U.)**	τ_1 (ns)	A_2 **(A.U.)**	τ_2 (ns)
Ubx	440	0.23(1)	0.115(4)	0.702(3)	1.01(2)
mCherry-Ubx	440	0.24(1)	0.11(1)	0.84(4)	1.81(18)
mCherry-Ubx	610	0.30(2)	0.09(1)	0.59(2)	0.58(4)

Table 3.3.3: The fluorescence lifetimes and pre-exponential components of Ubx fusions fibres measured in the 10 ns time range and centred at the 440 nm dityrosine emission peak.

Fusion	A_1 **(A.U.)**	τ_1 (ns)	A_2 **(A.U.)**	τ_2 (ns)	A_3 **(A.U.)**	τ_3 (ns)
Ubx	0.24(1)	0.190(4)	0.34(1)	0.83(2)	0.41(1)	2.72(4)
myoglobin-Ubx	0.117(4)	0.24(1)	0.876(4)	0.855(3)	N.A.	N.A.
mCherry-Ubx	0.18(1)	0.15(1)	0.53(4)	1.31(8)	0.30(4)	4.2(6)
EGFP-Ubx	0.69(2)	0.110(4)	0.26(2)	0.54(7)	0.10(2)	2.1(3)

Table 3.3.4: The fluorescence lifetimes and pre-exponential components of Ubx fusions fibres measured in the 10 ns time range and centred at the 510 nm and 610 nm emission peaks for EGFP-Ubx and mCherry-Ubx, respectively.

Fusion	A_1 **(A.U.)**	τ_1 (ns)	A_2 **(A.U.)**	τ_2 (ns)	A_3 **(A.U.)**	τ_3 (ns)
EGFP-Ubx	0.598(19)	0.143(5)	0.30(1)	0.64(6)	0.13(2)	2.56(30)
mCherry-Ubx	0.45(9)	0.25(2)	0.18(7)	0.63(26)	0.36(4)	2.25(13)

3.3.2 The electrical properties of Ubx fusion fibres

Electrical conductivity of Ubx-based fibres

Initially, the electrical conductivity of Ubx and Ubx fusion fibres was measured using DC current measurements in different voltage ranges up to −40 V-40 V. The measurements were taken in a humidity- and temperature-controlled room with room lighting. The relative humidity was between 40% and 50%. Sample current-voltage (I-V) curves are shown in figure 3.3.4. The I-V curves reveal differences in the response to applied voltage between fibres with different electrical conductivities. The myoglobin-Ubx fibre had a diameter of $(16.11 \pm 0.35)\,\mu m$, whereas the EGFP-Ubx fibre had a diameter of $(13.18 \pm 0.54)\,\mu m$. However, the fibres had different electrical conductivities of $(0.141 \pm 0.009)\,mS\,m^{-1}$ and $(7.2 \pm 0.8)\,mS\,m^{-1}$, respectively. The myoglobin-Ubx fibre exhibited an ohmic behaviour with significant noise (figure 3.3.4a). Interestingly, the higher conductivity EGFP-Ubx fibre deviated from the ohmic behaviour at high applied voltage, which could be the result of charge accumulation at the electrodes (figure 3.3.4b). The applied bias started at negative values, and with rising voltage, the initial rate of change decreased, culminating in another decrease at voltage close to 20 V. These differences indicate that charge carrier mobility issues may arise at higher currents.

The effect of protein fusions on the electrical properties of the protein fibres was investigated in more detail. The electrical resistance and conductivity of Ubx-based materials were calculated by measuring the I-V response for a range of Ubx, EGFP-Ubx, and myoglobin-Ubx fibres with varying diameters. The electrical conductivity measured for Ubx, EGFP-Ubx, and myoglobin-Ubx fibres is shown in

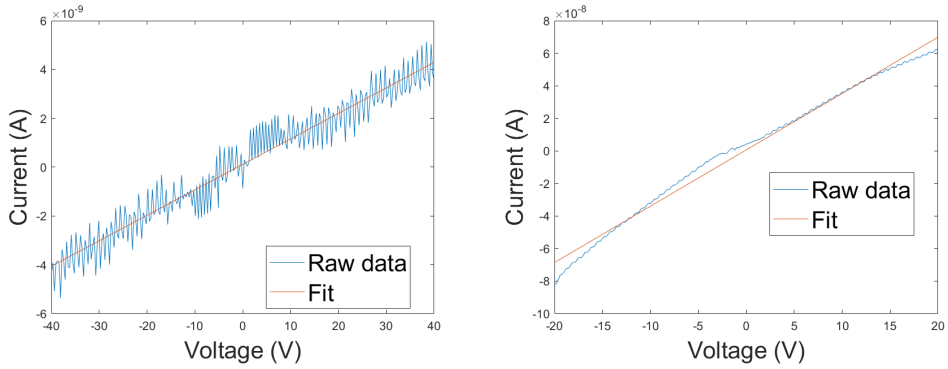

(a) (b)

Figure 3.3.4: (a) The DC current through a section of a myoglobin-Ubx fibre as a function of voltage in the -40 and 40 V region. (b) The DC current through an EGFP-Ubx fibre as a function of voltage between -20 and 20 V.

figure 3.3.5. The statistics arising from these measurements are presented in table 3.3.5. These measurements showed that the average electrical resistance of the fibres was large due to the small diameters of the fibres, but comparable between Ubx fusions, with no statistically significant differences. The electrical conductivity, the intensive property, was the largest for EGFP-Ubx fibres, although the differences were not quite statistically significant, with p-values of 0.0806 and 0.1286 for the comparison between EGFP-Ubx and Ubx fibres, and EGFP-Ubx and myoglobin-Ubx fibres, respectively. However, these differences could have been caused by the smaller average diameter of EGFP-Ubx fibres. The comparable electrical conductivity of Ubx and myoglobin-Ubx fibres suggests that the electrical conductivity of Ubx protein fibres is not affected by protein fusions.

Table 3.3.5: The average diameter, electrical resistance and conductivity of Ubx fusion fibres.

Fusion	Diameter (µm)	Resistance (GΩ)	Electrical conductivity ($mS\,m^{-1}$)
Ubx	17.6 ± 1.7	6.3 ± 2.4	0.35 ± 0.17
EGFP-Ubx	12.1 ± 2.2	2.0 ± 1.3	1.6 ± 0.7
myoglobin-Ubx	17.3 ± 1.9	2.9 ± 2.4	0.47 ± 0.31

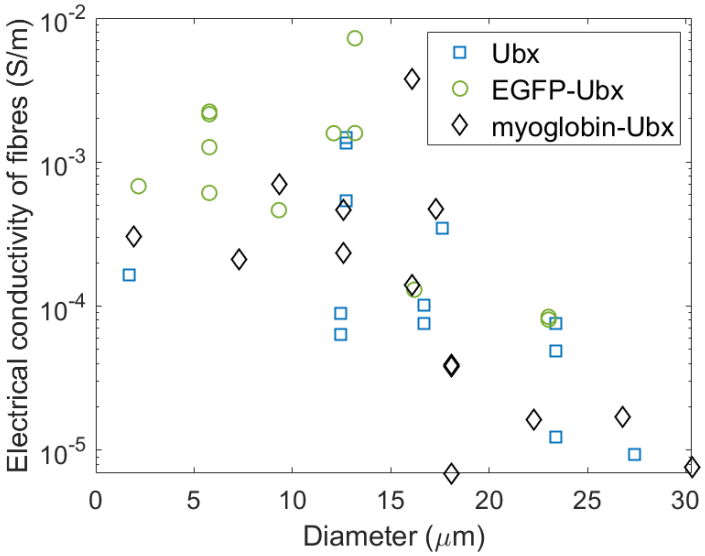

Figure 3.3.5: The plot of the electrical conductivity as a function of the diameter of Ubx, EGFP-Ubx, and myoglobin-Ubx fibres.

The effect of humidity on the electrical conductivity

The previously observed differences in the electrical conductivity of the Ubx fusion fibres prompted the question of how the relative humidity of the environment affects the electrical properties of the fibres through sample hydration. Initially, this effect was tested by briefly hydrating the sample using water vapour directly exhaled onto the fibres, and measuring their current-voltage characteristics. It was noted that there is a strong time-dependence of the measured electrical conductivity, which was observed by the rapid decline in the measured values of current in two measurements 95 s apart shown in figure 3.3.6, which corresponds to a 60-fold decrease in the electrical conductivity.

The comparison of the electrical conductivity of dry and hydrated Ubx-based fibres was shown in figure 3.3.7. The hydration of fibres with water vapour resulted in a large increase in the electrical conductivity. The average increase was by a factor of (30 ± 13) for Ubx fibres, (100 ± 80) for EGFP-Ubx fibres, and (20 ± 7) for myoglobin-Ubx fibres. These trends indicated that the ionic charge transfer is predominant within Ubx-based fibres. In this experiment, the average electrical conductivity of dry fibres was the largest for myoglobin-Ubx at $(640 \pm 230)\,\mu\mathrm{S\,m^{-1}}$, compared to $(250 \pm 110)\,\mu\mathrm{S\,m^{-1}}$ for EGFP-Ubx, and $(105 \pm 70)\,\mu\mathrm{S\,m^{-1}}$ for Ubx fibres. However, these differences were not statistically significant.

The effect of sample hydration on the electrical properties of Ubx-based fibres

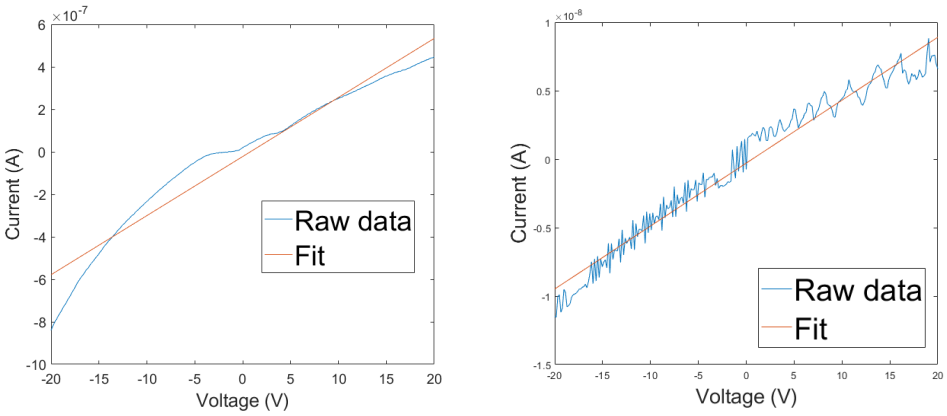

(a) (b)

Figure 3.3.6: (a) The I-V measurement of an EGFP-Ubx fibre (a) directly after fibre hydration with exhaled water vapour and (b) 95 s later.

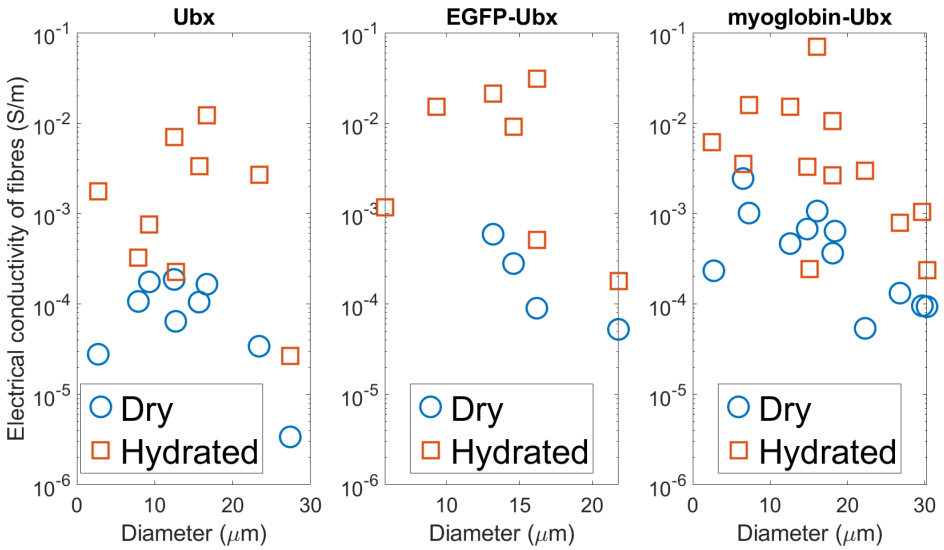

Figure 3.3.7: The comparison of the electrical conductivity of dry and hydrated Ubx, EGFP-Ubx, and myoglobin-Ubx fibres of different sizes.

was further explored in the impedance spectroscopy measurements with relative humidity control. The impedance spectroscopy measurements on the Ubx fusion fibres revealed a similar behaviour for all fusions tested. The impedance spectra were very strongly dependent on the relative humidity in the chamber. To achieve a considerable signal-to-noise ratio, measurements had to be taken at relative humidity (RH) above 50%, and in some cases 60%. Moreover, the spectra varied with RH. In the tested region between 0.1 Hz and 1 MHz, at low RH, the impedance spectra could be described by the equivalent circuit presented in figure 3.2.7, which is a modified Randles circuit with the Warburg element replaced by a constant phase element (CPE). The characteristic elements of impedance spectra for this circuit can be observed in the Nyquist plot of impedance, and include the semi-circle due to the resistor and capacitor being connected in parallel, and a linear diffusion tail due to the CPE connected in series with the resistor. The diffusive behaviour dominates at low frequencies, while the capacitive behaviour is observed at high frequencies.

The impedance spectra change when the RH is increased (figure 3.3.8). At larger RH, the semi-circle shrinks, which suggests a decrease in resistance and a potential increase in capacitance in the circuit in the high frequency regime. Additionally, the low frequency diffusion tail is split into two regions with different slopes, which suggests another diffusion mechanism connected in series with the previous circuit, e.g. another CPE, or two identical circuits connected in series. The change in the slope can be modelled by a change in the coefficient Y_0 in the equation for the impedance of a CPE, $Z_{CPE} = Y_0^{-1}(j\omega)^{-n}$, which represents a change in the behaviour of the CPE. In particular, for a perfect capacitor, Y_0 is equal to the capacitance C.

Since $n = 1$ corresponds to a perfect capacitor, and $n = 0$ to a resistor, an increase in n indicates an increase in the capacitive behaviour of this component, while a decrease means an increased resistance. Additionally, the coefficient Y_0 stores information about the capacitance of the CPE, hence an increase in Y_0 indicates an increase in the capacitance of the CPE. The physical interpretation of these elements is conventionally based on the equivalent Randles circuit describing an electrochemical cell with a charging electrical double layer in the presence of a redox probe, which was discussed in detail [72]. Crucially, the behaviour of this model is dictated by the capacitive charging and the resistance related to charge transfer at high frequencies, and the mass transfer (ion movement to the electrode) at low frequencies. Impedimetric biosensors employing this model have

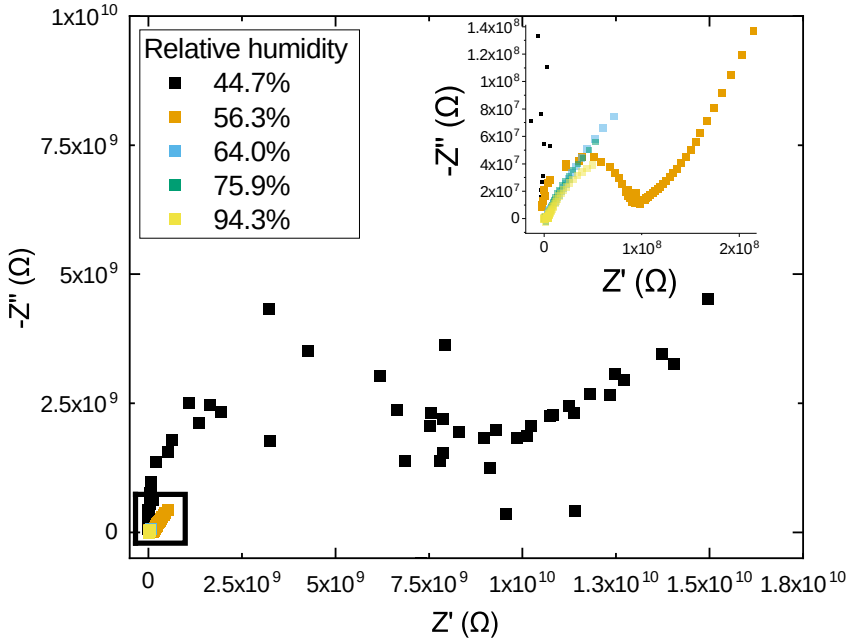

(a)

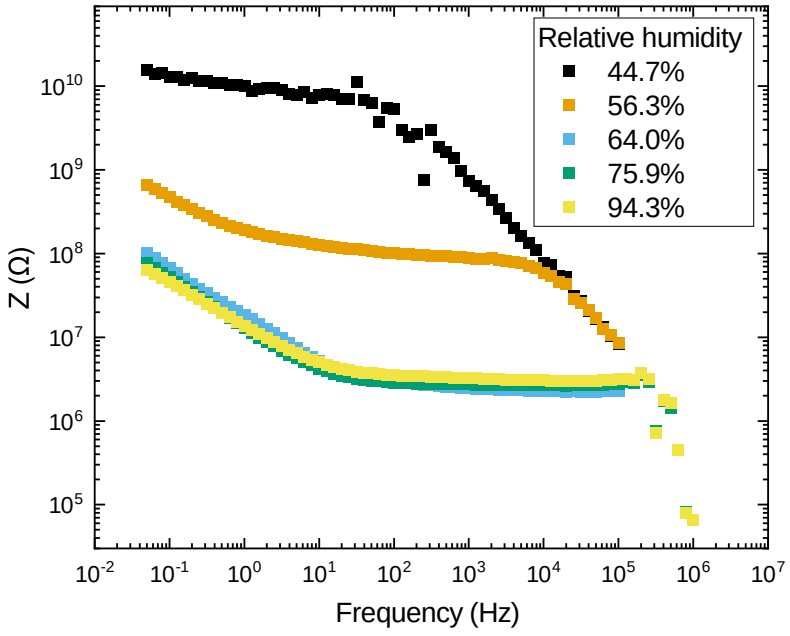

(b)

Figure 3.3.8: The comparison of the impedance spectra of a Ubx fibre at different values of relative humidity. (a) The Nyquist plot. The inset shows the magnified rectangle outlining the evolution of the impedance spectra with rising relative humidity. (b) The Bode plot.

been created, which consist of electrodes modified to immobilise antibodies, which trap antigens, and consequently create a barrier that affects the flux rate of the redox molecules to the electrode. This type biosensor measures the changes in the charge transfer resistance, which corresponds to the formation of antibody-antigen pairs [72, 86]. In the case of Ubx fusion fibres, the physical parameters related to the circuit differ from the electrochemical cell. The resistance R_1 might be related to the contact resistance between the probes and the fibres. The resistive element R_{ct} corresponds to the charge transfer resistance within the fibre, which can be used to extract the fibre's electrical conductivity. The double layer capacitance C might result from the charge build up between the individual nanofibril layers within the fibres. It could also be explained by the capacitive charging at the surface of the fibre at the respective electrical probes. Finally, the diffusive element CPE might describe the difficulty of mass transfer of the charged particles within the sample, which may result from the AC applied to the attached probes. The nature of the charged particles might be ionic, which is supported by previous experiments on the nature of charge transfer in biopolymers. Specifically, a large increase in electrical conductivity with rising relative humidity is indicative of ionic conductivity. Therefore, the additional energy dissipation represented by the CPE can be related to the resistance in ion movement within the fibres or at the fibre surface.

The impedance of Ubx fusion fibres was strongly dependent on the relative humidity in the vacuum chamber. At low relative humidity below 40%, the signal-to-noise ratio was too low to distinguish real data. The electrical conductivity reduces rapidly by up to 3 orders of magnitude in the humidity range between 40% and 70% and starts to plateau at larger relative humidity. The plots of DC and AC electrical conductivity measured at different values of relative humidity are shown in figures 3.3.9 and 3.3.10. The DC electrical conductivity was stratified, and the rise in relative humidity resulted in an increased value of conductivity for all samples. The AC conductivity calculated using the fitting parameter R_{ct} followed the same trend, although the fitting uncertainties at higher relative humidity caused more scatter in the data. However, there was a correspondence of the calculated AC and DC electrical conductivity at low relative humidity where the relative error resulting from fitting was small. The values of AC conductivity were higher, which could be a result of the non-linear effects visible in the I-V curves. Generally, the electrical conductivity of Ubx fusion fibres occupied the region between $1\,\mathrm{mS\,m^{-1}}$ and $100\,\mathrm{mS\,m^{-1}}$, with a rapid increase of several orders

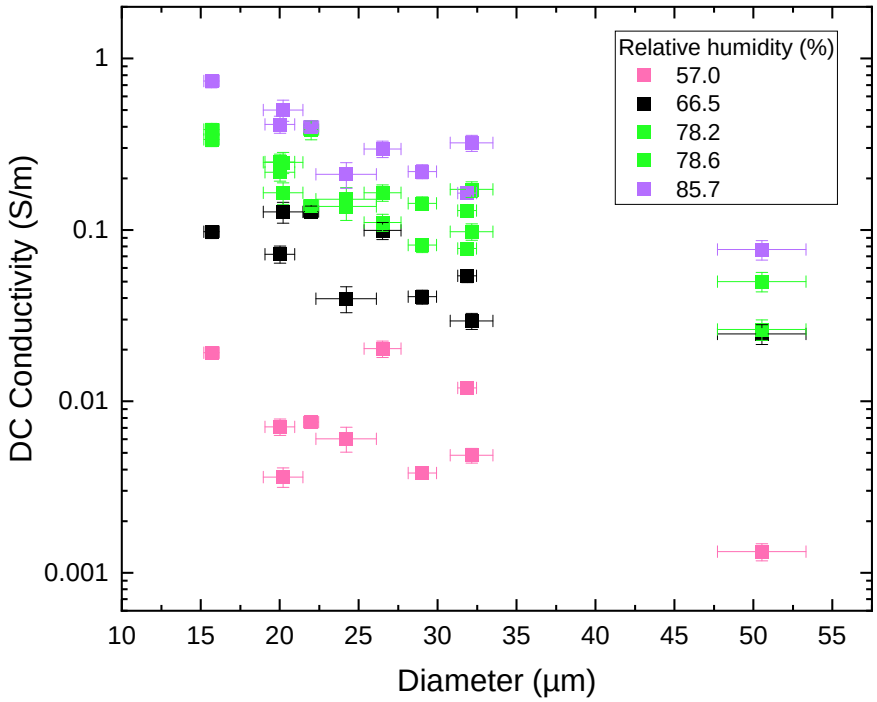

Figure 3.3.9: The plot of the DC electrical conductivity as a function of the diameter of the Ubx, EGFP-Ubx, and myoglobin-Ubx fibres at varying relative humidity.

of magnitude between 50% and 70% relative humidity.

The qualitative features of the impedance plots were reflected in the values of the fitting parameters in the model based on the equivalent circuit described in section 3.2.4. Not all fitting parameters could be fitted well to the model because of the large data scatter at large relative humidity. Therefore, a meaningful comparison of the fitting parameters for the different Ubx fusions could be offered at medium relative humidity, while at larger relative humidity the parameters C_{dl} and R_u were difficult to fit, perhaps due to the capacitive charging and contact resistance being less dominant.

The shape of the Nyquist and Bode plots also varied with relative humidity (see figure 3.3.8). In the Nyquist plot, the diffusion tail at low frequencies was longer at high relative humidity, while the semi-circle at high frequencies became less pronounced. Additionally, the scatter at high frequencies became very large at large relative humidity, and the semi-circle effectively vanished. The features of the Bode plot visible at low relative humidity also changed at higher values of the vapour pressure. Specifically, the rapid decrease in impedance at high frequencies became less pronounced in the range up to 1 MHz, which was a feature

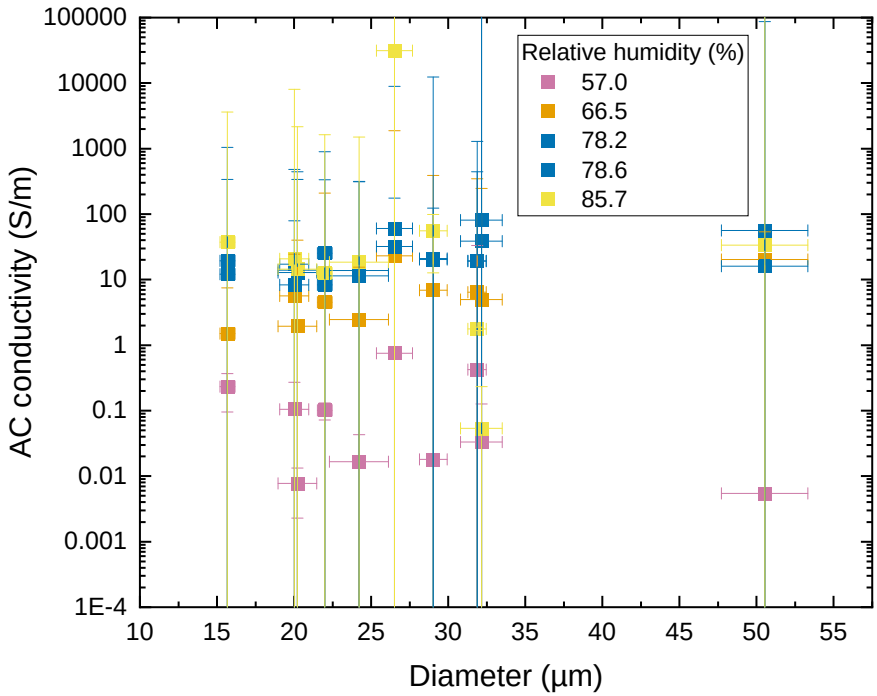

Figure 3.3.10: The plot of the AC electrical conductivity as a function of the diameter of the Ubx, EGFP-Ubx, and myoglobin-Ubx fibres at varying relative humidity.

corresponding to the lack or smaller size of the semi-circle in the Nyquist plot. The large diffusion tail was also visible in the Bode plot, and was signified by the steeper slope at low frequencies. The features of the semi-circle were dependent on the capacitance C_{dl} of the double layer and the charge transfer resistance R_{ct}, which are shown in figures 3.3.11 and 3.3.12. The charge transfer resistance decreased by several orders of magnitude with an increase in relative humidity. Moreover, it had a strong inversely proportional dependence on diameter. The range of resistance measured for Ubx fusion fibres ranged from 10 kΩ for hydrated samples to 1 GΩ for dry samples. The double layer capacitance took very small values for all fibres, with the majority of measurements ranging between 0.1 and 100 pF. The double layer capacitance appeared to increase by between one and two orders of magnitude with an increase in relative humidity, although the fitting uncertainty was large at higher RH due to the small size of the semi-circle in the Nyquist plot.

The impedance at low frequencies was dictated by the diffusive properties of the material, which were represented by the parameters n and Y_0, corresponding to the nature and capacitance of the constant phase element, respectively. The plots of these parameters as a function of fibre diameter and relative humidity

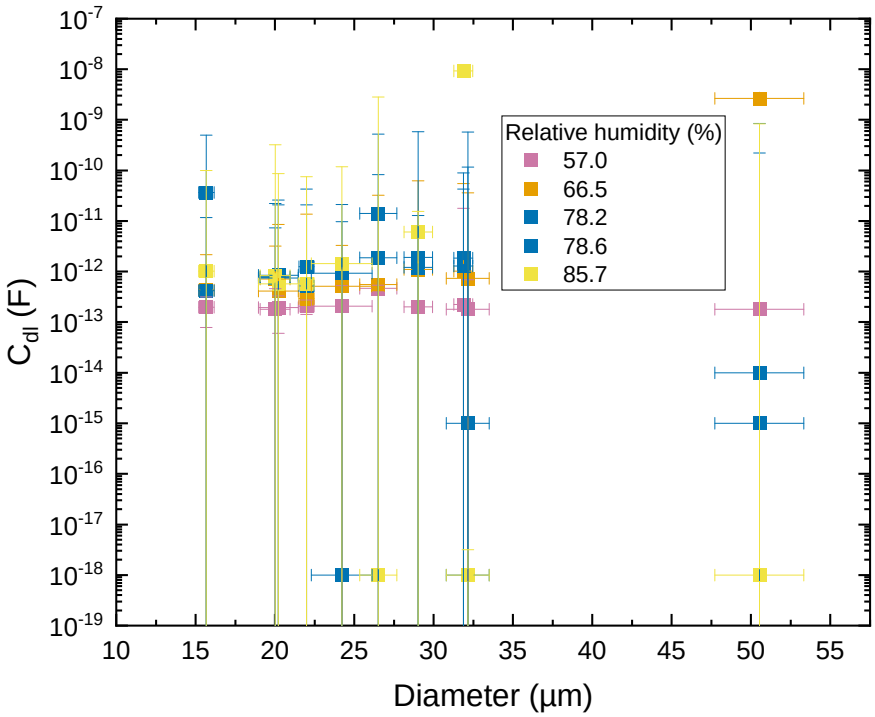

Figure 3.3.11: The fitting parameters of the equivalent circuit model. The plot of the parameter C_{dl} representing the double layer capacitance.

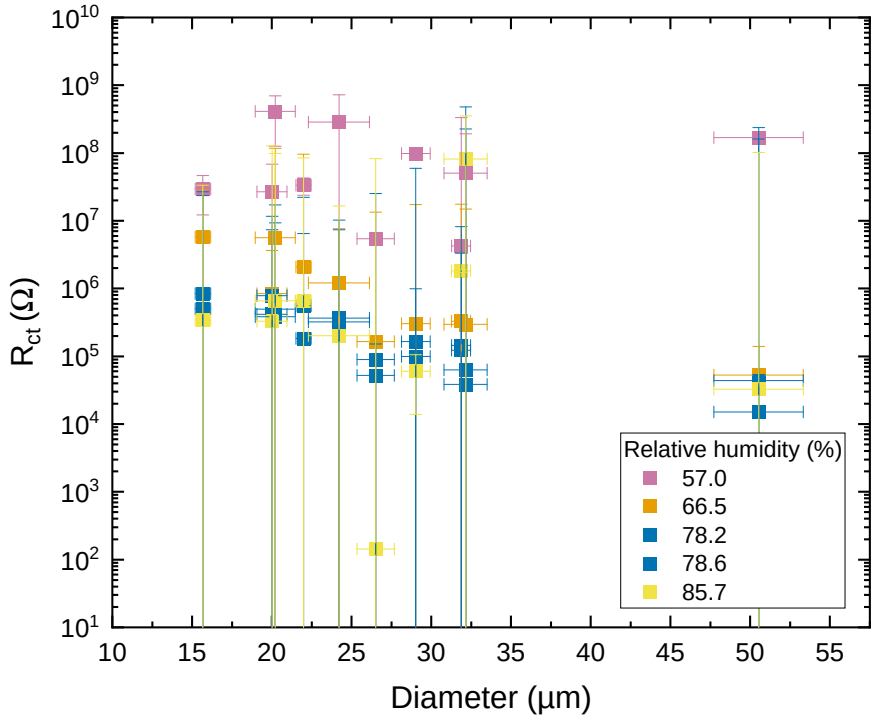

Figure 3.3.12: The fitting parameters of the equivalent circuit model. The plot of the parameter R_{ct} corresponding to the intrinsic fibre electrical resistance, as a function of fibre diameter and relative humidity.

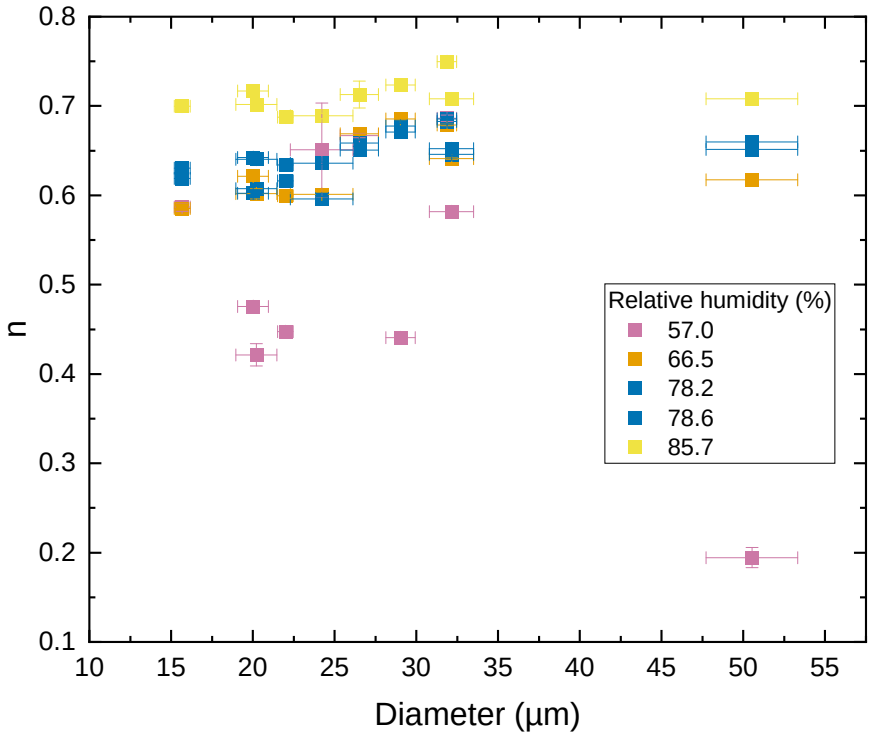

Figure 3.3.13: The fitting parameters of the equivalent circuit model. The plot of the parameter n indicating the nature of the constant phase element.

in the system are shown in figures 3.3.13 and 3.3.14. An increase in the slope of the diffusion tail observed in the Nyquist plot indicated that the constant phase element is closer to an ideal capacitor behaviour. The values of slope n increased with relative humidity at all fibre diameters, with a particularly large increase observed for the largest fibre with a 50 µm diameter. At 57% relative humidity, the CPE behaviour was close to that of a Warburg element with $n = 0.5$, and when the relative humidity was further increased, the behaviour changed and was more capacitive, with n ranging between 0.6 and 0.75. A strong stratification was also observed for the parameter Y_0, which stored information about the capacitance of the CPE. It increased from 5 to 70 $\mathrm{nFs^{n-1}}$ with a particularly large increase between 57% and 78% relative humidity. However, in this case, the capacitance only increased by about 1 order of magnitude within the measured humidity range.

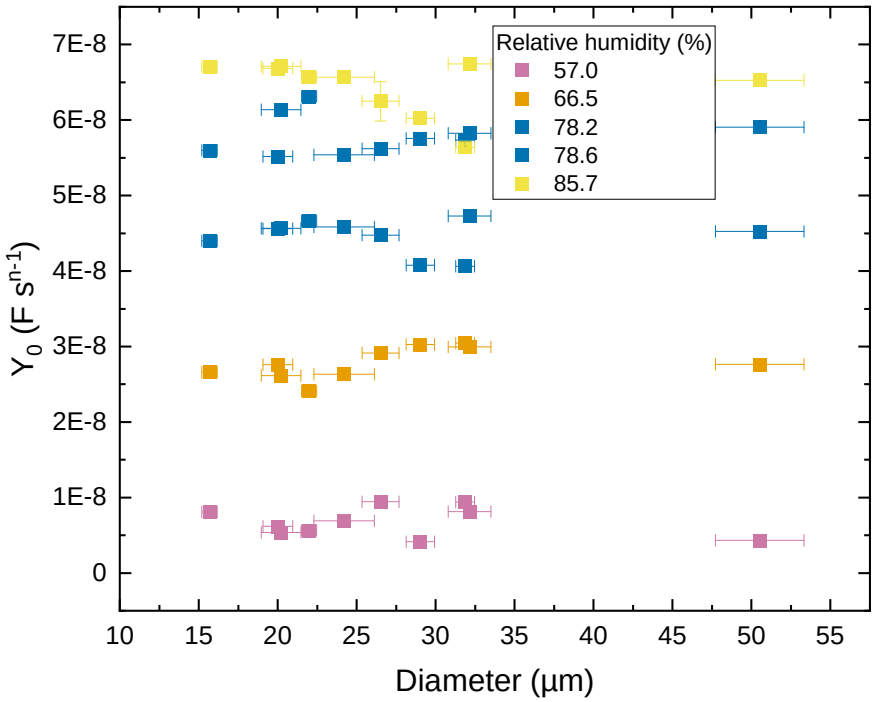

Figure 3.3.14: The fitting parameters of the equivalent circuit model. The plot of the parameter Y_0 indicating the capacitance of the constant phase element, as a function of fibre diameter and relative humidity.

3.4 Summary

3.4.1 Optical properties of Ubx fusion fibres

The steady-state and time-resolved fluorescence spectra were measured of pure Ubx and fusions with myoglobin and fluorescent proteins EGFP and mCherry. The fluorescence spectra of protein solutions were compared to those of fibres, all with 343 nm excitation. In solution, all Ubx fibres had an emission peak at 387 nm, and EGFP-Ubx and mCherry-Ubx fusions displayed one additional red-shifted peak each at 513 nm and 613 nm. In fibres, the blue fluorescence resulted from dityrosine bonds forming between Ubx molecules, which was visible for all fibres between 442 and 447 nm. The emission peak for EGFP was at 510 nm and for mCherry it was at 602 nm. The power-dependence of fibre fluorescence intensity was measured for laser power between 10 µW and 1 mW, which revealed a near-linear intensity increase with laser power, suggesting good photostability of the functional proteins.

The dependence of fluorescence lifetimes on protein fusions was investigated. Dityrosine, myoglobin and the fluorescent proteins EGFP and mCherry had

previously been shown to exhibit a bi- and tri-exponential fluorescence decay with lifetimes strongly dependent on the excitation and emission wavelength [51–56, 58–60]. The measurements presented here are the first measurements of Ubx materials fluorescence lifetimes. This work shows that at the 440 nm dityrosine peak, the average fluorescence lifetime of mCherry-Ubx increased, and that of EGFP-Ubx decreased, compared to pure Ubx, which suggests the presence of FRET mechanisms in these protein fusions, facilitated by the proximity of the proteins and the larger spectral overlap of dityrosine emission with EGFP excitation. The fluorescence lifetimes measured for the Ubx fusions with fluorescent proteins show similarities to the lifetimes of free fluorescent proteins. The dominant short lifetime (110 ps-143 ps) component of EGFP-Ubx at both 440 nm and 510 nm, the strong decay around 0.6 ns, and the long lifetime component at 2.1-2.56 ns, had all been observed, the last one had been measured to be longer at 2.8 ns [53, 54]. The average lifetimes of Ubx fusions centred at the dityrosine peak at 440 nm indicated strong FRET with estimated efficiency of (0.711 ± 0.024) between dityrosine and EGFP in EGFP-Ubx fibres, which also caused an increase in the relative height of the EGFP peak in the steady-state spectrum. This result suggested that FRET sensing of molecular bonding or changes in the structure of fusion proteins could be achieved using Ubx-based materials.

Ubx has shown promise as a functionalisable platform material and as a part of composite materials in biotechnological or biomedical applications. These applications often require specific material properties, and multiple functions to be incorporated within one device. For this purpose, protein fusions provide multiple benefits, which include the ability to add multiple functional proteins and the structural protection of appended proteins under denaturing conditions. The Ubx fusions with fluorescent proteins offer opportunities in biosensing due to the tunability of fluorescence spectra, and the possible applications of fluorescence lifetime imaging in detecting molecular binding to Ubx materials or biosensing of intracellular and other *in vivo* conditions, which is an important feature of implantable devices. Future studies measuring the fluorescence lifetimes of Ubx fibre-DNA aptamer complexes could indicate whether Ubx platforms are suitable for applications in biosensing, and in particular in filtering or pathogen detection systems. The measurements presented in this work offer a basis for future applications of optically active protein platform materials for biosensing and biomedical applications.

3.4.2 Electrical properties of Ubx fusion fibres

The measurements of electrical properties of Ubx fusion fibres inform the potential applications of these materials, and reveal how their properties relate to other biomaterials used in fields such as biolectronics or tissue engineering. Of particular interest are the electrical conductivity and impedance, and their dependence on environmental parameters such as the relative humidity, which is related to the hydration of the sample. Another area of interest is tissue engineering, where the electrical properties of materials affect the possibility of applying biopolymers for treatment of cardiovascular diseases, including heart implants after myocardial infarction, which require the matching of both electrical and mechanical properties of the implanted device to those of the surrounding healthy tissue in order to conduct electrical impulses and facilitate the contraction and expansion of the heart muscle [8,27,87,88]. The characterisation of electrical properties of biomaterials is therefore important for informing their applications and functionalisation strategies.

The electrical properties of Ubx materials reported in this paper suggest a strong dependence of the electrical conductivity on the hydration of the sample, which was controlled by changing the relative humidity. The electrical properties are tunable by changing the environmental conditions and fibre size, and the DC conductivity could take values between $(98 \pm 12)\,\mu\mathrm{S\,m^{-1}}$ for a relatively large $(20.6 \pm 1.2)\,\mu\mathrm{m}$ fibre at 45% RH to $(1.66 \pm 0.16)\,\mathrm{S\,m^{-1}}$ for a smaller $(7.7 \pm 0.3)\,\mu\mathrm{m}$ fibre at 94% RH. The electrical conductivity of the fibres decreased with their diameter, but for fibres of all diameters it also increased rapidly with the relative humidity, which is related to a change in the hydration of the sample. The conductivity increased by up to 3 orders of magnitude with the RH increase between 45% and 94%, which indicates that their conductivity mechanism is likely ionic [43]. The electrical conductivity of Ubx fusions fibres appears to exceed that of other protein materials and places Ubx microfibres in the same region of electrical conductivity as commercially used semiconductors. Moreover, humidity-dependent impedance spectroscopy measurements were conducted for Ubx fibres and Ubx fusions with myoglobin and fluorescent protein EGFP. A model based on the Randles equivalent circuit was developed to extract some material properties related to charge transfer, capacitive behaviour and diffusion of electrical charges. This model confirmed a strong increase of the electrical conductivity by 2-3 orders of magnitude with the relative humidity change between 57% and 86%. Additionally, a dominant weak double layer capacitive behaviour was observed at higher

frequencies. An increase in the diffusive behaviour at low frequencies was measured, and was modelled by a constant phase element. The nature of the constant phase element (CPE) changed from predominantly resistive to mostly capacitive in the same humidity range, with a 7-fold increase in the scaling parameter Y_0 indicating capacitance of the CPE. To summarise, a strong dependence of electrical properties of Ubx fusion fibres was observed with changing relative humidity, and this paper offers the first evaluation of both frequency and relative humidity effect on the electrical properties of Ubx materials.

Previously reported work on nanofunctionalisation of biopolymers and protein materials with carbon nanotubes and Au and Ag nanoparticles showed that the electrical conductivity of hydrogels and microfibres could be increased by several orders of magnitude up to $2\,\mathrm{kS\,m^{-1}}$ [27, 76–78, 80], which suggests that nanofunctionalisation can offer further tuning properties of electrical properties of Ubx materials. This could be explored in future designs of bioeletrical devices involving Ubx.

3.4.3 Other opportunities for biosensing and tissue regeneration using Ubx platform materials

Pathogen capture platforms can be used in both biotechnological and medical applications in the context of pollution detection or diagnostics of bacterial infections. Ubx can carry these functions and be used in conjunction with other biopolymers to create composite devices with multiple functions. Therefore, the physical properties reported in this paper can be used as a reference and an indicator of future applications of Ubx-based materials for biosensing. Many biopolymers have been developed for tissue engineering and regeneration applications to address issues such as bone fracture, wound healing, vascular disease or myocardial infarction. For best outcomes, the properties of these materials need to match the mechanical and electrical properties of the surrounding tissue, and satisfy the specific bio- and cytocompatibility requirements that allow a safe implantation of these devices.

Ubx materials could be further used as biosensors using fluorescent lifetime imaging. The creation of multiple protein fusions with myoglobin and fluorescent proteins could allow the monitoring of FRET-induced changes in the fluorescence lifetime as an oxygenation probe in biological systems or biotechnological applications. The efficiency of biosensors, including protein fusions of myoglobin and

fluorescent proteins, has previously been shown in work that constitutes a proof of concept for FLIM-based biosensing [64, 65].

Biodegradability of protein materials may also be a useful feature of devices which are required for tissue regeneration. The appended fluorescent proteins may allow the monitoring of the device degradation as well as structural changes of the devices. Additionally, the monitoring or prevention of biofilm growth on the implant surface can be achieved by functionalising the device with DNA aptamers or antimicrobial peptides. The wealth of available functional proteins allows for the use of Ubx materials as a facilitator of cell growth in tissue regeneration and as a structural material and a preventative measure from bacterial infections in the implant area.

Chapter 4

Mechanical properties of Ultrabithorax fibres

4.1 Introduction

This section will motivate the measurements of the mechanical properties of fibres. Then, it will discuss the literature on the mechanical properties of protein materials relevant to their applications for tissue engineering. The effect of protein composition in mammal tissues including tendons, skin, and myocardium, on their mechanical properties and functions will be outlined. In this context, the importance of considering the mechanical properties in the design of implantable devices will be highlighted. Previous literature on the mechanical properties of Ubx fibres included measurements only using freshly prepared fibres [17, 38]. The aim of this chapter was to investigate the mechanical properties of Ubx fusion material after prolonged storage, which would enable sample oxidation, which was reported to make Ubx fibres stiffer [38]. Because the oxidation of Ubx was shown to cause intermolecular bonding between tyrosine residues, which increased the mechanical strength of Ubx materials [39], these investigations can inform the real-world applications of Ubx materials, in which oxidation due to the prolonged storage is likely to affect the products. In addition, the differences in the mechanical properties of dry and rehydrated fibres were measured, which can provide additional information about the applicability of Ubx materials in the future device design process.

4.1.1 Mechanical properties and industrial use of fibres

The mechanical properties of fibres made using different materials, from metals to proteins and glass, have been routinely tested and compared to inform the design of structural and functional devices that had to satisfy strength and elasticity requirements dictated by their application. Metal fibres often constitute building blocks or feature as structural support in engineering. Steel fibres, with tensile strengths around 2000 MPa and an elastic modulus of 200 GPa, are used to reinforce concrete structures [89]. They enhance the heat conductivity and crack resistance of concrete beams, and they improve the post-crack residual tensile strength of the beam. Fibres made using other materials, such as carbon or basalt, have been used in automotive, aerospace and chemical industries to enhance the strength-to-weight ratio, ductility and thermal conductivity of materials, and to introduce corrosion and chemical protection [90]. Natural fibres made of biodegradable polymers have been considered for applications in the construction and other industries with a large carbon footprint and sustainability issues surrounding the use of petrochemicals and inability to recycle materials [90]. The natural fibres used in construction include coconut, jute, straw, flax, and cane, all of which were used due to their ready availability and mechanical strength. These fibres can provide other features such as thermal insulation, prevention from cracking and decreasing shrinkage.

The tensile strength of metal materials was recognised as one of the important characteristics in determining their applicability for different designs and the durability of resulting components. The wealth of tensile testing methods in application to metals has been subject to review and standardisation to ensure comparability and reliability of measurements [91]. The measurement and analysis methods could be applied to other materials, including natural and biopolymer fibres, to determine their mechanical properties and inform the design of devices for sustainable industries. Similarly to metals, the effects of production methods, composition, temperature and humidity can affect the mechanical properties of natural fibres [90]. Therefore, it is important to study the mechanical properties of natural materials and their dependence on the environmental and production conditions.

A pivotal study of the effect of molecular structure on mechanical properties of metals, glass and silica showed the effect of the production parameters and the material morphology on the tensile strength of thin fibres [92]. In a study of

thin glass fibres, their tensile strength was the highest for a few seconds after fibre preparation. Moreover, the freshly produced glass fibres appeared to be almost perfectly elastic up to high stresses approaching the breaking strength. A few hours after production, the strength of fibres increased to a steady value depending on the diameter of the fibre. The mechanical properties of fibres showed a strong diameter dependence with a rapid decrease in their breaking strength with rising diameter. This study of the mechanical properties of glass and silica fibres showed that the method of preparation of fibres, the preparation temperature, and the impurities within the fibres, all introduced irregularities in their breaking strength. This meant that both the fibre preparation and their age were important factors in determining actual tensile strength of glass fibres. These considerations led to the experiments in this thesis that determined whether oxidation during storage of Ubx fibres and rehydrating the fibres after storage could affect their mechanical properties.

4.1.2 Mechanical properties and applications of protein materials

Metals and synthetic materials have been used in biotechnology, medicine, and other industries including construction and electronics, because of their strength, durability, electrical and thermal properties. Proteins offer improvements in material properties, biodegradability and sustainability of devices, compared to metals and synthetics, in an analogous way to that, in which natural fibres have been used to improve the material properties or sustainability credentials of construction materials.

Protein materials have a range of different mechanical characteristics, and often their mechanical properties need to be adjusted to form tissues. Composite materials made of a blend of collagen and elastin create a range of tissue types in mammals, each exhibiting different mechanical and structural properties that suit their functions [3, 13, 93–95]. The comparison of properties of individual proteins allows to understand their specific functions. Within mammalian tissues, collagen provides the mechanical strength of tissues, which is evidenced by its high breaking strength of approximately 120 MPa in human tendons [93]. The load-carrying capability of collagen was confirmed in an investigation of the mechanical properties of skin and thoracic aorta in the presence of elastase, hyaluronidase and collagenase [94]. Both elastase and collagenase significantly weakened pure col-

lagen films, and collagenase degraded skin and aorta specimens, which indicated that collagen provided most of the tensile strength in these tissues [94]. Collagen forms stiff and not very extensible structures, with its Young's modulus of 1.2 GPa and breaking strain of 13% [93]. On the other hand, elastin from bovine ligaments forms extensible but weaker and less stiff materials, with a breaking strength of 2 MPa, Young's modulus of 1.1 MPa and large breaking strain of 150% [93]. Elastin affected the elastic behaviour of thoracic aorta, which could mean that while it did not provide significant tensile strength to aorta samples, it enabled the extension and elastic behaviour in the toe region of the stress-strain curve [94]. Interestingly, the same study found that hyaluronic acid did not appear to affect the mechanical properties of the tissue specimens [94].

Tissues made of a combination of collagen and elastin form a significant portion of the musculoskeletal system and exhibit a wide range of mechanical properties, from soft and extensible to stiff and strong. Locomotion is possible thanks to the development of strong and elastic connective tissues enabled by cross-linking of collagen [13]. In particular, the elastic energy storage and release in tendons enables movement and conservation of energy [13]. The mechanical properties of tendons are largely determined by the behaviour of collagen both on molecular and fibrillar scale [95]. The shape of the stress-strain curve of tendons results from the fibrillar and molecular straightening of kinks followed by molecular gliding [95]. These phenomena, along with interfibrillar gliding, play a large part in providing tendons with the stress-carrying mechanical strength [95]. The development of mechanical properties of tendons suggested that their tensile strength and Young's modulus depended largely on the collagen fibril length within the fibres instead of on the fibre diameter [13]. The fibril length appeared to increase during the development of tendons in a chicken embryo, which caused an increase in tensile strength from 2 MPa after 14 days of development to 60 MPa 2 days after birth, which enabled movement [13]. The elastic modulus of turkey tendons made predominantly of collagen type I was between 5 GPa and 7.75 GPa, which was similar to rat tail tendon [13]. Type I collagen fibrils tended to increase linear rather than lateral size of self-assembled fibres, and the breaking strength (approximately 0.6 MPa) of these fibrils did not depend on the diameter in the range between 10 and 40 µm [13]. These findings suggested that the length and stretching of individual fibrils constituting collagen fibres rather than the fibre diameter, both in collagen self-assembled *in vitro* and grown in chicken and turkey tendons, affected their mechanical properties and the elastic behaviour [13]. The

mechanical properties of self-assembled collagen fibres could be altered by pre-stretching before cross-linking of collagen, with the pre-stretched fibres exhibiting significantly larger tensile strength and stiffness, and reduced extensibility, compared to unstretched fibres [9]. In addition to stretching, the extensibility, tensile strength and stiffness of collagen fibres could be increased by adding decorin, which interacted strongly with collagen fibrils and was suggested to assist inter-fibrillar gliding in collagen fibres [9].

Proteins are widely used to design scaffolds for tissue engineering. Scaffolds made of type I collagen, elastin and gelatin were cross-linked using carbodiimides [3]. They exhibited favourable properties for applications in myocardial tissue engineering, including the mechanical properties matching those of the native tissue, and porosity and biocompatibility that could allow cell proliferation [3]. The combination of cross-linked collagen and insoluble elastin for scaffold design matched the mechanical properties of the native heart tissue [3]. Substituting collagen for gelatin as a base protein decreased the mechanical strength and stiffness, and increased the scaffold degradation rate. These features were suggested as suitable for skin repair where faster degradation is preferable [3]. An alternative design showed that incorporation of collagen fibres in collagen gel scaffolds offered a way to improve the mechanical properties of the scaffolds to mimic ligaments [10]. Moreover, the incorporation of cells in the scaffold increased both the stiffness and maximum stress supported by the scaffold, which suggested that these scaffolds supported cell proliferation and potential tissue formation, which strengthened the engineered ligaments [10]. The cell-seeded gel-fiber scaffolds could develop properties resembling those of ligaments with sufficient cell culture growth and an appropriate composition, which could be enriched by other proteins, such as elastin, to enhance the elastic behaviour at low strains [10]. Collagen and elastin scaffolds with varying compositions could be used for tissue engineering and regeneration of skin, ligament and heart tissue.

Other protein materials exhibit combinations of mechanical properties that are necessary for survival in their natural environment. Mussel byssal fibres are strong, stiff and have low resilience, all of which allow their effective attachment to rocks and survival of significant stress exerted during in-life extension of the fibres due to waves [93]. These fibres are very extensible with breaking strains of 109% for distal and 200% for proximal fibres. In combination with a breaking strength of 35 MPa for proximal, and 75 MPa for distal fibres, and their respective Young's moduli of 16 MPa and 870 MPa, these fibres provide extraordinary mechanical

properties allowing the mussels to remain securely attached despite strong applied forces [93]. The toughness of these fibres is comparable to that of carbon fibre and Kevlar [93].

Silk is another protein-based material widely present in nature in organisms such as *Bombyx mori* and spiders. Silk derived from the silkworm *Bombyx mori* is generally weaker (breaking strength of 0.5 GPa) and less extensible than spider dragline silk, although changing the spinning conditions could increase its extensibility from 15% to 37% [22]. Spider silk comes in a range of forms, which have different mechanical properties and functions. Silk produced in spider's major ampullate (MA) gland, such as dragline silk, has different properties depending on the genetic sequence and the species it is produced by. MA silk extracted by *Araneus diadematus* has higher extensibility and similar breaking strength and Young's modulus compared to that from *Nephila clavipes* (both *A. diadematus* and *N. clavipes* are commonly studied orb-weaver spiders). This suggested that the more amorphous structure of *Araneus diadematus* silk enhanced its elasticity [96]. Dragline silk is extremely strong. Its breaking strength is 1.1 GPa, and it has high stiffness with a Young's modulus of 10 GPa [93]. However, with a breaking strain of 30%, it is not as extensible as viscid silk whose extensibility is 270%. Viscid silk has a lower strength of 500 MPa and a much lower stiffness with a Young's modulus of 3 MPa [93]. These properties reflect the applications of these two types of silk. Dragline silk is used to provide structural strength to support the spider's weight, whereas viscid silk is used to capture insects, and needs a combination of strength and elasticity to survive the impact and keep the captured organism in place. These examples, along with the range of the properties of tendons, show how protein materials can have a range of properties depending on their composition, cross-linking method, and environmental conditions, all of which can serve their respective functions in living organisms [93].

Genetically engineered silk was developed as a more sustainable alternative to naturally occurring spider silk with the genetic sequence optimised for protein yield, antimicrobial and cell binding properties. [15]. A genetically engineered 4RepCT silk construct contained a large, repetitive core with a lot of glycine (G) and alanine (A) - up to 90% amino acid sequence length. A-rich parts were likely forming β-sheet crystals while G-rich parts constituted amorphous regions, and their combination contributed to an exceptional mechanical strength of the construct [15]. The tensile strength of a 1 mm diameter fibre was 200 MPa, which was comparable to the tensile strength of tendons [15, 93]. Therefore,

the mechanical properties of this construct could be sufficient for use in tendon replacement.

4.1.3 Mechanical properties of Ubx fibres

Ubx was found to self-assemble into elastic and moderately strong materials, including fibres [38]. Significant differences in fibre length were observed depending on concentration of Ubx proteins used to form the material. Ubx auto-fluoresces in blue due to the dityrosine in its structure [39]. The length of fibres and their fluorescent intensity were correlated, which suggested that dityrosine formed intermolecular bonds and that it was responsible for the strength of formed materials [39]. These dityrosine bonds formed due to the oxidation of Ubx monomers, which suggested that oxidation had an important role in Ubx material formation. Ubx contains 15 tyrosines in different regions of the protein sequence [39]. The formation of dityrosine bonds in Ubx materials is likely due to the bonds between tyrosines in N-terminus and the homeodomain (Y4/Y296 or Y12/Y293), with another bond between Y167 and Y240. Crucially, the homeodomain tyrosines lie on the surface of the domain, and the N-terminus tyrosines are also exposed to enable bonding [39]. These factors contribute to the ability of Ubx to form materials in solution. In addition, the presence of dityrosine in Ubx materials was only observed in fibres produced in an oxygen-rich environment, in which the Ubx materials were also stronger. These observations suggested that the formation of dityrosine bonds by oxidation at the air-water interface is responsible for the strength of Ubx materials and contributes significantly to their strength. The exposure of tyrosines responsible for intermolecular bonding could facilitate material formation during the conformational change at the air-water interface.

The properties of freshly prepared Ubx fibres were measured. Ubx fibres were highly extensible with breaking strains between 25% and 160%, while their breaking strength spanned between 2 and 30 MPa [17]. The tensile strength measurements of EGFP-Ubx fibres yielded an average breaking strain of 53% and breaking strength in the range between 5 and 65 MPa [17, 38], depending on the fibre diameter. Fibres with increasing diameter had lower breaking stress and higher strain [17]. EGFP-Ubx fibres had lower breaking strain and higher breaking stress than Ubx fibres [17], which indicated that Ubx functionalized with other proteins created materials with different mechanical properties. This could allow tuning of these properties using different Ubx fusions. Ubx materials also stiffened when

dried, and maintained their shape after drying and a subsequent return to aqueous environment [38], which could enable the use of Ubx materials after prolonged storage. Because the mechanical properties of Ubx materials were studied only in a freshly prepared, hydrated form [17,38], there was a need to investigate how oxidation during storage affects the mechanical properties and applicability of Ubx fusion fibres.

Applying protein materials for tissue engineering is challenging because of the required material properties of created scaffolds [97], some of which have to be adapted for use within specific organs, e.g. myocardium [88], to match the properties of the native tissue and facilitate the heartbeat. A versatile material must allow tuning the size and pore size of scaffolds, and should be readily functionalised or shaped to have high elastic modulus or low electrical resistance. The elastic properties of Ubx varying with fibre diameter and fusion type could allow the control over the strength of scaffolds [17, 38]. They must attain very high elastic moduli to be used as vascular grafts or myocardial patches. EGFP-Ubx fibres with reported strength up to 70 MPa [17,38] exceeded the breaking strength of arteries and saphenous veins [98], which meant that both Ubx and EGFP-Ubx materials could have sufficient strength and tensile modulus for applications in tissue engineering of vascular grafts. The comparison of mechanical properties of Ubx fibres and protein materials used in tissue engineering is shown in table 4.1.1.

The knowledge of mechanical properties of protein material such as Ubx is required to inform the use of protein materials to create tissue scaffolds with desirable mechanical properties. Previous investigations of the mechanical properties of tissues such as skin, tendons, ligaments, and blood vessels showed the characteristics needed in novel biomaterials. The effects that both protein degradation and addition in composite materials had on the mechanical properties of scaffolds showed that these properties could be tuned in a wide range of values. The work shown here highlights the systematic measurements of the mechanical properties of Ubx and EGFP-Ubx after a period of storage of several weeks. These measurements are important because they highlight the effect of oxidation on the material properties of Ubx, which can affect the real-world applications of Ubx materials. Moreover, the tensile tests of protein fusion fibres were conducted for dry and rehydrated fibres after storage to measure the effect of fibre rehydration on their strength and extensibility. These measurements can influence the design of protein fusions and protein material preparation for applications in tissue en-

Table 4.1.1: The mechanical properties of protein materials considered for tissue engineering and biomedical applications.

Protein (source)	**Tensile strength** (MPa)	**Breaking strain** (%)	**Young's modulus** (GPa)
Collagen (mammalian tissue) [93]	120	13	1.2
Elastin (bovine ligaments) [93]	2	150	0.001
Silk (*Bombyx mori*) [22,93]	500	15	7
Dragline spider silk (*Araneus diadematus*) [93]	1100	30	10
Viscid spider silk *Araneus diadematus* [93]	500	270	0.003
Silk (genetically engineered 4RepCT) [15]	200	-	-
Ubx (recombinant) [17, 99]	30	120	0.4
EGFP-Ubx (recombinant) [17, 38, 42]	65	40	0.975

gineering and biotechnology. They can also suggest the strategies for choosing the protein fusions appropriate for applications in composite materials, in which biosensing and good mechanical and biological properties can all be achieved by combining a range of functional proteins.

4.2 Experimental section

The experiments conducted in this chapter aimed to investigate the mechanical properties of Ubx fusion fibres subject to oxidation during a prolonged storage, which could affect the protein structure and the mechanical properties of the materials. The dityrosine bonds between Ubx monomers are formed because of the oxidation of tyrosine residues. The strength of the Ubx materials, including fibres, was attributed to the stable dityrosine bonds [39]. Therefore, it was hypothesised that the oxidation of Ubx fusions during storage could change the mechanical properties of Ubx fusion fibres compared to those of freshly pulled fibres [17, 38]. This section will describe the experimental methods used in the current investigations. It will detail the preparation of fibres for tensile testing after storage, including rehydration and fibre mounting onto the tensile stage. The tensile stage will be described. The resolution limitations of the measurements of

the tensile strength of the Ubx microfibres will be discussed. The processing of the force-elongation curves generated by the software will be detailed. The data analysis pipeline enabled filtering of the noise present in the measurements, and the subsequent extraction of the mechanical properties of Ubx fusion fibres.

4.2.1 Fibre rehydration

The measurements of the mechanical properties of dry and rehydrated EGFP-Ubx fibres after several weeks of storage were conducted. Ubx materials stiffened when dried [38], which led to an investigation into whether rehydrating the samples in a high humidity environment could affect the elasticity or tensile strength of the fibres.

A polystyrene container was prepared with approximately 500 mL of warm water. Fibres were placed on a polystyrene platform, which was floating on the water surface. The lid of the polystyrene container was replaced, and the fibres were incubated in the container for 1 h. It was found that longer storage led to excessive condensation, which caused the fibres to break. Then, the fibres were prepared for tensile testing.

4.2.2 Fibre preparation for tensile testing

A rectangular piece of cardboard approximately 25 mm x 10 mm was prepared, and a square 8 mm hole was cut out to form a frame. These frame sizes were appropriate for the sample placement onto the tensile stage used in this experiment (section 4.2.3). A small drop of ethyl 2-cyanoacrylate (Loctite Super Glue) was placed on each of the short sides of the square hole to enable fibre attachment. A fibre attached to the U-shaped hook was placed above the frame and the ends of the fibre were pressed down against glue, which caused the fibre to adhere to the cardboard (figure 4.2.1). The glue was allowed to set for 5 min before the fibre was placed on the tensile stage.

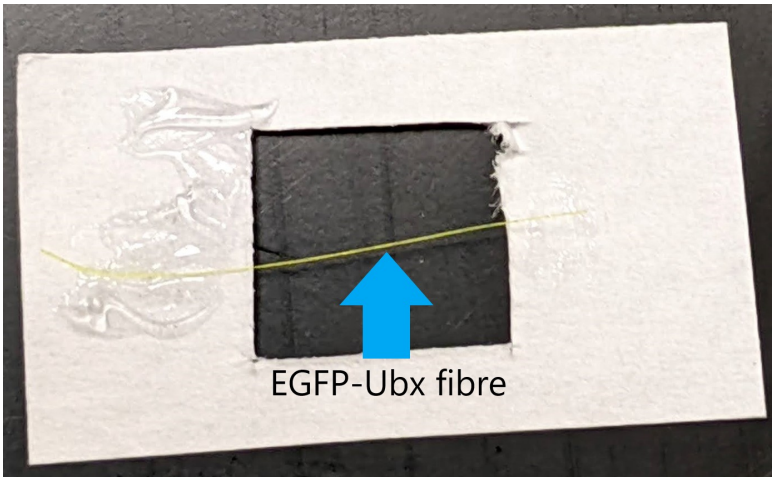

Figure 4.2.1: Photograph of an EGFP-Ubx fibre attached using ethyl 2-cyanoacrylate to a piece of cardboard before mounting onto the tensile stage.

4.2.3 The tensile stage

A Deben MT200 tensile stage (figure 4.2.2) was used for tensile testing of Ubx fusion fibres. A 2 N load cell was used to measure the tensile strength of fibres in the extension mode. The device allowed carriage movement between 10 and 20 mm extension, and the force was measured to a resolution of 0.1 mN. The resolution of the elongation measurements was 1 µm.

Despite the resolution of the force measurements using this tensile stage and loadcell, a systematic error was observed in the force measurements provided by the stage, which was occurring with a spatial frequency of approximately 2 mm^{-1}. The measurement of noise and the Fourier transform of this signal is shown in figure 4.2.3. In practice, this systematic error caused the resolution of the force readings to decrease to about 0.7 mN. This was a limiting factor in the resolution of the measurements of mechanical properties of Ubx fusion fibres because their breaking force ranged between 0.3 mN and 10 mN. The systematic error had to be addressed during data analysis to account for the limited measurement resolution and filtering of the raw data was applied to extract information about the mechanical properties of Ubx fusion fibres (see section 4.2.5).

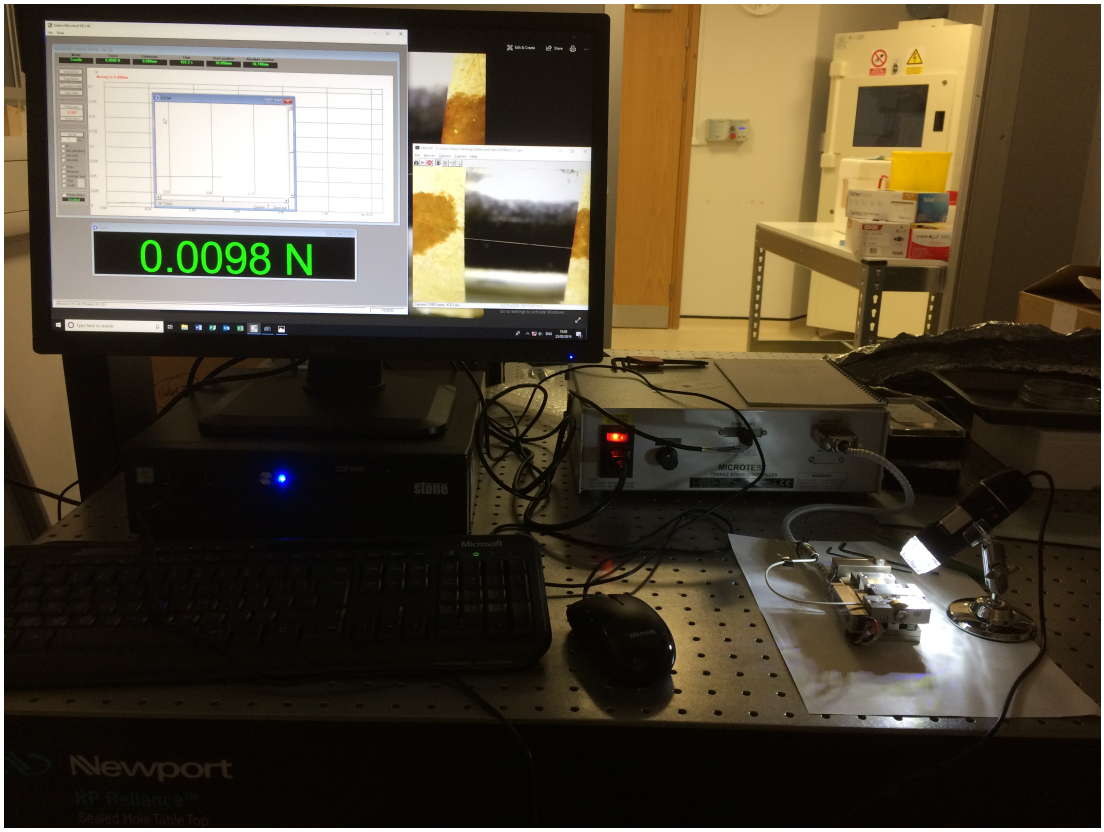

(a)

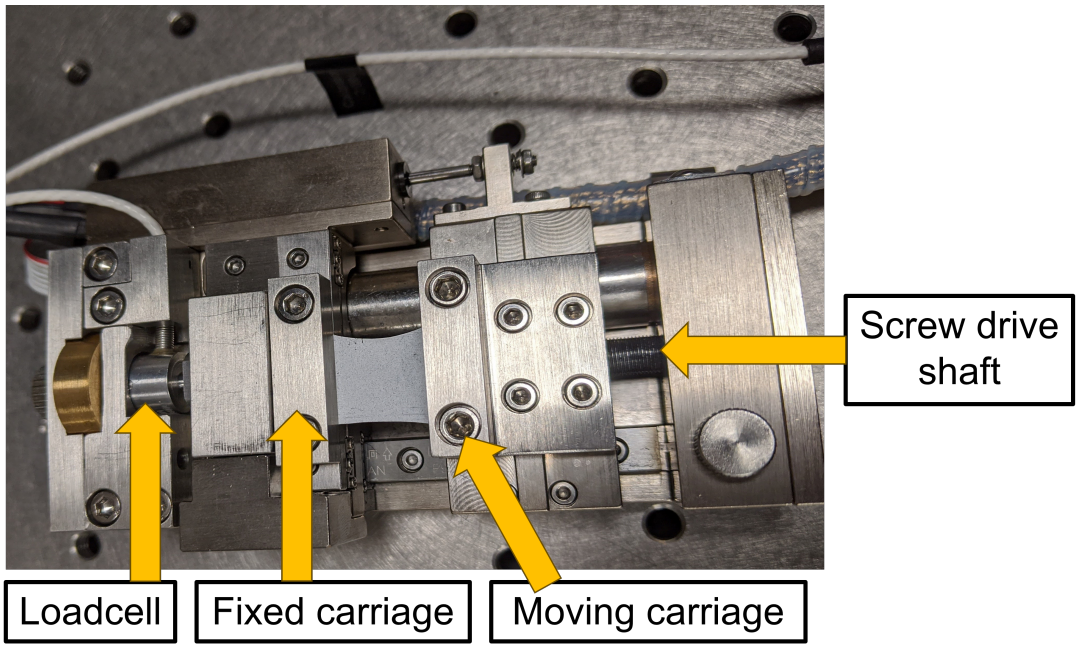

(b)

Figure 4.2.2: (a) The tensile testing setup used to measure the mechanical properties of Ubx fusion fibres. (b) Diagram of the tensile stage.

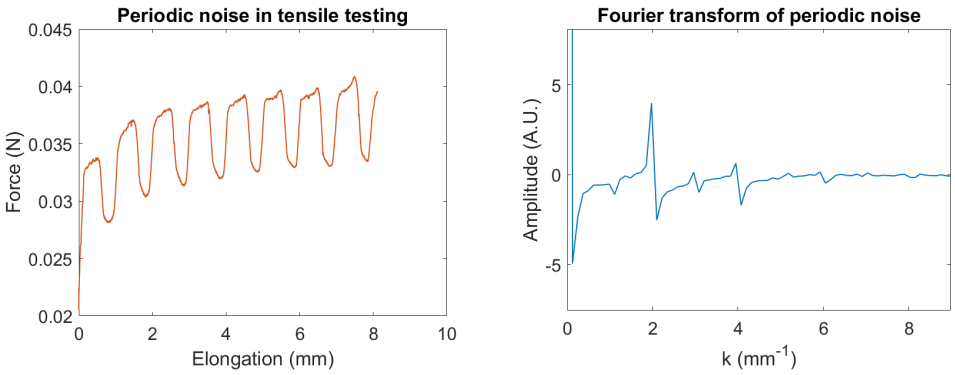

(a) (b)

Figure 4.2.3: (a) The force-elongation plot for an unloaded Deben MT200 tensile stage without a sample. carriages were fitted with flat mounts that were later used to mount fibres in the tensile tests. (b) The Fourier transform of the force-elongation plot, where the y-axis shows the amplitude, and the x-axis shows the spatial frequency k of the signal. The Fourier transform outlines the systematic signal (periodic noise) in the tensile stage reading. This periodic noise limited the resolution of the tensile stage force measurements to approximately 0.4 mN.

4.2.4 Tensile testing

The fibres were mounted onto the stage using flat sample mounts that were placed atop the sides of the cardboard containing the tested fibre. The sample mounts were screwed onto the stage to fix the cardboard in place. The sides of the cardboard were snipped to ensure that the two carriages of the tensile stage were only connected by the fibre, which enabled the reading of the tensile force during fibre extension. Photographs showing the tensile stage, the mounting of Ubx fusion fibres before tensile testing, and the software controlling the tensile stage are shown in figure 4.2.4.

After the fibre was mounted onto the tensile stage, the force-elongation curve was generated by the precise measurements of the force exerted on the loadcell by the extending fibre. The movement of the carriage took place at a controlled speed of $0.1\,\mathrm{mm\,min^{-1}}$ to mitigate the effects of fibre elongation rate on the measured forces, and to enable the comparison to previous measurements on the mechanical properties of Ubx fusions [17]. The measurements were taken with the maximum gain (x50) of the digital signal processor to enhance the measurement resolution. The readings were continued until after fibre fracture, after which the fibre was removed and the tensile stage carriage returned to the starting position.

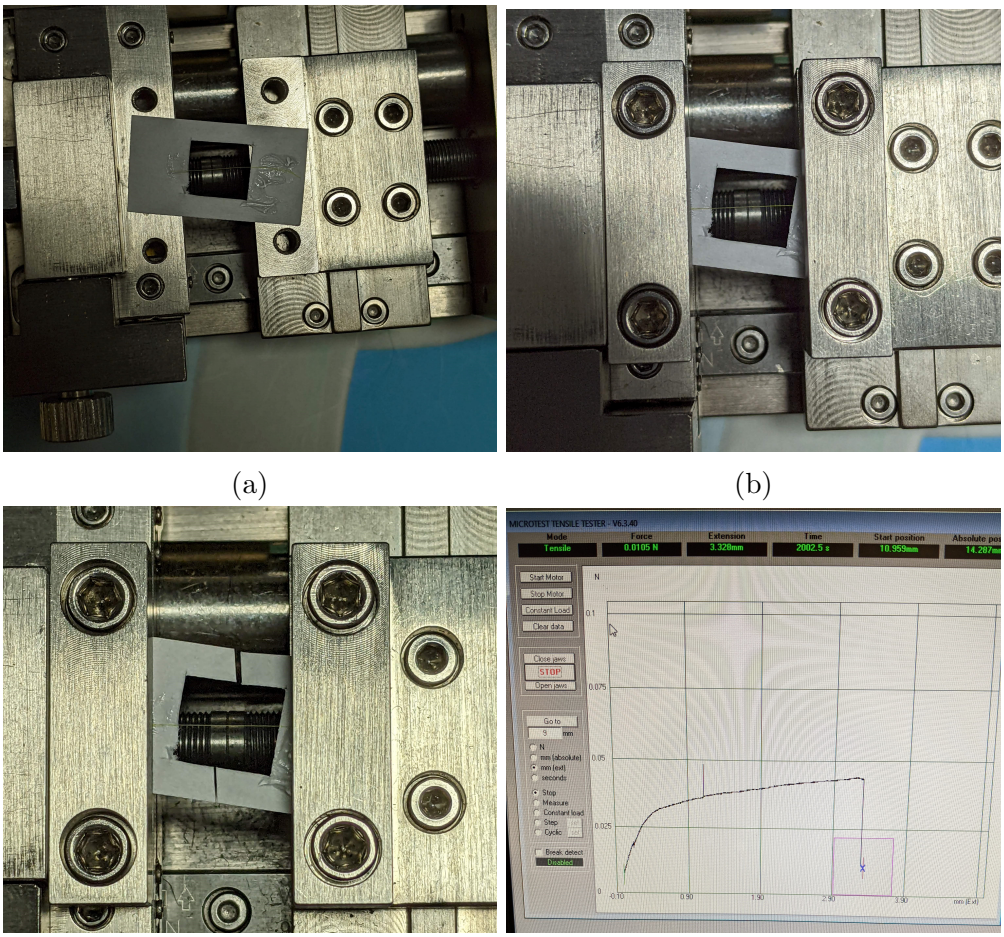

Figure 4.2.4: (a) Photograph of the tensile stage with a fibre placed across the carriages using a cardboard sheet and 2-cyanoacrylate. (b) The fibre fixed onto the tensile stage using the flat sample mounts. (c) Sides of the cardboard were snipped to ensure that only the force exerted on the fibre was measured by the loadcell. (d) The software used to control the tensile stage and record and monitor the force-elongation curves in real time.

4.2.5 Analysis pipeline

MATLAB [84] was used to analyse the force-elongation curves generated using the tensile stage. The box car (moving average) filter was used throughout data processing. The box car filter calculated the force (or stress) value at each elongation (or strain) point by averaging the stress of w data points including and preceding the starting point. The output of the filter $y(n)$ with window size w for an initial value $x(n)$ can be described by

$$y(n) = \frac{1}{w}(x(n) + x(n-1) + ... + x(n-(w-1))). \tag{4.2.1}$$

This filter was applied using the *filter* function in MATLAB. Because the single box car filter introduced a delay in the filtered data and provided inferior noise elimination, the double box car filter was used where indicated. This filter's function involved running the box car filter twice, the first run was a standard box car filter, and the second run acted on the filtered data in reverse, i.e. starting from the last data point. This filter was applied using the *filtfilt* function in MATLAB.

To analyse the force-elongation measurements for Ubx fibres, the fracture point of the fibre was determined by finding the minimum of the first derivative of the force-elongation curve from a force-elongation curve smoothed with the box car (moving average) filter with a window size of 5. The data was cut off at a point preceding the minimum of the first derivative to enable further analysis. The data was shifted to start at the origin. The result of this initial step is shown in figure 4.2.5.

The force-elongation curve was translated into a stress-strain plot (figure 4.2.6) using equations 4.2.2 and 4.2.3:

$$\sigma = \frac{F}{A} \tag{4.2.2}$$

$$\epsilon = \frac{l - l_0}{l_0}, \tag{4.2.3}$$

where σ is the stress, F is the force, A is the cross-sectional area of the fibre approximated as a circle using the fibre diameter, ϵ is strain, l is the absolute length of the fibre during elongation, and l_0 is the initial length of the fibre.

The corresponding standard errors were calculated using equations 4.2.4 and

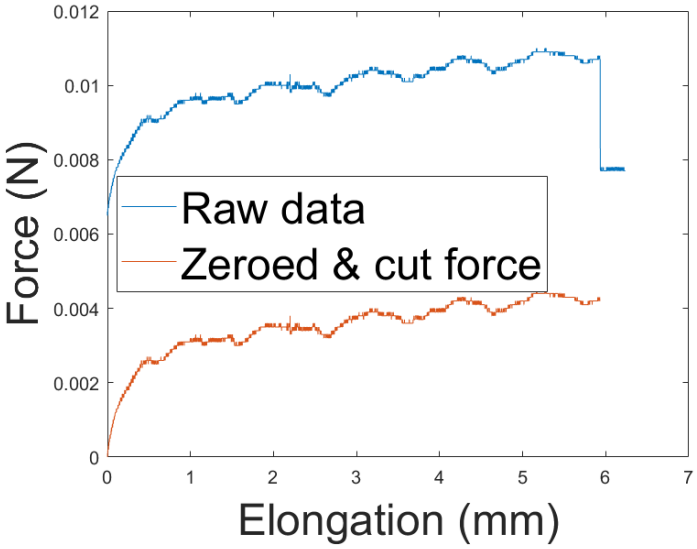

Figure 4.2.5: Shifting the force-elongation data to start at the origin and finding the fracture point.

4.2.5:

$$\Delta\sigma = \sqrt{\left(\frac{\Delta F}{A}\right)^2 + \left(\frac{F\Delta A}{A^2}\right)^2}, \tag{4.2.4}$$

$$\Delta\epsilon = \sqrt{\left(\frac{\Delta(l-l_0)}{l_0}\right)^2 + \left(\frac{(l-l_0)\Delta l_0}{l_0^2}\right)^2}. \tag{4.2.5}$$

The measured forces exerted on the fibre were close to the limit of the resolution of the tensile stage loadcell, which caused a significant periodic background reading. The systematic error was caused by the rotation of the screw driving the moving carriage, which caused the extension of the sample (see figure 4.2.2), which repeated approximately every 1 mm. The Fourier transform of the control force-elongation curve for an unloaded tensile stage was calculated to determine the spatial frequency of the noise in the background measurement (see figure 4.2.3). Based on the frequency of the periodic noise, the signal was filtered using a single or double moving average filter with a calculated window size corresponding to a movement of the carriage of 1 mm (approximately 1204 points). Both the box car and the double box car filters with this window size eliminated the periodic error introduced by the movement of the stage, which is shown in figure 4.2.7. The use of a wide window size required the minimum elongation of approximately 3 mm, which was not achieved by all tested fibres. In these cases, the window size was reduced by a factor of two in order to enable filtering and

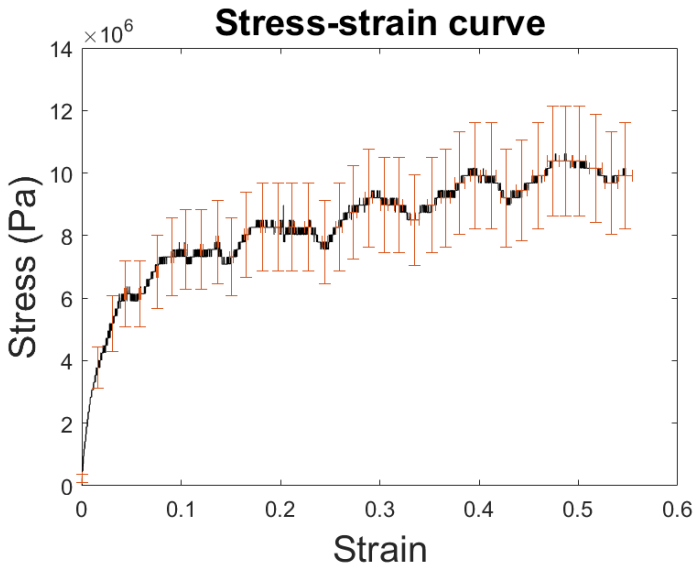

Figure 4.2.6: The stress-strain curve generated using the shifted force-elongation plot. Error bars correspond to the standard errors in the mean measurements of force, elongation, fibre diameter and length.

the noise reduction was achieved without complete elimination. However, the filtering of the periodic noise enabled the extraction of material properties based on the tensile force-elongation measurements of Ubx fusion fibres.

The double box car filter was the most effective at reducing the systematic noise and did not shift the data relative to the origin of the movement. The single box car filter shifted the strain, which required corrections based on the window size of the filter. The onset of the plastic deformation region was found by calculating the location of the minimum of the second derivative of the stress-strain curve smoothed using the double box car filter (figure 4.2.8.)

The Youngs's modulus was calculated by measuring the slope of the stress-strain curve after applying the double box car filter. The slope was determined using a linear fit to the filtered data. An illustration of this slope is shown in figure 4.2.9.

The breaking strain of the fibre was calculated using the elongation at fracture and equations 4.2.3 and 4.2.5. The process is illustrated in figure 4.2.10. The corresponding breaking strength was calculated using equations 4.2.2 and 4.2.4. The intercept of the linear fit to the linear part of the stress-strain curve smoothed using the double box car was subtracted from this breaking strength in order to obtain a representation of the breaking strength that accounted for the periodic noise. An example of the measured breaking strength is shown in figure 4.2.11.

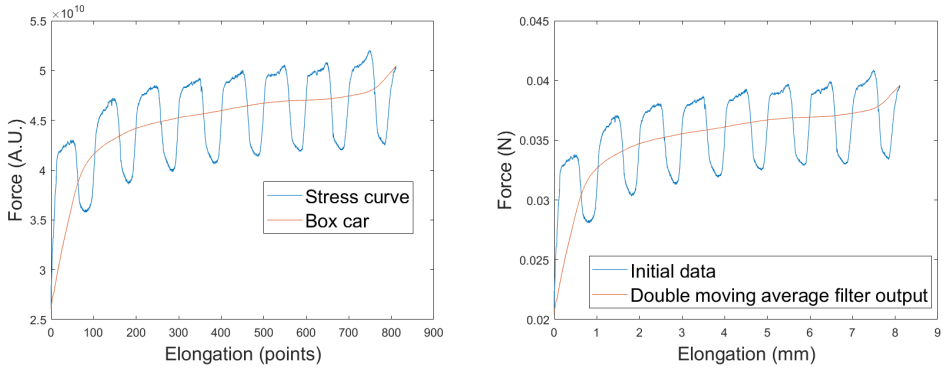

(a) (b)

Figure 4.2.7: The output of the box car and double box car filters applied to the periodic systematic noise introduced by the rotation of the screw drive shaft of the tensile stage. This output shows that the periodic oscillation is eliminated by applying the filter with a window size corresponding to the elongation by 1 mm.

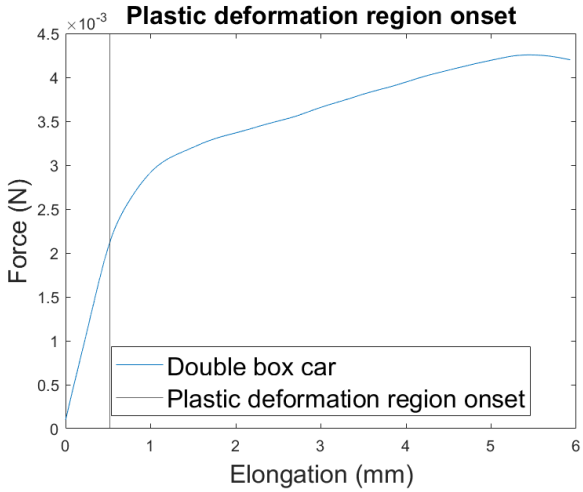

Figure 4.2.8: The onset of the plastic deformation region was found at the minimum of the second derivative of the force-elongation curve smoothed using a double box car filter.

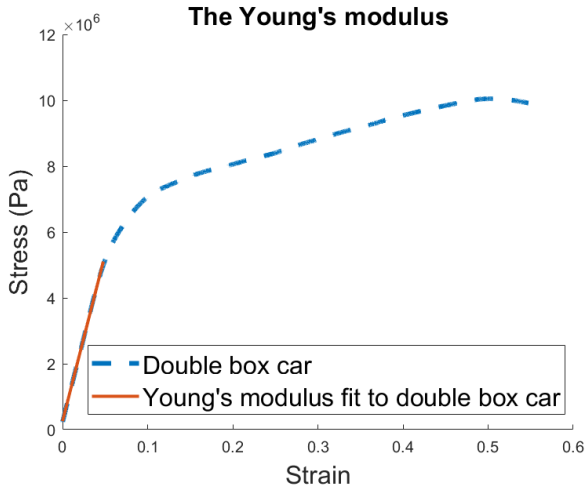

Figure 4.2.9: The Young's modulus was determined by calculating the slope of the stress-strain curve using a linear fit to the data processed with the double box car filter.

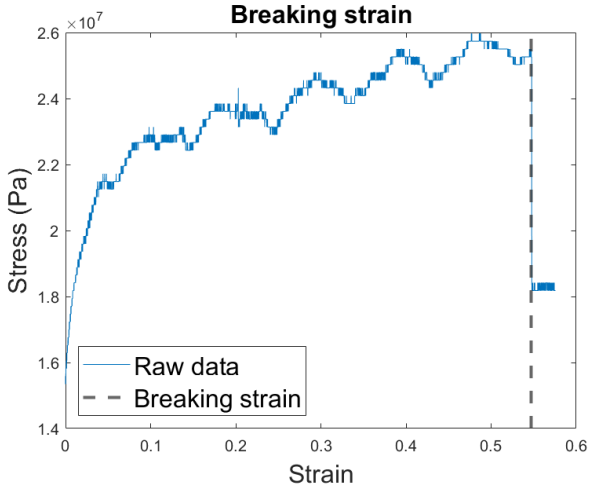

Figure 4.2.10: The breaking strain was determined by measuring the minimum of the first derivative of the stress-strain curve smoothed using a box car filter.

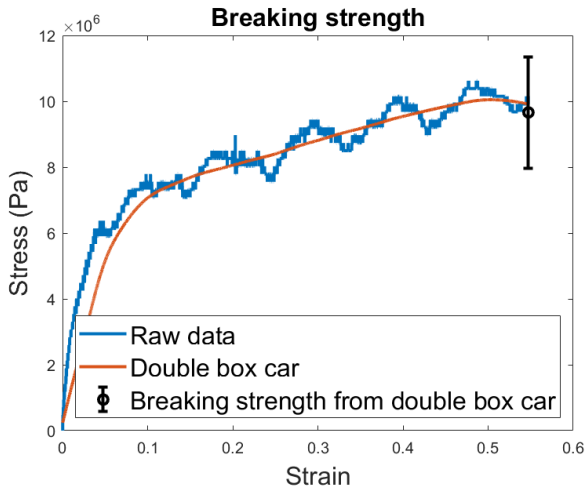

Figure 4.2.11: The breaking strength was determined by subtracting the intercept of the linear fit to the stress-strain curve processed with the double box car filter from the breaking strength determined with the filter.

4.3 Results and discussion

4.3.1 Fibre behaviour during tests

The tensile force exerted on the fibres during stretching caused the fibres to elongate and change their external features. Changes such as stretching of beads of material on the fibre surface were visible. The illustration of changes in fibre structure is shown in figure 4.3.1. The stretching of a bead of rehydrated protein was seen between 0 and 10 min of extension, and the general extension and elongation of the fibre features was observed during testing.

The force-elongation curves generated during tensile testing differed for fibres of different sizes, which corresponded to the varying maximum loads and extensions for fibres of each size. The force-elongation curves were translated to stress-strain graphs. A sample stress-strain plot for a Ubx fibre is shown in figure 4.3.2. A characteristic feature of the stress-strain plots was a sharp increase in the stress at low strain followed by a slower rise after the yield point. These two behaviours correspond to linear and plastic deformation regions, which are normally separated by a yield point, after which a material cannot return to its original shape. The values of force exerted on the fibres due to strain were often of the same order of magnitude as the systematic error introduced by the movement of the screw that drove the moving carriage of the tensile stage (see section 4.2.3). This effect introduced a periodic oscillation around the actual

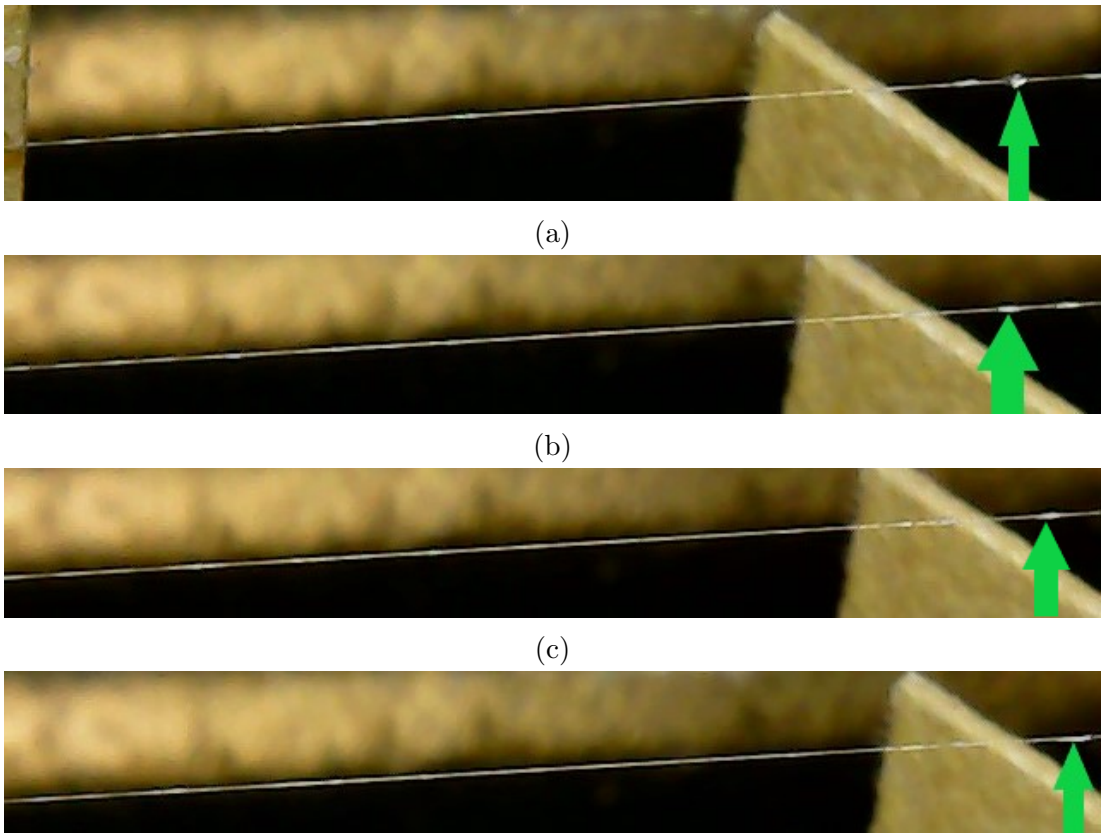

(a)

(b)

(c)

(d)

Figure 4.3.1: Pictures of a sample EGFP-Ubx fibre (a) before extension, (b) after 10 min, (c) after 20 min, (d) before breaking.

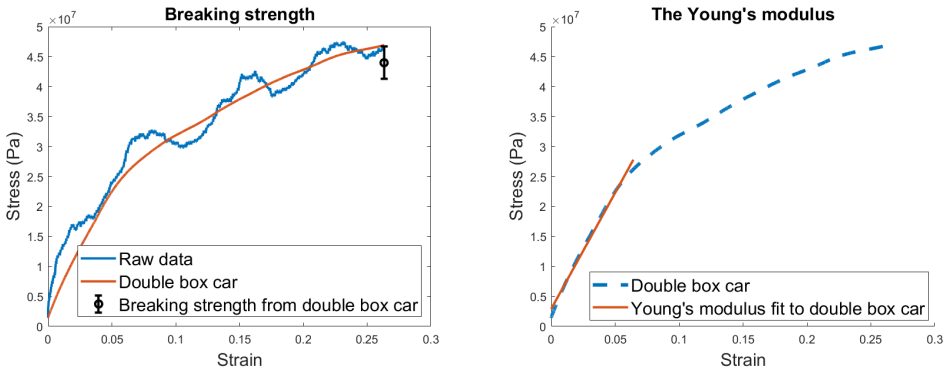

(a) (b)

Figure 4.3.2: (a) A sample stress-strain plot for a Ubx fibre tested until fracture and the double box car filtered data to remove the periodic noise. (b) A plot showing the filtered data linear fit applied to calculate the Young's modulus.

force reading, which was filtered from the data using the moving average (box car) filters. Figure 4.3.2b showed an illustration of the effect of applying different filters and the linear fits used to calculate Young's modulus for the fibres. The data was cut off before breaking point to enable filtering and finding the breaking strength. The values of the breaking strength were of the order of magnitude of 10 MPa to 100 MPa. The values of breaking strain spanned between 5% and 55%, the breaking strength ranged from 5 MPa to 1 GPa, and the Young's modulus took values from 71 MPa to 56 GPa. The large differences in these results indicated that the size of fibres strongly influenced their mechanical properties.

A sample graph for an EGFP-Ubx fibre shown in figure 4.3.3 exhibits a steeper initial increase in the stress-strain curve, followed by a slower rise in stress in the plastic deformation region. The length of the plateau depended on the elasticity of the fibre. The sharp increase in stress allowed a more accurate calculation of the Young's modulus because of the lower effect of the periodic noise at short elongation, which meant that a sharp linear increase in stress at low strain was observed. Data filtering was less relevant and offered smaller improvements when larger forces were registered. The range of breaking strain of EGFP-Ubx fibres was narrower than for Ubx with values between 3% and 38%. Similarly, the range of the breaking strength for these fibres was between 7 MPa and 110 MPa, and the Young's modulus spanned between 130 MPa to 10 GPa. These results emphasised a strong dependence of the mechanical properties of EGFP-Ubx fibres on their diameter, although the smaller range of diameters of these fibres was reflected in

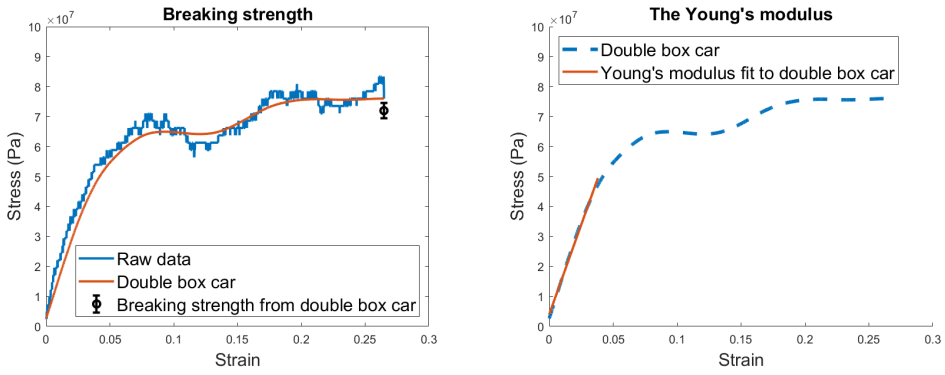

(a) (b)

Figure 4.3.3: A sample stress-strain plot for an EGFP-Ubx fibre tested until fracture and the double box car filtered data to remove the periodic noise. (b) A plot showing the filtered data linear fit applied to calculate the Young's modulus.

the narrower range of values of mechanical properties.

4.3.2 Comparison of the behaviour of dry and rehydrated fibres

Table 4.3.1: The comparison of the mechanical properties of EGFP-Ubx fibres dry or rehydrated after prolonged storage.

EGFP-Ubx fibres	**Dry**	**Rehydrated**
Diameter (µm)	29.8 ± 3.7	25.2 ± 4.9
Mean breaking strain (%)	23.7 ± 2.3	20.1 ± 2.9
Min breaking strain (%)	4.09 ± 0.02	9.54 ± 0.03
Max breaking strain (%)	31.88 ± 0.08	45.52 ± 0.09
Mean breaking strength (MPa)	16.8 ± 2.3	50 ± 34
Min breaking strength (MPa)	6.4 ± 2.5	4.3 ± 3.1
Max breaking strength (MPa)	38 ± 29	386 ± 132
Mean Young's modulus (GPa)	0.35 ± 0.09	1.1 ± 0.9
Min Young's modulus (GPa)	0.1260 ± 0.0002	0.0640 ± 0.0001
Max Young's modulus (GPa)	1.441 ± 0.007	10.195 ± 0.022

The effect of desiccation during storage of fibres on their mechanical properties was investigated by tensile testing dry fibres and fibres rehydrated by incubation in a humidity chamber for 60 min. Two groups of EGFP-Ubx fibres were chosen with a similar distribution of sizes to ensure comparability of the data for dry and rehydrated samples. The average diameter of the dry fibres was (29.8 ± 3.7) µm and that of rehydrated fibres was (25.2 ± 4.9) µm. The summary of the mean,

minimum and maximum of the breaking strength, breaking strain and Young's modulus for the dry and rehydrated EGFP-Ubx fibres is shown in table 4.3.1.

The comparison of the breaking strain of dry and rehydrated fibres is shown in figure 4.3.4. The average breaking strain was higher for the dry fibres, although the maximum of the breaking strain was larger for rehydrated fibres at $(45.52 \pm 0.09)\%$ compared to $(31.88 \pm 0.08)\%$ for dry samples. The minimum of the breaking strain for rehydrated fibres was also higher. The mean breaking strain of the two groups was not statistically significantly different ($P = 0.3432$) but the extremities were higher for the rehydrated fibres, which could mean that hydration allowed for larger extension of fibres.

The difference in the breaking strength of dry and rehydrated EGFP-Ubx fibres was not statistically significant ($P = 0.2778$), even though the mean for the rehydrated fibres was three times higher (figure 4.3.5). The maximum value for the rehydrated fibres was an order of magnitude higher than that for the dry samples at $(386 \pm 132)\,\mathrm{MPa}$ compared to $(38 \pm 29)\,\mathrm{MPa}$. The range of values taken by the rehydrated fibres was wider. Both groups of fibres exhibited a strong dependence of their breaking strength on fibre diameter. The breaking strength of rehydrated fibres decreased by two orders of magnitude with a diameter decline from $(56 \pm 7)\,\mu\mathrm{m}$ to $(6.3 \pm 1.0)\,\mu\mathrm{m}$.

The range of values of the Young's modulus (figure 4.3.6) was wider for the rehydrated samples, and their maximum modulus was seven times higher, while the mean was three times larger than that of dry fibres. The difference in the mean Young's modulus was not statistically significant ($P = 0.3120$), but the properties of fibres appeared to be more varied, and their general stiffness was three times larger for the rehydrated samples, which was a reflection of their larger breaking strength and comparable breaking strain.

To summarise, the mechanical properties of fibres were compared after extended storage in a dry or rehydrated form. Two fibre groups were chosen with comparable average diameters of $(29.8 \pm 3.7)\,\mu\mathrm{m}$ and $(25.2 \pm 4.9)\,\mu\mathrm{m}$. The average breaking strain of rehydrated fibres was comparable to that of dry samples, while their mean breaking strength and Young's modulus were approximately three times larger, which could be an indication of an increase in the fibre stiffness and load-carrying ability with a higher water content. The differences in the mean breaking strength and Young's modulus were not statistically significant, which was caused by a large scatter in the measured properties between individual fibres.

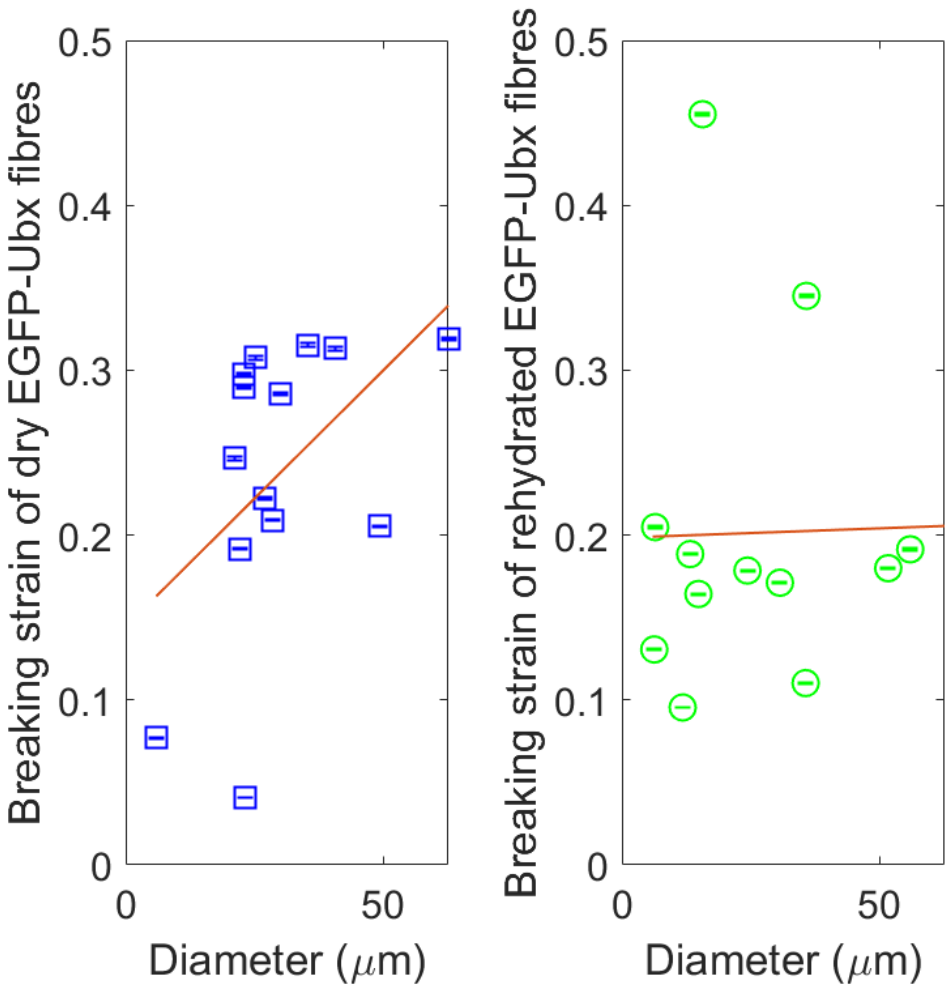

Figure 4.3.4: The comparison of the breaking strain of dry (left) and rehydrated (right) EGFP-Ubx fibres The breaking strain of dry fibres increases with their diameter ($intercept = 0.14 \pm 0.05$, $slope = 0.0031 \pm 0.0016$, $P = 0.0769$), whereas that of rehydrated fibres was nearly constant ($intercept = 0.20 \pm 0.06$, $slope = 0.0001 \pm 0.0019$, $P = 0.953$).

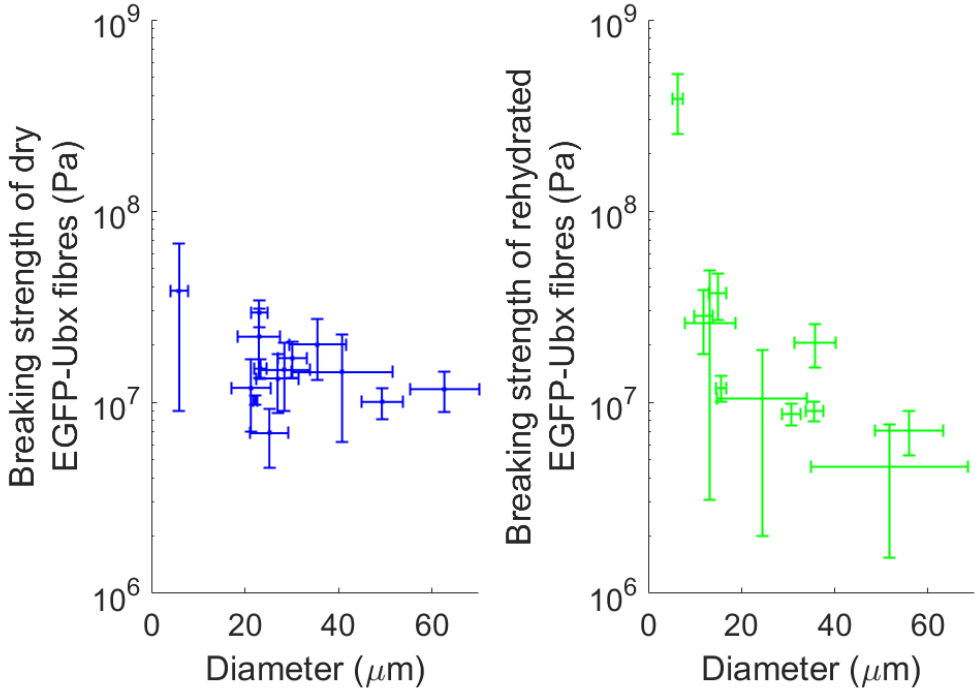

Figure 4.3.5: The comparison of the breaking strength of dry (left) and rehydrated (right) EGFP-Ubx fibres. The breaking strength of fibres decreased rapidly with their diameter. The range of breaking strengths was wider for rehydrated fibres.

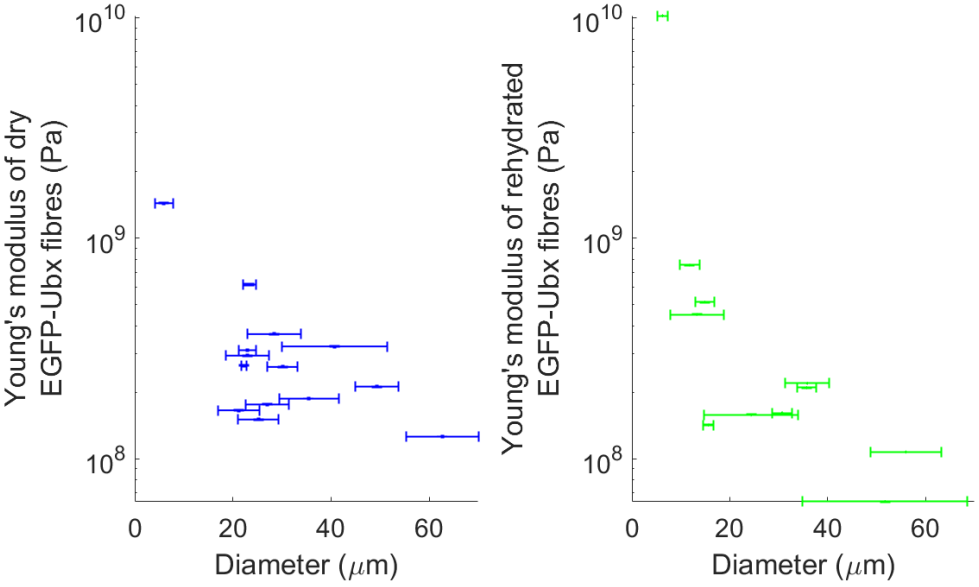

Figure 4.3.6: The comparison of the Young's modulus of dry (left) and rehydrated (right) EGFP-Ubx fibres. The Young's modulus of both dry and rehydrated fibres decreased with the fibre diameter.

However, the trends observed in this experiment indicated that rehydration of fibres could increase their breaking strength and stiffness, and moderately reduce their average extensibility.

4.3.3 The mechanical properties of Ubx and EGFP-Ubx fibres rehydrated after storage

The mechanical properties of Ubx and EGFP-Ubx fibres were measured for rehydrated fibres of different diameters and shown in table 4.3.2. In this section, the statistics of data sets for all fibres will be presented, regardless of their size. In section 4.3.4, a summary of mechanical properties of fibres with comparable size will be presented to offer a direct comparison between the mechanical properties of fibres made using pure Ubx and the protein fusion with EGFP. The EGFP-Ubx fibres had a 44% smaller diameter on average ($P = 0.0001$), and the fibre diameter was previously shown to have a significant effect on the mechanical properties of Ubx fusion fibres [99]. Specifically, the increase in diameter caused a rise in the breaking strength and a decrease in the breaking strain of fibres [17].

Table 4.3.2: The comparison of the mechanical properties of Ubx and EGFP-Ubx fibres rehydrated after prolonged storage.

Ubx fusion	**Ubx**	**EGFP-Ubx**
Diameter (µm)	14.4 ± 1.5	8.0 ± 0.6
Mean breaking strain (%)	21.3 ± 2.0	15.2 ± 1.8
Min breaking strain (%)	4.834 ± 0.009	2.813 ± 0.009
Max breaking strain (%)	54.77 ± 0.06	37.51 ± 0.07
Mean breaking strength (MPa)	90 ± 47	35 ± 5
Min breaking strength (MPa)	5.5 ± 1.7	4.3 ± 2.7
Max breaking strength (MPa)	1390 ± 40	122 ± 15
Mean Young's modulus (GPa)	3.1 ± 2.0	1.5 ± 0.4
Min Young's modulus (GPa)	$0.071\,13 \pm 0.000\,03$	0.1334 ± 0.0002
Max Young's modulus (GPa)	56.16 ± 0.26	10.07 ± 0.10

Breaking strain of rehydrated fibres

The comparison of the breaking strain of rehydrated Ubx and EGFP-Ubx fibres is shown in figure 4.3.7. The breaking strain of fibres did not have a strong dependence on their size. The behaviour of Ubx and EGFP-Ubx fibres after storage differed in this aspect from freshly pulled fibres. This difference could be due to the stiffening of fibres following their production, which was irreversible even after rehydration [38]. This trend needs to be taken into account when

designing Ubx-based materials because the storage time and conditions appeared to affect the extensibility and strength of fibres.

In the comparison between rehydrated Ubx and EGFP-Ubx fibres, Ubx exhibited a wider range of values, which reflected its larger mean breaking strain. However, the statistically significant difference could partially be explained by the larger average diameter, which was previously indicated as a factor causing an increase in the breaking strain and elasticity of fibres. The previous study reported a higher breaking strain for Ubx fibres compared to EGFP-Ubx, with values of breaking strain reaching 120% for Ubx fibres and 40% for EGFP-Ubx fibres with 20 µm diameter [17]. The measured values of breaking strain in that experiment were significantly higher than those reported in this thesis. The reason for this difference was the method of fibre preparation. Previously, Ubx and EGFP-Ubx fibres were tested directly after pulling, which allowed them to maintain the hydration caused by the buffer. In this work, the fibres were stored for several days before testing, which caused desiccation. Rehydration did not restore the larger values of breaking strain seen previously [17, 38]. However, as shown in section 4.3.2, hydration could increase the stiffness and the breaking strength by a factor of 3.

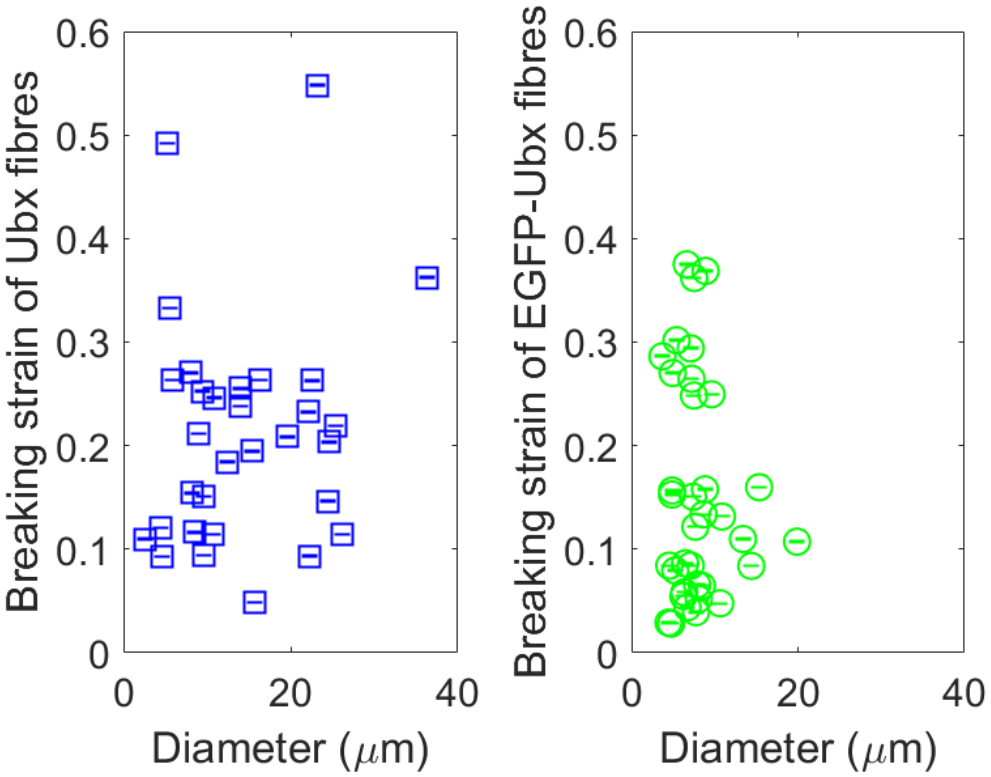

Figure 4.3.7: A comparison of the breaking strain of rehydrated Ubx (left) and EGFP-Ubx (right) fibres. There is no statistically significant trend in the breaking strain-diameter dependence for either Ubx or EGFP-Ubx fibres, although the general trend is increasing for Ubx, and decreasing for EGFP-Ubx fibres.

Breaking strength of rehydrated fibres

The breaking strengths of individual rehydrated Ubx and EGFP-Ubx fibres are presented in figure 4.3.8. The breaking strength of both Ubx and EGFP-Ubx fibres decreased rapidly with fibre diameter, which was consistent with the behaviour previously reported for Ubx and EGFP-Ubx fibres tested directly after pulling [17]. The rate of decrease of the breaking strength was more rapid at low diameters below 10 µm, which confirmed the previously seen trends [17].

The average breaking strength of Ubx fibres was 2.57 times higher than that of EGFP-Ubx but this difference was not statistically significant ($P = 0.27$). The maximum value for Ubx fibres was an order of magnitude higher but the general distribution of breaking strength was within the same order of magnitude for fibres made using pure Ubx and EGFP-Ubx. However, the trend presented in this work suggested that the breaking strength of Ubx fibres after rehydration was larger than that of EGFP-Ubx fibres, contrary to the previous report [17].

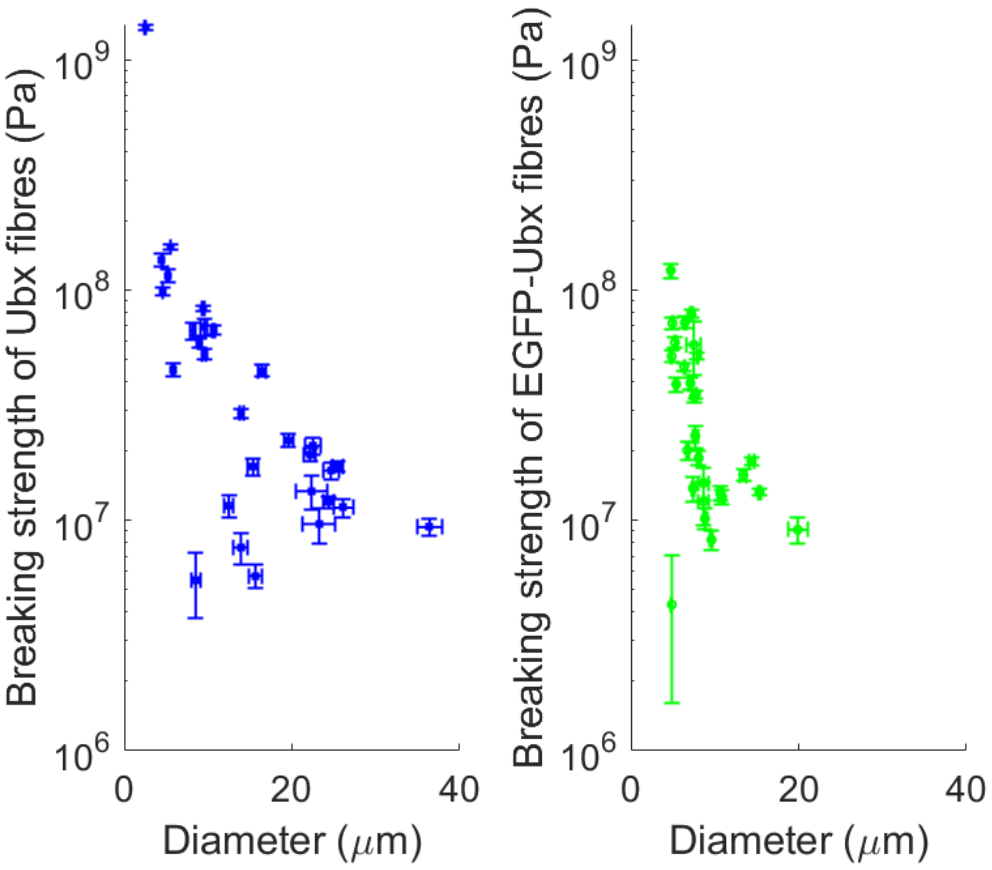

Figure 4.3.8: A comparison of the breaking strength of rehydrated Ubx (left) and EGFP-Ubx (right) fibres.

Young's modulus of rehydrated fibres

The Young's moduli of rehydrated Ubx and EGFP-Ubx fibres are shown in figure 4.3.9. The Young's modulus exhibited a strong decrease with a rise in fibre diameter, particularly at diameters lower than 10 µm. The stiffness (measured by the Young's modulus) of Ubx fibres was approximately twice as large as that of EGFP-Ubx, and the maximum value of their Young's modulus was over five times larger, which indicated that Ubx fibres could provide more strength and stiffness than EGFP-Ubx. Therefore, consideration for the mechanical properties should be taken when producing materials made of different protein fusions, particularly for applications where mechanical properties play a key role in maintaining structural stability or providing functionality of materials.

A comparison of the mechanical properties of Ubx and EGFP-Ubx fibres showed differences in their properties that were not statistically significant. However, taking into account the decreasing trends in the breaking strength and Young's modulus with rising diameter and the larger average diameter of Ubx fibres, the higher strength (ratio of 2.57, $P = 0.27$) and stiffness (ratio of 2.07, $P = 0.44$) of Ubx materials indicated that they were stronger and stiffer than EGFP-Ubx fibres. Ubx fibres were also 32% more extensible than EGFP-Ubx fibres. These observations indicated that storage could affect the mechanical properties of Ubx and EGFP-Ubx fibres differently, because freshly pulled EGFP-Ubx fibres had higher breaking strength [17]. The larger extensibility of Ubx fibres was confirmed in this work, even though the difference in the mean breaking strain could be partly due to their larger average diameter.

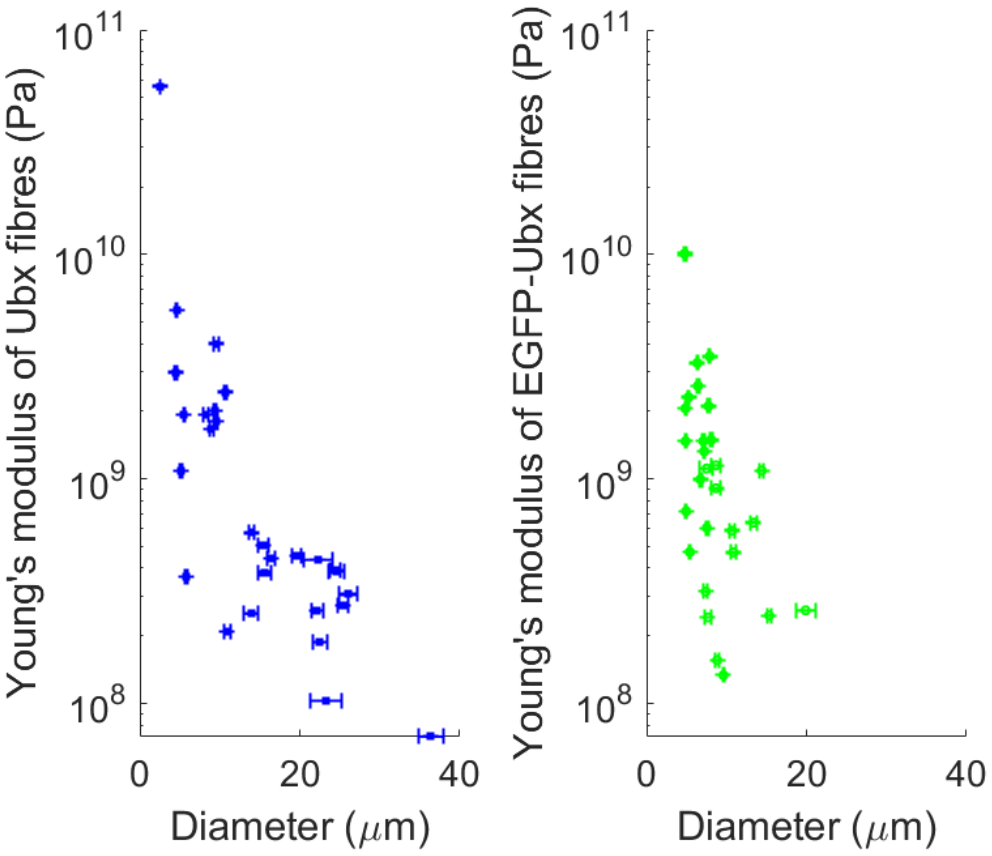

Figure 4.3.9: A comparison of the Young's modulus of rehydrated Ubx (left) and EGFP-Ubx (right) fibres.

4.3.4 Comparison of mechanical properties of Ubx and EGFP-Ubx fibres of similar sizes

Table 4.3.3: The comparison of the mechanical properties of subgroups of Ubx and EGFP-Ubx fibres with similar average diameters. The fibres were rehydrated after prolonged storage.

Ubx fusion	Ubx	EGFP-Ubx	P-value
Diameter (µm)	9.97 ± 0.95	8.0 ± 0.6	0.0701
Mean breaking strain (%)	20.1 ± 2.1	15.2 ± 1.8	0.0843
Mean breaking strength (MPa)	120 ± 60	35 ± 5	0.0747
Mean Young's modulus (GPa)	4.5 ± 2.5	1.5 ± 0.4	0.1511

To provide a direct comparison of the mechanical properties of Ubx and EGFP-Ubx fibres, a subgroup of Ubx fibres with diameters less than 20 µm was selected. 22 Ubx fibres were chosen with an average diameter of (9.97 ± 0.95) µm. Their mechanical properties were compared to 35 EGFP-Ubx fibres with a mean diameter of (8.0 ± 0.6) µm. The average size of Ubx fibres was 25% larger than that of EGFP-Ubx fibres ($P = 0.0701$). The properties of these two groups are shown in table 4.3.3.

The average breaking strain of Ubx fibres within this group was $(20.1 \pm 2.1)\%$ compared to $(15.2 \pm 1.8)\%$ for EGFP-Ubx fibres. The breaking strain of Ubx fibres was 32% larger than that of EGFP-Ubx fibres (P=0.0843), which could be caused by the larger average size of Ubx fibres. More Ubx (9) than EGFP-Ubx fibres (6) were in the diameter range between 10 µm and 20 µm, but interestingly, for both protein types, the breaking strain of larger fibres exhibited a smaller variation than for fibres with diameters smaller than 10 µm.

The mean breaking strength for rehydrated fibres with diameters smaller than 20 µm was compared. The average for Ubx was (120 ± 60) MPa, compared to (35 ± 5) MPa for EGFP-Ubx (P=0.0747). This difference was not statistically significant. However, the trend in breaking strength was decreasing with diameter. Despite the average diameter being 25% larger compared to EGFP-Ubx, the 3.4-fold increase in the mean breaking strength for Ubx fibres suggested that they could withstand significantly more load before fracture. Therefore, Ubx fibres appeared to provide more structural strength in the tensile tests.

The average value of Young's modulus for the subgroup of Ubx fibres was (4.5 ± 2.5) GPa, and that for EGFP-Ubx was (1.5 ± 0.4) GPa (P=0.1511). The trend in the Young's modulus was also decreasing with diameter, similarly to that in the

breaking strength. The Young's modulus was 3 times higher for Ubx fibres compared to EGFP-Ubx despite their larger average diameter. Therefore, Ubx fibres had more stiffness than EGFP-Ubx fibres, which could be an important consideration when choosing the optimal protein fusion for device design.

The transition between the regions of elastic and plastic deformation was monitored for the fibres. The yield point indicates the value of strain when the sample no longer exhibits elastic deformation. This quantity was measured for both Ubx and EGFP-Ubx fibres in the subgroup of fibres. The average yield strain was $(3.3 \pm 0.4)\%$ for Ubx fibres and $(3.1 \pm 0.7)\%$ for EGFP-Ubx fibres ($P = 0.9085$). All fibres exhibited a short elastic deformation region followed by long irreversible deformation. The protein fusion with EGFP did not alter the reversibility of fibre deformation during tensile testing compared to Ubx fibres.

To summarise, the mechanical properties of subgroups of Ubx and EGFP-Ubx fibres with sizes smaller than 20 µm were compared. The average diameter was 25% larger for Ubx fibres, which could have caused an increase their breaking strain by 32% compared to EGFP-Ubx fibres. However, both the breaking strength and Young's modulus of Ubx fibres were larger by factors of 3.4 and 3, respectively. These increases indicated that Ubx fibres provided more strength and were stiffer in tensile tests despite the overall decreasing trend in these properties with diameter. Both the size and protein fusion type need to be considered when choosing the optimal material to produce protein-based devices.

4.4 Summary

Proteins constitute some of the most impressive materials obtained in nature, such as spider webs or organs like heart and skin. Some proteins, e.g. spider silk and collagen, are capable of forming extraordinarily strong materials, while others, like elastin, make extensible but less strong and stiff structures. In nature, composite materials are ubiquitous. Animal tissues such as skin, ligaments or tendons are composed of multiple proteins including collagen and elastin. These composites perform specific functions within organisms, and individual proteins contribute towards achieving required mechanical properties by providing structural stability and strength (collagen) or ready elastic deformation (elastin). The requirements of modern medicine call for the development of biocompatible and biodegradable materials with suitable mechanical properties to act as tissue scaf-

folds or biosensors. The knowledge of mechanical properties of protein materials, and the ability to tune these properties by functionalisation and changing material composition, are crucial to form tissue scaffolds that match the properties and mimic functions of native tissue.

Proteins such as collagen, elastin and silk were previously characterised and their properties thoroughly tested (table 4.1.1). Ubx fibres had been mechanically tested in one study and only shortly after fibre pulling [17, 38]. Current work investigated the mechanical properties of Ubx and EGFP-Ubx fibres, and the effect of storage and subsequent hydration on their properties. During tensile testing, the visible changes in the fibres were extension and then straightening of protrusions resulting either from the fibre pulling process or rehydration (figures 4.3.1a and 4.3.1b). Then, elongation would occur with no superficial changes in the fibre until fracture. The shape of the stress-strain curve indicated that the fibres initially extended elastically, which was followed by plastic, irreversible deformation (figures 4.3.2 and 4.3.3).

Both Ubx and EGFP-Ubx had different mechanical behaviour after storage compared to the freshly pulled fibres. The freshly pulled fibres tested in previous studies were significantly more extensible with the reported maximum breaking strain of fibres with a 20 µm diameter of 120% for Ubx and 40% for EGFP-Ubx. The breaking strain for fibres with a 10 µm diameter was approximately 50% for Ubx and 25% for EGFP-Ubx fibres [17]. The breaking strains of fibres reported in this work were much smaller with the averages of $(20.1 \pm 2.1)\%$ and $(15.2 \pm 1.8)\%$ for Ubx and EGFP-Ubx fibres, respectively. Therefore, the fibres became less extensible after prolonged storage. However, the breaking strength of fibres increased after storage from approximately 10 MPa and 30 MPa to (120 ± 60) MPa and (35 ± 5) MPa for a 10 µm Ubx or EGFP-Ubx fibre, respectively. These differences indicate that prolonged storage and subsequent rehydration of fibres made them less elastic but stronger, particularly for Ubx. This finding supports the hypothesis that Ubx oxidation leads to intermolecular dityrosine bonding, which increases the strength of Ubx fibres after storage.

This work provided a contrast to the previous work on the mechanical properties of Ubx and EGFP-Ubx fibres [17]. The previous report indicated that freshly prepared Ubx fibres were more extensible and had a lower breaking strength than EGFP-Ubx samples. This trend changed after a period of storage and oxidation. In this work, Ubx fibres were confirmed to be more extensible but also

stronger than EGFP-Ubx fibres. This could be due to the lack of the appended fluorescent protein, which might affect the availability of the tyrosine residues for intermolecular dityrosine bonding during oxidation.

The mechanical properties could also change with fibre hydration. The mean breaking strain of fibres was comparable before and after rehydration. However, the rehydrated fibres had approximately three times larger breaking strength and Young's modulus, which suggested that rehydration contributed to the strength and stiffness of the fibres. However, these differences were not statistically significant.

The mechanical properties of Ubx fusion fibres after a prolonged storage, presented in this work, placed them in the biologically relevant region with their breaking strain, breaking strength, and Young's modulus between those of elastin and collagen. Ubx and EGFP-Ubx fibres were shown to be similarly strong and extensible as human tendons and exceed the properties of some veins, which suggests that their mechanical properties should be sufficient for tissue engineering. Ubx fibres were stronger and more extensible than collagen fibrils with similar diameters [13] and had a comparable strength to collagen in mammalian tissues (see table 4.1.1), while being two times weaker than the silk genetically modified for biomedical applications [15]. This indicated that, if scaled up, the Ubx materials could have the mechanical strength and elasticity precisely matching that of tissue, which could lead to exciting applications in tissue engineering. The average extensiblity of Ubx fusion fibres exceeds that of both collagen and *Bombyx mori* silk [22, 93], while their breaking strength was comparable to that of structures such as mussel byssal fibres and turkey tendons [13, 93]. Mammal tissues and tissue scaffolds mimicking them are often made using composite materials [3,9,10,13,88,93,94,97,98]. The mechanical properties of Ubx fibres, including their strength and considerable Young's modulus, could contribute to the design of moderately strong and extensible materials made of Ubx or Ubx composites with other biomaterials. Scaling up the production of both Ubx protein and Ubx materials could lead to the enhancement of the extensibility or mechanical strength of these materials, depending on their size and three-dimensional structure. It could be hypothesised that creating scaffolds made of interwoven or cross-linked Ubx fibres would increase the breaking strength or extensibility of resulting materials, in a similar way to collagen-based tendons, which were constituted of collagen fibrils of similar size to Ubx fusion fibres [13]. Moreover, Ubx exhibits bio- and cytocompatibility [2, 40], and Ubx gene fusions with a range of

functional molecules such as fluorescent proteins or growth factors could be used in biosensing, wound healing or tissue regeneration [16, 17, 26, 100]. Therefore, Ubx materials have functional and mechanical properties that can be used to create standalone platform materials or composite materials for applications in tissue engineering, biosensing, and biotechnology.

Chapter 5

Binding DNA to Ultrabithorax fibres and analyte binding using DNA-based aptamers

5.1 Introduction

The mechanical, electrical and optical properties of Ubx fusions were characterised and shown to be suitable for biomedical applications because of the intrinsic physical properties and the protection that the Ubx structure gives to the appended fluorescent proteins. This chapter investigates the feasibility of binding DNA aptamers to Ubx fusion monomers and fibres using long oligonucleotide sequences designed within the research group. Moreover, the long oligonucleotides contained analyte aptamers specific to *E. coli* or the SARS-CoV-2 spike RBD protein, which could enable capturing the pathogens in solution. The binding efficiency of the Ubx protein-oligonucleotide systems is investigated in fluorescence studies to determine whether these conjugates could be used for biosensing to detect pathogens of interest.

5.1.1 Design and applications of aptamers

Aptamers are short oligonucleotides composed of DNA or RNA, whose function is to bind specifically to selected molecules. Aptamers bind to targets by folding into various secondary and tertiary structures that are capable of binding the target specifically and with high affinity [18, 101]. These three-dimensional structures

can include loops, bulges, and hairpins [102]. The binding can occur through different mechanisms including the recognition of a complementary shape, hydrophobic and electrostatic interactions, base stacking, hydrogen bonding or van der Waals forces [18, 102]. The three-dimensional structure of aptamers can be altered by target binding, which is a feature used in the design of therapeutics and diagnostic devices, such as those based on the signal-on or signal-off fluorescence detectors [18]. Aptamer applications have been developed in medicine to combat neurodegenerative disease, viral infections, macular degeneration, and cancer [101]. Aptamers are usually derived in an iterative selection process called systematic evolution of ligands by exponential enrichment (SELEX), which allows a rapid selection of structures that bind chosen targets with high affinity at concentrations as low as nano- or micromolar [19]. A measure of aptamer affinity to their target is the dissociation constant K_d. Currently, aptamer selection using SELEX is preceded by computational predictions of their structure and binding affinity, which decreases the production cost. Post-production chemical modifications further increase aptamer stability [19]. Another strategy for aptamer selection is cell-SELEX, which selects those aptamers with high affinity to whole cells instead of specific targets like proteins [18, 20]. This method is useful for recognition of cancerous or virus-infected cells. It can also be used to discover new biomarkers of disease without prior knowledge of the cell membrane-bound proteins [18]. Cell-SELEX identifies aptamers against targets that are more complex than purified proteins. Some examples of possible targets are fragments of cells and dead cells, parasites and bacteria, viruses, and animal or human cells [20]. Fluorescent biosensors based on cell-specific aptamers show promise in diagnostics [21]. They feature a signal-on or signal-off function upon binding with the target, which allows the detection of specific cells along with targeted drug delivery. The aptamer-based fluorescent probes were successfully used to detect blood clot marker thrombin, adenosine and adenosine triphosphate, and toxins in blood, serum, plasma and food samples [18, 21]. The promising applications of cell-specific aptamers led to the design of the Ubx and *E. coli* binding aptamers tested in this work, which could be used to immobilise the bacteria on the fibre surface. This system could be designed as a diagnostic tool to detect the presence of bacteria in solution, or as a targeted therapeutic device against the bound *E. coli*.

Another class of targets available for aptamers are proteins and their conjugates with disease-specific molecules. Challenges in the diagnostics of infectious diseases

can be addressed by using aptamers with high specificity and binding affinity. The feasibility of tuberculosis diagnostics was implied in a study, in which a selection of single-stranded DNA oligonucleotides were shown to bind with relatively high sensitivity and specificity to a protein-antigen dimer present in patients with tuberculosis [103]. The capability of aptamers to bind to proteins inspired the design of single- and double-stranded long oligonucleotide sequences binding Ubx, which can also bind other proteins or cells of interest. This was proposed as the first step towards the production of biosensors based on the Ubx-aptamer conjugates.

An aptamer-based bioelectronic sensor was shown as a viable method for the detection of viruses in point-of-care applications [104]. A single-stranded DNA (ssDNA) aptamer probe immobilised on a conductive polymer microelectrode formed an impedimetric sensor, which detected the intact influenza A virus in phosphate buffered saline (PBS) and saliva samples [104]. The detected concentration range was in the clinically relevant region and had high specificity and sensitivity to the virus [104]. This result showed that aptamers could be used as a viable diagnostic tool for inexpensive and rapid detection of intact viruses without using laboratory-intensive methods.

In addition to impedimetric and fluorescent sensors, several other types of aptamer-based sensors have been created [21]. An electrochemiluminescence sandwich biosensor detected cocaine with the detection range in the picomolar [105]. The field-effect transistor effect between aptamers and carbon nanotubes was used to achieve high detection sensitivity in the femtomolar [21]. Other sensor designs monitored the surface plasmon resonance (SPR) on a thin gold layer. In this device, target binding induced a change in the refractive index of the thin layer and the change in the SPR angle, resulting in a change in the recorded signal. This method allowed the detection of molecules with concentrations as low as nanomolar [21].

Aptamers have also been used in cancer diagnostics. Various aptamers were produced using cell-SELEX that bind specifically to cell lines derived from cancers such as hepatocarcinoma, small cell lung cancer, or colorectal cancer [19]. A ssDNA aptamer Wy-5a was developed to specifically detect the presence of a prostate cancer cell line PC-3 with a nanomolar detection limit. This detection occurred through the measurement of fluorescence intensity of fluorescently labelled Wy-5a [106]. In addition to detecting certain cancer cells, aptamers

were proposed as a tool for cancer biomarker discovery with a particular utility in detecting cancer-specific proteins. They were suggested as a highly specific diagnostic system because of their high specificity, ability to penetrate cell membranes, and the comparatively low development cost. Strategies for detection of cancer development stage using aptamers were reviewed with a focus on protein biomarkers [107]. Specifying the stage of cancer development is important for treatment planning.

Cell-SELEX allows the development of aptamers that exhibit high specificity binding to bacteria strains [19]. This process is possible by binding to specific proteins present in the bacteria [19, 108], which allows the diagnostics of specific strains of bacteria in biological samples. Development of bacteria-specific aptamers with nanomolar dissociation constants was demonstrated for strains such as *Vibrio parahemolyticus*, *Salmonella enterica* or *Escherichia coli*, where the binding was observed by quantitative polymerase chain reaction (qPCR) or fluorescent labelling of oligonucleotides [109–111].

In this work, we used several *E. coli* aptamers to test the possibility of immobilising them at the surface of Ubx protein fibres to investigate the effect the presence of aptamers has on the quantity of bacteria bound to fibres. The first aptamer was developed using sequential toggle cell-SELEX, and was termed STC-12 [112]. This selection method allowed the choice of single stranded DNA structures targeting six bacteria from different genera by sequentially choosing aptamers that bound to each individual strain, which ensured affinity to only selected bacterial strains. STC-12 had a dissociation constant of 38.5 nM for *E. coli* [112]. The second construct used in this work was a ssDNA aptamer called P12-31, which had a high specificity for *E. coli* and was the first aptamer that showed binding to meningitis or sepsis associated *E.coli* (MNEC) [113]. Out of its SELEX pool, this aptamer showed the lowest affinity to other bacterial strains, while also showing binding to different types of *E. coli*. The dissociation constant of P12-31 to *E. coli* ATCC 25922 was (87.03 ± 17.32) nM [113]. Finally, the last aptamer tested in this project was Antibac2, which targets the bacterial peptidoglycan [114]. This aptamer had a dissociation constant to *E. coli* of (31.82 ± 4.38) nM. Moreover, it showed a high affinity to other bacterial strains that act as sepsis agents, which addressed the need to find an aptamer that can target several bacteria strains in clinical diagnostics [114].

The applications of cell-SELEX have been extended to aptamers binding to

viruses. Aptamer generation against the rabies virus (RABV) showed that aptamers were an effective tool to both bind to the virus in baby hamster kidney BHK-21 cells and inhibit replication of RABV in these cells [115]. The blocking of RABV infection in cells was possible in the early stages of infection, while it did not have a similar effect in an established infection (24 hours after introduction of the virus) [115]. The blocking of RABV spread in the early stages of the infection is particularly important because rabies has a high mortality rate once it spreads to the central nervous system [115]. The ssDNA probes had dissociation constants as low as $(28.0 \pm 1.9)\,\text{nM}$ [115]. This result indicated that aptamers can be used as therapeutic agents to slow down the replication of viruses and aid the immune response by slowing down the infection and allowing the immune system to produce an adequate response [115].

The COVID-19 pandemic announced by the WHO in 2020 was caused by the SARS-CoV-2 virus, which causes a severe acute respiratory syndrome [116]. The severity of the disease and its ease of transmission in humans prompted research into the development of diagnostic and therapeutic agents that could address this global health threat [116, 117]. The infection is facilitated by the interaction of the receptor binding domain (RBD) of the SARS-CoV-2 spike glycoprotein (S protein) with membrane-bound angiotensin-converting enzyme 2 (mACE2) expressed by host cells [117]. Aptamers CoV2-RBD-1C and CoV2-RBD-4C were selected as high-affinity binding agents targeting the SARS-CoV-2 RBD protein with affinities of 5.8 nM and 19.9 nM [117]. In addition to the high affinity, these aptamers were shown to compete with ACE2 for SARS-CoV-2 RBD binding, which suggested that they could be used as an anti-viral agent because of their potential to prevent virus-ACE2 interactions [117]. To address the need for development of diagnostic and therapeutic devices against SARS-CoV-2, the CoV2-RBD-4C aptamer was incorporated in a longer protein binding oligonucleotide sequence, which was subsequently immobilised at the surface of Ubx materials and tested for SARS-CoV-2 S protein RBD binding.

The development of aptamers and their modifications for enhanced stability resulted in clinical trials of therapeutics such as pegaptanib, an anti-vascular endothelial growth factor (VEGF) aptamer in treatment of pathological angiogenesis [118]. Pegaptanib was the first FDA-approved aptamer therapeutic. Since its approval, several other aptamers entered clinical trials, all of which are antagonists, i.e. they prevent the interactions associated with the disease such as those between proteins or receptors and ligands [18].

The use of aptamers as targeted therapeutics was proposed by means of specific target-binding and subsequent drug release [19]. The limitations of this approach include aptamer degradation in blood by nucleases and their renal clearance [19]. These issues can be resolved by further functionalisation using a polyethylene glycol molecule or modifications in the oligonucleotide structure following the SELEX process [19,119]. However, the effect of any modifications on the binding affinity needs to be monitored for successful application.

5.1.2 Binding aptamers to proteins

Nanofunctionalisation of protein materials using DNA-based aptamers is possible due to the presence of DNA-binding domains in the protein structure. Single or double stranded oligonucleotides can be attached to the DNA-binding domain of a protein in its monomeric state or after material formation. DNA-based aptamers can immobilise molecules of interest, such as ions, proteins or cells. The immobilisation of analytes of interest was used both in biosensing of cells and proteins of interest, and in therapeutics to inhibit protein-protein interactions or viral infection in host cells [18,115,117].

Nucleic acid aptamers are capable of binding and detecting proteins and often inhibit protein-protein interactions upon binding [18]. Biopolymer based drug delivery vehicles containing aptamers were made to address the degradation and renal clearance issues related with the use of unprocessed aptamers [120]. Moreover, more complex oligonucleotides incorporating several aptamers were created to detect their targets with higher sensitivity [102]. The ability of aptamers to bind to proteins can be used to create more robust sensors or therapeutics platforms by designing longer oligonucleotides containing two aptamers, one for the structural protein or biopolymer, and another used to bind the target analyte. To create composite aptamers, both flexible linkers such as polyethylene glycol, and rigid ones such as double-stranded DNA or RNA were used [102]. The use of appropriate linkers and monitoring of the aptamer structure are crucial to ensure that the high binding affinity of individual aptamers is maintained after the modifications [102]. Ubx materials can be used as a platform for robust protein-aptamer composite sensors. Such biosensors could exploit the changes in fluorescence of the fluorescently labelled aptamers [18,21,102]. Alternatively, changes in the physical properties of Ubx materials could be used to detect target binding and provide additional sensing capabilities using electrical impedance

measurements or changes in their fluorescence characteristics due to light absorption or Förster resonance energy transfer (FRET). Oligonucleotides incorporating Ubx homeodomain binding sequence and *E. coli* or SARS-CoV-2 RBD aptamers were tested in this project.

5.1.3 Current investigations

This project aimed to investigate the possibility of functionalisation of Ubx with aptamers to bind analytes. A protein fusion designed to include a pRep domain (pRep-Ubx) can covalently bind single stranded DNA (ssDNA) at a specific motif. In addition, the Ubx homeodomain can reversibly bind double stranded DNA (ds-DNA) containing a longer motif. In this series of experiments, we investigated the oligonucleotide binding to Ubx and pRep-Ubx protein fusions in solution and in fibres, and the ability of the protein-aptamer complex to capture analytes. *E.coli* and the SARS-CoV-2 spike protein were used as targets. The *E.coli* aptamers STC-12 [112], P12-31 [113], and Antibac2 [114], and the SARS-CoV-2 spike RBD protein aptamer CoV2-RBD-4C [117] were tested. These experiments used a series of oligonucleotides designed to incorporate these aptamers together with a binding domain – either the single stranded motif bound by pRep or the double stranded domain bound by the Ubx homeodomain. Binding pathogens enables biosensing using fluorescence or impedimetric measurements. Moreover, targeted therapeutics using drug delivery systems, antimicrobial agents, or inhibition of protein-protein interactions could be achieved using these systems. Therefore, this work examines the feasibility of binding both structural protein (Ubx) and pathogens (*E. coli* or SARS-CoV-2 spike RBD protein) using aptamers to create platforms that could have applications in biosensing and therapeutics.

Successful capture of analytes using the Ubx fibre-aptamer construct could allow the creation of a multi-use platform that could be functionalised after production of Ubx materials of different morphologies (fibres, fibre meshes, coatings, electrospun mats, and composites). Relevant aptamers could be applied to these materials and bound using procedures described in this report, and the materials could be used for biosensing, therapeutics or filtering purposes.

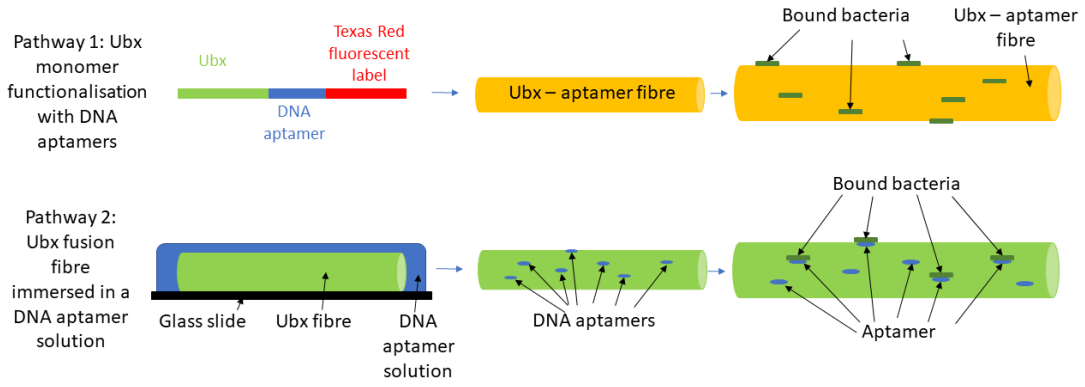

Figure 5.2.1: The two pathways for functionalisation of Ubx fusions with DNA aptamers, and the subsequent analyte capture using aptamers bound to Ubx. The first method (top panel) involves binding oligonucleotides to Ubx monomers in solution followed by fibre formation. The second method (bottom panel) includes oligonucleotide binding to Ubx fibres.

5.2 Experimental section

5.2.1 Experimental aims

The biomedical applications of DNA aptamers benefit from their capability for specific high affinity target binding. DNA aptamers have been used for biosensing of cells and proteins, targeted drug delivery, and therapeutics [18, 19]. Aptamers are capable of binding small molecules, such as proteins, and whole cells [18]. This thesis describes the first ever experiments aiming to use longer DNA oligonucleotide sequences to bind both a structural Ubx protein and analytes of interest, which in this case are *E. coli* and the SARS-CoV-2 spike RBD protein. The designed oligonucleotide sequences contained both Ubx and analyte aptamers (oligonucleotide sequences were designed by Carolyn Greig). Both single stranded DNA (ssDNA) and double stranded DNA (dsDNA) aptamers were used in these experiments to evaluate how these two types of structures affect the binding efficiency.

Binding DNA aptamers to monomeric Ubx fusions and to fibres

The first aim of these experiments was to investigate the possibility of binding DNA aptamers to Ubx. The two ways to bind DNA aptamers to Ubx fusions are direct binding of oligonucleotides to Ubx monomers before fibre formation and oligonucleotide binding to pre-made Ubx fusion fibres (figure 5.2.1).

To attempt aptamer binding to monomeric pRep-Ubx, ssDNA aptamers were

used with a pRep binding sequence. The aptamer solution was mixed with a pRep-Ubx solution, and an electrophoretic gel assessment of the molecular weight of the protein with and without the aptamer was conducted to examine binding. The second way to functionalise Ubx with aptamers in solution involved binding a dsDNA oligonucleotide containing a Ubx aptamer and a Texas Red fluorescent label, which had a fluorescence emission maximum at 612 nm. The Texas Red label enabled the quantitative analysis of aptamer binding efficiency using fluorescence microscopy images. The procedures are described in section 5.2.7.

The binding of designed Ubx aptamers to Ubx fusion fibres was achieved by incubation of a fibre in an aptamer solution. The dsDNA aptamers used for this purpose were labelled with the Texas Red fluorescent label to enable the detection of binding by a quantitative comparison of the mean fluorescence intensity of the whole fibres and the area of bright red fluorescence within the fibres. The protocol for these experiments is outlined in section 5.2.7.

The effect of the DNA concentration in solution on the fluorescence intensity was measured to choose the optimal DNA concentration for binding to Ubx fusions. The mean fluorescence intensity in both the blue channel (due to dityrosine) and the red channel (due to the Texas Red label present in the DNA) were compared to inform this choice. The methods were described in section 5.2.8.

The non-specific binding of oligonucleotides and analytes to Ubx fusion fibres was considered as a factor affecting the measurements of the binding efficiency. To examine the extent of non-specific binding of oligonucleotides to Ubx, the protein was treated with either oligonucleotides that contained a Texas Red label without a Ubx aptamer (control group), or oligonucleotides containing both the Ubx aptamer and the Texas Red label (experimental group). The fluorescence intensity of both control and experimental fibres was measured in the red channel, which would correspond to the Texas Red presence in the sample. A similar method was used in the design of experiments involving analyte binding. The control group was a group of samples that did not contain aptamers, which were treated with a solution of fluorescently-labelled analytes. The samples in the experimental group contained either *E. coli* or SARS-CoV-2 spike RBD protein aptamers, which also were treated with the fluorescently-labelled analytes. The blocking of non-specific binding of analytes was attempted using a blocking buffer containing bovine serum albumin and a TWEEN 20 surfactant, both of which were identified as suitable agents blocking non-specific binding of cells [121]. The

method for the optimisation of the blocking buffer is described in section 5.2.8.

Capturing analytes using Ubx functionalised with DNA aptamers

The second aim of the experiments was to test whether analyte capture using the long oligonucleotide structures was possible once they were bound to Ubx fibres. This would enable the production of Ubx-aptamer platform materials that could be used for biosensing or therapeutics production, in which targeted treatment of bound analytes could be applied.

In these experiments, a few combinations of Ubx fusions and oligonucleotides were used. The oligonucleotides included ssDNA and dsDNA constructs with both Ubx or pRep aptamers that bound to Ubx fusions, and *E. coli* or SARS-CoV-2 spike RBD protein aptamers that bound to the analytes. In the initial experiments, dsDNA constructs including the Texas Red fluorescent label were tested. In addition, the Ubx fusions used initially were EGFP-Ubx and pRep-phiLOV-Ubx, both of which contained green fluorescent proteins (EGFP and phiLOV2.1 [122]). The methods used to conduct these experiments were described in sections 5.2.9 and 5.2.10, respectively for GFP-labelled *E. coli* binding and Texas Red-labelled SARS-CoV-2 spike RBD protein binding. This protocol was later changed to avoid the fluorescence emission overlap between the green fluorescent proteins EGFP and phiLOV present in the fibres, and the GFP and Texas Red fluorescent labels attached to both the oligonucleotides and the analytes of choice.

In the later experiments, Ubx and the pRep-Ubx protein fusion were chosen for fibre production, and the resulting fibres exhibited autofluorescence with the emission peak at approximately 440 nm due to the dityrosine presence. The aptamers without the Texas Red label were used. The choice of analyte was changed to mCherry-labelled *E. coli*. These choices were made to enable the qualitative detection and quantitative analysis of bacteria binding by measuring the fluorescence intensity in the red channel, which would correspond to the mCherry fluorescence emission with a maximum at 610 nm. The corresponding experimental methods are detailed in section 5.2.9.

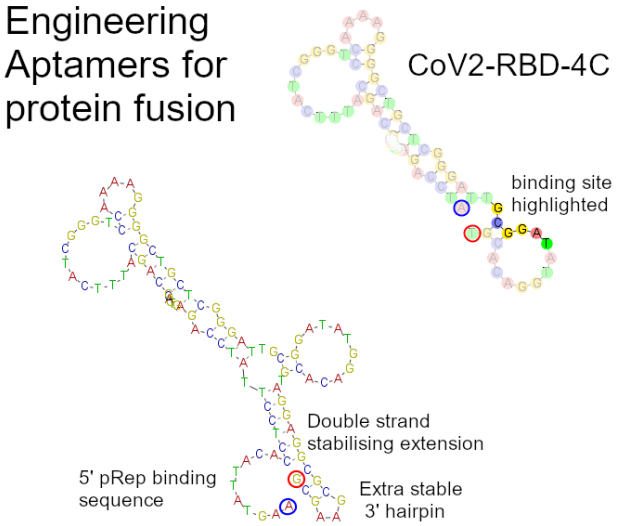

Figure 5.2.2: A visualisation of the engineered oligonucleotide sequence containing a pRep aptamer and a SARS-CoV-2 spike RBD protein aptamer. The visualisation was produced by Carolyn Greig of Swansea University and used with permission.

5.2.2 Aptamer design and preparation

Oligonucleotides structure containing aptamers

Long oligonucleotide sequences were designed that contained a protein aptamer for binding Ubx protein fusions (Ubx or pRep-Ubx), and an analyte aptamer for binding either *E. coli* or the SARS-CoV-2 spike RBD protein. The oligonucleotides were designed by Carolyn Greig. A visualisation of a sample single stranded DNA sequence with a pRep binding sequence and a SARS-CoV-2 spike RBD protein aptamer is shown in figure 5.2.2.

Three aptamers for *E. coli* were used, which were the STC-12 [112], the Antibac2 [114], and the P12-31 [113] constructs. An aptamer called CoV2-RBD-4C was chosen to test binding of the SARS-CoV-2 RBD protein [117].

Single stranded DNA (ssDNA) and double stranded DNA (dsDNA) sequences containing the aptamers were used. The single stranded sequences could contain both the protein and analyte aptamers. The dsDNA sequences were formed by annealing the ssDNA constructs with a complementary sequence that was label-free (termed B4) or contained the Texas Red fluorescent label (termed B5). Table 5.2.1 details oligonucleotide type, the aptamers contained by the specified sequences and whether a fluorescent label was present in the construct. The DNA

sequences encoding the oligonucleotides used in these experiments are shown in appendix A.

Table 5.2.1: The summary of the aptamers and fluorescent labels included in the long oligonucleotides constructs used for the aptamer binding experiments. ssDNA constructs could be made of either of the B1, B3, B10 and B11 oligonucleotides when they were used without the complementary sequence B4 or B5.

Name	**Type**	**Ubx fusion aptamer**	**Analyte aptamer**	**Fluorescent label**
RS1	ssDNA	pRep-Ubx	N.A.	No
RS2	ssDNA	pRep-Ubx	*E. coli* P12	No
RS3	ssDNA	pRep-Ubx	CoV2-RBD-4C	No
B0+B4	dsDNA	Ubx homeodomain	N.A.	No
B0+B5	dsDNA	Ubx homeodomain	N.A.	Texas Red
B1+B4	dsDNA	Ubx homeodomain	*E. coli* P12	No
B1+B5	dsDNA	Ubx homeodomain	*E. coli* P12	Texas Red
B10+B4	dsDNA	Ubx homeodomain	*E. coli* STC-12	No
B10+B5	dsDNA	Ubx homeodomain	*E. coli* STC-12	Texas Red
B11+B4	dsDNA	Ubx homeodomain	*E. coli* Antibac2	No
B11+B5	dsDNA	Ubx homeodomain	*E. coli* Antibac2	Texas Red
B3+B4	dsDNA	Ubx homeodomain	CoV2-RBD-4C	No
B3+B5	dsDNA	Ubx homeodomain	CoV2-RBD-4C	Texas Red

Preparation of oligonucleotide solutions

The oligonucleotides were purchased from Eurofins Scientific. The dried oligonucleotide was centrifuged for 1 min at 8000 rpm. A sterile solution of 10 mM Tris in ultrapure water at pH 8.0 was prepared. The oligonucleotide was dissolved by vortexing in the Tris solution to a final concentration of 100 µM. This concentrated solution was stored at −20 °C.

Preparation of ssDNA working solutions

The ssDNA oligonucleotides were prepared for binding to the pRep sequence of pRep-Ubx protein fusion. A 2.4 µM solution of the ssDNA oligonucleotide was made in pRep binding buffer, which contained 2.5 mM sterile $MgCl_2$ dissolved in sterile PBS. Alternatively, ssDNA oligonucleotides containing the Ubx homeodomain binding sequence could be used for non-covalent binding to Ubx. They were prepared as a 2.4 µM solution in PBS.

Preparing and annealing dsDNA oligonucleotides

To create dsDNA aptamers, the ssDNA structure containing the Ubx homeodomain binding sequence (B0, B1, B3, B10 or B11) was annealed with a short complementary oligonucleotide (B4 or B5) to create a double stranded sequence. The oligonucleotide was used at 2.4 µM final concentration. The working solution of dsDNA oligonucleotides was prepared by mixing the following sterile solutions: 10 µL of 10x STE buffer (10 mM Tris, pH 8.0, 100 mM NaCl, 1 mM EDTA), 20 µL of both labelled and unlabelled oligonucleotide solution, and 50 µL ultrapure water. 24 µL of this solution were diluted in 176 µL sterile PBS. The oligonucleotides were annealed by heating in a large beaker of water at 94 °C and cooled at room temperature for 6 h. The annealed solutions were used or stored at −20 °C.

5.2.3 Selection of Ubx fusions and aptamers for fluorescent visualisation of binding

The Ubx fusions used in these experiments included Ubx, EGFP-Ubx, pRep-Ubx, and pRep-phiLOV-Ubx. Ubx and pRep-Ubx exhibited blue fluorescence in the blue due to dityrosine with a maximum at 440 nm. EGFP and phiLOV2.1 have a fluorescence emission peak at approximately 508 nm, which enabled the detection of the fluorescence of fibres in the green channel separately from the dityrosine fluorescence. Ubx fusions with EGFP and phiLOV2.1 were used in the initial experiments involving aptamer binding to fibres. However, due to the relatively large spectral overlap between the emission of green fluorescent proteins and the excitation of red fluorescent labels, mCherry and Texas Red, Ubx fibres were used to detect aptamer and analyte binding in later experiments. The fluorescence spectra of Ubx fusions and the fluorescent labels are shown in figure 5.2.3.

Figure 5.2.3 also shows the fluorescence excitation and emission spectra of the labels used to detect *E. coli* binding (with an mCherry label), aptamer binding (Texas Red label), and SARS-CoV-2 spike RBD protein binding (Texas Red label). Both mCherry and Texas Red can be excited in the red channel with the excitation maxima at 587 nm and 595 nm, respectively. Their respective emission maxima are at 610 nm and 613 nm. The separation of Ubx emission and mCherry and Texas Red excitation (figures 5.2.3a and 5.2.3b) meant that the spectral overlap was relatively small, which enabled the detection of binding of molecules with the red fluorescent labels to Ubx and pRep-Ubx fibres.

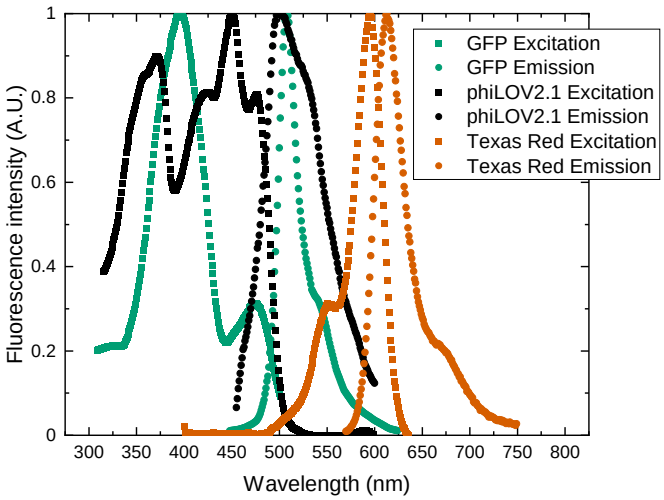

(a)

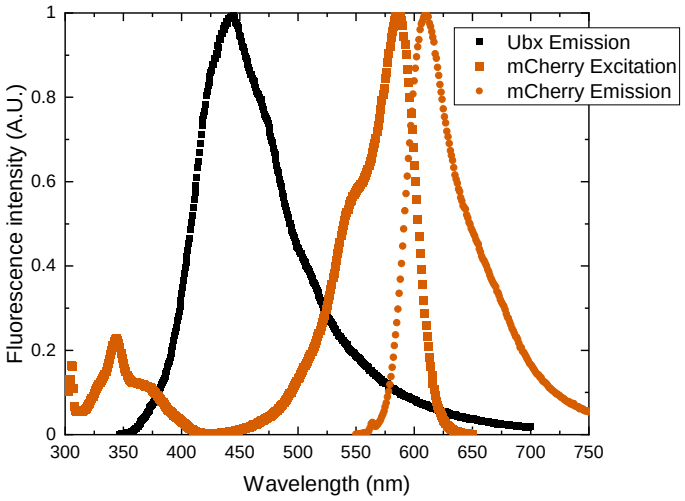

(b)

Figure 5.2.3: The fluorescence spectra of Ubx fusions and the fluorescent labels appended to the analytes used in the experiments involving DNA binding to Ubx and analyte capture using Ubx fibre-aptamer complexes. (a) The selected excitation and emission spectra of fluorescent labels used in the initial experiments: GFP, phiLOV2.1 and Texas Red. The spectral overlap between GFP, EGFP (see figure 3.3.2), and phiLOV2.1 prompted the use of unlabelled Ubx for further experiments. (b) The emission spectrum of a Ubx fibre, and the excitation and emission spectra of mCherry used as a fluorescent label attached to *E. coli* in the bacteria binding experiments. Low overlap of Ubx emission and mCherry excitation enabled bacteria binding detection. Sources: GFP [123], mCherry [52], phiLOV2.1 [122], and Texas Red [124]. Spectra reproduced using FPbase [57]

To aid the visualisation of fibres, fluorescent EGFP-Ubx and pRep-phiLOV-Ubx fusions were used in the initial experiments. To form the dsDNA aptamers, the Ubx homeodomain binding arm could be annealed with a complementary oligonucleotide that was either label-free or was labelled with Texas Red fluorescent dye. To identify the analytes captured, *E. coli* were either transformed with the pGLO plasmid (for GFP expression) or labelled with the mCherry fluorescent protein to enable microscopic imaging and identification of the bacteria labelled with a fluorescent dye. To visualise binding of the SARS-CoV-2 spike protein RBD to the fibres, the protein was biotinylated and the high-affinity binding of the streptavidin-Texas Red complex to biotin [125, 126] was used to assess the amount of SARS-CoV-2 spike protein bound to the fibres. As previously stated, after the initial experiments, Ubx and pRep-Ubx fibres without the green fluorescent labels (EGFP and phiLOV2.1) were chosen for aptamer and analyte binding experiments to decrease the spectral overlap between the fibre fluorescence emission and the excitation of the fluorescently-labelled analytes. The area and intensity of the regions of bright red fluorescence due to the red fluorescent labels, mCherry and Texas Red, were used to compare the specific binding efficiency between the fibres functionalised with DNA aptamers and those fibres that were not functionalised (controls). Fibres not functionalised with DNA and not immersed in the analyte solution were referred to as the negative controls.

5.2.4 Imaging and image analysis using ImageJ (FIJI version)

Fluorophores

To visualise the fibres and examine binding, a laser scanning confocal microscope (Zeiss LSM 710) was used. Several fluorescence sources were identified in the fibres that were used in the analysis. The first is the autofluorescence of Ubx fibres caused by the presence of dityrosine bonds with a steady-state excitation maximum at 323 nm and the emission maximum at 404 nm. Moreover, the protein fusions that formed fibres included fluorescent dyes. Among them was EGFP-Ubx, with the EGFP excitation maximum at 488 nm and the emission maximum at 507 nm. The pRep-phiLOV-Ubx construct was used, for PhiLov the excitation maximum was 450 nm and the emission maximum was 496 nm.

To visualise DNA and analyte binding, Texas Red was used as a fluorescent label in some dsDNA samples as well as the biotin-streptavidin-Texas Red bind-

ing assays. Texas Red has an excitation wavelength of 586 nm and an emission wavelength of 603 nm.

Two strains of *E. coli* were used in these experiments. The first type of cells were the HB-101 competent cells that were transformed with the pGLO plasmid (Bio-Rad) in order to induce GFP expression in the presence of arabinose. The excitation wavelength of GFP is 395 nm, whereas the emission peak is at 509 nm. The second type were Rosetta(DE3) competent cells, which were transformed with plasmid encoding mCherry-Ubx protein fusion. The excitation wavelength of mCherry is 587 nm and the emission wavelength is 610 nm.

Imaging wavelengths and parameters

The common factor in all the samples was the presence of Ubx, which has fluorescence characteristic to the dityrosine bonds, which was imaged using the DAPI detector channel with the excitation wavelength of 405 nm. The other fluorescence sources in the fibre were EGFP and PhiLov, which originate from protein fusions. These were imaged using the EGFP fluorescence filter with an excitation wavelength 488 nm. The GFP from pGLO transformed *E. coli* was imaged using the same filter with 488 nm excitation. Finally, Texas Red both as a fluorescent label on the dsDNA and in the conjugated streptavidin-Texas Red complex was imaged using 594 nm excitation wavelength and the Texas Red emission filter, while the Rosetta cells expressing mCherry-Ubx were imaged using 594 nm excitation with the mCherry emission filter.

The detector gain and laser attenuation were set empirically for each set of samples by determining the appropriate values for the first fibre within each triplicate. Then, the imaging settings were kept consistent between the different sample types for each protein fusion, i.e. the same settings were used for all of the controls and aptamer samples using Ubx or EGFP-Ubx fibres. Separately, consistent settings were used for pRep-Ubx or pRep-phiLOV-Ubx fibres, for which the fluorescence of PhiLov was significantly less bright than that of EGFP.

The fibre mounted on the microscope slide was placed on the sample stage. Because of the fibre mounting method, the cover glass could not be placed on the samples due to the insufficient working distance between the cover glass and the objective. This disabled the use of oil immersion objectives (63x or 100x). Samples were imaged using the 20x (N.A. 0.3) objective of the Zeiss LSM 710 confocal microscope using multichannel image acquisition, where the blue channel was al-

ways set to capture the dityrosine fluorescence, and the remaining green and red channels were used to image either GFP, EGFP or PhiLov, and mCherry or Texas Red, respectively.

Quantitative image analysis

Image analysis was conducted using the FIJI version of ImageJ. Both the pre-processing method and measurements were chosen based on the sample type. The type of protein fusions used to make fibres and fluorescent labels in oligonucleotides or analytes were considered when choosing the analysis method. The general pipeline included segmentation of the image to find the area occupied by the fibre, taking intensity measurements across the whole fibre, then choosing the bright region of interest (ROI) within the fibre by thresholding and performing measurements in the ROIs.

The fibre segmentation was done in two ways, depending on the experiment. Primarily for measurements on the streptavidin-Texas Red fibres, the process (see figure 5.2.4) started with removing the salt-and-pepper noise, if needed, by using the Despeckle function. Then, the Find Edges function was used to define edges of the fibre for further masking and remove out-of-focus light. The image was made binary with the Make binary function. Any holes in the selection were filled using the Fill Holes command. The fibre area defined in that way was selected and added as a region of interest (ROI), and if more objects outside of the fibre were identified, the ROI was split and only the fibre area was chosen. Then, the measurements on the fibre fluorescence intensity could be taken.

For the *E. coli* binding measurements (see figure 5.2.5), the process to define fibre area involved thresholding the fluorescence intensity using the MaxEntropy method. If salt-and-pepper noise was present, Despeckle function was used to remove it. The selection of fibre area was made using the Create Selection function after thresholding.

Once the selection containing the fibre was created, measurements were taken on the fibre that included the area of the fibre and the mean, minimum, maximum, median and mode of the fluorescence intensity within the ROI.

To observe aptamer binding to fibres and analyte binding to aptamers, a further analysis of fluorescence within the ROI containing the fibre was required. That was done in the red channel for Texas Red and mCherry labelled analytes (see

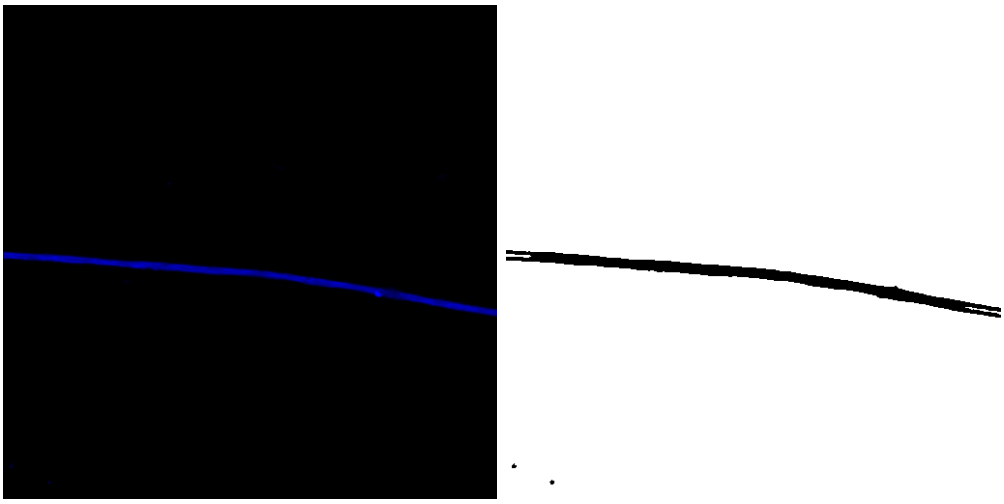

Figure 5.2.4: The sample images showcasing the creation of the binary mask encasing the fibre from the blue fluorescence channel image for the SARS-CoV-2 protein binding experiment.

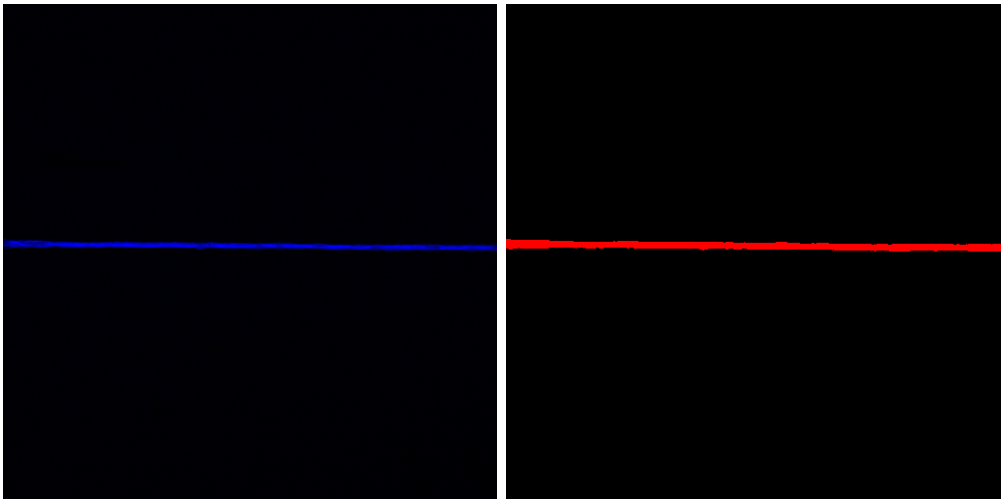

Figure 5.2.5: The sample images showcasing the creation of the binary mask encasing the fibre from the blue fluorescence channel image for the *E. coli* binding experiments.

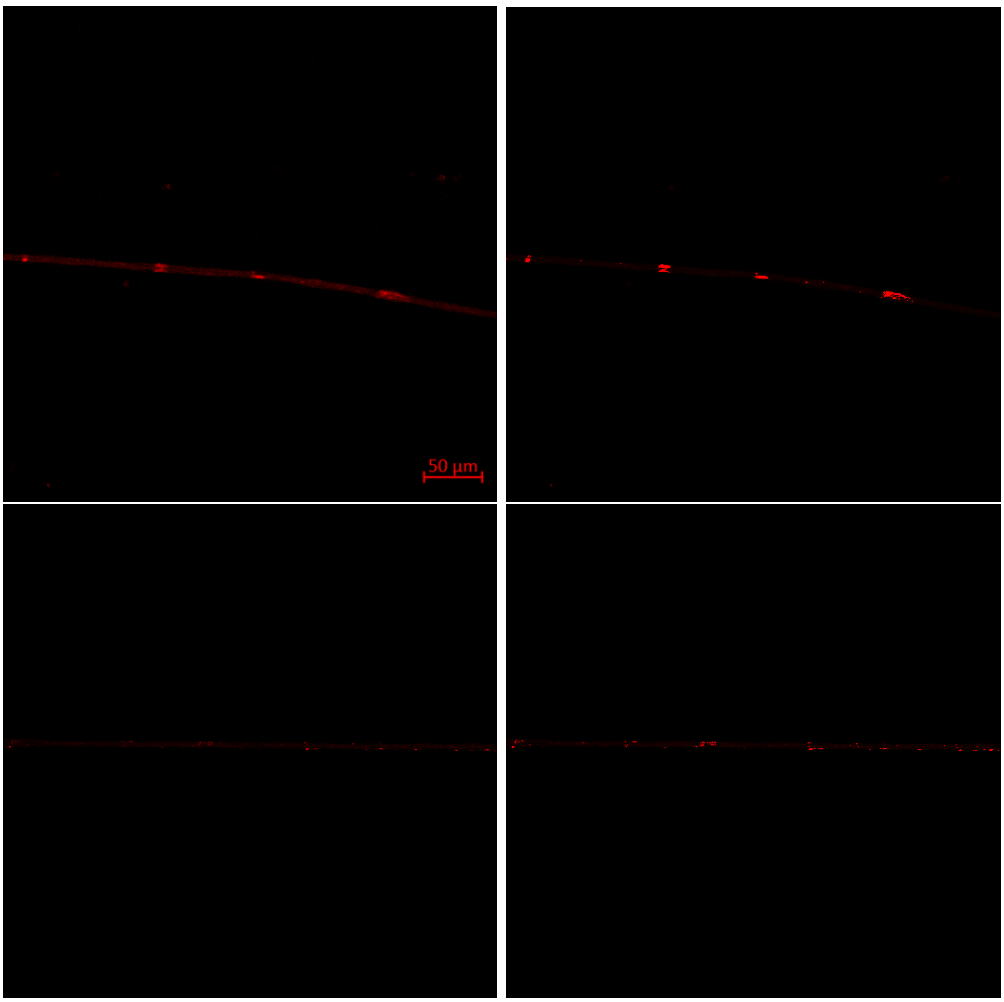

Figure 5.2.6: The sample images showing the Maximum Entropy thresholding method to isolate the brightest regions within the fibre for further analysis.

figure 5.2.6). Fluorescent labels were used both for aptamer detection and the detection of biotinylated SARS-CoV-2 RBD protein, while in the case of *E. coli* binding, the bacteria expressed fluorescent proteins GFP or mCherry were used to enable easier observation. Therefore, a method to distinguish brightly fluorescent regions within the fibre from the background was needed to quantify binding. It was empirically found that the MaxEntropy thresholding method was the most suitable to find both the fluorescent *E. coli* and bright regions of the fibre, in which the presence of Texas Red was suspected. Following that, further measurements were taken on these bright regions using the Analyze Particles function. This function counted the number of bright objects within the fibre ROI, their average size, percentage of the area within the ROI occupied by the bright features, and their mean and median fluorescence intensity. Both the area percentage of bright objects and their mean intensity give valuable information about the extent of binding that occurred within the sample, the non-specific binding and background intensity within the fibres.

5.2.5 Fibre pre-selection

Ubx fusion fibres were prepared using the procedure described in section 2.2. They were imaged using a Zeiss fluorescence microscope with the DAPI filter used to image the dityrosine autofluorescence. Their average diameter and fluorescence intensity in at least three regions were measured using the ImageJ software. Fibres of similar size and fluorescence intensity were chosen for each of the experiments to enable direct comparison of quantitative fluorescence intensity measurements. Fibres were chosen in triplicates for each experimental group.

5.2.6 Fibre treatment and storage during hybridisation of Ubx-aptamer systems

Binding studies on fibres required incubation in a humid environment to prevent evaporation, which could result in salt and glucose crystallisation during hybridisation (30 minutes to overnight, depending on sample type). For this, a humidity chamber was created using an upside-down Petri dish. A folded medical wipe was placed at the bottom of the Petri dish and then soaked with deionised water until saturated. A strip of Parafilm was placed on the wipe and the glass slide with attached fibres was placed on the Parafilm.

All solutions were applied using an adjustable 100 or 200 µL pipette. Then, they

were removed by aspirating the liquid using the same pipette. Evaporation that occurred during this process could mean that there is a cell or crystal residue on the slide following fibre treatment. Thorough washing of fibre was applied to minimise unbound cell and protein residue, and salt and glucose crystallisation. Washing of fibres was done by repeatedly pipetting 100 µL of a wash buffer (detailed for each experiment) onto the fibre, and aspirating.

5.2.7 Binding aptamers to Ubx fusions

Direct oligonucleotide binding to Ubx or pRep-Ubx protein fusions in solution

When binding ssDNA to pRep-Ubx, 10.5 mL of pRep-Ubx protein solution at a concentration of 7.5 µM was mixed with 60 µL of RS2 oligonucleotide solution at 100 µM to give an effective concentration of DNA of 0.57 µM. This solution was incubated at 37 °C for 30 min, and then deposited into the trough, after which fibres were made as described in section 2.2. The surface protein film formed by the Ubx fusion-aptamer complex was gathered together 16 h after protein deposition. The fibres were pulled 2 h after gathering the surface film. Plain pRep-Ubx fibres without oligonucleotides were used as a control for *E. coli* binding to fibres.

To bind the fluorescently labelled dsDNA constructs to Ubx monomers, 8 mL of Ubx protein at a concentration 2.13 µM was mixed with 600 µL of the dsDNA Texas Red labelled Ubx binding oligonucleotide solution (construct B0+B5) at 2.4 µM to give an effective concentration of DNA of 0.17 µM. The solution was incubated for 6 h at room temperature and then added to the buffer-filled trough. Fibres were prepared using the method described in section 2.2. As a control, 6 mL of protein and 10 µL of Texas Red labelled oligonucleotide solution at 100 µM were mixed and fibres were made using the same procedure. In this case, no Ubx homeodomain binding sequence was present in the oligonucleotide, which provided a measure of non-specific DNA binding to Ubx protein in solution.

Binding oligonucleotides to pre-made Ubx fusion fibres

Binding ssDNA oligonucleotides (constructs RS1, RS2, and RS3) to pRep-Ubx or pRep-phiLOV-Ubx fibres was done at an elevated temperature to induce covalent binding to the pRep binding sequence. 100 µL of the pRep binding buffer (section 5.2.2) was pipetted onto the fibre to hydrate the sample and aspirated after 5 min.

100 µL of a 2.4 µM ssDNA solution was pipetted onto a fibre fixed to the glass slide. The fibre was placed in the humidity chamber in a Petri dish (section 5.2.6) and incubated for 6 h or overnight at 37 °C. Then, the fibre was washed three times with pRep binding buffer.

2.4 µM solutions of dsDNA oligonucleotides (constructs B0, B1, B3, B10, and B11 annealed with B4 or B5 complementary oligonucleotide sequence to create dsDNA) were used for binding to Ubx or EGFP-Ubx fibres. The fibre was hydrated using 100 µL of PBS, which was aspirated after 5 min. 100 µL of a dsDNA solution was pipetted onto the fibre. The fibre was placed in a humidity chamber to prevent liquid evaporation and incubated for 6 h or overnight at room temperature. After oligonucleotide binding, the fibre was washed three times with PBS solution.

5.2.8 Optimisation of the oligonucleotide concentration and the blocking of non-specific binding of analytes

Optimisation of the oligonucleotide concentration for binding to fibres

The pRep-Ubx fibres were functionalised with biotinylated ssDNA oligonucleotides containing the pRep binding sequence (construct RS1). Solutions containing between 0.5 µM and 9.6 µM ssDNA were prepared and 100 µL of the solution was applied to pre-selected fibres, which were incubated at 37 °C for 30 min. 100 µL of the pRep binding buffer without the ssDNA was applied to the "no DNA control". Fibres were washed three times using the pRep binding buffer. Then, a blocking buffer containing 0.05% TWEEN 20 and 0.5% BSA was applied with an incubation time of 15 min. Fibres were washed three times. Lastly, a 2.4 µM solution of streptavidin-Texas Red, which will bind tightly to the biotinylated ssDNA and label it with a fluorophore, was applied to fibres with an incubation time of 1 h. The fibres were washed twice with a solution of 0.05% TWEEN 20 in PBS and imaged under the confocal microscope to detect streptavidin-Texas Red binding to fibres. Three pRep-Ubx fibres treated with neither the ssDNA nor the streptavidin-Texas Red solution were used as the "negative control".

The binding of streptavidin-Texas Red was used as an indicator of the efficacy of ssDNA oligonucleotide binding to pRep-Ubx fibres. The binding was assessed by measuring the percentage area of regions of bright red fluorescence intensity within the fibre and the mean fluorescence intensity of these regions (figure 5.2.7).

The first experiment (figure 5.2.7a) showed that the mean fluorescent intensity due to streptavidin-Texas Red binding is significantly higher for all samples, including the control without ssDNA solution, compared to the fibres used as the negative control, which means that there was a significant background fluorescence due to non-specific binding of streptavidin-Texas Red. The mean fluorescence intensity of the bright regions increased with the DNA concentration, which prompted another investigation into how higher ssDNA concentrations affect the binding efficacy (figure 5.2.7b). It was found that the largest integrated density of the bright regions was recorded for 2.4 µM, and no statistically significant increase in the mean fluorescence intensity was recorded beyond that DNA concentration. The concentration of oligonucleotides of 2.4 µM was used in further experiments.

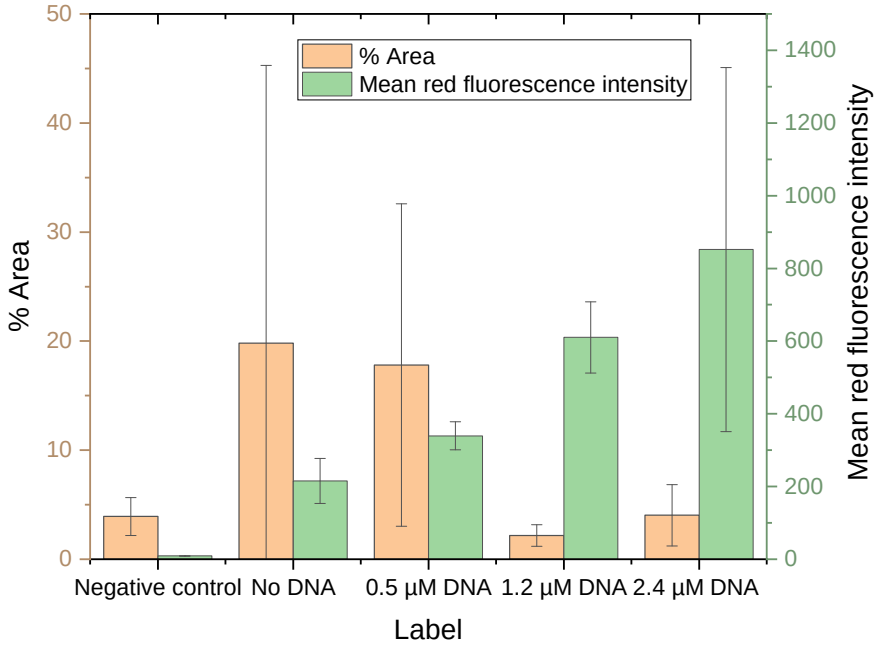

(a)

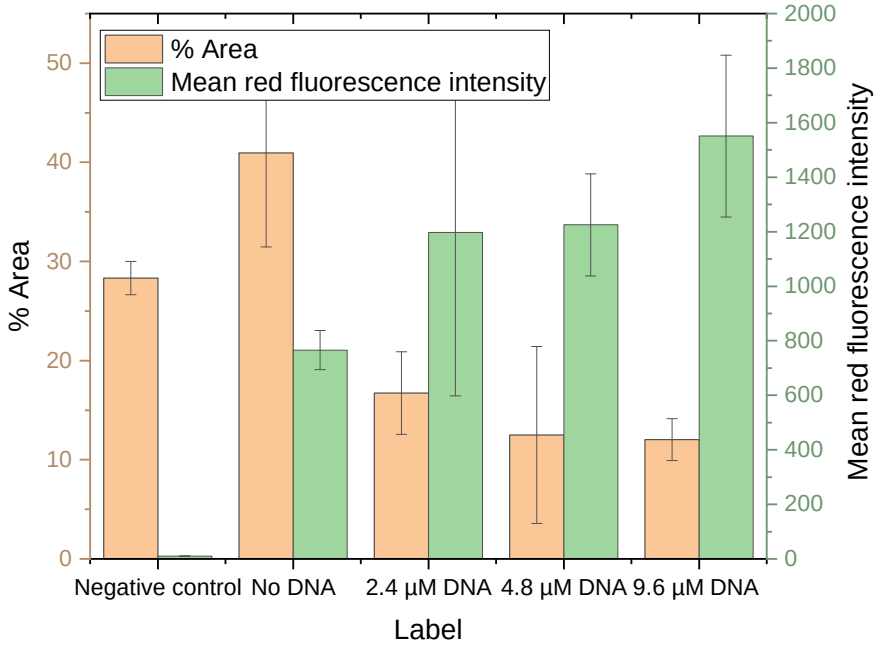

(b)

Figure 5.2.7: The fluorescence intensity and percentage area of bright red fluorescence intensity within fibres after streptavidin-Texas Red binding to pRep-Ubx fibres functionalised with: (a) between 0.5 and 2.4 µM ssDNA, (b) and between 2.4 µM ssDNA and 9.6 µM ssDNA.

The optimisation of buffers blocking non-specific binding of analytes using bovine serum albumin (BSA)

Non-specific binding of biotinylated dsDNA oligonucleotides (solution B0+B4) was blocked by covering the fibre in 100 µL of the PBS-based blocking buffers containing between 0.05% and 0.1% TWEEN 20, and between 0.5% and 5% BSA. Then, the fibres were washed three times with PBS. 100 µL of 2.4 µM solution of streptavidin-Texas Red was applied to fibres, and the fibres were incubated for 1 h and washed three times with PBS and subsequently they were imaged using a fluorescence microscope. The area of regions of bright red fluorescence and their mean intensity were compared for different blocking buffers (figure 5.2.8). Blocking buffer 3 containing 0.1% TWEEN 20 and 2% BSA was deemed best for further applications because of its lowest background mean fluorescence intensity.

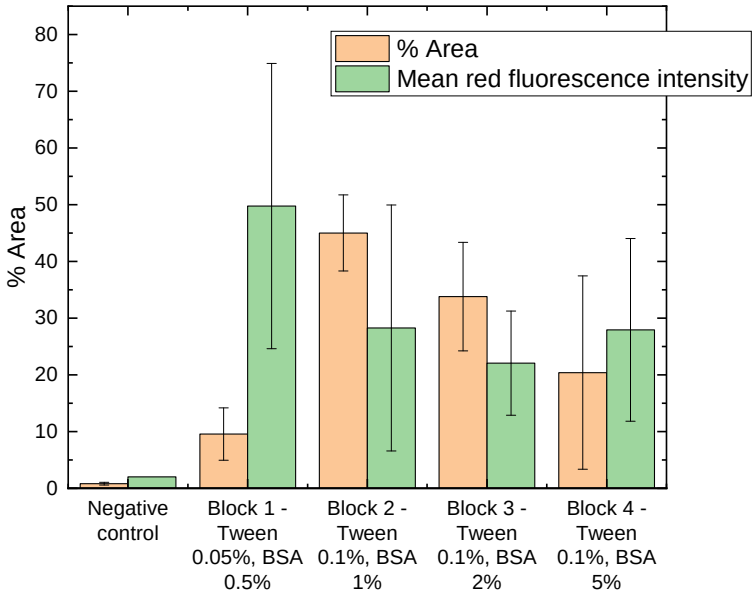

Figure 5.2.8: Comparison of the area of regions of bright red fluorescence intensity and their mean intensity within fibres after blocking of non-specific streptavidin-Texas Red binding with different blocking buffers with TWEEN 20 content between 0.05% and 0.1%, and BSA content between 0.5% and 2%.

The final choice of blocking buffer

The blocking buffer was prepared by preparing a sterile solution of 0.1% w/v (weight per volume) TWEEN 20 and 2% w/v BSA in phosphate buffered saline (PBS). When working with the STC-12 aptamer, sterile $MgCl_2$ solution was

added to the final concentration of 1.4 mM. After binding oligonucleotides to Ubx protein or Ubx fibres, the non-specific binding of analytes to fibres was blocked by applying 75-100 µL of blocking solution to each fibre using a pipette, incubating for 1 hour, and washing the fibre three times using sterile PBS-based wash buffer containing 0.1% w/v TWEEN 20, and when working with the STC-12 aptamer, adding sterile $MgCl_2$ solution to the final concentration of 1.4 mM.

5.2.9 Capturing *E. coli*

Preparation of *E. coli* culture

An overnight culture of *E. coli* was prepared by collecting a single *E. coli* colony using a pipette tip, suspending it in 5 mL of LB media, and incubating at 37 °C with shaking at 200 rpm overnight. This was estimated to produce 1×10^9 cells/mL. The working solution of *E. coli* cells was prepared by transferring 1 mL of the overnight culture to a microcentrifuge tube and washing it twice in PBS by centrifugation at 8000 rpm for 5 min, removing the supernatant, and adding 1 mL of PBS. Finally, the cells were resuspended in 1 mL of PBS.

Binding GFP-labelled *E. coli* using aptamers bound to the Ubx fusion fibres

The oligonucleotides were bound to Ubx as detailed in section 5.2.7. The constructs containing *E. coli* aptamers were: RS2, B1+B4, B1+B5, B10+B4, B10+B5, B11+B4, B11+B5. The fibres were washed three times, and the blocking buffer was applied to prevent non-specific binding of *E. coli*, after which the fibres were washed three times. Then, the solution of *E. coli* containing the GFP fluorescent label was pipetted onto the fibre and incubated for 1 h before washing six times with the washing buffer containing 0.1% TWEEN 20 and 1.4 mM $MgCl_2$ (washing buffer without $MgCl_2$ was used when working with the STC12-31 aptamer).

Binding mCherry-labelled *E. coli* using aptamers bound to the Ubx fusion fibres

The oligonucleotides were bound to Ubx as detailed in section 5.2.7. The fibres were washed three times, and the blocking buffer was applied to prevent non-specific binding of *E. coli*, after which the fibres were washed three times. Then, the solution of *E. coli* containing the mCherry fluorescent label was pipetted onto the fibre and incubated for 1 h before washing six times with the washing buffer

containing 0.1% TWEEN 20 and 1.4 mM $MgCl_2$ (washing buffer without $MgCl_2$ was used when working with the STC12-31 aptamer).

5.2.10 Binding the SARS-CoV-2 spike RBD protein

An oligonucleotide solution with the CoV2-RBD-4C aptamer (constructs RS3, B3+B4, or B3+B5) was applied to the fibres as described in section 5.2.7. To prevent non-specific binding of the SARS-CoV-2 spike RBD protein, a blocking buffer containing 0.05% TWEEN 20, 0.55% $MgCl_2$ and 0.5% BSA was applied. Then, the sample was washed three times using a washing buffer containing 0.05% TWEEN 20, 0.55% $MgCl_2$. 75 µL of the 1.2 µM SARS-CoV-2 Spike RBD protein (Bio-Techne) was applied to the fibre, following a 1 h incubation at room temperature. The samples were washed three times, after which the blocking buffer was applied. Then, the fibres were washed again. Finally, a 2.4 µM solution of streptavidin-Texas Red was applied to the fibres. The samples were washed three times before imaging using a confocal microscope.

5.3 Results and discussion

5.3.1 Assessment of aptamer binding to Ubx in solution and in fibres

Direct ssDNA oligonucleotide binding to pRep-Ubx in solution

The binding of ssDNA with pRep binding sequence to pRep-Ubx protein fusion was examined in solution by direct mixing and incubation. It was proposed that if the ssDNA binds covalently to pRep-Ubx molecules, then the gel electrophoresis will reveal a protein molecular weight band shift compared to pure pRep-Ubx protein, which could evidence the oligonucleotide binding to the protein. The photo of the SDS-PAGE gel (figure 5.3.1) shows the protein bands corresponding to the protein elutions of pRep-Ubx, and the solution of pRep-Ubx with ssDNA containing the pRep aptamer. An extra band with a higher molecular weight than pRep-Ubx was visible in the sample corresponding to pRep-Ubx conjugated with the oligonucleotide. Therefore, binding of ssDNA containing the pRep binding sequence was suggested as a viable path to functionalise pRep-Ubx fusion fibres with aptamers of choice.

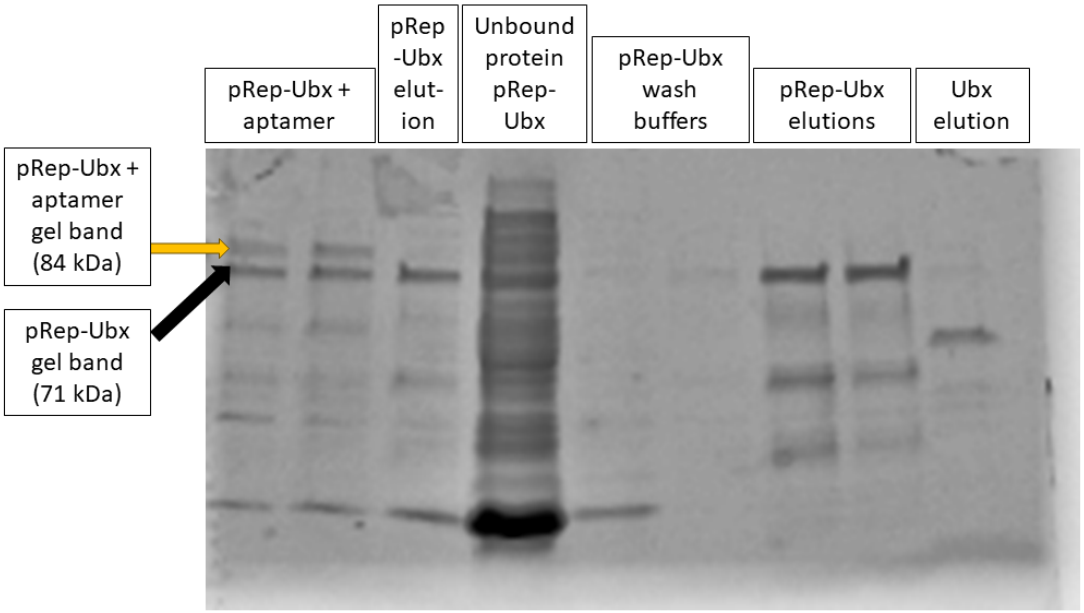

Figure 5.3.1: A photograph of the SDS-PAGE gel showing the protein band shift due to ssDNA oligonucleotide binding to pRep-Ubx protein fusion.

Direct dsDNA oligonucleotide binding to Ubx in solution

Another route to bind oligonucleotides to Ubx fusions in solution was explored by mixing a solution of myoglobin-Ubx protein fusion with a solution of fluorescently (Texas Red) labelled dsDNA containing the Ubx binding sequence. This solution was incubated for 6 h and then added to the regular buffer used to prepare Ubx fibres. The DNA binding was examined by measuring the fluorescence of the fibres in the blue and red channels, which corresponded to Ubx autofluorescence and Texas Red fluorescence, respectively. To control for non-specific DNA binding, a DNA sequence containing the Texas Red label was added to myoglobin-Ubx before fibre formation. The comparison of fluorescence intensities was shown in figure 5.3.2b. The mean fluorescence intensity, in both the blue channel and in the red channel, was higher for fibres treated with the oligonucleotide that contained the Ubx binding sequence. In the blue channel, it was 36% higher (P=0.1069), while in the red channel, the fluorescence difference was 130% (P=0.0018). The ratio of the red and blue mean fluorescence intensity was 0.69 ± 0.07 for the sample with Ubx aptamer compared to 0.39 ± 0.04 for the control (P=0.0012). The background fluorescence intensity in the red channel was high for the control, which suggests that either some non-specific binding was occurring, or the laser power and gain needed to obtain signal for the Texas Red labelled aptamers was

very high, and enabled measurement of background dityrosine autofluorescence in the red channel. These results indicate that binding of the dsDNA oligonucleotide containing the Ubx aptamer is a viable way to functionalise Ubx fibres with DNA aptamers.

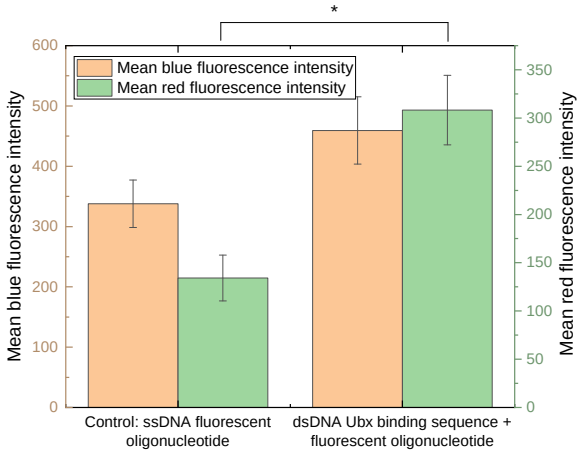

(a)

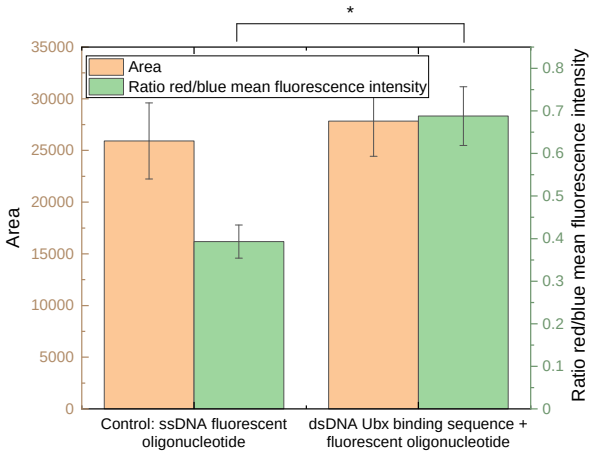

(b)

Figure 5.3.2: Comparison of the mean blue and red fluorescence intensity and their ratio within myoglobin-Ubx fibres made using protein mixed with a fluorescently-labelled ssDNA solution without Ubx binding sequence, and those made with myoglobin-Ubx mixed in solution with 2.4 µM of Texas Red-labelled dsDNA oligonucleotide with Ubx binding sequence. The statistically significant differences were marked with an asterisk.

Binding single-stranded oligonucleotides to pRep-Ubx fibres

The aim of this experiment was to investigate the ability to bind ssDNA to pRep-phiLOV-Ubx fibres using a biotinylated test aptamer with a pRep binding sequence. The detection of binding was possible by conjugating the streptavidin-Texas Red complex to biotinylated oligonucleotides.

The binding of the biotinylated ssDNA with pRep-Ubx binding sequence to pRep-Ubx fibres was investigated by measuring the fluorescence intensity of the fibres due to the attached streptavidin-Texas Red molecules applied to the fibres after ssDNA binding. The measurements are shown in figure 5.3.3. For the fibres functionalised with 2.4 µM oligonucleotide solution, the ratio of the mean red to mean blue fluorescence intensity was $(64 \pm 12)\%$, which was almost twice the value of $(34 \pm 2)\%$ for the sample without ssDNA.

The comparison of the area and fluorescence intensity regions of bright red fluorescence between the fibres with and without ssDNA was shown in figure 5.3.4. The area of bright regions increased from $(44 \pm 6)\%$ to $(57 \pm 13)\%$ while their mean fluorescence intensity rose from (401 ± 26) A U to (940 ± 110) A U. These results indicate a significant specific binding of the ssDNA construct containing the pRep binding sequence to pRep-Ubx fibres.

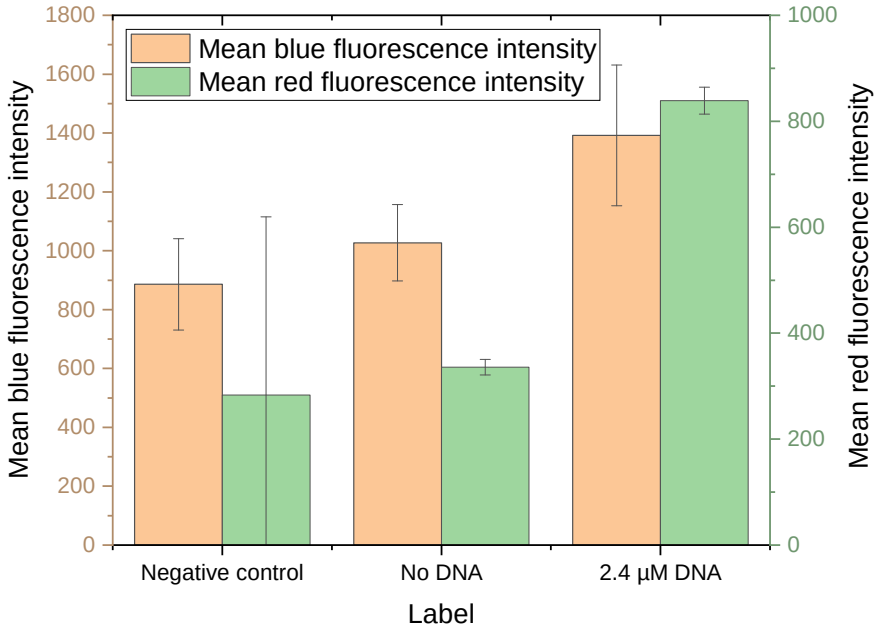

(a)

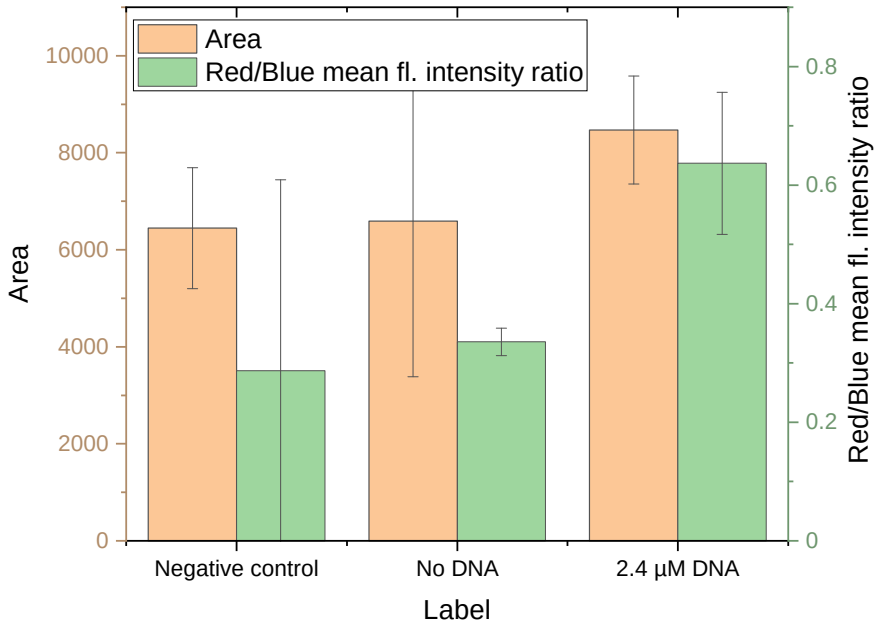

(b)

Figure 5.3.3: Comparison of the mean blue and red fluorescence intensity and their ratio within regular pRep-Ubx fibres and those functionalised with 2.4 µM of biotinylated ssDNA oligonucleotide with pRep-Ubx binding sequence. 2.4 µM streptavidin-Texas Red was applied to the no DNA and 2.4 µM ssDNA fibres.

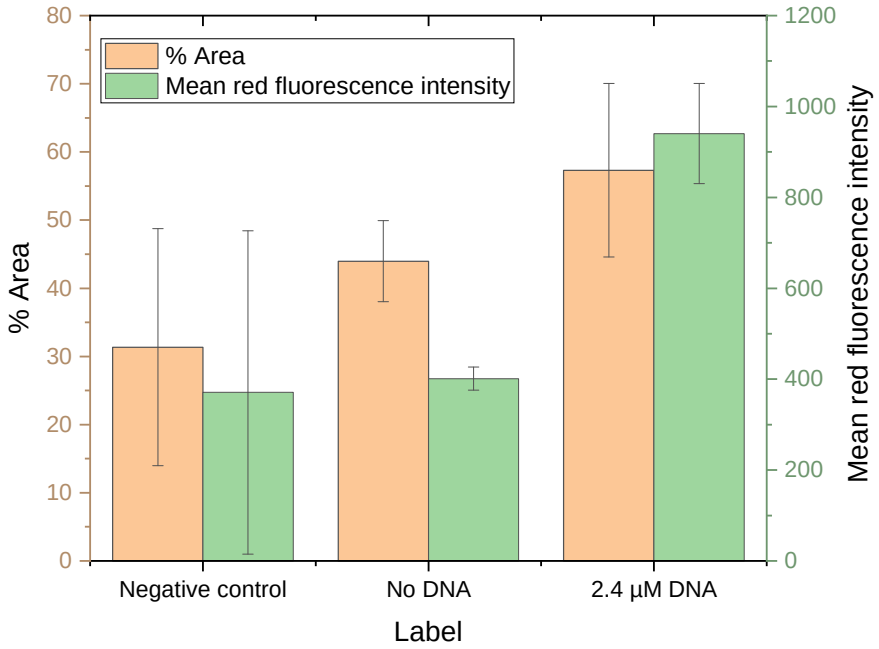

Figure 5.3.4: Comparison of the area of regions of bright red fluorescence intensity and their mean intensity within regular pRep-Ubx fibres and those functionalised with 2.4 µM of biotinylated ssDNA oligonucleotide with pRep-Ubx binding sequence. 2.4 µM streptavidin-Texas Red was applied to the no DNA and 2.4 µM ssDNA fibres.

Binding double-stranded oligonucleotides to Ubx fusion fibres

The binding of dsDNA to EGFP-Ubx fibres was achieved using the Ubx homeodomain binding sequence within the oligonucleotide. The binding was monitored by fluorescent labelling of oligonucleotides with the Texas Red fluorescent protein. The fluorescence intensity of fibres functionalised with a range of dsDNA constructs was measured and compared in the blue, green, and red channel to compare the binding efficacies (figure 5.3.5). All fibres treated with oligonucleotides exhibited a statistically significant increase in the mean red fluorescence intensity compared to the PBS control. Additionally, the dsDNA containing the P12-31 and STC-12 *E. coli* aptamers increased both the red fluorescence intensity and the area of bright regions of EGFP-Ubx fibres in the red channel by 44% and 32% for intensity, and by factors of 9.4 and 8.3 for the area. These results indicate a significantly increased oligonucleotide binding for the constructs containing the P12-31 and STC-12 aptamers, indicating that the dsDNA constructs can be used to bind to Ubx fusion fibres.

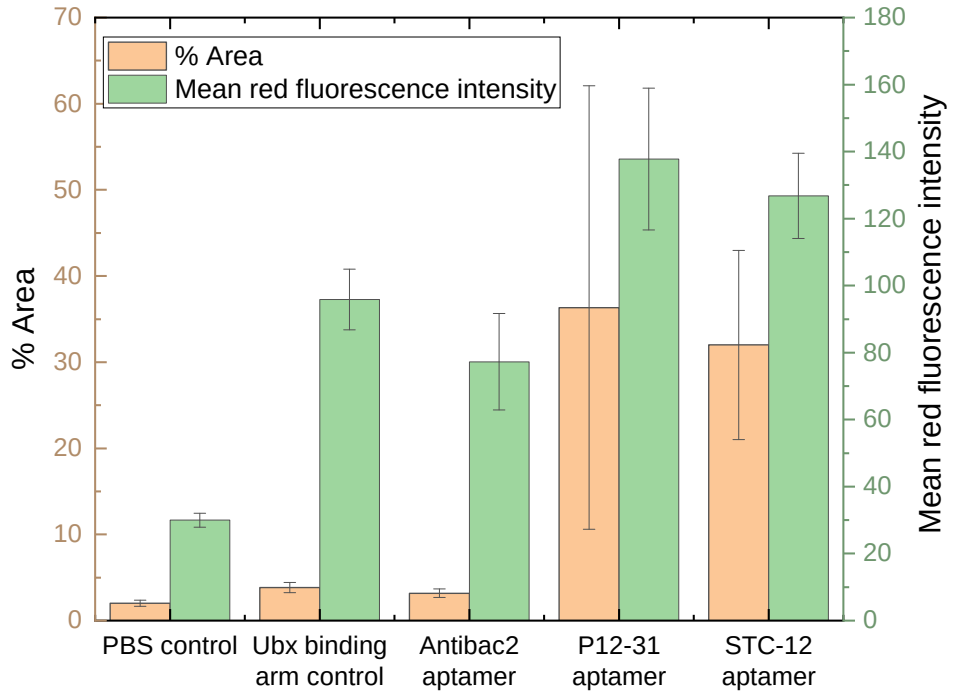

Figure 5.3.5: Comparison of the area of regions of bright red fluorescence intensity and their mean intensity within regular EGFP-Ubx fibres and those functionalised with 0.5 µM of dsDNA oligonucleotide with Ubx binding domain and Texas Red label. The red fluorescence in these fibres was caused by oligonucleotide binding to the fibres. The fibres were also tested for capturing GFP-labelled *E. coli* in solution.

5.3.2 *E. coli* binding to fibres

This section will discuss the initial experiments with binding *E. coli* with a GFP fluorescent label (section 5.3.2), and the subsequent measurements of binding of *E. coli* with the mCherry fluorescent label (sections 5.3.2 and 5.3.2). The first experiments involving binding *E. coli* with an mCherry fluorescent label showed an increase in the mean red to mean green fluorescence intensity ratio for the EGFP-Ubx fibres functionalised with oligonucleotides containing both the P12-31 and Antibac2 aptamers, which indicated that the bacteria binding was possible using oligonucleotides containing DNA aptamers (section 5.3.2).

Binding *E. coli* with a GFP fluorescent label using ssDNA and dsDNA aptamers

The first experiment involving *E. coli* expressed with the pGLO plasmid involved testing oligonucleotides containing three different *E. coli* aptamers in the presence of the Ubx binding arm and the Texas Red fluorescent label. This experiment showed an increase in the ratio of mean fluorescence intensity in the green channel to that in the blue channel for all three *E. coli* aptamers compared to the dsDNA sample without a bacteria aptamer (figure 5.3.6). Additionally, the ratio of the red to blue fluorescence intensity rose for the fibres treated with P12-31 and STC-12 aptamers, compared to the control dsDNA with Ubx binding arm and Texas Red label. The only statistically significant difference between the samples containing oligonucleotides was the rise in the red fluorescence intensity for the STC-12 aptamer compared to Control 2 (P=0.0065), which signifies more DNA binding to the fibre. However, the increase in the ratios of green to blue and red to blue mean fluorescence intensity (figure 5.3.6b) for fibres treated with *E. coli* aptamers suggested that this functionalisation method could be used efficiently in capturing bacteria.

Another experiment tested the binding of the same *E. coli* strain with an ssDNA construct including the Antibac2 aptamer and the Ubx binding domain. The binding was compared by measuring the fluorescence intensity in the green channel and the blue channel. Both the green fluorescence intensity and the ratio of green to blue mean fluorescence intensity increased (by 119% and 67%, respectively) for the fibres functionalised with the Antibac2 aptamer compared to the control. These results suggested an increase in *E. coli* binding, consistently with those for EGFP-Ubx fibres functionalised with dsDNA. However, these differences

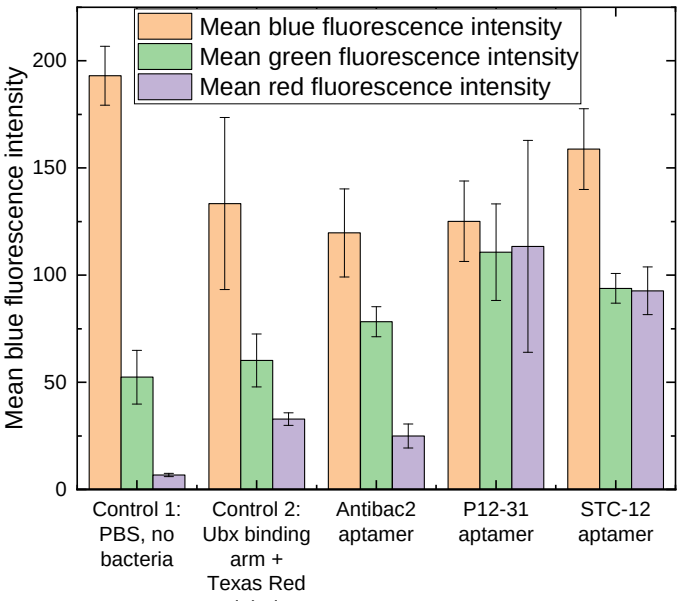

(a)

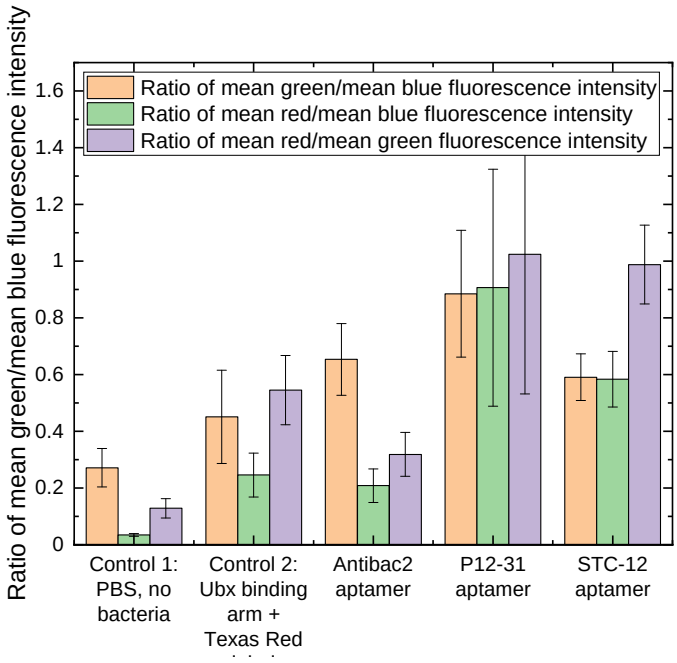

(b)

Figure 5.3.6: Comparison of the mean blue, green and red fluorescence intensity, and their ratios within EGFP-Ubx fibres functionalised with 0.5 µM of dsDNA oligonucleotide with Ubx binding domain and three *E. coli* aptamers, Antibac2, STC-12 and P12-31.

were not statistically significant due to the large deviation in the results.

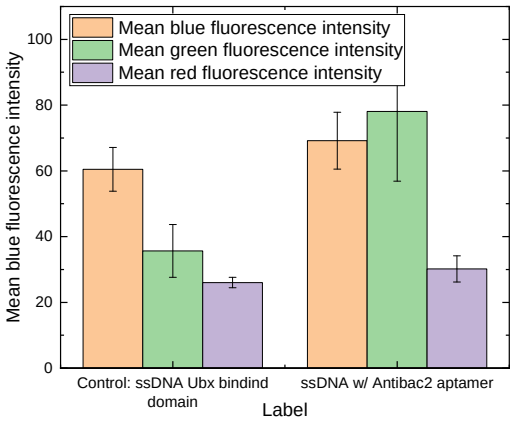

(a)

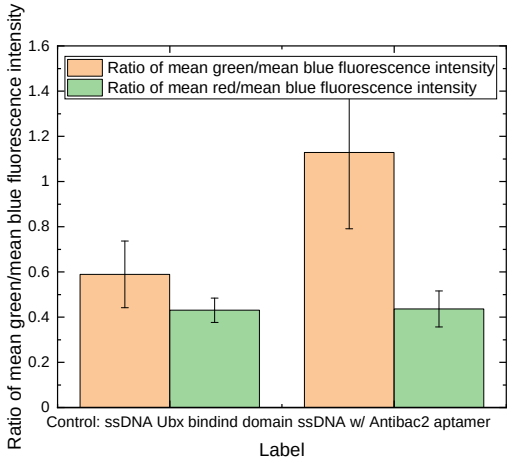

(b)

Figure 5.3.7: Comparison of the mean blue, green and red fluorescence intensity, and their ratios within EGFP-Ubx fibres functionalised with 0.5 µM of ssDNA oligonucleotide with Ubx binding domain and an *E. coli* aptamer Antibac2.

Binding *E. coli* with mCherry fluorescent label using ssDNA and dsDNA aptamers

To further examine the bacteria binding to fibres functionalised with aptamers, the dsDNA construct with the Ubx binding domain, the Texas Red fluorescent label and the Antibac2 aptamer was tested. In this case, the ratio of the mean red to green fluorescence intensity decreased for the aptamer samples, while the red fluorescence intensity was the same as for the control (figure 5.3.8). These

results indicated that no increase in *E. coli* binding was achieved by using the Antibac2 aptamer.

Then, an experiment with ssDNA containing P12-31 and Antibac2 aptamers was conducted. The results are shown in figure 5.3.9. In this experiment, it was shown that the absolute red fluorescence intensity for the Antibac2 aptamer was higher than that for both the P12-31 aptamer and the control (both statistically significant, P=0.011 and P=0.0001, respectively). The ratio of the mean red to green fluorescence intensity was higher for both aptamer groups compared to control. The increase was 2-fold for the Antibac2 aptamer (P=0.0007) and by 134% for the P12-31 aptamer, although this increase was not statistically significant (P=0.0659). These results suggest that the Antibac2 aptamer increased the specific binding of *E. coli* to pRep-phiLOV-Ubx fibres.

The measurements of the mean fluorescent intensity and the area occupied by bright bound cells in the red channel confirmed the increase in fluorescence intensity for both P12-31 and Antibac2 aptamers (figure 5.3.10). The increase was 36% (P=0.2402) for the P12-31 aptamer and 66% for the Antibac2 aptamer (P=0.0024). The statistically significant increase in *E. coli* binding for the sample treated with the Antibac2 aptamer was confirmed in these measurements.

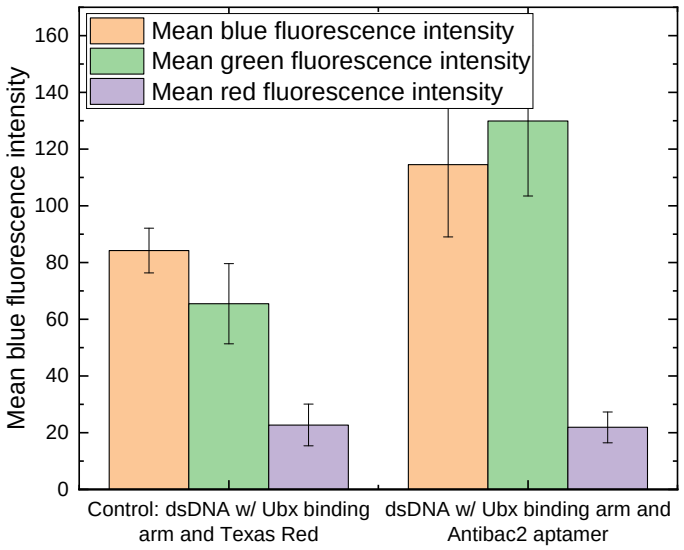

(a)

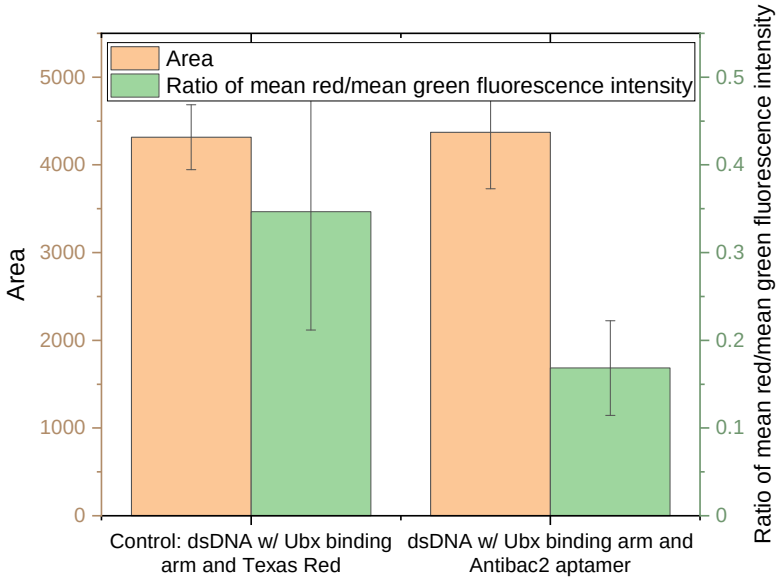

(b)

Figure 5.3.8: Comparison of the mean blue, green and red fluorescence intensity and their ratios within EGFP-Ubx fibres functionalised with 0.5 µM of dsDNA oligonucleotide with Ubx binding domain, the Texas Red fluorescent label and the Antibac2 *E. coli* aptamer.

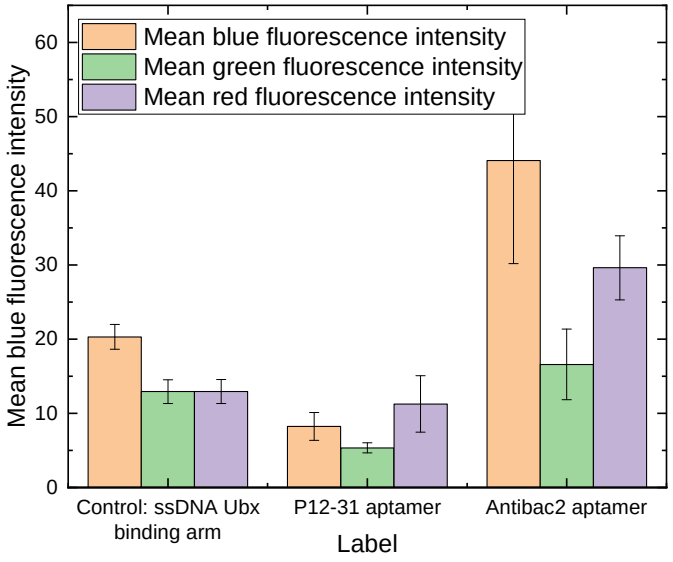

(a)

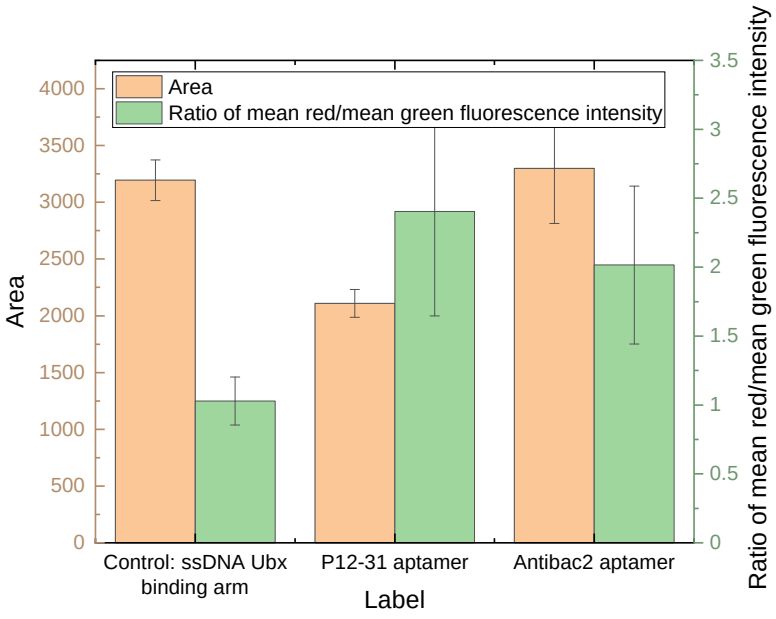

(b)

Figure 5.3.9: Comparison of the mean blue, green and red fluorescence intensity and their ratios within pRep-phiLOV-Ubx fibres functionalised with 0.5 µM of oligonucleotides with the Antibac2 and P12-31 *E. coli* aptamers.

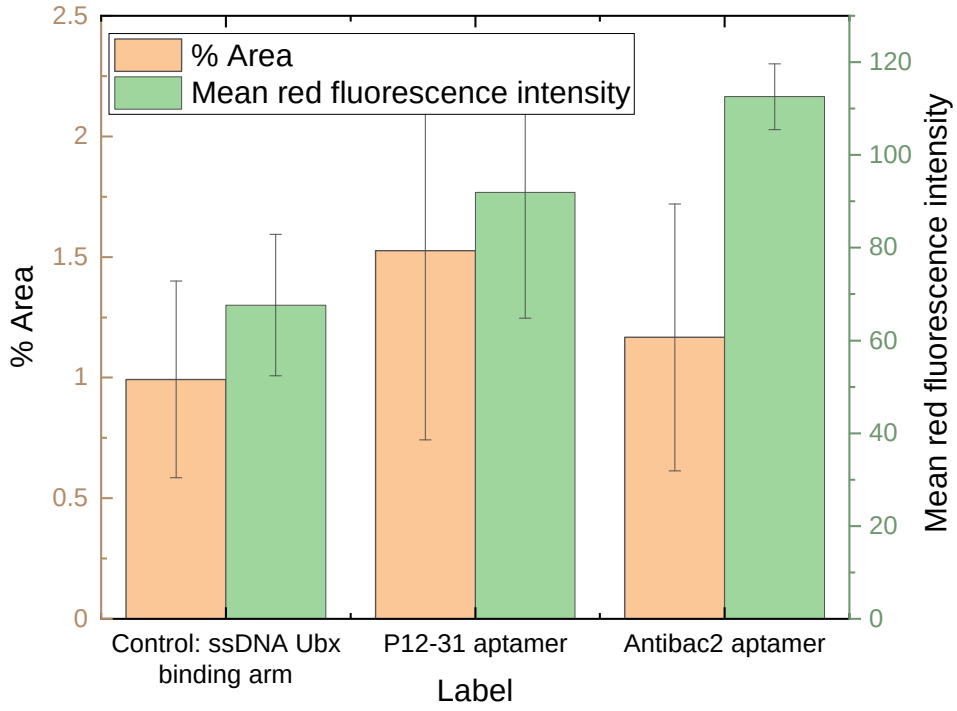

Figure 5.3.10: The statistics of cells bound to the pRep-phiLOV-Ubx fibres functionalised with 0.5 µM of oligonucleotides with the Antibac2 and P12-31 *E. coli* aptamers.

Binding *E. coli* with an mCherry fluorescent label after optimisation of blocking buffer and oligonucleotide concentration

The following experiments used the blocking buffer and DNA concentration chosen in the optimisation experiments described in section 5.2.8. These experiments had the aim of measuring the change in binding of *E. coli* with an mCherry fluorescent label by quantifying the changes in the fluorescence intensity of the fibres in the red channel compared to the blue channel. The fibres were pre-selected based on their diameter and base autofluorescence intensity in the blue channel.

The *E. coli* binding to Ubx fibres was measured after functionalisation with ds-DNA including the P12-31, STC-12 and Antibac2 aptamers (figures 5.3.11 and 5.3.12). The general levels of blue and red fluorescence (figure 5.3.11) did not show significant changes in the ratio of red to blue fluorescence intensity between the aptamer-functionalised fibres and controls. However, the measurements of the fluorescence of bright regions in the red channel showed an increase in the fibre area covered by these objects by 51% for P12-31 and 44% for the Antibac2 aptamer, and an increase in their fluorescence intensity by 15% for P12-31, 93% for STC-12, and 168% for Antibac2 aptamer. However, these differences were not statistically significant.

A similar experiment was conducted for pRep-Ubx fibres functionalised with ss-DNA containing the P12-31 aptamer. In this case, no significant changes in the general fluorescence intensity in blue and red channels were observed for the fibres functionalised with the P12-31 aptamer compared to the controls (figure 5.3.13). A 123% increase in the area covered by attached cells was observed for the aptamer sample compared to the control without DNA, along with a 20% increase in their fluorescence intensity (figure 5.3.14). These differences also were not statistically significant.

These experiments showed increases in either the area covered by bound bacteria, or the fluorescence intensity of these bright regions, which could correspond to larger clumps of cells being attached to the fibre surface. These changes were not statistically significant, which left an open question to whether this technique could enable efficient bacteria capture in solution. However, the trends discovered in this data indicated that applying an oligonucleotide solution to the fibres could be used to functionalise Ubx fusion fibres with DNA aptamers, which would more significantly boost bacteria capture when applied with materials with a larger surface area. These experiments also indicate a large role of non-specific

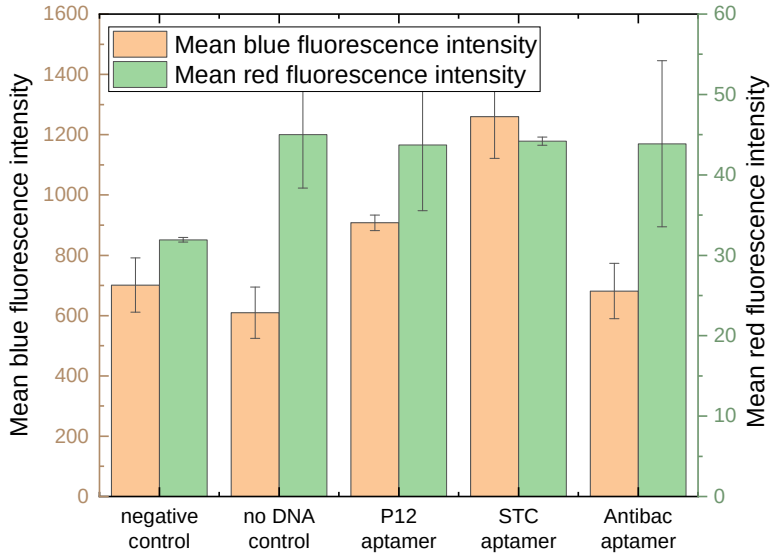

(a)

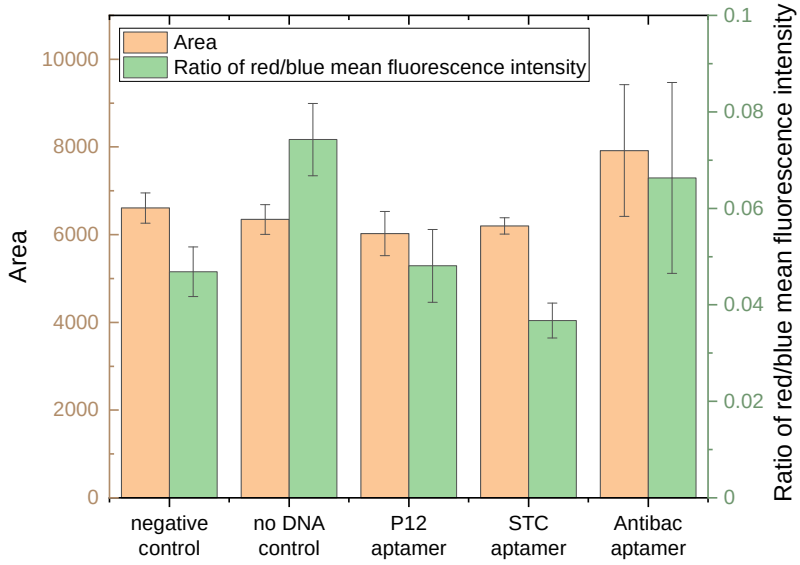

(b)

Figure 5.3.11: Comparison of the mean blue and red fluorescence intensity and their ratios within Ubx fibres functionalised with 2.4 µM of oligonucleotides with the STC-12, P12-31 and Antibac2 *E. coli* aptamers.

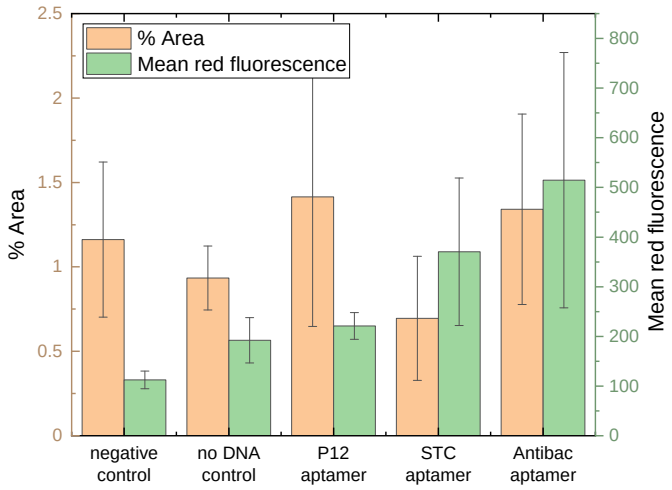

Figure 5.3.12: The statistics of cells bound to the Ubx fibres functionalised with 2.4 µM of oligonucleotides with the Antibac2 and P12-31 *E. coli* aptamers.

binding of *E. coli* to Ubx fusion fibres, which is evidenced by the larger mean red fluorescence intensity of the bound objects and the relative increase in the area covered by these objects and their fluorescence intensity.

Further experiments were conducted with longer time of oligonucleotide binding, blocking non-specific binding, and binding *E. coli* to DNA functionalised fibres. The oligonucleotide binding time was increased to overnight. The blocking of non-specific binding step lasted 2 h, and the *E. coli* binding took 1 h. Some aptamer-treated fibres showed no increase in *E. coli* binding, with a very high non-specific binding or background fluorescence intensity (as seen previously in figures 5.3.10 and 5.3.12). However, further indications for the increased *E. coli* binding were shown in an experiment with dsDNA constructs containing the Antibac2 *E. coli* aptamer. The first indication was a statistically significant increase by 180% (P=0.0044) in the area occupied by the cells bound to the fibres treated with 2.4 µM dsDNA compared to the control without DNA (figure 5.3.15b). In this experiment, the background intensity in the negative control was very high and no statistically significant differences in the fluorescence intensity or the area of bright objects were recorded between the negative control and the aptamer samples. However, the differences between the fibres treated with dsDNA and controls were pronounced when the ratio of mean fluorescence intensity in the red and blue channel was considered (figure 5.3.15a). There was an increase by a

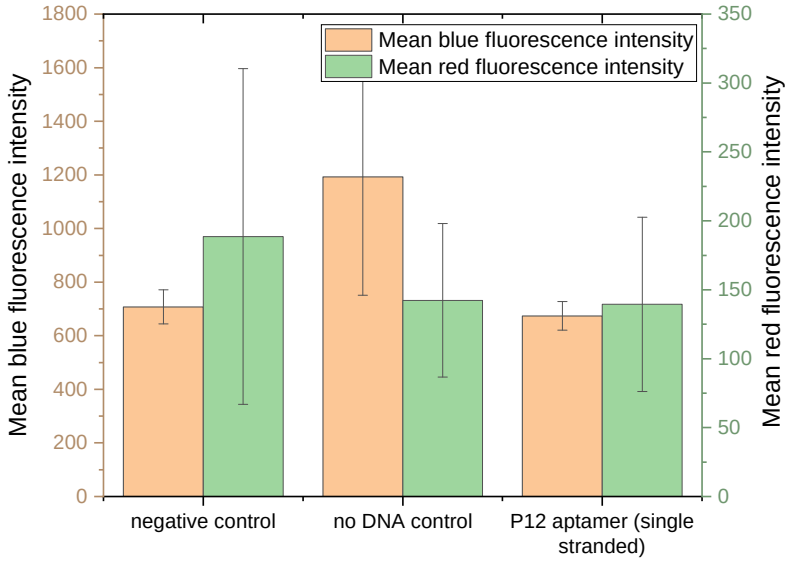

(a)

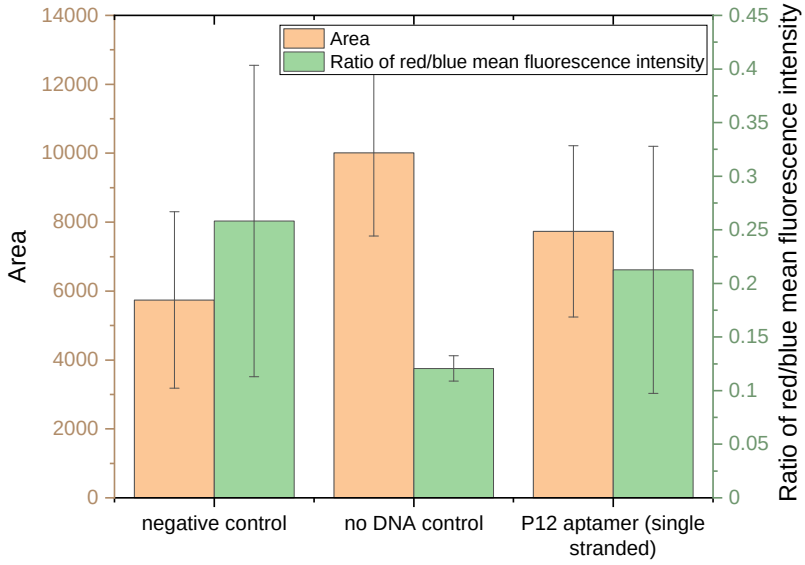

(b)

Figure 5.3.13: Comparison of the mean blue and red fluorescence intensity and their ratios within Ubx fibres functionalised with 2.4 µM of ssDNA with the P12-31 *E. coli* aptamer.

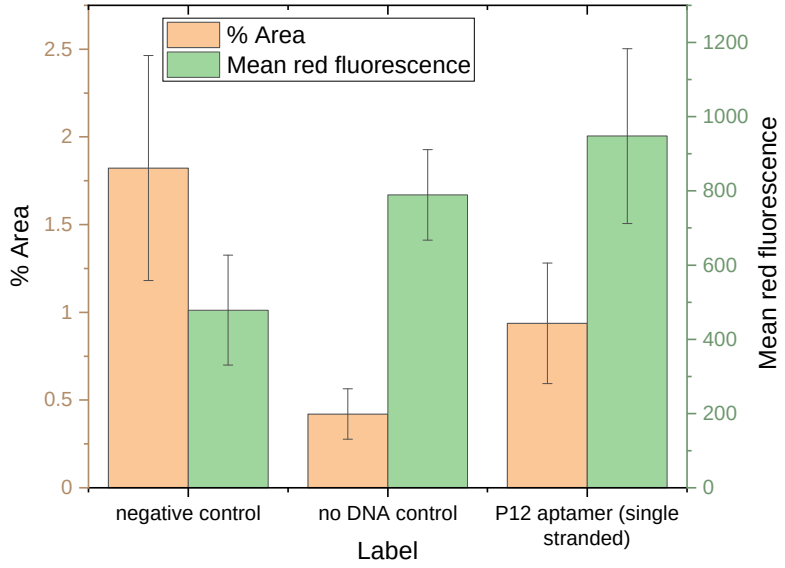

Figure 5.3.14: The statistics of fluorescence of cells bound to the pRep-Ubx fibres functionalised with 2.4 µM of ssDNA with the P12-31 *E. coli* aptamer.

factor of 5.33 compared to the negative control (P=0.0004), and 4.06 compared to the control without DNA (P=0.0001). These results put together indicated that the aptamer functionalised fibres increased the *E. coli* binding to Ubx fusion fibres despite the high rate of non-specific binding and background fluorescence.

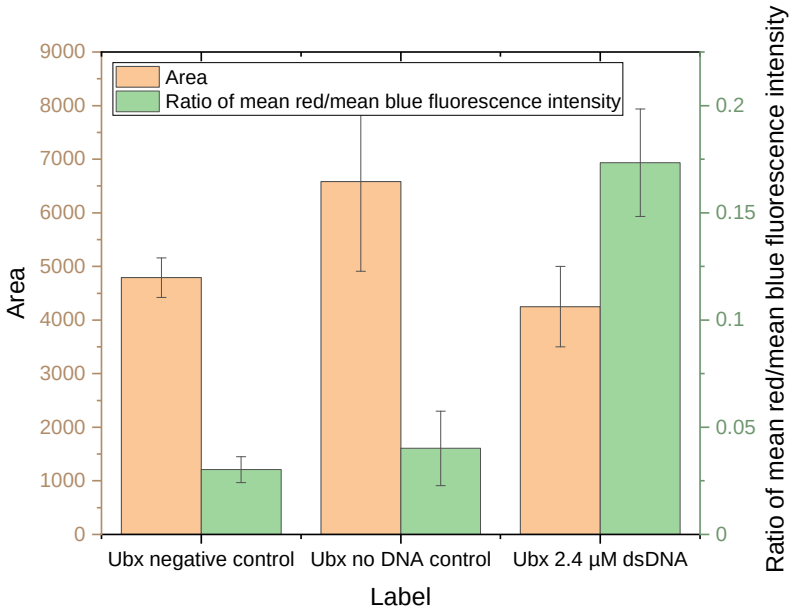

(a)

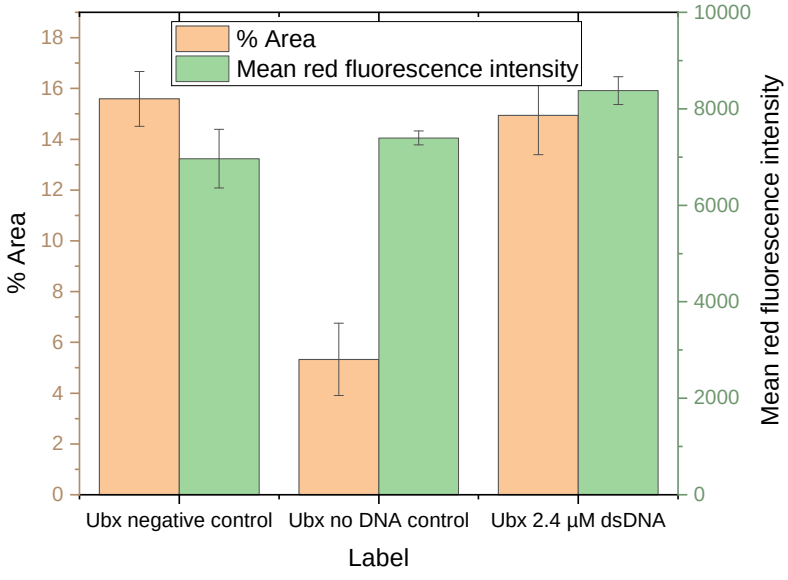

(b)

Figure 5.3.15: Comparison of: (a) the mean blue and red fluorescence intensity and their ratios, (b) the area of bound objects and their fluorescence intensity in the red channel, within Ubx fibres functionalised with 2.4 µM of dsDNA with the Antibac2 *E. coli* aptamer.

5.3.3 SARS-CoV-2 spike RBD protein binding to fibres

Experiment involving ssDNA and dsDNA oligonucleotide binding to Ubx-pRrep-PhiLov

In this experiment, either ssDNA or dsDNA aptamer constructs were bound to pRep-phiLOV-Ubx fibres. Then, the biotinylated SARS-CoV-2 spike RBD protein was captured from the solution by aptamers bound to the fibre. Finally, the streptavidin-Texas Red complex binding to biotin was used to investigate the extent of the aptamer-facilitated CoV protein binding to fibres. Importantly, fibre pre-selection was not used for this experiment, which is reflected in the varying diameter and fluorescence intensity in the blue and green channel, which corresponds to the dityrosine autofluorescence and PhiLov emission.

The control samples exhibited similar features to those presented in the previous experiment involving streptavidin-Texas Red binding (see figure 5.2.6). Sample images of a control fibre is shown in figure 5.3.16. The fibre's green fluorescence from PhiLov is solid throughout the fibre with the exception of a brighter striation towards the lower edge of the fibre. This feature is reflected in the red channel, which suggests that there is bleed-through of the PhiLov fluorescence into the red channel detector, which would explain the high background in the red channel image. Similar to figure 5.2.6, the brighter region is localised towards the centre of the fibre.

In contrast to the control fibre, a significant portion of the bright fluorescence regions in the aptamer samples (figures 5.3.17 and 5.3.18) was observed close to the edges of the fibres. Importantly, their brightness was not colocalized with an abnormally bright region in the green channel, which suggests the presence of a significant amount of Texas Red dye in the bright regions. This formed evidence for binding of streptavidin-Texas Red to those regions of the fibre, which in turn suggests that the SARS-CoV-2 spike protein was captured using both the ssDNA and dsDNA constructs containing the CoV2-RBD-4C aptamer.

When the mean fluorescence intensity of the fibres was considered, it was noted that the blue and green fluorescence intensity were correlated to the size of the fibre, which could have been due to the depth of field being larger than the diameter of the smaller fibres. Control fibres were significantly larger than the fibres to which aptamers were bound, which may account for some differences in the fluorescence intensity. The mean fluorescence intensities in different chan-

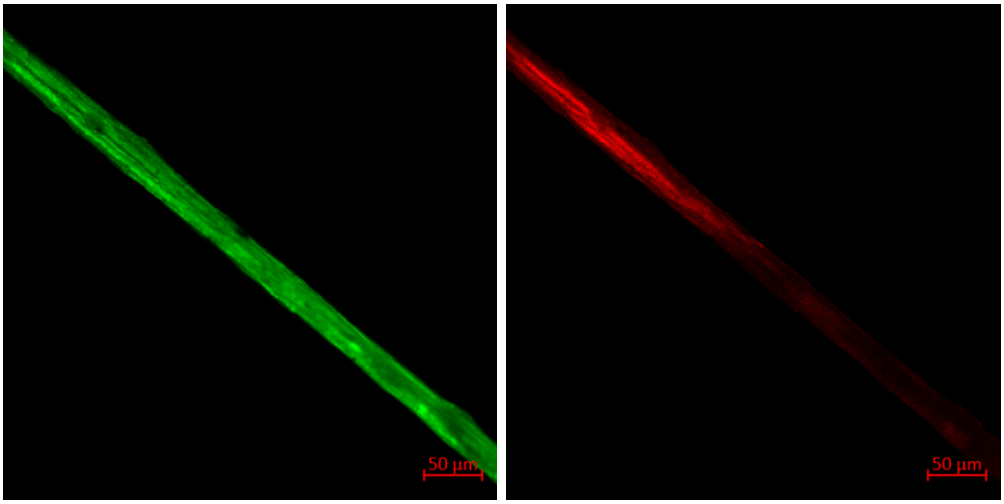

Figure 5.3.16: The sample images of the control pRep-phiLOV-Ubx fibre (no DNA) treated with the biotinylated SARS-CoV-2 spike protein and then the streptavidin-Texas Red complex.

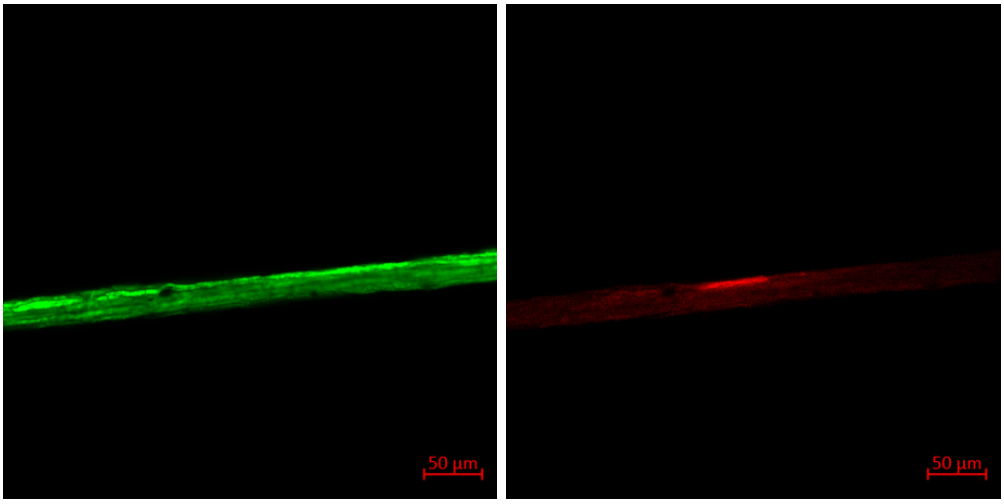

Figure 5.3.17: The sample images of the pRep-phiLOV-Ubx with attached ssDNA CoV2-RBD-4C aptamer treated with the biotinylated SARS-CoV-2 spike protein and then the streptavidin-Texas Red complex.

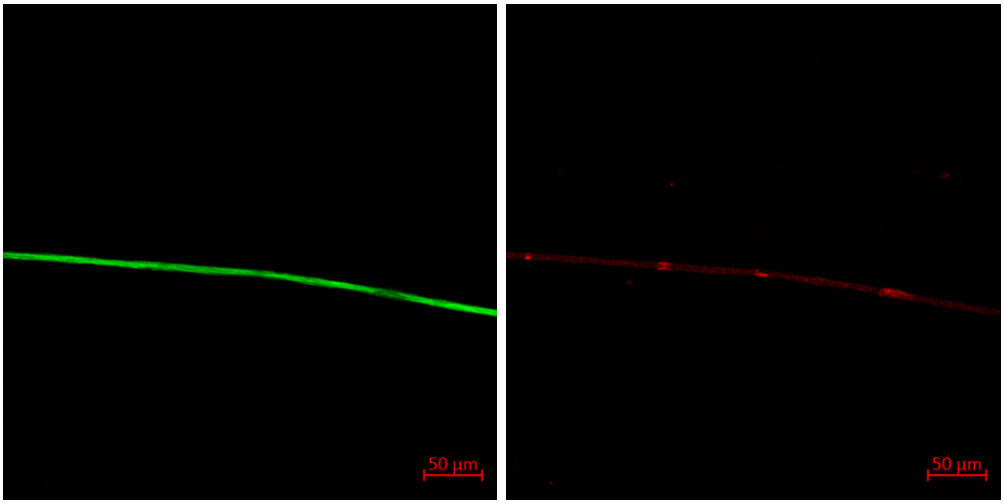

Figure 5.3.18: The sample images of the pRep-phiLOV-Ubx with attached dsDNA aptamer treated with the biotinylated SARS-CoV-2 spike protein and then the streptavidin-Texas Red complex.

nels were presented in figures 5.3.19a and 5.3.20a for the 20x objective and 63x objective images, respectively. Similarly, the mean fluorescence ratios between different channels were presented in figures 5.3.19b and 5.3.20b for the two objectives. These figures show that the ratio of mean red to mean green fluorescence is higher in the ssDNA oligonucleotide with the CoV2-RBD-4C aptamer compared to the control for both magnifications, whereas in the case of the dsDNA oligonucleotide with the CoV2-RBD-4C aptamer, the ratio is lower compared to control for the 20x magnification images, and only slightly higher for the 63x magnification images. This suggests that the SARS-CoV-2 spike RBD protein binding may be more prevalent in the ssDNA aptamer sample compared to the other samples. However, the background fluorescence due to the fluorescence bleed-through or non-specific binding is too high to draw conclusions from this data.

When the fluorescence intensity of the bright regions within the fibres is considered, as in the case of 20x magnification images (figure 5.3.21a), there is little difference in the percentage area within the fibre occupied by these regions, although the mean fluorescence intensity of these regions is the highest within control fibres. However, in the case of the 63x magnification images (figure 5.3.21b), the background in the red fluorescence images was much lower and, in this case, the mean fluorescence of the bright areas within the aptamer samples was higher compared to the control. The percentage area occupied by these regions was the highest for the fibres with the ssDNA CoV2-RBD-4C aptamer. This data again does not provide a conclusive answer to the question of whether capturing the

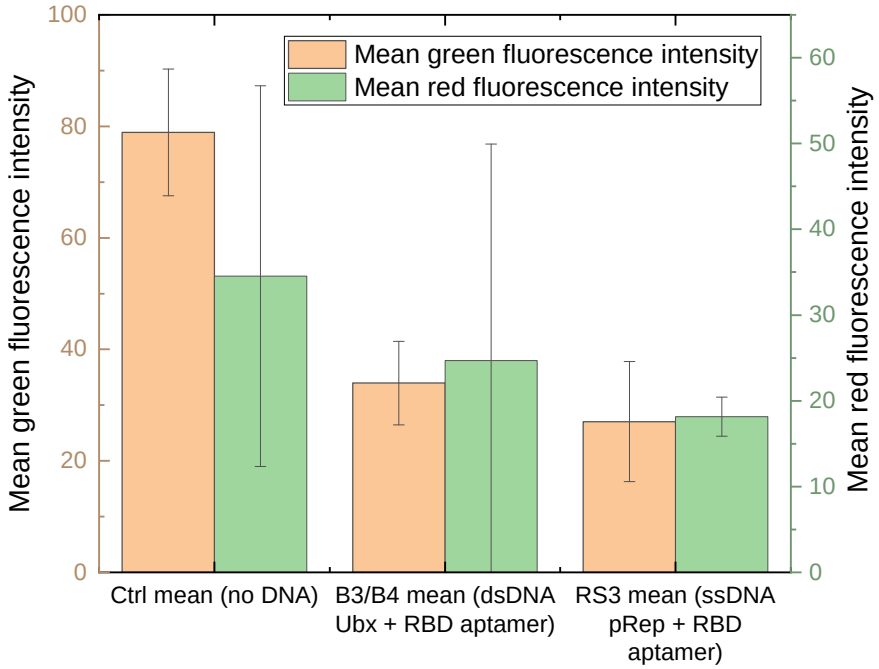

(a)

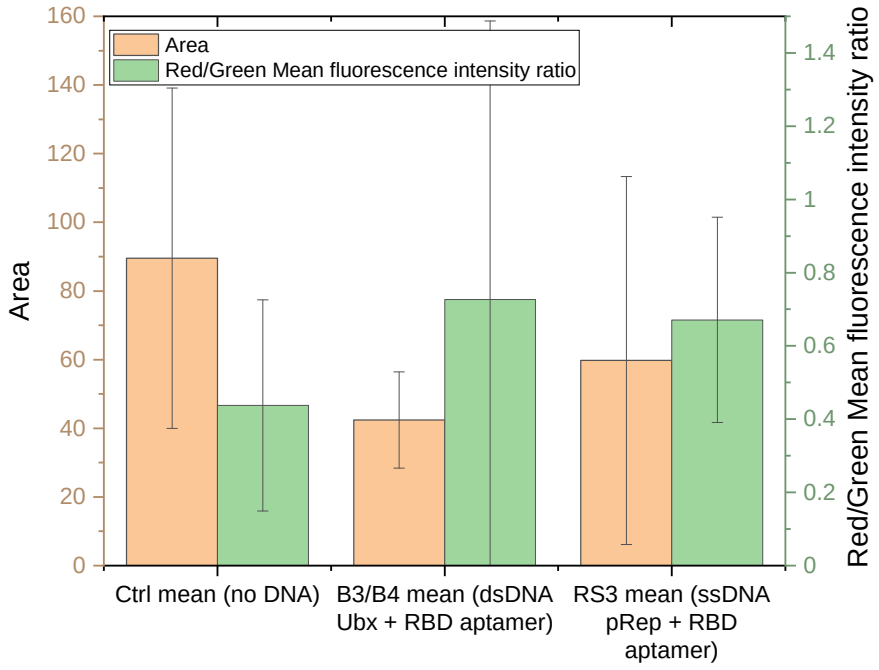

(b)

Figure 5.3.19: The fluorescence in different channels in the 20x objective images of fibres exposed to the SARS-CoV-2 spike protein.

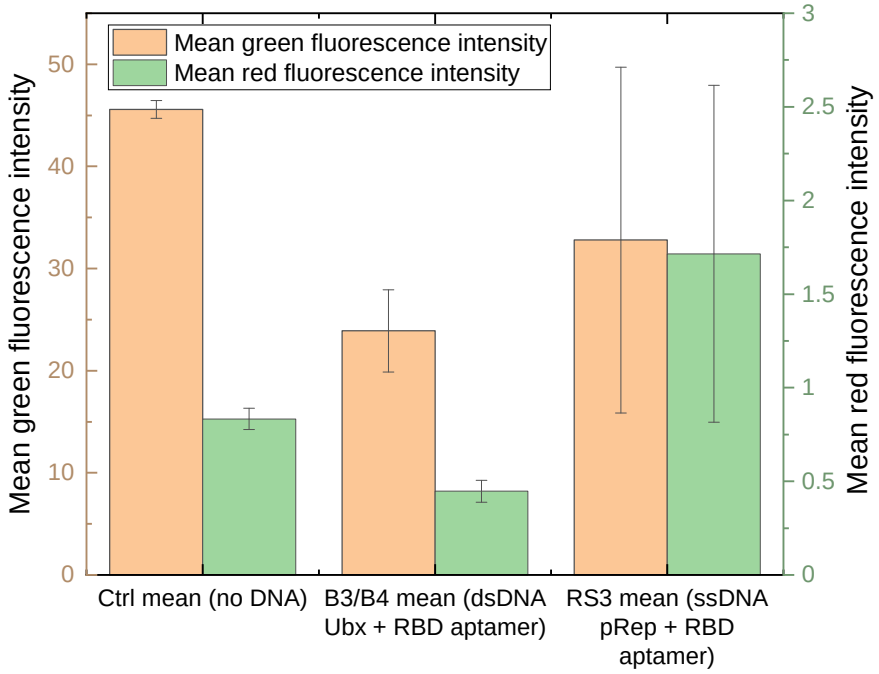

(a)

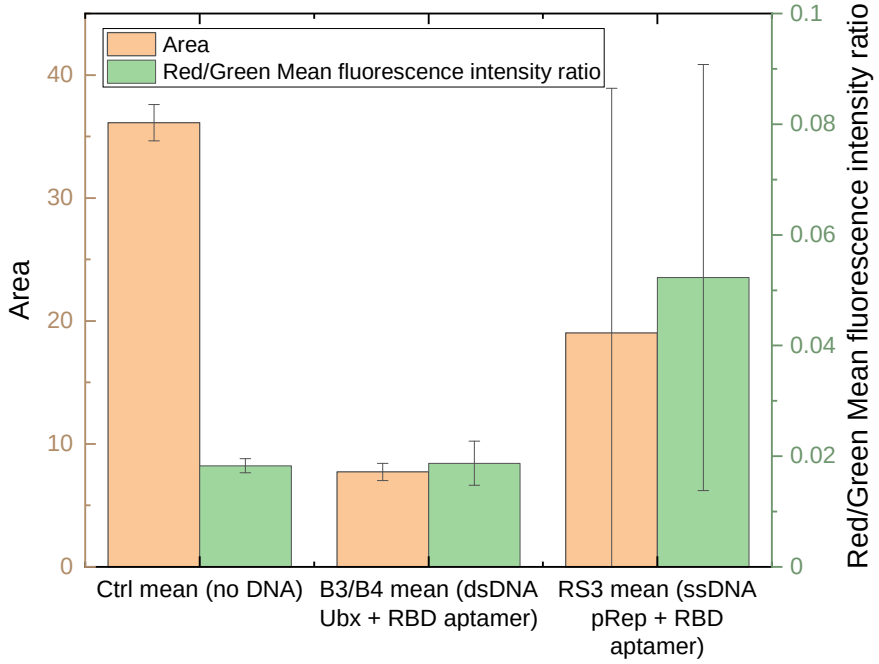

(b)

Figure 5.3.20: The fluorescence in different channels in the 63x objective images of fibres exposed to the SARS-CoV-2 spike protein.

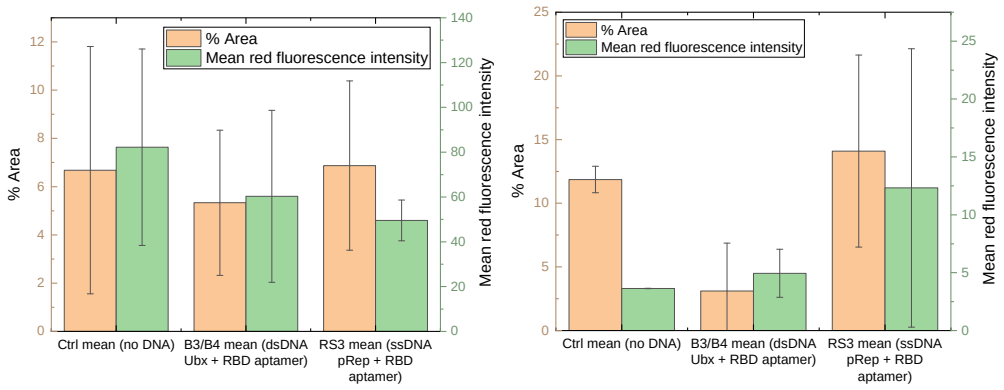

(a) (b)

Figure 5.3.21: The statistics related to fluorescence in bright regions within the fibre in the red channel (Texas Red) in the (a) 20x and (b) 63x objective images of fibres exposed to the SARS-CoV-2 spike protein.

SARS-CoV-2 spike RBD protein is possible using the aptamers used in the experiments. However, there are visual and numerical indications that functionalisation of fibres with these aptamers may increase the binding of the protein, particularly when the 63x magnification images with lower fluorescence background levels are considered. In the next experiments, limiting the background fluorescence in the red channel could be crucial to evidence the effect that the aptamers have on analyte binding.

Experiment involving ssDNA oligonucleotide binding to pRep-Ubx fibres and dsDNA binding to Ubx fibres

In this experiment, ssDNA or dsDNA oligonucleotides were bound to pRep-Ubx or Ubx fibres, respectively. We measured the capturing efficacy of biotinylated SARS-CoV-2 RBD protein in solution by aptamers bound to the fibre. Finally, the streptavidin-Texas Red complex binding to biotin was used to investigate the extent of the aptamer-facilitated CoV protein binding to fibres.

Several protocol changes were implemented compared to the experiment described in section 5.3.3. Plain Ubx fibres were used instead of EGFP-Ubx and pRep-Ubx without the PhiLov label to limit bleed-through to the red channel detector. Fibres were pre-selected to ensure comparable size and fluorescence background. The availability of preliminary fluorescence microscopy data enabled the measurement of fibre diameters and choosing fibres with similar intensity and size. This helped to use a large part of the dynamic range in the fluorescence measurements without sacrificing the consistency of imaging parameters between different

samples. Plain Ubx fibres (for dsDNA binding) and pRep-Ubx fibres (for ssDNA binding) were used instead of pRep-phiLOV-Ubx to limit bleed-through to the red channel detector caused by the PhiLov fluorescence emission.

The extent of binding of biotinylated SARS-CoV-2 RBD protein to pRep-Ubx fibres functionalised with the ssDNA oligonucleotide sequence was measured. Regular pRep-Ubx fibres were used as a negative control, and pRep-Ubx fibres unexposed to the ssDNA solution formed the control for binding using 2.4 µM ssDNA. The measurements of fluorescence intensity across the fibre are shown in figure 5.3.22. The mean blue fluorescence intensity was 5% lower (P=0.95) and the mean red fluorescence intensity was 3% lower (P=0.93) for the control fibres compared to those functionalised with oligonucleotides (figure 5.3.23). The ratio of the mean red to blue fluorescence intensity was 0.41 for the control and 0.38 for the ssDNA functionalised pRep-Ubx fibres (P=0.81). The differences were considered not statistically significant. The area of the fibres was not significantly different (P=0.16) even though it was 37% larger for the control fibres.

The percentage area and fluorescence intensity of the bright regions in the red fluorescence channel were compared in figure 5.3.23. The area of the bright red fluorescence regions within control fibres was 9% larger (P=0.81), and their mean fluorescence intensity was 7% lower (P=0.74) than in the functionalised fibres. These differences were not statistically significant and they indicated a large presence of non-specific binding of streptavidin-Texas Red to both fibre groups. The negative control exhibited a small background intensity, which was about 5% of the absolute signal for the samples treated with streptavidin-Texas Red.

Ubx fibres were functionalised with the dsDNA oligonucleotide with CoV-2 RBD-4C aptamer. The binding of biotinylated SARS-CoV-2 spike RBD protein to these fibres was assessed using the streptavidin-Texas Red probe that binds to biotin (figure 5.3.24). The background fluorescence intensity in the red channel for the negative control was low at about 5% of the values for the samples exposed to streptavidin-Texas Red. Both the mean blue and red fluorescence intensity were higher for the control fibres compared to those treated with dsDNA solution, by 17% (P=0.54) and 38% (P=0.36), respectively. The ratio of the red to blue mean fluorescence intensity was 28% higher (P=0.50) for the control fibres. These measurements did not indicate statistically significant differences between the two groups of fibres, suggesting that the use of the dsDNA oligonucleotides with the

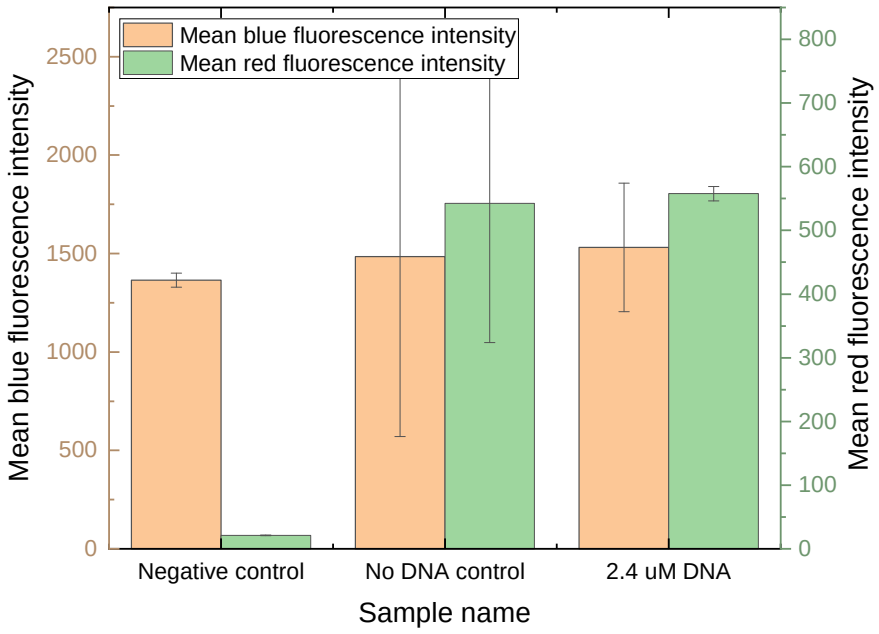

(a)

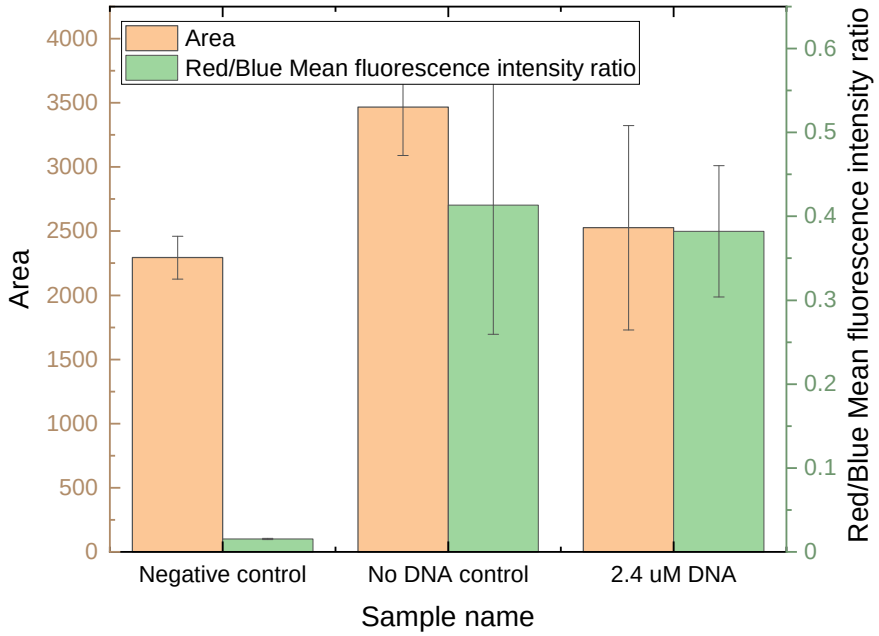

(b)

Figure 5.3.22: The statistics of fluorescence in images of pRep-Ubx fibres exposed to ssDNA oligonucleotides and the SARS-CoV-2 spike protein.

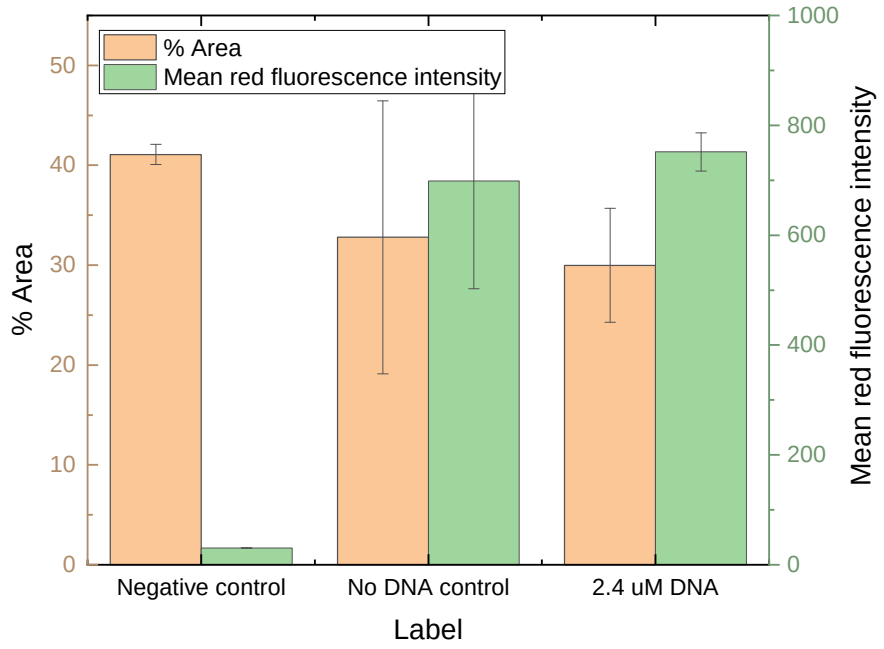

Figure 5.3.23: The statistics for regions of strong red channel fluorescence in images of pRep-Ubx fibres exposed to ssDNA oligonucleotides and the SARS-CoV-2 spike protein.

CoV2-RBD-4C aptamer did not increase the SARS-CoV-2 spike RBD protein binding capacity.

The binding of SARS-CoV-2 RBD protein and subsequently streptavidin-Texas Red to Ubx fibres was also assessed by measuring the fluorescence intensity in the bright regions in the red fluorescence channel determined by fluorescence thresholding (figure 5.3.25). These measurements confirmed previous observations that the binding of the RBD protein was not increased by using oligonucleotides. The area of the bright regions as a percentage of the fibre area was 57% larger (P=0.06) and the mean fluorescence intensity was 11% higher (P=0.78) for the control fibres. Moreover, the fluorescence intensity was very high for the samples treated with streptavidin-Texas Red, which suggests a high rate of non-specific binding of streptavidin-Texas Red to the fibres occurring despite the attempt to block it using a BSA blocking buffer. Therefore, this method did not show any stastistically significant differences in the SARS-CoV-2 RBD protein binding caused by the application of dsDNA oligonucleotides to Ubx fibres.

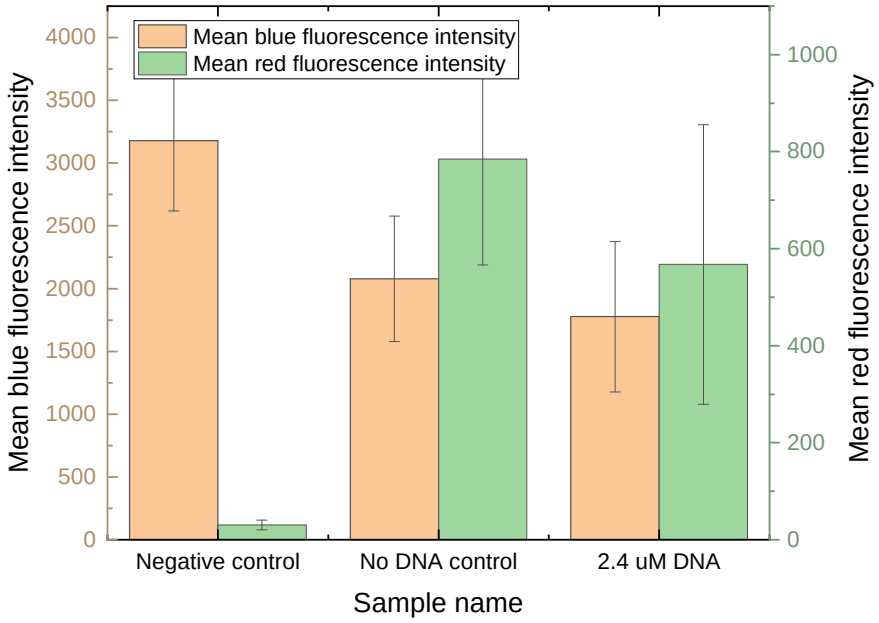

(a)

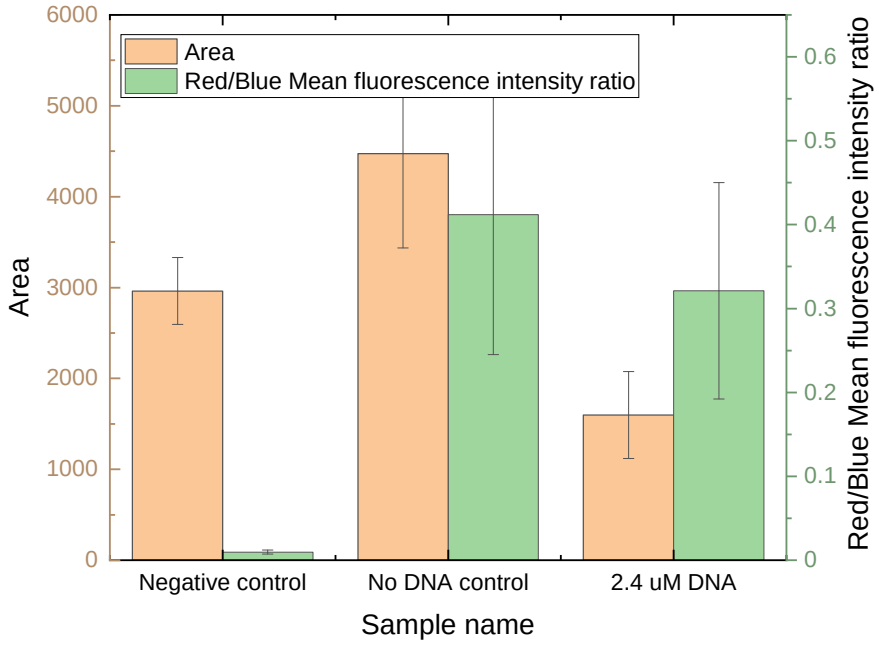

(b)

Figure 5.3.24: The statistics of fluorescence in images of Ubx fibres exposed to dsDNA oligonucleotides and the SARS-CoV-2 spike protein.

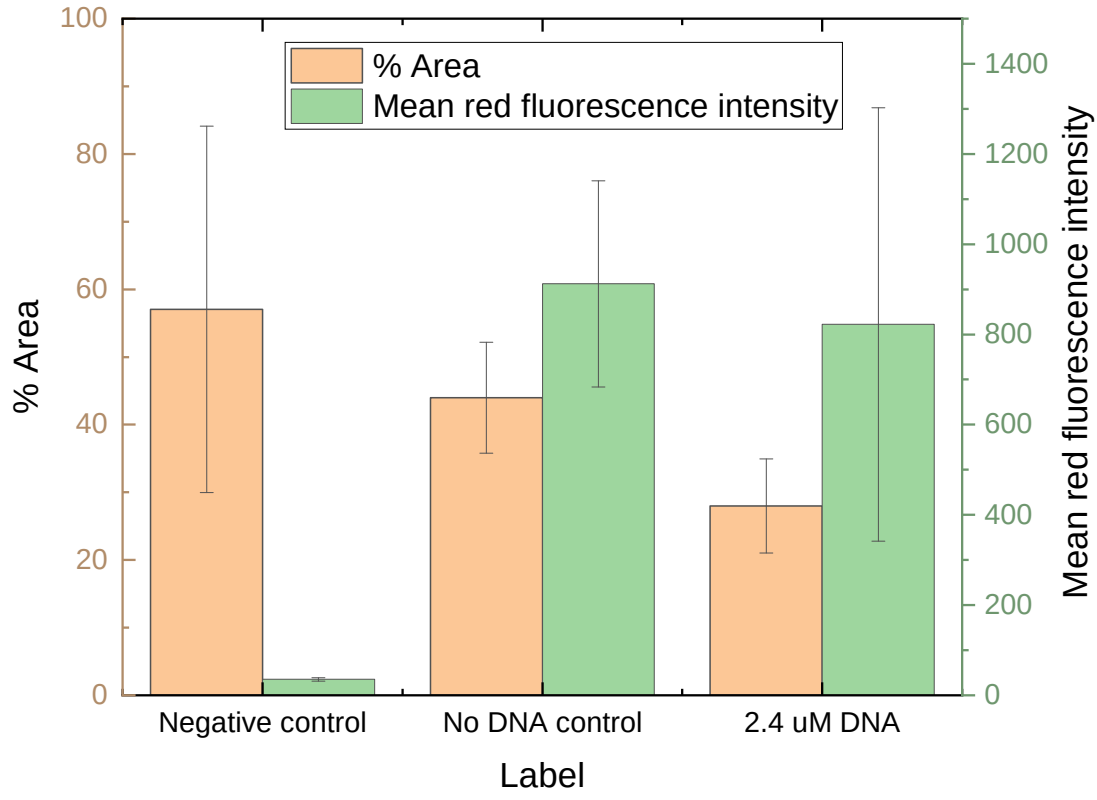

Figure 5.3.25: The statistics for regions of strong red channel fluorescence in images of Ubx fibres exposed to dsDNA oligonucleotides and the SARS-CoV-2 spike protein.

5.4 Summary

Aptamers were identified as a useful tool to enable diagnostic and therapeutic applications by highly specific, high affinity binding to targets [18,19]. The binding is followed by an emission of fluorescence or an alteration of the physical properties of the aptamer-target system such as that in impedimetric sensors [104]. Aptamers present functional improvements compared to antibodies. These include a lower production cost, low batch-to-batch variation, ability of functionalisation with reporter (fluorescent) molecules, and high affinity and specificity of binding [18]. All these features indicate a wealth of potential medical applications of aptamers, and the applicability of aptamers has been proven when pegaptanib was approved as a therapeutic agent against age-related macular degeneration [118].

Ubx is a protein material with several desirable properties in biosensing and tissue engineering. It readily forms bio- and cytocompatible materials with good elasticity and considerable electrical conductivity [2, 17, 38, 40]. Moreover, it can be functionalised with fluorescent proteins, growth factors, and other functional proteins [16, 17, 26]. The research into electrical and optical properties of Ubx fusion fibres presented in this thesis also indicated possible avenues for applications of Ubx as an impedimetric or fluorescence-based sensor, with its eletrical conductivity and fluorescence lifetime and spectra changing with different protein fusions and environmental conditions. The stability of the protein and its versatility allowed its application in experiments involving functionalisation with oligonucleotides for sensing of biological targets such as bacteria and viruses. This chapter outlined the details of oligonucleotide binding and detection of binding of *E. coli* and novel SARS-CoV-2 RBD protein to aptamer-functionalised Ubx fibres. The detection was enabled by using fluorescent labels in both the targets, and on the oligonucleotides. A quantitative method for the detection of fluorescence changes in fibres treated with oligonucleotides was developed and used to measure DNA and target binding.

5.4.1 Oligonucleotide binding to Ubx in solution and in fibres

Single- and double-stranded DNA (ssDNA and dsDNA) constructs were designed, which contained either a pRep or Ubx homeodomain binding sequence. Short oligonucleotides were used as initial proof of concept for binding to Ubx in solution and in fibres. Subsequently, longer structures were tested, which additionally

contained *E. coli* or SARS-CoV RBD protein aptamers.

The ssDNA constructs showed binding to pRep-Ubx in solution after 30 min of incubation, which was evidenced by the gel band shift in a SDS-PAGE gel, where the higher molecular weight band appeared above the pRep-Ubx band (see figure 5.3.1). The binding of the pRep aptamer to pRep-Ubx was later used to make fibres containing the pRep binding sequence and the P12-31 *E. coli* aptamer, which combined the two functions of the oligonucleotide.

The binding of dsDNA oligonucleotides with a Ubx aptamer and a Texas Red fluorescent label was shown to significantly increase both the fluorescence intensity in the red channel (by 130%, P=0.0018), and the ratio of red to blue fluorescence intensity (by 77%, P=0.0012), compared to a fluorescently labelled oligonucleotide without the Ubx binding sequence. This result, shown in figure 5.3.2, indicated that mixing both ssDNA and dsDNA with the protein in solution was a viable method of producing oligonucleotide-functionalised Ubx fusion fibres.

Ubx fusions can also be functionalised with oligonucleotides by immersing the protein fibres in a ssDNA (figure 5.3.3) or dsDNA solution (figure 5.3.4). Binding of the ssDNA oligonucleotide containing the pRep binding sequence was evidenced by the increase in Texas Red fluorescence, which resulted from the binding of streptavidin-Texas Red complex to the biotinylated oligonucleotide. Both the area of bright objects and their fluorescence intensity in the red channel increased by 30% and 134%, respectively, for the ssDNA aptamer compared to the control without DNA functionalisation.

The oligonucleotide binding protocol was optimised by testing the effect of DNA concentration and blocking buffers on fluorescence intensity of fibres following functionalisation. 2.4 µM was selected as an optimal DNA concentration, which significantly increased the fluorescence intensity corresponding to the binding probe, streptavidin-Texas Red. The blocking buffer containing 0.1% TWEEN 20 and 2% BSA was chosen as it significantly limited the background fluorescence intensity corresponding to non-specific binding.

The binding of dsDNA oligonucleotides containing *E. coli* aptamers was significantly increased for the sequences containing the P12-31 and STC-12 aptamers, which resulted in an increase of the area and intensity of bright fluorescence regions in the red channel in fibres functionalisaed with these aptamers (see figure 5.3.5).

This work showed that the DNA functionalisation of Ubx in solution and in materials is possible, as evidenced by a significant increase in the fluorescence of the functionalised fibres and a gel band shift in an SDS-PAGE gel. Therefore, analyte binding and detection could be attempted using longer oligonucleotides containing aptamers.

5.4.2 *E. coli* binding to Ubx fusion fibres functionalised with DNA aptamers

The experiments involving *E. coli* binding to oligonucleotide functionalised fibres indicated that the Antibac2 aptamer in both the ssDNA and dsDNA constructs was the most effective in enhancing the specific *E. coli* binding. Figures 5.3.9, 5.3.10, and 5.3.15 show that the differences between the *E. coli* binding efficiency of the aptamer samples and controls were statistically significant, and several other experiments indicated an increase in either the area of bound cells, or their fluorescence intensity, for the STC-12 and P12-31 aptamers. Therefore, increasing the specific bacteria capture using the aptamer functionalised Ubx fusion fibres was demonstrated as a technique that can be optimised to create biosensors or diagnostic devices based on Ubx materials.

5.4.3 SARS-CoV-2 RBD protein binding to Ubx fusion fibres functionalised with DNA aptamers

Ubx fusion fibres were functionalised using ssDNA and dsDNA oligonucleotides with both the Ubx and the CoV-RBD-4C aptamer. The binding of the biotinylated SARS-CoV-2 RBD protein was tested by incubation of the protein solution with fibres and the following binding of the streptavidin-Texas Red conjugate, which exhibits a high affinity to biotin. The initial experiment showed the percentage of the area of the fibre covered by streptavidin-Texas Red was higher than for the control (see figure 5.3.20), which could indicate an increase in the target binding to aptamer-functionalised samples. Although these results were not statistically significant, the ssDNA approach showed an increase in the fluorescence intensity compared to the dsDNA samples, which could indicate increased SARS-CoV-2 RBD protein binding to Ubx fibres functionalised with the aptamers.

Following the optimisation of DNA concentration and blocking of non-specific binding, the findings of the experiments did not confirm the hypothesis that the

application of a dsDNA oligonucleotide could be used to enhance the SARS-CoV-2 RBD protein binding detection. The use of an optimised DNA construct or a more direct binding probe is suggested to improve the detection of the bound protein. Perhaps the method described here could be enhanced by further increasing the oligonucleotide and SARS-CoV-2 RBD protein concentration. Because of the cost of materials, testing this idea was outside of the scope of this project.

5.4.4 Future work

Based on the experiments described in this thesis, potential improvements to analyte capture and possible applications of aptamer functionalised Ubx materials were identified. Larger surface area materials (coatings and mats) could be used to increase the area available for interactions between protein, oligonucleotides and target analytes. Increasing DNA concentration and the concentration of *E. coli* and the SARS-CoV-2 RBD protein is another change that could make the detection of the targets easier. Increasing the signal-to-noise or the ratio of the signal from the fluorescent reporter proteins compared to background ratio could significantly improve the detection of bacteria or virus binding to the Ubx fibres. The issues encountered in this study indicate that the analyte concentration of 2.4 µM is currently close to the detection limit for this system because of the large scatter in the data, significant fluorescence background, and high non-specific binding. Labelling the SARS-CoV-2 RBD protein with a different reporter than biotin could improve detection capabilities and the signal-to-noise ratio. It could also remove a step in the sensing pipeline if it did not require binding of streptavidin-Texas Red to the biotinylated SARS-CoV-2 RBD protein, which could improve the sensitivity of this system.

To promote applications of Ubx materials as biosensors, physical properties of Ubx materials following target binding for potential sensing applications could be tested. Changes in the material impedance, fluorescence spectra of fibres or their fluorescence lifetime could indicate analyte binding, which could be employed in biosensing of bacteria or viruses in solution. To confirm target binding, cross-examination of protein binding to aptamers could be conducted using methods such as qPCR or ELISA. Incorporating aptamer functionalised Ubx in platform materials based on Ubx or other structural biomaterials, such as collagen or alginate, could be used to create multifunctional devices for tissue engineering and biosensing. These materials could be further functionalised to have antimicro-

bial properties or to promote cell proliferation using growth factors, which could further increase their applicability.

Ubx fusion fibres were functionalised using ssDNA and dsDNA oligonucleotides with the CoV-RBD-4C aptamer. The binding of biotinylated SARS-CoV-2 RBD protein was tested by incubation of the protein solution with fibres and the following binding of the streptavidin-Texas Red conjugate, which exhibits a high affinity to biotin. The initial experiment showed an increase in the ratio of the mean red to green fluorescence intensity for the pRep-phiLOV-Ubx fibres functionalised with the ssDNA aptamer compared to a sample without the aptamer. Additionally, when a high magnification objective was used for imaging, the percentage of the area of the fibre covered by streptavidin-Texas Red was higher than for the control. These results were not statistically significant. However, the ssDNA approach showed an increase in the fluorescence intensity compared to the dsDNA samples. Following the optimisation of DNA concentration and blocking of non-specific binding, functionalisation with ssDNA oligonucleotides did not show an increase in streptavidin-Texas Red binding to fibres. Application of the dsDNA construct did not improve the binding of SARS-CoV-2 RBD protein. The differences in the fluorescence intensity in the red channel and the area and intensity of the fluorescent probes between the aptamer samples and controls were not statistically significant. Therefore, these findings did not confirm the hypothesis that the application of a dsDNA oligonucleotide could be used to enhance the SARS-CoV-2 RBD protein binding detection. To summarise, the results of one experiment showed that the ssDNA oligonucleotide appeared to improve the RBD protein binding to pRep-phiLOV-Ubx fibres. However, this result was not confirmed in the second experiment following the optimisation of oligonucleotide concentration and the blocking buffer. The dsDNA oligonucleotides containing the CoV-RBD-4C aptamer did not increase the binding of the streptavidin-Texas Red molecule to the fibres following immersion in the SARS-CoV-2 RBD protein, compared to the control. There is some indication that the aptamer could be increasing the protein binding to fibres but the use of an optimised DNA construct or a more direct binding probe is suggested to improve the detection of the bound protein. Perhaps the method described here could be enhanced by further increasing the oligonucleotide and SARS-CoV-2 RBD protein concentration. The cost of the materials did not allow testing of these ideas within the scope of this project.

Chapter 6

Composite materials for tissue engineering

6.1 Introduction

Biomedical applications often require a mix of functions, which may not be achievable using just a single biopolymer. Using composite materials for purposes of delivering multiple functions could effectively mitigate structural or property mismatch issues encountered when designing devices. The use of composite materials can enhance the applicability and efficiency of the developed structures. Electrospinning materials and creating hydrogels both offer increased material porosity, which can therefore create additional surface area to aid binding of cells and other functional molecules. Advances in soft tissue engineering [4, 98], osteogenesis and bone tissue engineering [97, 127] and cardiac tissue engineering [8, 14, 27, 87] were achieved using both composite and nanofunctionalised materials. Therefore, the ability to produce composite materials and use them for drug delivery, sensing or tissue engineering gives ample possibilities to address biocompatibility, mechanical property mismatch, and biodegradability issues. It also offers better control over mechanical properties of materials, while enabling the production of gradient materials that can further stimulate tissue growth in a structured manner [7, 128, 129].

Several systems involving composites of polymers and protein materials, or solely protein materials, have been developed to aid tissue growth or create implantable tissue scaffolds. Selected examples include stimulating osteogenesis *in vitro* using

a composite material made of an organic semiconductor polyaniline and collagen type I [127], tissue engineered myocardial implants [87], or collagen-based wound healing patches [4]. Some of these applications require a specific matching of material properties. In particular, myocardial tissue engineering requires conductive implantable materials that can both conduct electrical impulses and facilitate the cardiac cycle, while remaining biocompatible [8, 14, 27, 87]. One scaffold investigated for cardiac tissue engineering was made with 1% sodium alginate mixed with Au nanowires [27]. Alginate scaffolds presented favourable porosity and biocompatibility. Functionalising alginate scaffolds with Au nanowires increased their electrical conductivity sufficiently to stimulate the growth of thicker tissues and synchronous contraction of cells grown on the matrix under electrical stimulation [27]. Alginate was used to produce materials used in wound healing, drug delivery, and bone and cartilage replacement and regeneration [130, 131]. Examples of these designs include a silk fibroin-alginate scaffold for soft tissue engineering [132] and a nanocellulose-alginate bioink for 3D bioprinting of a biocompatible scaffold with potential applications in nasal cartilage bioprinting [133]. Incorporating Ubx into alginate bioprinting ink was attempted in this project to exhibit the potential of including Ubx fusions in porous tissue scaffolds.

Collagen has different mechanical properties than alginate. Because alginate does not form elastic scaffolds, it is particularly suitable for bioprinting designs [133]. Collagen forms strong materials with considerable elasticity. These properties were used to design devices for wound healing and tissue regeneration [3, 9, 10]. Selected composite materials for tissue engineering containing type I collagen, elastin and silks are discussed in section 4.1. A particular emphasis was placed on the tunability of the mechanical properties and porosity of these materials, both of which are important for cell proliferation and the structural stability of the scaffold [3,10]. Type I collagen is an important material in tissue engineering because of its low immunogenicity, good biocompatibility and biodegradability with human collagenases, and its natural ability to bind to cells using the protein RGD sequence [5,6]. Structures as varied as porous sponges and cast mats were developed for bone and cartilage tissue engineering [11,12] and wound healing [4]. The multitude of features desirable in medical applications could be complemented by modifications such as cross-linking [3, 6, 9, 13] or the addition of functional and structural proteins and fibres [3, 9, 10]. These changes enhanced the mechanical properties of collagen scaffolds to better mimic those of the native tissue [3, 9, 10]. In this chapter, the optical and structural properties of EGFP-Ubx functionalised

cast collagen sheets and collagen decorated EGFP-Ubx fibres were examined to show the feasibility of creating Ubx-collagen composite materials.

Protein materials are used to address other challenges in the medical community. Antibiotic resistance has been recognised as a threat to global health. Research into alternative ways to combat bacterial infections is crucial to address this issue. Protein materials can be functionalised with antimicrobial peptides (AMPs) to achieve antimicrobial properties to prevent infections or bacteria spread. For example, AMPs can be fused recombinantly with a 4RepCT silk construct [15]. AMPs are positively charged and amphiphilic. Because of this, they can disrupt cell integrity since they are prone to interacting with and incorporating into cell membranes. While most AMPs have broad antimicrobial activity, some have immune modulating properties [134, 135], and others act on cancer cells [135, 136]. To test coatings of silk fused with an AMP Mag, a live-dead staining assay was used and area coverage of bacteria was calculated based on the fluorescence micrographs of samples (the ratio of green pixels attributed to live bacteria to the total number of pixels) [15]. Both 4RepCT and 4RepCT fused with antimicrobial peptide Mag showed reduced bacteria viability on the coating, compared to uncoated surface. Short peptide glycine-aspartic acid (RGD) or a small loop simulating RGD was recombinantly added to 4RepCT, which promoted the mammalian cell binding, but did not allow bacteria binding. Combining the antimicrobial peptides or enzymes with the cell-binding motif created dual-functional surfaces, which improved the chances of successful implantation [15]. Silk materials provided a platform for cell proliferation, which is an important feature for tissue regeneration platforms. Human dermal fibroblasts and human dermal microvascular endothelial cells showed an increased activity on silk coatings, compared to uncoated surfaces. Specifically the FN-silk stimulated cell adsorption by allowing integrin receptors on the cell surfaces to bind to the RGD-motif from fibronectin [15]. The production of protein fusions composed of engineered proteins such as 4RepCT and Ubx or collagen could provide a versatile platform for tissue engineering implants with antimicrobial, biosensing and tissue regeneration capabilities.

Other protein fusions with molecules such as the vascular endothelial growth factor (VEGF) can be produced to aid cellular growth and tissue reconstruction. For example, the protein fusion of Ubx with VEGF (VEGF-Ubx) was demonstrated to enhance angiogenic activity both *in vitro* and *in vivo* [16]. Multiple protein fusions such as VEGF-Ubx-EGFP were reported to further increase the yield and

solubility of the protein fusions compared to single fusions, and amongst other functions, facilitate fluorescence reporting for cellular activity and monitoring of cell and other biological environment conditions [17]. Opportunities for creating platform materials for biosensing and tissue growth and regeneration arise thanks to the structural and physical properties, functionalisability, and bio- and cytocompatibility of protein materials like Ubx [2, 40].

This chapter will detail preliminary experiments that aimed to produce composite materials consisting of EGFP-Ubx and collagen or EGFP-Ubx and sodium alginate. Techniques such as collagen casting, EGFP-Ubx self-assembly, and alginate-based ink bioprinting were used to produce composite structures. The optical and structural properties of the materials were measured and the differences between pristine and composite materials are highlighted. To conclude, directions for future work on Ubx composite materials and Ubx functionalisation was suggested, which could result in developing applications in tissue engineering and biosensing.

6.2 Composite collagen-Ubx materials

6.2.1 Methods

Imaging and photoluminescence spectra

Spectrophotometer readings of absorption and emission at specified wavelengths and wider spectra were taken for the Ubx and collagen solutions. Photoluminescence spectra for fibres and sheets were taken using the procedure described in section 2.3.1. The dilutions of EGFP-Ubx and type I collagen in G0 buffer in ratios 1:5, 1:10, and 1:20 were prepared as well as the solutions of 4 µM human recombinant triple helix collagen in PBS buffer and bovine triple helix collagen in 0.5 M acetic acid. The excitation spectra for these samples were taken with 440 nm emission wavelength. The emission spectra were measured with excitation at wavelengths 320 nm and 360 nm, which corresponded to the excitation peaks of EGFP-Ubx and type I collagen, and triple helix collagen, respectively. All collagen samples were kindly provided by ProColl Ltd., Swansea, UK.

Figure 6.2.1: The type I collagen and EGFP-Ubx solutions, and their mixture, cast in the wells of a 96 well plate. The samples were cast in triplicates.

Casting type I collagen with EGFP-Ubx in a 96-well plate

Solutions of type I collagen, EGFP-Ubx, and their mixture at a ratio of 1:1 were incubated in a 96-well dish. These three assays were prepared in triplicates in the wells of a 96-well plate (figure 6.2.1). The first assay consisted of 200 µL of 1.83 µM type I collagen (kindly provided by ProColl Ltd., Swansea, UK) dissolved in deionised water. The second assay was 200 µL of EGFP-Ubx at concentration 4.17 µM dissolved in G0 buffer. The third assay was the mixture of 100 µL each of the collagen and EGFP-Ubx. The solutions were incubated in a biological safety cabinet for 48 h.

Deposition of collagen onto the self-assembled Ubx film

This experiment investigated the possibility of creating an EGFP-Ubx-collagen composite material by depositing collagen dropwise onto the self-assembled EGFP-Ubx film. This method was inspired by a similar experimental design, in which quantum dots were deposited ont a formed Ubx film to form Ubx-quantum dot fibres, which exhibited altered optical properties after functionalisation and the optical activity of both the EGFP-Ubx protein fusion and the quantum dots [100]. The deposition of quantum dots onto the protein film did not affect self-assembly.

To test material formation capability of polymeric EGFP-Ubx with a collagen

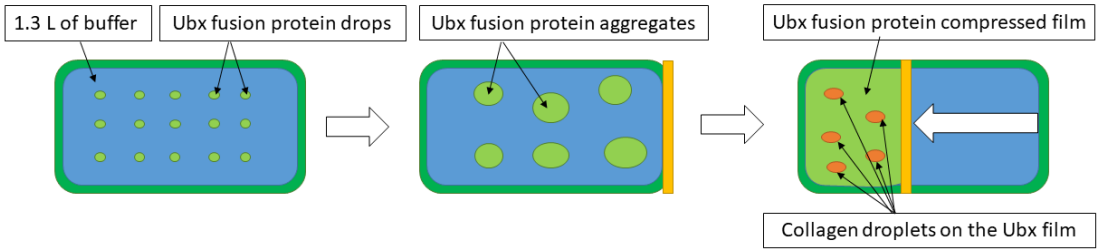

Figure 6.2.2: To create EGFP-Ubx-collagen composite fibres, the EGFP-Ubx film was formed by self-assembly. The protein film was gathered together and the collagen solution was deposited onto the film dropwise. The fibres were pulled from the surface film 4 h later.

solution deposited onto the EGFP-Ubx film, a trough with G0 buffer was prepared and a film formed as previously described in section 2.2. 2 mL of 19.94 µM EGFP-Ubx was added into the G0 buffer. Following protein aggregation, the surface film was gathered together, and a collagen solution was deposited dropwise onto the surface film. A diagram of this process is shown in figure 6.2.2. Resulting fibres were pulled 4 h after collagen deposition. This procedure was tested with two types of collagen were tested. In separate experiments, 1 mL of either 1.83 µM type I colagen in deionised water or 5.5 µM bovine triple helix collagen in 0.5 M acetic acid was deposited onto the film. The protective properties of Ubx materials against denaturing conditions [17, 100] were tested in this experiment because of the addition of acetic acid onto the surface film. The measurements of the photoluminescence spectra of the self-assembled fibres produced using this method were used to assess whether both EGFP-Ubx and collagen were present in the composite materials.

Cast bovine triple helix collagen sheets with EGFP-Ubx fibres

This experiment investigated the possibility of incorporating EGFP-Ubx fibres into the collagen cast sheet. However, due to the triple helix collagen being dissolved in acetic acid, the protective properties of Ubx structures against the denaturing conditions were required [17, 100]. Similarly to the experiment with Ubx self-assembly, this structural protection of appended proteins was be tested by the measurements of the photoluminescence spectra. The spectra provided indication whether the EGFP-Ubx fibres could retain their fluorescence, which would mean that they retained their structural stability.

Casting of bovine triple helix collagen dissolved in acetic acid was performed by

pouring a 10 mL solution of collagen into a Petri dish and covering the Petri dish with a lid. Then, the Petri dish was placed in a biological safety cabinet to prevent contamination and aid solvent evaporation. When EGFP-Ubx fusion fibres were incorporated in the casting solution, they were removed from their storage platform and placed directly in the solution before casting.

6.2.2 Results and discussion

Fluorescence excitation and emission spectra of EGFP-Ubx and collagen solutions

The fluorescence excitation and emission spectra of EGFP-Ubx and collagen solutions were measured using the spectrophotometer. In the excitation scan with 440 nm emission (figure 6.2.3), EGFP-Ubx had a strong excitation peak at 315 nm. type I collagen excitation spectrum was similar with a strong excitation peak at 315 nm, and an additional small peak at 360 nm. The triple helix collagen samples both had an excitation peak at approximately 360 nm.

The emission spectra at 320 nm (figure 6.2.4) showed a strong fluorescence peak at 380 nm for both EGFP-Ubx and the human recombinant triple helix collagen samples. In the case of EGFP-Ubx, an EGFP emission peak at approximately 512 nm was also measured. The bovine triple helix collagen sample had an emission peak at 415 nm (also visible in the recombinant sample), and both triple helix collagen solutions exhibited a smaller emission peak at 470 nm. The type I collagen solutions showed the same emission peak at 368 nm, which was blue-shifted compared to EGFP-Ubx and the other triple helix collagen samples.

When excited at 360 nm (figure 6.2.5), EGFP-Ubx solutions had a strong EGFP peak at 512 nm. The type I collagen samples had an emission peak at 412 nm and a smaller one at approximately 460 nm, which matched the emission peak of the triple helix collagen samples.

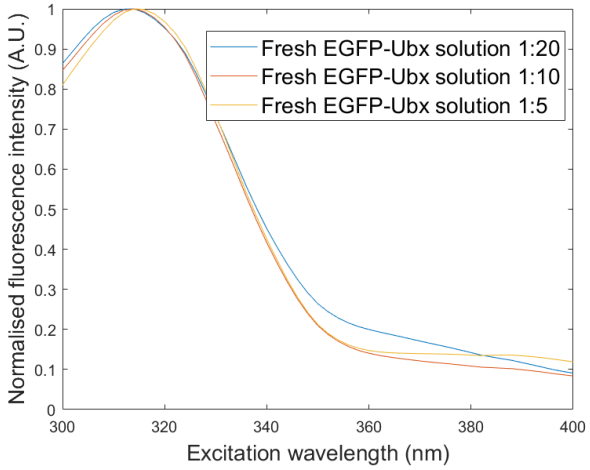

(a)

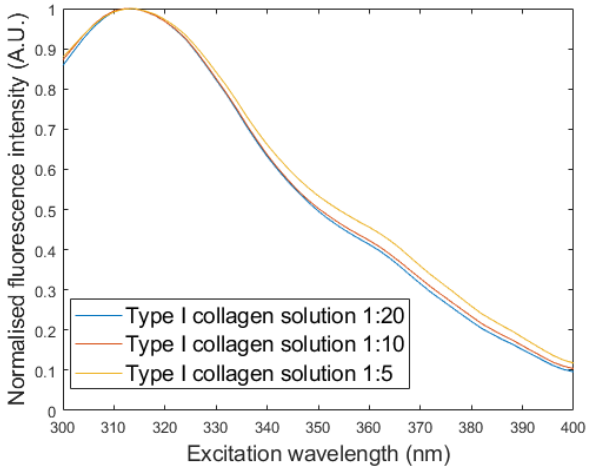

(b)

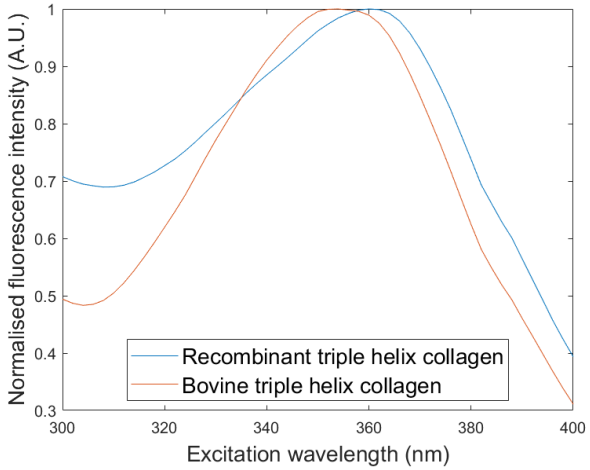

(c)

Figure 6.2.3: The excitation scan for solutions of (a) EGFP-Ubx, (b) type I collagen, and (c) bovine and human recombinant triple helix collagen solutions with 440 nm emission wavelength.

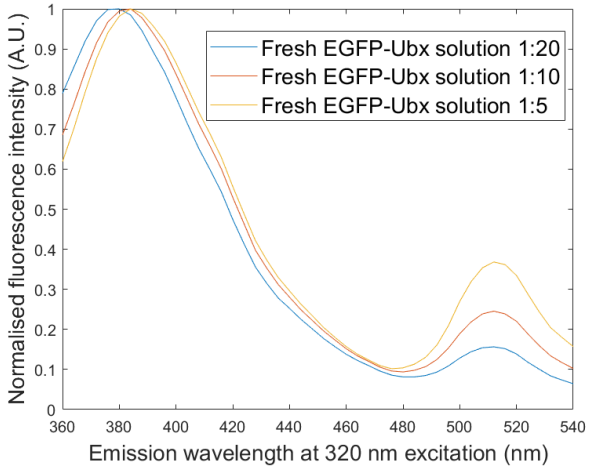

(a)

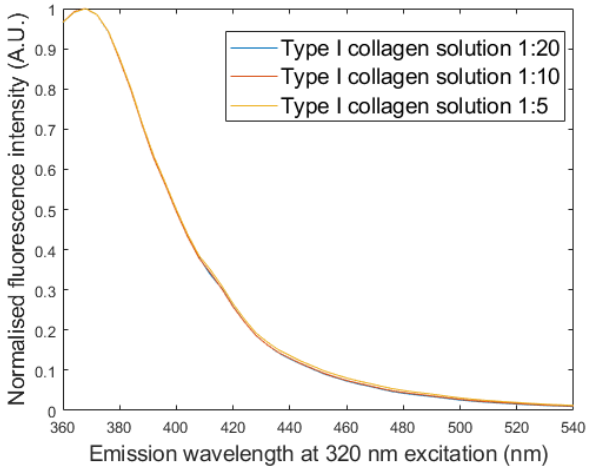

(b)

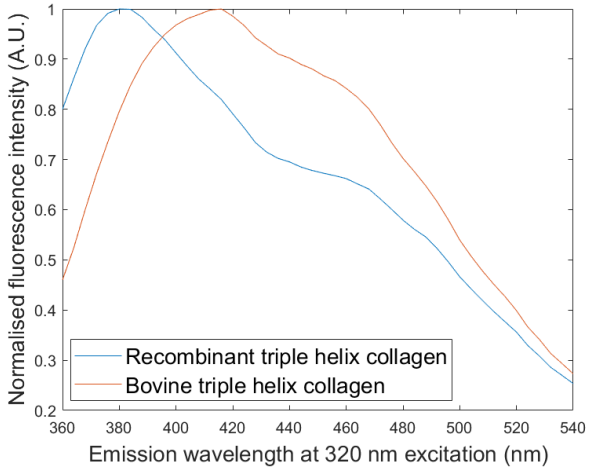

(c)

Figure 6.2.4: The emission scan for solutions of (a) EGFP-Ubx, (b) type I collagen, and (c) bovine and human recombinant triple helix collagen solutions with 320 nm excitation wavelength.

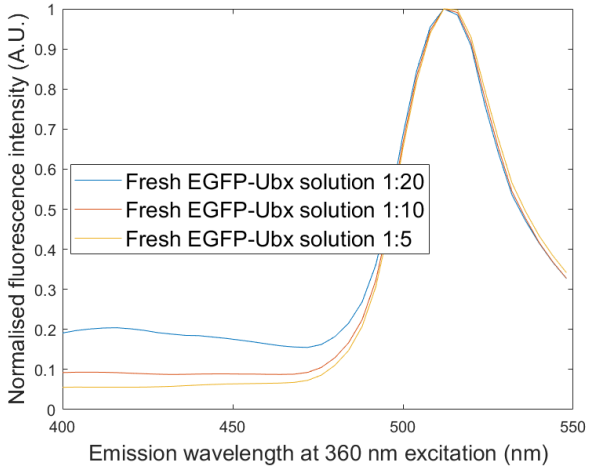

(a)

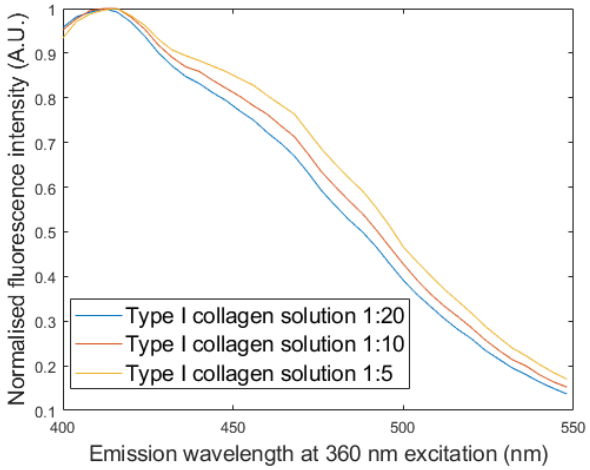

(b)

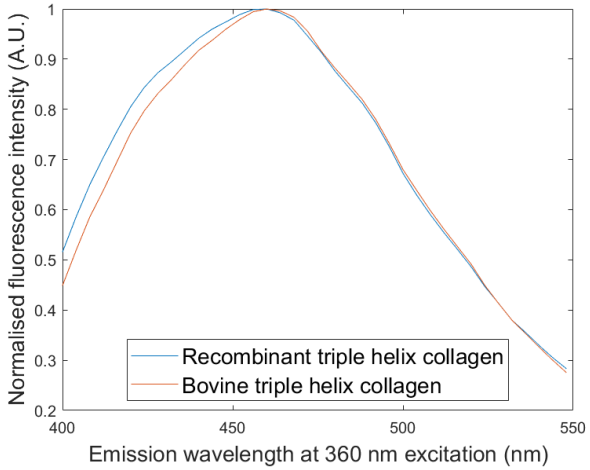

(c)

Figure 6.2.5: The emission scan for solutions of (a) EGFP-Ubx, (b) type I collagen, and (c) bovine and human recombinant triple helix collagen solutions with 360 nm excitation wavelength.

Casting type I collagen with EGFP-Ubx in a 96-well plate

Solutions of type I collagen, EGFP-Ubx, and their mixture at a ratio of 1:1 were incubated in a 96-well dish. The mixture of monomeric EGFP-Ubx and bovine triple-helix collagen yielded the most elastic materials out of the three assays. The collagen solution did not produce any material after overnight incubation, whereas the EGFP-Ubx cast mixture crystallised and produced a thick material with emerging short and brittle fibres. A comparison of the structures of materials produced by the EGFP-Ubx solution and the mixture of EGFP-Ubx and collagen is shown in figure 6.2.6

(a) (b)

Figure 6.2.6: The materials resulting from incubation of protein solutions in a 96-well plate. (a) A brittle fibre made of 200 µL of EGFP-Ubx at concentration 4.17 µM, (b) An elastic fibre produced from a mixture of 100 µL of the EGFP-Ubx and 100 µL of 1.83 mg mL^{-1} type I collagen.

Incorporating collagen into self-assembled EGFP-Ubx films

A solution of collagen, either type I collagen or bovine triple helix collagen, was deposited dropwise onto the surface film made by self-assembly of EGFP-Ubx in an aqueous buffer. The comparison of the fluorescence of EGFP-Ubx fibres made with and without addition of the bovine triple helix collagen is shown in figure 6.2.7. Adding the bovine triple helix collagen did not appear to strongly change the distribution of the fluorescence. Regions of weaker fluorescence appeared in both fibres, which could correspond to impurities in the fibrillar structure though both the dityrosine autofluorescence intensity across the fibres, and the EGFP emission presented a similar distribution across the fibre.

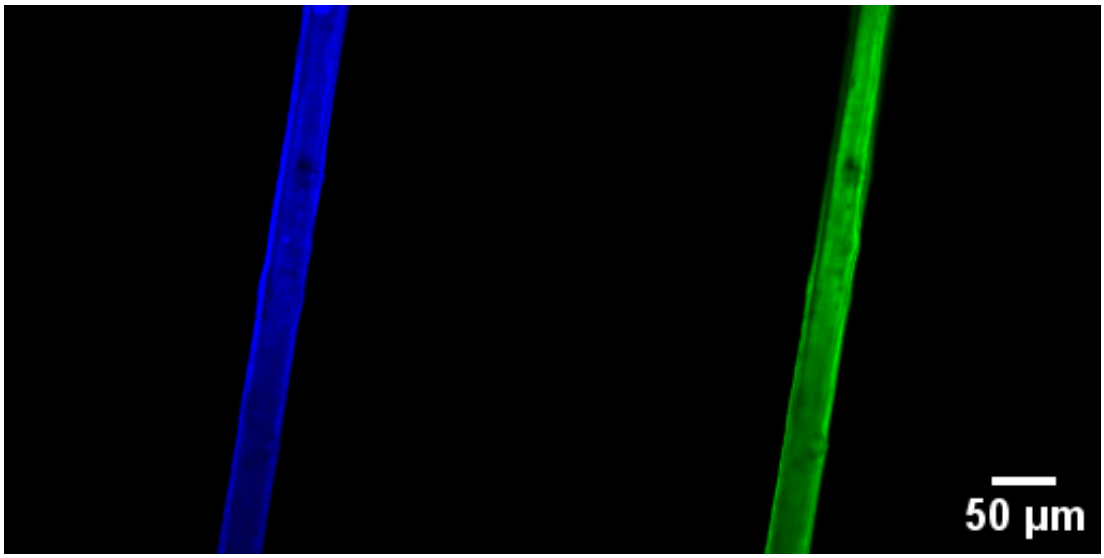

(a)

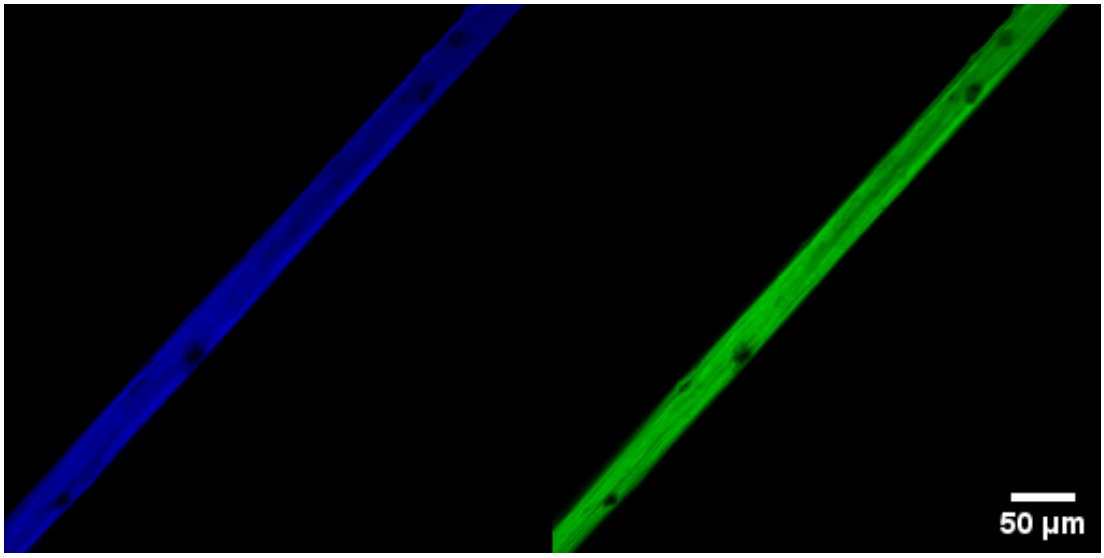

(b)

Figure 6.2.7: Micrographs of EGFP-Ubx fibres made from a self-assembled protein film (a) without collagen, and (b) with bovine triple helix collagen deposited dropwise onto the EGFP-Ubx film.

The ratios of the green to blue fluorescence intensity were measured to examine whether adding collagen could influence this ratio. The hypothesis was that the additional fluorescence in the blue channel due to the presence of collagen could decrease this ratio for the composite EGFP-Ubx-collagen fibres. The graph of this ratio for both fibre groups is shown in figure 6.2.8a. The mean diameter of an EGFP-Ubx fibre was $(16.4 \pm 1.9)\,\mu m$ and the mean ratio of green to blue fluorescence intensity within these fibres was 1.30 ± 0.14. For the EGFP-Ubx-collagen composite fibres, the average diameter was $(17.8 \pm 3.1)\,\mu m$ and the mean ratio of green to blue fluorescence intensity was 0.79 ± 0.09. The difference between the diameters of these fibres was not statistically significant ($P = 0.7022$), whereas the decrease in the average ratio of fluorescence intensities in the green and blue channels for the EGFP-Ubx-collagen fibres was statistically significant ($P = 0.0363$). This result meant that the addition of the bovine triple helix collagen solution onto the self-assembled EGFP-Ubx film decreased the ratio of mean green to blue fluorescence intensity within the fibres, which indicated that collagen was present in the samples. A similar analysis was undertaken for EGFP-Ubx samples containing type I collagen. The average diameter of EGFP-Ubx fibres was $(10.0 \pm 1.5)\,\mu m$ while that of the samples containing collagen was $(8.2 \pm 1.0)\,\mu m$ ($P = 0.3490$). Importantly, the ratio of mean green to blue fluorescence intensity was statistically significantly higher for plain EGFP-Ubx fibres compared to the samples made with EGFP-Ubx and collagen, with values of 0.64 ± 0.12 and 0.21 ± 0.07 ($P = 0.0161$), respectively, as shown in figure 6.2.8b. These results suggest that adding both the bovine triple helix and type I collagen to the self-assembled EGFP-Ubx film changed the fluorescence ratios in the produced fibres.

Fluorescence spectra were measured for the fibres made using self-assembled EGFP-Ubx film with added collagen (figure 6.2.9). These spectra showed a small increase in the strength of the dityrosine peak at 444 nm compared to the EGFP peak at 508 nm. The ratio of the intensities at these peaks was the highest for the EGFP-Ubx and type I collagen fibre at 0.85, followed by the EGFP-Ubx and triple helix collagen sample at 0.83, and the EGFP-Ubx fibre at 0.80. The differences in the relative heights of the fluorescence peaks indicated the presence of a small quantity of collagen in the fibres.

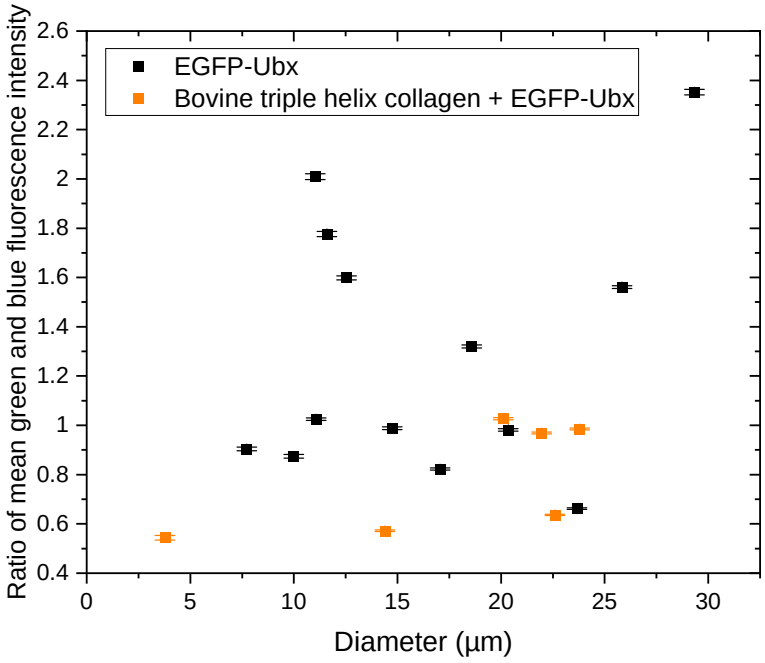

(a)

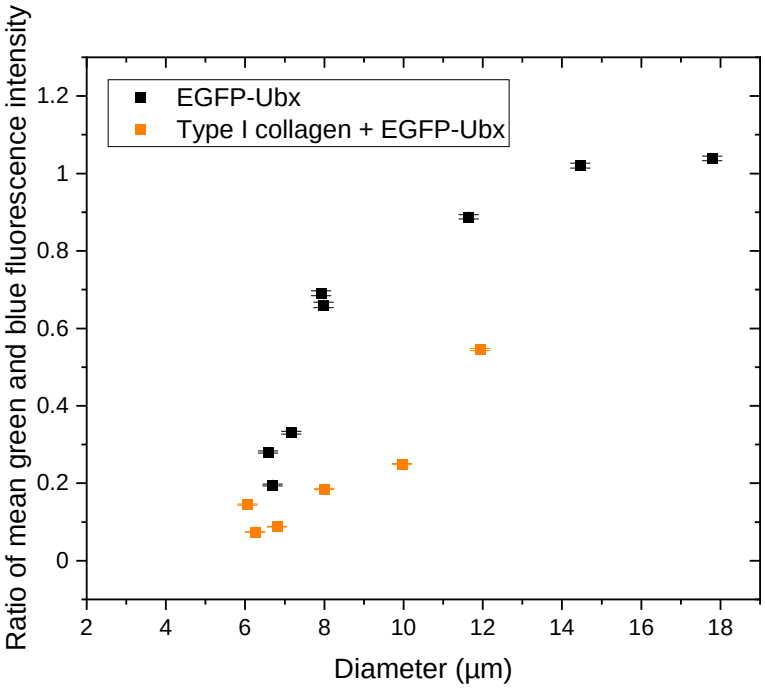

(b)

Figure 6.2.8: The comparison of the ratios of the mean green to blue fluorescence intensity of EGFP-Ubx fibres made from a self-assembled protein film (a) without collagen, and (b) with bovine triple helix collagen deposited dropwise onto the EGFP-Ubx film.

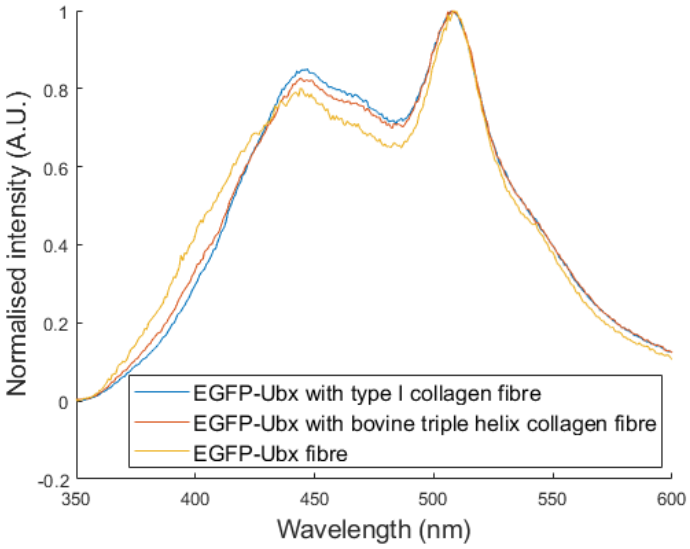

Figure 6.2.9: The fluorescence spectra of EGFP-Ubx fibres containing type I and bovine triple helix collagen. The spectra were taken using 343 nm laser source for excitation.

Casting of bovine triple helix collagen sheets with EGFP-Ubx fibres

Thin bovine triple helix collagen sheets were made by casting in a Petri dish. Incorporation of monomeric Ubx fusions was impossible due to the use of acetic acid as a solvent. Moreover, casting the water-soluble recombinant triple-helix collagen in a similar manner was not achieved due to crystallisation of the buffer during drying (figure 6.2.10). To test the interaction of Ubx fusion materials with collagen, EGFP-Ubx fibres were placed within the bovine triple-helix collagen solution. The resulting cast solution is shown in figure 6.2.11. The EGFP-Ubx fibres retained their structure and were visibly unchanged. This meant that the self-assembly process provided structural stability and protection from protein denaturation in acetic acid. The addition of EGFP-Ubx fibres showed that the functional properties of this protein fusion remained, which was an indication that these fibres can be used to functionalise even those tissue scaffolds that are treated using denaturing chemicals or processes.

The photoluminescence spectra of bovine triple helix collagens with added EGFP-Ubx fibres are shown in figure 6.2.12. The spectra were measured with 343 nm laser excitation. The fluorescence spectra of the collagen sheets had an emission peak at approximately 420 nm with secondary peaks at around 442 nm and 470 nm. For the samples containing EGFP-Ubx fibres, the fluorescence peak was at 440 nm, which corresponded to dityrosine autofluorescence. There were sec-

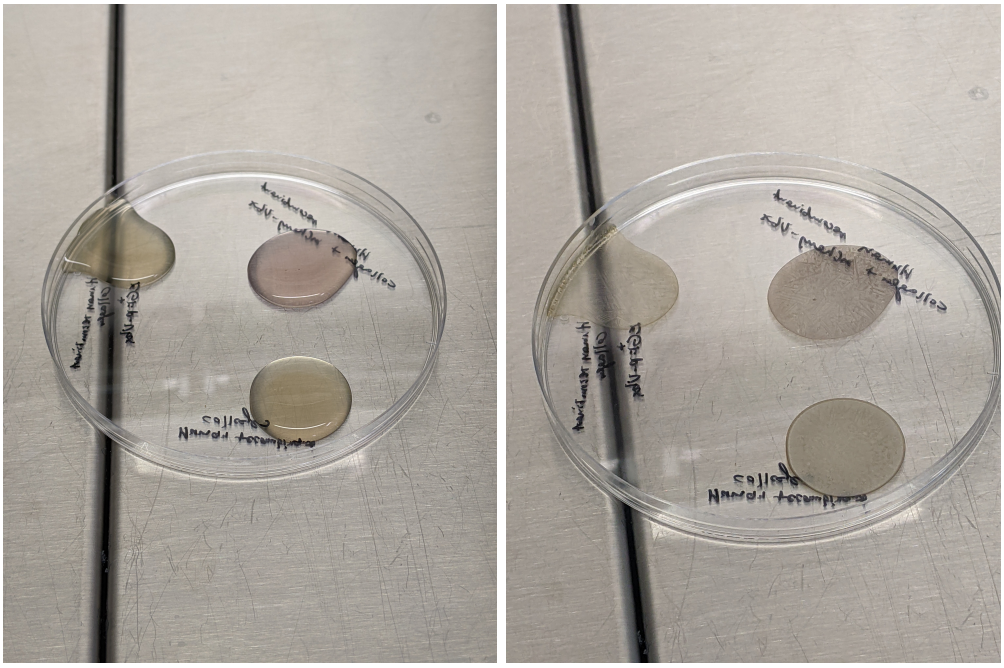

(a) (b)

Figure 6.2.10: Photographs of the attempt to cast recombinant triple helix collagen sheets. Collagen and EGFP-Ubx mixtures (a) before incubation, and (b) after incubation, with visible crystallisation of the buffer.

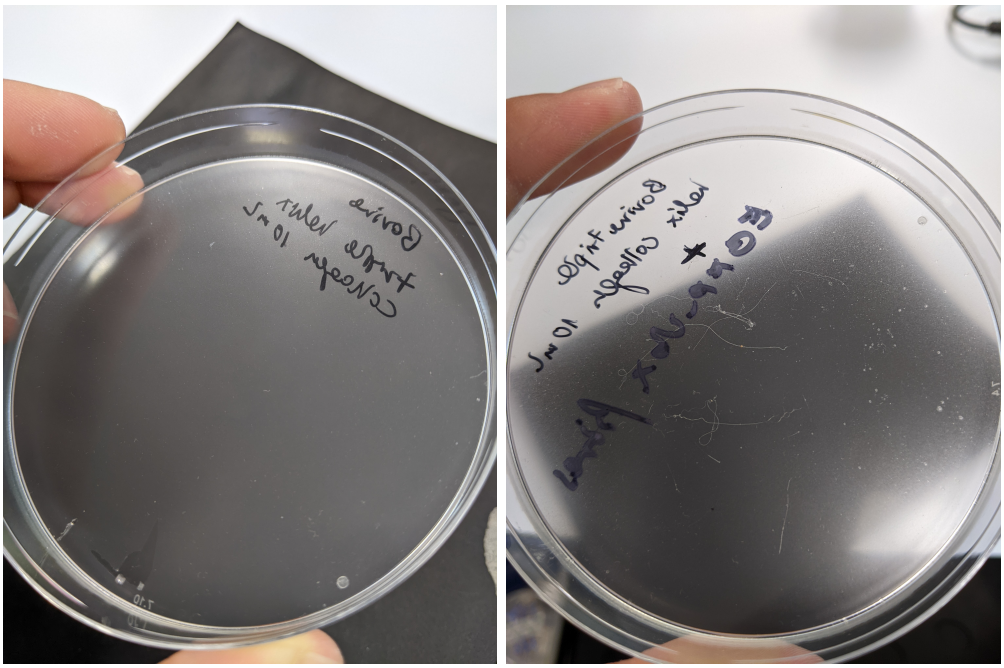

(a) (b)

Figure 6.2.11: Photographs of cast triple helix bovine collagen sheets (a) plain, and (b) with EGFP-Ubx fibres placed in the solution before casting.

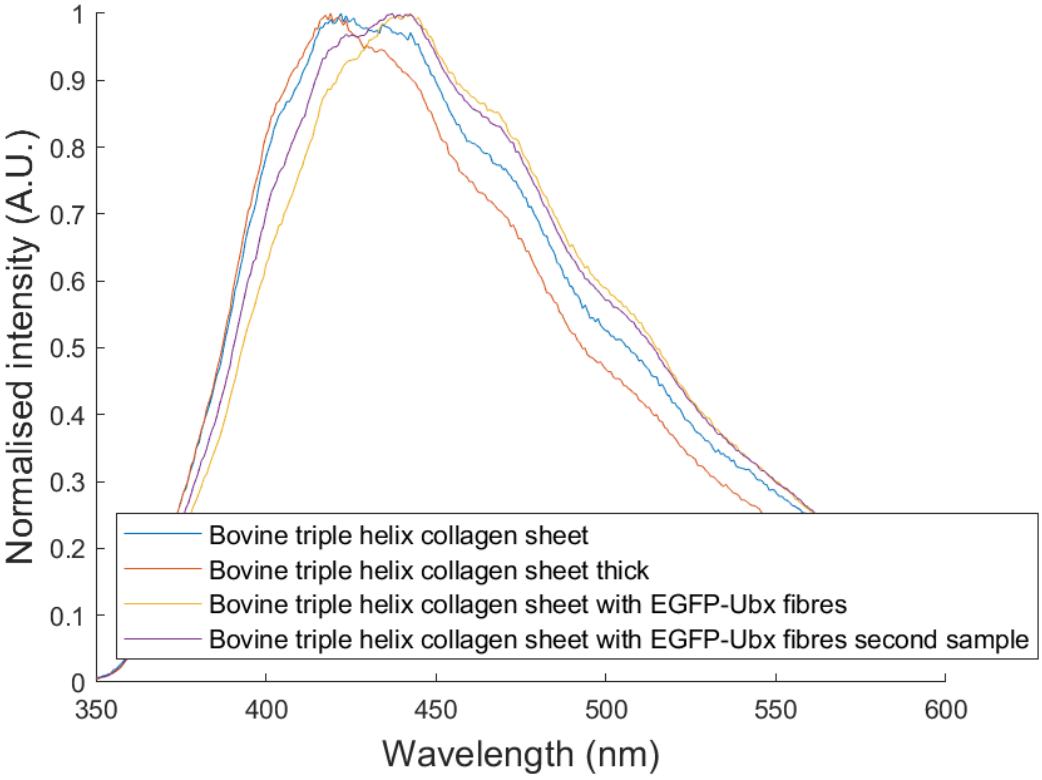

Figure 6.2.12: The fluorescence spectra of bovine triple helix collagen sheets, two of which contained EGFP-Ubx fibres, added before casting the sheets. The spectra were taken using a 343 nm laser source for excitation.

ondary peaks at 420 nm and 470 nm, similar to the collagen samples. There was also a weak secondary peak at 508 nm, which was the specific EGFP peak. These results indicate a shift in the fluorescence spectra of bovine triple helix collagen sheets when EGFP-Ubx fibres were added. These fibres retained their structure and fluorescent properties, which allowed for a functionalisation of the collagen sheets with the fluorescently labelled Ubx fibre. This result also suggested the structural protection of the functional proteins within Ubx fibres from denaturing conditions, which confirmed the previous reports [17, 100]

6.3 Cross-linking sodium alginate-Ubx materials

These experiments tested the possibility of producing an alginate-Ubx bioprinted material, which would be cross-linked and the presence of alginate and Ubx fusions would be tested using the fluorescence spectroscopy. Because of the ubiquitous

applications of alginate in tissue engineering [130, 131], this system was identified as a potential pathway to incorporating Ubx functions in tissue scaffolds.

6.3.1 Methods

Selection of Ubx fusion concentration for cross-linking experiments

The aim of this experiment was to assess the sufficient concentration of EGFP-Ubx in the EGFP-Ubx-alginate solution, which allowed for the detection of the EGFP fluorescence in the solution. Solutions of 16.53 µM EGFP-Ubx in G0 buffer, 1% sodium alginate in deionised water, and the mixtures of EGFP-Ubx and 1% sodium alginate at the ratios of 1:10, 1:20, and 1:50 were prepared. Their absorbance was measured at 488 nm using a spectrophotometer. Their emission intensity at 512 nm was measured with 472 nm excitation. Subsequently, the excitation scan with the emission wavelength of 400 nm, and an emission scan with the excitation wavelength of 320 nm were conducted. The results are shown in figures 6.3.1 and 6.3.2. The concentration of Ubx fusion to alginate of 1:20 was chosen for the next experiments involving cross-linking the Ubx-alginate composite materials.

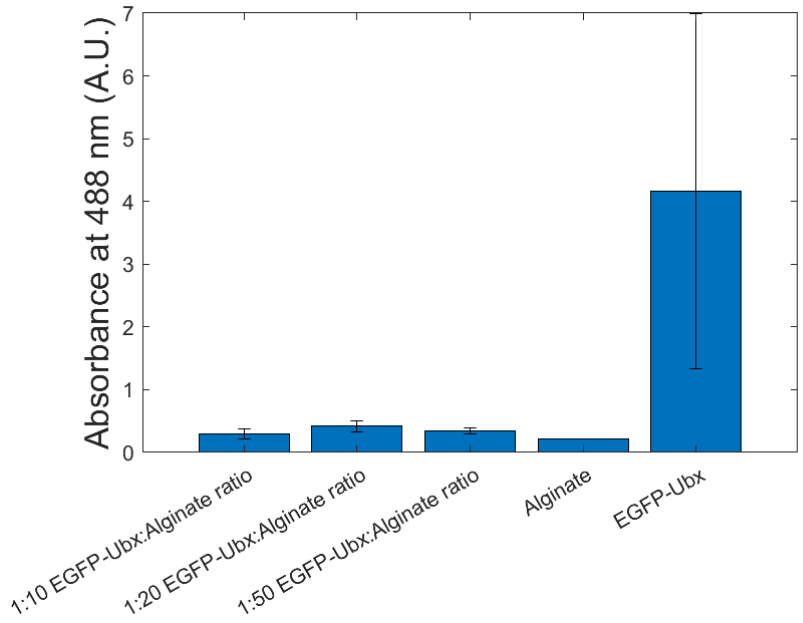

(a)

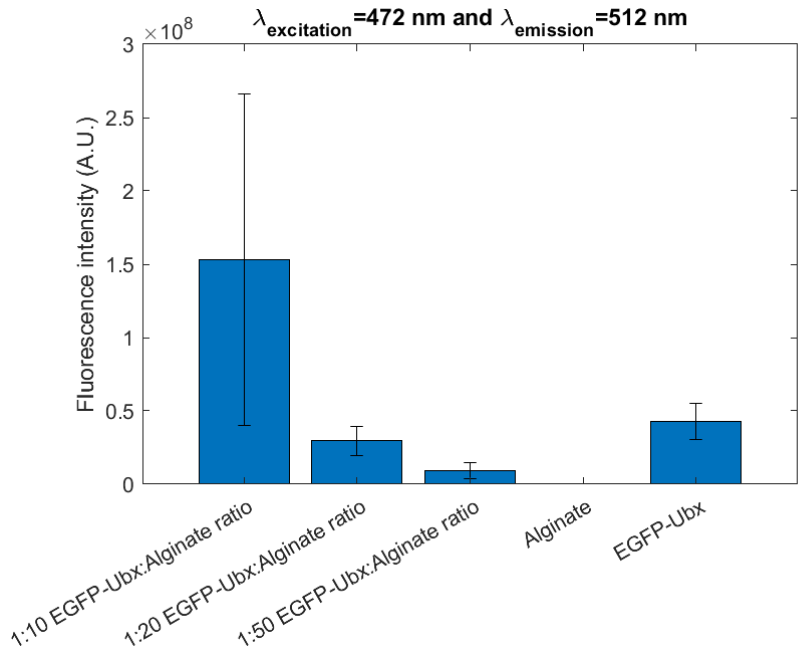

(b)

Figure 6.3.1: The optical spectra of EGFP-Ubx and alginate, and their solutions mixed in ratios of 1:10, 1:20, and 1:50. (a) The absorbance at 488 nm, (b) The emission intensity at 512 nm with excitation at 472 nm.

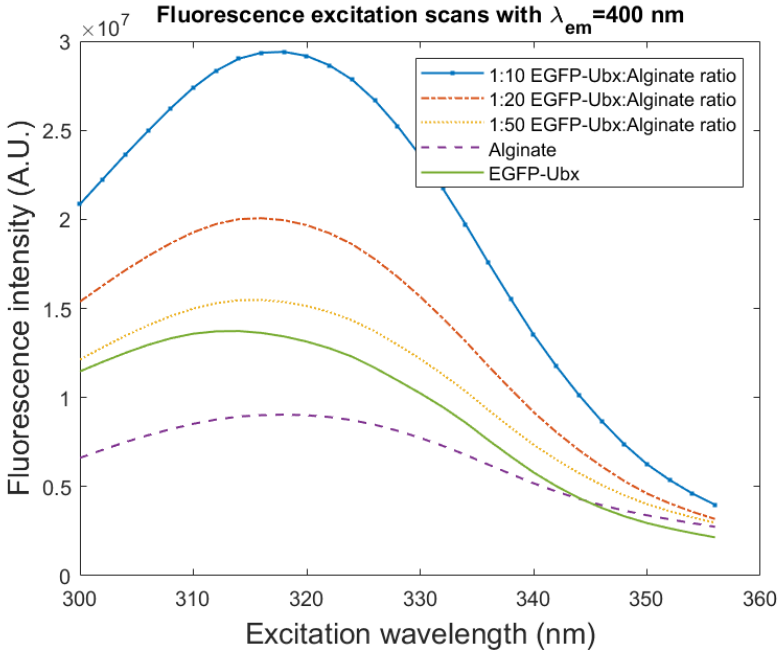

(a)

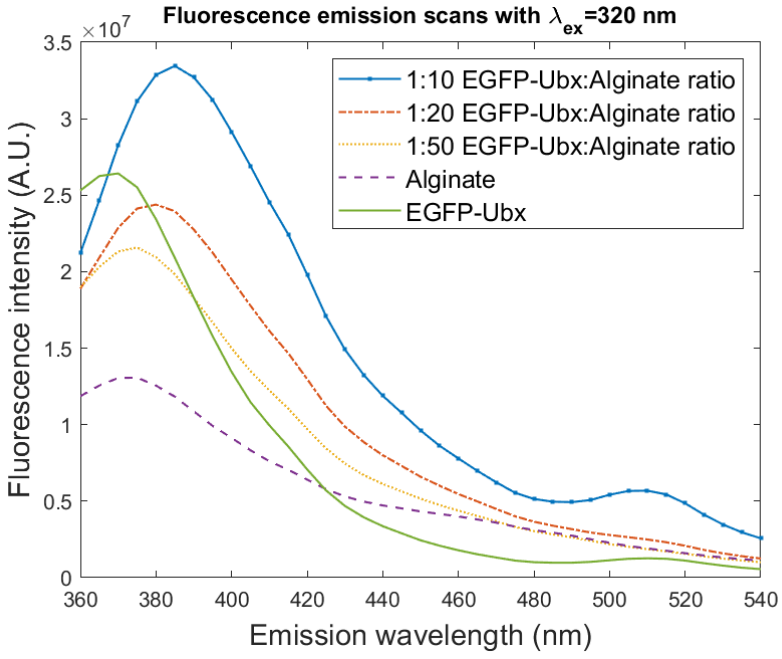

(b)

Figure 6.3.2: The optical spectra of EGFP-Ubx and alginate, and their solutions mixed in ratios of 1:10, 1:20, and 1:50. (a) The excitation scan with emission at 400 nm, and (b) The emission scan with excitation at 320 nm.

Cross-linking of the sodium alginate-Ubx fusion composites

0.15 mL EGFP-Ubx (at concentration 23.57 µM) and mCherry-Ubx (at concentration 21.25 µM) solutions in G0 buffer were mixed with 2.85 mL of 1% sodium alginate in deionised water with a ratio of 1:20. The mixture was extruded using a syringe with a 250 µm nozzle tip (CELLINK) into a Petri dish filled with a $CaCl_2$ solution. The cross-linking between alginate molecules occurred in the $CaCl_2$ solution for 5 min, after which the resulting material was removed. The photographs of the bioprinting and cross-linking processes are shown in figure 6.3.3. The excitation and emission spectra of the resulting materials were measured using a spectrophotometer.

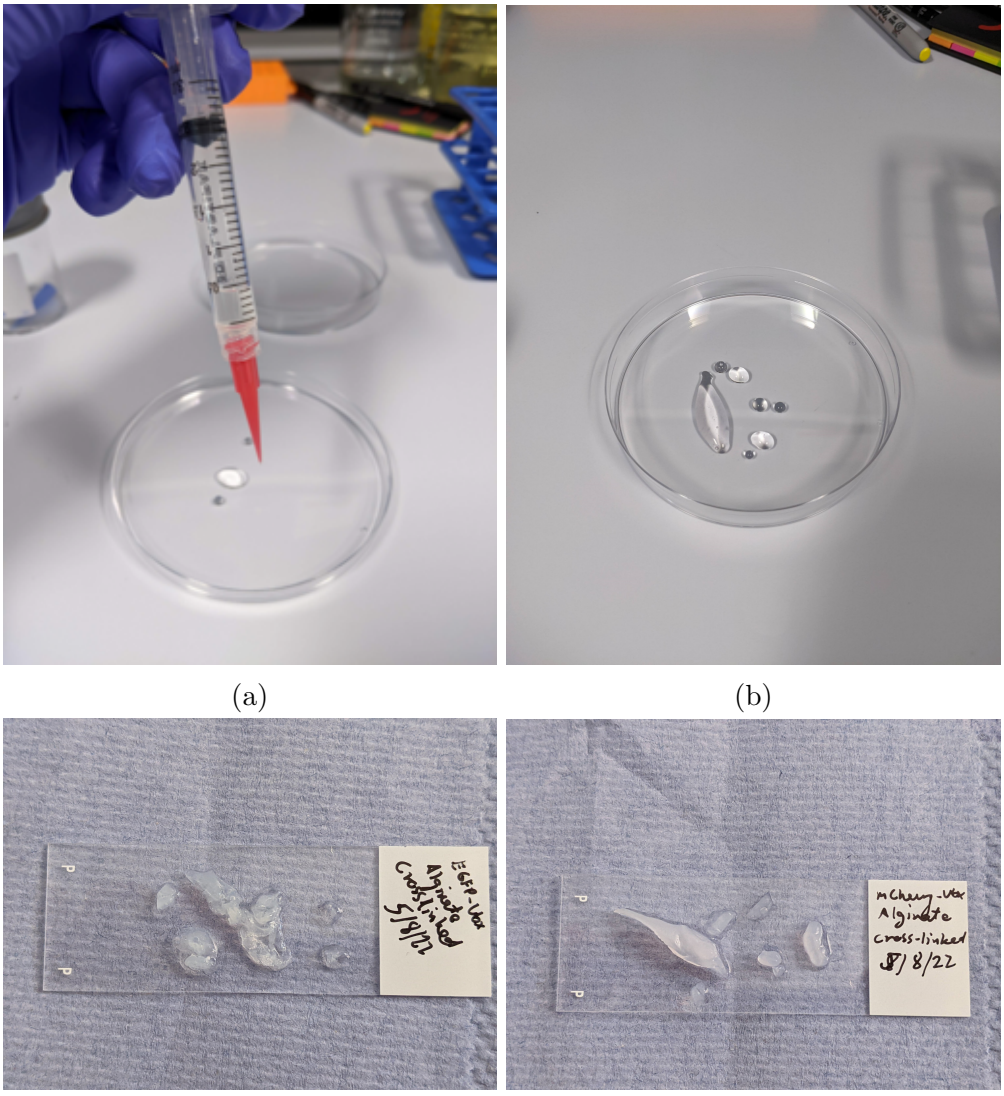

(a) (b)

(c) (d)

Figure 6.3.3: The photos of EGFP-Ubx and mCherry-Ubx with 1% sodium alginate in solution and after cross-linking. (a) The EGFP-Ubx and sodium alginate solution before cross-linking, (b) the mCherry-Ubx and sodium alginate solution during cross-linking, (c) the EGFP-Ubx and sodium alginate solution after cross-linking, and (d) the mCherry-Ubx and sodium alginate solution after cross-linking.

6.3.2 Results and discussion

The sodium alginate and EGFP-Ubx solutions, with concentrations of 1:10, 1:20, and 1:50, were prepared to assess whether EGFP fluorescence could be measured at these concentrations. The comparisons of measured solution absorbance at 488 nm and fluorescence emission intensity at 512 nm are shown in figures 6.3.1a and 6.3.1b, respectively. The absorbance at 488 nm was the highest for the EGFP-Ubx solution and the lowest for the 1% sodium alginate solution. It increased with a rise in EGFP-Ubx to alginate ratio in the solution from 1:50 to 1:20, although it then decreased for the 1:10 ratio. The emission intensity at 512 nm was increasing significantly with EGFP-Ubx content in solution. The ratio of 1:20 was deemed sufficient to detect EGFP-Ubx in potential bioprinted samples. Excitation and emission spectra of these solutions were also analysed. The excitation maximum of the solutions shifted from 314 nm for pure EGFP-Ubx to 318 nm for both the pure alginate and 1:10 EGFP-Ubx:Alginate samples when emitting at 400 nm. When the samples were excited at 320 nm, their emission peaks shifted from approximately 370 nm and 375 nm for EGFP-Ubx and alginate, respectively, to 385 nm for the sample with the 1:10 ratio. The prominence of the EGFP peak at 510 nm increased with EGFP-Ubx content in the mixture.

Following the investigation of fluorescence intensity in solution, EGFP-Ubx and mCherry-Ubx were mixed with 1% sodium alginate, and the resulting mixture was cross-linked using $CaCl_2$. The photographs (figure 6.3.3) showed that the extruded materials hardened after bioprinting and created solid structures after cross-linking. The optical spectra of the cross-linked materials are shown in figure 6.3.4. The emission scan with excitation at 343 nm exhibited the maximum at the alginate peak at 389 nm, and strong peaks corresponding to the fluorescence of EGFP at 507 nm and mCherry at 611 nm. When excited at 420 nm, mCherry-Ubx with alginate had an emission peak at 494 nm and the mCherry emission peak at 610 nm while the material containing EGFP-Ubx only had a strong EGFP peak at 512 nm. The strong mCherry peak was also seen with 560 nm excitation wavelength. Finally, at 507 nm emission, the excitation spectrum of mCherry-Ubx with alginate had a maximum at 364 nm, and both Ubx fusions had secondary peaks at between 266 nm and 278 nm. These measurements indicated the presence of EGFP-Ubx and mCherry-Ubx in the cross-linked alginate-based materials. This result suggests that Ubx fusions could be incorporated into alginate scaffolds to be used as functional proteins for biosensing and stimulating cell proliferation.

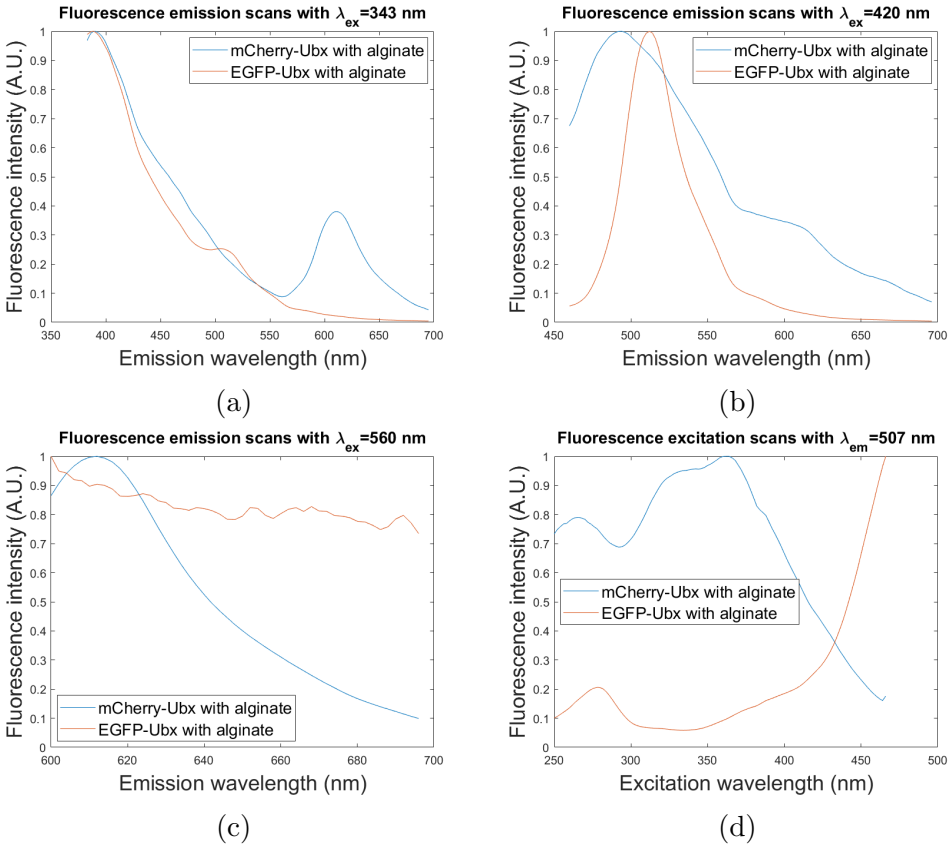

Figure 6.3.4: The optical spectra of solutions EGFP-Ubx and mCherry-Ubx with 1% sodium alginate. (a) The emission scan with 343 nm excitation, (b) the emission scan with 420 nm excitation, (c) the emission scan with 560 nm excitation, and (d) the excitation scan with emission at 507 nm.

6.4 Summary

This chapter presented the preliminary work on the production of collagen-Ubx and alginate-Ubx composite materials. Both collagen and alginate have been used for tissue engineering [4, 127, 130–133]. Creation of composite EGFP-Ubx-collagen materials by self-assembly and casting was demonstrated in this work. Both the cast sheets made predominantly with bovine triple helix collagen and self-assembled fibres made with mainly EGFP-Ubx exhibited changed fluorescence properties in composite materials compared to those with a homogenous composition. This result indicated that the functional properties of Ubx fusions could be harnessed to add additional features to collagen materials, and vice versa. This result can be considered in the context of the mechanical properties of Ubx and the aptamer functionalisation described in previous chapters. The mechanical properties of Ubx fusion fibres were shown to be similar to those of collagen in tissues such as tendons, which means that the composite materials made of Ubx and collagen could benefit from a comparable strength and elasticity. In addition to the bio- and cytocompatibility of both proteins, the cell-binding properties of collagen, and the functionalisation of Ubx with DNA aptamers could provide a good platform for biosensing and targeted drug delivery. Inclusion of Ubx in composite alginate-Ubx materials could add similar functions, which could be used to create bioprinted tissue scaffolds with aptamers for therapeutic or sensing purposes. The work in this thesis indicated that 3D printing alginate-EGFP-Ubx materials is possible and could be considered as a potential functionalisation route for existing alginate tissue scaffolds.

Chapter 7

Summary and future work

7.1 Summary

This project aimed to investigate the feasibility of applying Ubx materials for biosensing and tissue engineering. To assess this, the effects of sample storage, treamtent, and the relative humidity on the optical, electrical and mechanical properties of Ubx fusions in solution and in fibres were investigated. Functionalisation of Ubx materials with DNA aptamers and subsequently capturing bacteria and the SARS-CoV-2 spike RBD protein binding were attempted to assess the potential of applications in biosensing or targeted therapeutics. Finally, composite materials were produced containing Ubx and biopolymers collagen or alginate, which are biomaterials with a wide use in tissue engineering.

The measurements of the optical properties of Ubx fusion in solution and in fibres revealed that the spectra of Ubx fusions in solution differed compared to those in self-assembled fibres. A 50 nm dityrosine emission peak red-shift was observed after the Ubx fusions had formed fibres. In addition, the relative height of the EGFP and mCherry emission peaks with respect to the dityrosine emission in fibres increased in the case of EGFP, and decreased in the case of mCherry, compared to the solution. The fluorescence lifetime studies also indicated a decrease in all the fluorescence lifetime components of the EGFP-Ubx decay, which, along with the larger EGFP emission peak, indicated that FRET occurred between the dityrosine fluorescence and EGFP emission in the EGFP-Ubx fibres, which increased the EGFP emission peak. The FRET efficiency was estimated to be 0.711 ± 0.024. The excitation power dependence on the fluorescence intensity

of fibres was nearly linear, which indicated that no significant photobleaching of EGFP-Ubx fluorescence occurred, which could be an important feature of this probe in biosensing applications. The fluorescence lifetime measurements indicated that the fluorescence decay time constants of mCherry-Ubx fibres increased compared to Ubx fibres, which did not indicate a significant energy transfer in these samples, unlike for EGFP-Ubx. These measurements also provide the first step towards using Ubx fusions in the design of FLIM biosensors, which could use the shifts in the fluorescence lifetime to measure analyte binding or environmental conditions.

This thesis presented the first investigation of the effect of relative humidity on the electrical properties of Ubx fusion fibres. The electrical conductivity of Ubx, EGFP-Ubx, and myoglobin-Ubx fibres were not significantly different in ambient conditions with the 40% relative humidity. It had previously been shown that relative humidity and sample hydration played an important role in determining the electrical conductivity of biomaterials [43]. The work presented here confirmed this trend for Ubx materials. An increase in the DC electrical conductivity of all Ubx fusion fibres was observed in the preliminary experiments, and later in the systematic measurements of the electrical properties using a cryogenic probe station with humidity control. A rise in the DC electrical conductivity by two orders of magnitude was measured between 57% and 86% relative humidity, which indicated the likely ionic conductivity mechanism in Ubx fusion fibres. In addition, an increase in the AC electrical conductivity of up to three orders of magnitude was observed in the same humidity range. An equivalent electrical circuit based on the Randles circuit was proposed to model the impedance spectra, which revealed that the behaviour of the circuit changes from that of the Randles circuit to a more capacitive with the increase in the relative humidity. These measurements formed the basis, on which the design of Ubx-based impedimetric biosensors could be made, particularly when used in conjunction with functionalisation with nanoparticles or DNA aptamers.

An investigation into the effect of fibre storage on their mechanical properties was conducted. The sample oxidation leading to the formation of dityrosine bonds was suggested as the mechanism leading to the self-assembly of Ubx materials, and the development of their mechanical strength [38,39]. Both Ubx and EGFP-Ubx fibres exhibited a large decrease in the breaking strain after prolonged storage compared to the previous measurements on freshly prepared fibres [17]. However, the tensile strength of Ubx fibres increased by an order of magnitude after stor-

age, while that of EGFP-Ubx only increased by about 16%. This work provides evidence for the claim that oxidation could increase the strength of Ubx materials and that storage causes stiffening of fibres and a decrease in extensibility. An important factor in the increase of the strength of fibres after storage was the sample rehydration, which appeared to increase both the breaking strength and the Young's modulus of rehydrated EGFP-Ubx fibres by a factor of 3 compared to dry stored fibres. The mechanical properties of Ubx fibres were comparable to those of collagen in mammal tissues, and placed Ubx strength and elasticity between collagen and elastin, which suggested that larger Ubx scaffolds could be used for tissue engineering. Biomedical products made of Ubx materials are likely to require storage, therefore the results presented here provide information about the mechanical properties of Ubx materials relevant for future applications in tissue engineering.

Aptamers have been an important research topic in the last decades. They have been applied in diagnostics, targeted therapeutics, and biosensing. This thesis tested long oligonucleotide sequence binding that contained Ubx fusion aptamers, and analyte aptamers against *E. coli* and the SARS-CoV-2 spike RBD protein. Binding of both single and double stranded DNA aptamers to Ubx fusion fibres was shown, which meant that functionalisation of Ubx with DNA aptamers was feasible. The analyte aptamers appended to the Ubx aptamer sequence appeared to cause a statistically significant increase in *E. coli* binding by functionalised Ubx fibres in a number of experiments, although the non-specific binding of analytes was a large issue encountered in these experiments. The functionalisation of Ubx materials with DNA aptamers could be another feature of platform Ubx materials for applications in biosensing or targeted therapeutics.

Collagen and alginate have been used extensively in the production of tissue scaffolds and implantable devices. The feasibility of producing simple composite materials containing Ubx and collagen or alginate was demonstrated in this thesis, which could provide a pathway to using the functionalisability of Ubx and its ready self-assembly to enhance the designs of tissue scaffolds. The production of collagen sheets with immersed EGFP-Ubx fibres emphasised the protective nature of the Ubx fusion materials against conditions harsh for proteins, such as immersion in acetic acid.

This thesis provided the measurements of physical properties of Ubx materials under conditions relevant for physiological applications (changing humidity and

sample hydration) and product durability (long-term storage of materials), both of which show the potential for tunability of material properties with changing storage time, rehydration, and relative humidity. In addition, Ubx fusions were functionalised with DNA aptamers, and included in composite materials with biomaterials commonly used as tissue scaffolds. This work paves the way for future applications of Ubx materials in biosensing through impedimetric or fluorescence-based measurements, and tissue engineering through the creation of functionalisable composite materials.

7.2 Future work

7.2.1 Scaling up Ubx protein and Ubx materials production

Production of composite materials and protein fusions both provide multiple functionality benefits and better mechanical properties compared to pristine protein materials [3, 7, 9, 15, 17, 132, 133]. Scaling up the Ubx protein production is necessary in order to more effectively use its functional properties. Creating larger Ubx materials could enhance its sensing and analyte binding capabilities by producing structures with a larger surface area and porosity, and a wider range of morphologies such as hydrogels and electrospun mats. To achieve this goal, more protein needs to be produced and purified. Currently, Ubx is produced in batches in flasks, which provides a reproducible way of protein production at a small scale. Approximately 4 L of culture can be produced, which yields up to about 2 µmol or 160 mg of protein. The use of larger bioreactors could provide benefits of better control over production conditions, including pH, temperature, and oxygen level. Additionally, the increased volume to 15 L or 100 L could significantly increase the protein output and yield protein amounts sufficient to prototype platform materials for biosensing or tissue engineering.

The downstream processing including protein purification would need to be adjusted for the larger protein yield. Scaling up the purification volumes or decreasing its cost could be beneficial for future applications. The use of a French press or sonication to lyse the *E. coli* prior to purification in a chromatography column could decrease the cost of purification by reducing the costs associated with chemical lysis and DNA breakdown using lysozyme and DNase I. Additionally, higher purification throughput could be achieved by using a larger purification column in

a cold room at 4 °C. Desalting buffer solutions and removing glucose from the purification process could enable freeze drying Ubx to increase Ubx concentrations. Freeze drying could also allow incorporation of Ubx in other composite materials or creating pristine Ubx hydrogels. Production of larger platform materials would allow functionalisation and testing the properties of Ubx fusions on a larger scale. These changes could include the addition of nanoparticles, nanowires or DNA aptamers, which could positively affect the electrical and mechanical properties of Ubx materials, as well as their capability to bind and sense analytes.

The increase in the amount of produced protein and the subsequent design of larger Ubx structures could change the physical properties of these new materials. The production of electrospun mats, freeze dried gels and composite materials could be envisaged, all of which would have different structure and properties. The physical characterisation, analysis, and functionalisation methods presented in this thesis could be used for the future work with these materials, and comparisons could be made to Ubx fusion fibres. This work indicated that functionalisation of Ubx fibres with DNA aptamers might increase pathogen binding. Scaling up the material size and the available surface area could trigger a rapid increase in the binding efficiency using aptamers, which might lead to applications of functionalised Ubx platforms in biosensing and therapeutics, as well as tissue engineering.

7.2.2 Composite materials

Composite collagen-EGFP-Ubx materials were produced in this work. The existing applications of collagen in tissue engineering and wound healing could be enhanced by the addition of Ubx functionalised with growth factors such as VEGF. This could further stimulate tissue regeneration. Bioprinting of EGFP-Ubx and mCherry-Ubx with alginate was described in this thesis. The inclusion of Ubx fusions in the bioprinting ink added fluorescence peaks respective to EGFP or mCherry, while maintaining the alginate peak at approximately 390 nm. The functional properties of Ubx and Ubx fusions could enhance the use of alginate in tissue engineering. Functionalisation of Ubx with antimicrobial peptides might add antibacterial properties, and the addition of DNA aptamers could result in applications in biosensing or in design of targeted therapeutics. The scaling up of Ubx protein and Ubx materials production could lead to the modified design and further testing of composite collagen-Ubx and alginate-Ubx materials introduced

in this work. This could have applications in tissue engineering and biosensing, particularly when the combined functions of both Ubx and conjugated collagen or alginate are considered.

7.2.3 Nanofunctionalisation

There are a range of nanofunctionalisation strategies that could be used to improve the properties of protein or composite materials. Addition of nanostructures such as nanoparticles or nanowires can have a positive effect on the electrical and mechanical properties of biomaterials [8, 27]. Nanofunctionalisation of alginate scaffolds with Au nanowires enhanced their electrical conductivity sufficiently to facilitate synchronous contraction and stimulate structured tissue growth, while also increasing its compressive modulus [27]. Electron beam evaporation of gold nanoparticles onto functionalised autologous scaffolds was shown to increase their electrical conductivity while maintaining their mechanical strength, which increased the amplitude of synchronous contraction of neighbouring cells in the myocardium [8]. The improvements in the physical properties of protein materials resulting from functionalisation with nanomaterials were discussed in more depth in sections 1.1, 1.2, 3.1, and 4.1.

Other properties that can be attained by the use of nanomaterials include antimicrobial properties of silver particles proved against *E. coli* and yeast [24,137], which can eventually be used to mitigate issues of inflammation and rejection of implants in bone tissue engineering [24]. There are also multiple applications of nanomaterials in biosensing. Fluorescent dyes can be substituted with carbon quantum dots with increased water solubility and luminescence [138]. Advantages of carbon dots in biosensing include their biocompatibility and stable emission intensity over longer times [138]. Functionalisation of Ubx with carbon quantum dots or their adsorption onto the scaffold may allow to either trace the removal of the degrading scaffold from organism or localise the scaffold and monitor its movement or contraction. Impedance measurements using colloidal gold can be employed to sense antibody-antigen interactions, as was demonstrated using the hepatitis B virus [139].

Nanofunctionalisation using all the methods described in this section could be used with Ubx materials. The immediate advantages of this approach could be an increased electrical conductivity, additional antimicrobial properties, or enhanced fluorescence. The inherent properties of Ubx materials described in

this thesis placed them in a biological relevant region in terms of their mechanical properties. The electrical conductivity of fibres was comparable to that of semiconductors, and the optical stability of these materials allowed for measurements of their fluorescence after months of storage, even after exposure to acetic acid. The construction of Ubx-based biosensors could be achieved by exploiting the physical characteristics of Ubx materials including the considerable electrical conductivity, good mechanical properties, and large surface area-to-volume ratio of fibres. These biosensors could be realised by functionalising Ubx with nanomaterials or biomolecules such as Au and Ag nanoparticles or DNA aptamers. Such devices could be used to detect a range of analytes like metal ions, proteins, bacteria, viruses, and even animal or human cells such as cancer cells.

Appendix A

The DNA sequence of the oligonucleotides used in the aptamer binding experiments

The DNA sequences of long oligonucleotides used in the aptamer binding experiments in chapter 5 are shown in figure A.0.1. The constructs were designed by Carolyn Greig at Swansea University and tested as part of the experimental work in this thesis by the author.

No.	Oligo Name	Sequence (5' -> 3')
1	B0_UBX_bind_motif	ATAATAATTAATGGTTTAATGGTTAATGGATAATTTAATGGAAGTATTAC (50)
2	B1_UBX_bind&Apt-P12Ecoli	ATAATAATTAATGGTTTAATGGTTAATGGATAATTTAATGGAAGTATTACTCCCTCCGGGGGGGTCATCGGGATACCTGGTAAGGATA (88)
3	B4_UBX_bind-anneal	CTTAGTCCATTAAATTATCCATTAACCATTAAACCATTAATTATTAT (47)
4	B5_UBX_bind_Fluor-anneal	CTTAGTCCATTAAATTATCCATTAACCATTAAACCATTAATTATTAT (47)

No.	Oligo Name	Sequence (5' -> 3')
1	B5_UBX_bind_Fluor-anneal	CTTAGTCCATTAAATTATCCATTAACCATTAAACCATTAATTATTAT (47)

No.	Oligo Name	Sequence (5' -> 3')
1	RS1_Mie_genome25	AAGTATTACCAGCGCACTTCGGCAG (25)
2	RS2_EcoliP12.31_pRepL3&H	AAGTATTACCTTCTTATACCCTCCGGGGGGGTCATCGGGATACCTGGTAAGGATAAAGAAGCGCGAAGCG (70)
3	RS3_CoV2-RBD-4CpRepL3&H	AAGTATTACCTTCTTTATCCAGAGTGACGCAGCATTTCATCGGGTCCAAAAGGGGCTGCTCGGGATTGCGGATATGGACACGTAAGAAGCGCGAAGCG (98)
4	B11_UBXb&A.Antibac2Ecol	ATAATAATTAATGGTTTAATGGTTAATGGATAATTTAATGGAAGTATTACTTCGCGCGAGTCGTCTGGGGGACTAGAGGACTTGTGCGGCCCCGCATCGTCCTCCC (106)
5	B3_UBX_bind&Apt-CoV2	ATAATAATTAATGGTTTAATGGTTAATGGATAATTTAATGGAAGTATTACATCCAGAGTGACGCAGCATTTCATCGGGTCCAAAAGGGGCTGCTCGGGATTGCGGATATGGACACGT (117)

No.	Oligo Name	Sequence (5' -> 3')
6	B10_UBXb&A.STC12Ecoli	ATAATAATTAATGGTTTAATGGTTAATGGATAATGAAGTATTACCGTACGGAATTCGCTAGCGGACCGCAGGTGCACTGGGCGACGTCTCTGGGTGTGGTGTGGATCCGAGCTCCACGTG (120)

Figure A.0.1: The DNA sequences of the oligonucleotides used in the aptamer binding experiments.

Bibliography

[1] Roberto De La Rica and Hiroshi Matsui. Applications of peptide and protein-based materials in bionanotechnology, aug 2010.

[2] Jan L. Patterson, Angela M. Arenas-Gamboa, Ting Yi Wang, Hao Ching Hsiao, David W. Howell, Jean Philippe Pellois, Allison Rice-Ficht, and Sarah E. Bondos. Materials composed of the Drosophila Hox protein ultrabithorax are biocompatible and nonimmunogenic. *Journal of Biomedical Materials Research - Part A*, 103(4):1546–1553, 2015.

[3] Chloe N. Grover, Ruth E. Cameron, and Serena M. Best. Investigating the morphological, mechanical and degradation properties of scaffolds comprising collagen, gelatin and elastin for use in soft tissue engineering. *Journal of the Mechanical Behavior of Biomedical Materials*, 10:62–74, jun 2012.

[4] Vivek A Kumar, Jeffrey M Caves, Carolyn A Haller, Erbin Dai, Liying Liu, Stephanie Grainger, and Elliot L Chaikof. Collagen-based substrates with tunable strength for soft tissue engineering. *Biomaterials Science*, 1(11):1193–1202, 2013.

[5] Rémi Parenteau-Bareil, Robert Gauvin, and François Berthod. Collagen-Based Biomaterials for Tissue Engineering Applications. *Materials 2010, Vol. 3, Pages 1863-1887*, 3(3):1863–1887, mar 2010.

[6] Chanjuan Dong and Yonggang Lv. Application of collagen scaffold in tissue engineering: Recent advances and new perspectives, feb 2016.

[7] Kai U Claussen, Eileen S Lintz, Reiner Giesa, Hans-Werner Schmidt, and Thomas Scheibel. Protein Gradient Films of Fibroin and Gelatine. *Macromolecular Bioscience*, 13(10):1396–1403, oct 2013.

[8] Michal Shevach, Sharon Fleischer, Assaf Shapira, and Tal Dvir. Gold nanoparticle-decellularized matrix hybrids for cardiac tissue engineering. *Nano Letters*, 14(10):5792–5796, 2014.

[9] George D Pins, David L Christiansen, Raj Patel, and Frederick H Silver. Self-assembly of collagen fibers. Influence of fibrillar alignment and decorin on mechanical properties. *Biophysical Journal*, 73(4):2164–2172, 1997.

[10] Eileen Gentleman, Andrea N Lay, Darryl A Dickerson, Eric A Nauman, Glen A Livesay, and Kay C Dee. Mechanical characterization of collagen fibers and scaffolds for tissue engineering. *Biomaterials*, 24(21):3805–3813, 2003.

[11] Julie Glowacki and Shuichi Mizuno. Collagen scaffolds for tissue engineering. *Biopolymers*, 89(5):338–344, may 2008.

[12] Youbin Li, Yuzhe Liu, Ronghang Li, Haotian Bai, Zhengqing Zhu, Liwei Zhu, Chenyi Zhu, Zhenjia Che, He Liu, Jincheng Wang, and Lanfeng Huang. Collagen-based biomaterials for bone tissue engineering. *Materials & Design*, 210:110049, nov 2021.

[13] Frederick H Silver, Joseph W Freeman, and Gurinder P Seehra. Collagen self-assembly and the development of tendon mechanical properties. *Journal of Biomechanics*, 36(10):1529–1553, 2003.

[14] Jean Pierre Karam, Claudio Muscari, Laurence Sindji, Guillaume Bastiat, Francesca Bonafè, Marie Claire Venier-Julienne, and N. Claudia Montero-Menei. Pharmacologically active microcarriers associated with thermosensitive hydrogel as a growth factor releasing biomimetic 3D scaffold for cardiac tissue-engineering. *Journal of controlled release*, 192:82–94, oct 2014.

[15] Linnea Nilebäck. *Expanded knowledge on silk assembly for development of bioactive silk coatings*. PhD thesis, KTH, Stockholm, 2019.

[16] David W. Howell, Camille L. Duran, Shang Pu Tsai, Sarah E. Bondos, and Kayla J. Bayless. Functionalization of Ultrabithorax Materials with Vascular Endothelial Growth Factor Enhances Angiogenic Activity. *Biomacromolecules*, 17(11):3558–3569, nov 2016.

[17] Shang-Pu Tsai, David W Howell, Zhao Huang, Hao-Ching Hsiao, Yang Lu, Kathleen S Matthews, Jun Lou, and Sarah E Bondos. The Effect of

Protein Fusions on the Production and Mechanical Properties of Protein-Based Materials. *Advanced Functional Materials*, 25(9):1442–1450, mar 2015.

[18] Domenica Musumeci, Chiara Platella, Claudia Riccardi, Federica Moccia, and Daniela Montesarchio. Fluorescence Sensing Using DNA Aptamers in Cancer Research and Clinical Diagnostics. *Cancers 2017, Vol. 9, Page 174*, 9(12):174, dec 2017.

[19] Mariia Darmostuk, Silvie Rimpelova, Helena Gbelcova, and Tomas Ruml. Current approaches in SELEX: An update to aptamer selection technology. *Biotechnology Advances*, 33(6):1141–1161, sep 2014.

[20] Steven M. Shamah, Judith M. Healy, and Sharon T. Cload. Complex target SELEX. *Accounts of Chemical Research*, 41(1):130–138, jan 2008.

[21] R. E. Wang, Yin Zhang, J. Cai, Weibo Cai, and Ting Gao. Aptamer-Based Fluorescent Biosensors. *Current Medicinal Chemistry*, 18(27):4175–4184, sep 2011.

[22] Zhengzhong Shao and Fritz Vollrath. Surprising strength of silkworm silk. *Nature*, 418(6899):741, 2002.

[23] Xiaohui Zhang, Cassandra B. Baughman, and David L. Kaplan. In vitro evaluation of electrospun silk fibroin scaffolds for vascular cell growth. *Biomaterials*, 29(14):2217–2227, may 2008.

[24] Sekaran Saravanan, Sricharan Nethala, Soumitri Pattnaik, Anjali Tripathi, Ambigapathi Moorthi, and Nagarajan Selvamurugan. Preparation, characterization and antimicrobial activity of a bio-composite scaffold containing chitosan/nano-hydroxyapatite/nano-silver for bone tissue engineering. *International Journal of Biological Macromolecules*, 49(2):188–193, 2011.

[25] Xiao Hu, Peggy Cebe, Anthony S Weiss, Fiorenzo Omenetto, and David L Kaplan. Protein-based composite materials. *Materials Today*, 15(5):208–215, 2012.

[26] Zhao Huang, Taha Salim, Autumn Brawley, Jan Patterson, Kathleen S. Matthews, and Sarah E. Bondos. Functionalization and Patterning of Protein-Based Materials Using Active Ultrabithorax Chimeras. *Advanced Functional Materials*, 21(14):2633–2640, jul 2011.

[27] Tal Dvir, Brian P Timko, Mark D Brigham, Shreesh R Naik, Sandeep S Karajanagi, Oren Levy, Hongwei Jin, Kevin K Parker, Robert Langer, and Daniel S Kohane. Nanowired three-dimensional cardiac patches. *Nature Nanotechnology*, 6(11):720–725, 2011.

[28] Sirinrath Sirivisoot and Thomas J Webster. Multiwalled carbon nanotubes enhance electrochemical properties of titanium to determine in situ bone formation. *Nanotechnology*, 19(29):295101, 2008.

[29] Jin Oh You, Marjan Rafat, George J.C. Ye, and Debra T. Auguste. Nanoengineering the heart: Conductive scaffolds enhance connexin 43 expression. *Nano Letters*, 11(9):3643–3648, sep 2011.

[30] Cynthia L. Hughes and Thomas C. Kaufman. Hox genes and the evolution of the arthropod body plan1. *Evolution & Development*, 4(6):459–499, nov 2002.

[31] Peter A. Lawrence. *The Making of a Fly: The Genetics of Animal Design*, volume 6. Blackwell Scientific Publications, jul 1993.

[32] Keith E Young Doris P von Kessler Benjamin I Sun Philip A. Beachy Jacob Varkey and Stephen C Ekker. Cooperative Binding of an Ultrabithorax Homeodomain Protein to Nearby and Distant DNA Sites. *Molecular Cellular Biology*, 13(11):6941–6956, 1993.

[33] Sarah E Bondos and Alicia Bicknell. Detection and prevention of protein aggregation before, during, and after purification. *Analytical Biochemistry*, 316(2):223–231, may 2003.

[34] Pedro Romero, Zoran Obradovic, Xiaohong Li, Ethan C Garner, Celeste J Brown, and A Keith Dunker. Sequence complexity of disordered protein. *Proteins: Structure, Function and Genetics*, 42(1):38–48, jan 2001.

[35] Ying Liu, Kathleen S Matthews, and Sarah E Bondos. Multiple Intrinsically Disordered Sequences Alter DNA Binding by the Homeodomain of the Drosophila Hox Protein Ultrabithorax. *Journal of Biological Chemistry*, 283(30):20874–20887, jul 2008.

[36] Valeria Italia. *Understanding novel protein-derived biopolymers to enable biomimetic devices*. PhD thesis, Université Grenoble Alpes, Swansea University, dec 2021.

[37] Alex Bateman, Maria Jesus Martin, Sandra Orchard, Michele Magrane, Shadab Ahmad, Emanuele Alpi, Emily H Bowler-Barnett, Ramona Britto, Hema Bye-A-Jee, Austra Cukura, Paul Denny, Tunca Dogan, Thank God Ebenezer, Jun Fan, Penelope Garmiri, Leonardo Jose da Costa Gonzales, Emma Hatton-Ellis, Abdulrahman Hussein, Alexandr Ignatchenko, Giuseppe Insana, Rizwan Ishtiaq, Vishal Joshi, Dushyanth Jyothi, Swaathi Kandasaamy, Antonia Lock, Aurelien Luciani, Marija Lugaric, Jie Luo, Yvonne Lussi, Alistair MacDougall, Fabio Madeira, Mahdi Mahmoudy, Alok Mishra, Katie Moulang, Andrew Nightingale, Sangya Pundir, Guoying Qi, Shriya Raj, Pedro Raposo, Daniel L Rice, Rabie Saidi, Rafael Santos, Elena Speretta, James Stephenson, Prabhat Totoo, Edward Turner, Nidhi Tyagi, Preethi Vasudev, Kate Warner, Xavier Watkins, Rossana Zaru, Hermann Zellner, Alan J Bridge, Lucila Aimo, Ghislaine Argoud-Puy, Andrea H Auchincloss, Kristian B Axelsen, Parit Bansal, Delphine Baratin, Teresa M Batista Neto, Marie Claude Blatter, Jerven T Bolleman, Emmanuel Boutet, Lionel Breuza, Blanca Cabrera Gil, Cristina Casals-Casas, Kamal Chikh Echioukh, Elisabeth Coudert, Beatrice Cuche, Edouard de Castro, Anne Estreicher, Maria L Famiglietti, Marc Feuermann, Elisabeth Gasteiger, Pascale Gaudet, Sebastien Gehant, Vivienne Gerritsen, Arnaud Gos, Nadine Gruaz, Chantal Hulo, Nevila Hyka-Nouspikel, Florence Jungo, Arnaud Kerhornou, Philippe Le Mercier, Damien Lieberherr, Patrick Masson, Anne Morgat, Venkatesh Muthukrishnan, Salvo Paesano, Ivo Pedruzzi, Sandrine Pilbout, Lucille Pourcel, Sylvain Poux, Monica Pozzato, Manuela Pruess, Nicole Redaschi, Catherine Rivoire, Christian J.A. Sigrist, Karin Sonesson, Shyamala Sundaram, Cathy H Wu, Cecilia N Arighi, Leslie Arminski, Chuming Chen, Yongxing Chen, Hongzhan Huang, Kati Laiho, Peter McGarvey, Darren A Natale, Karen Ross, C R Vinayaka, Qinghua Wang, Yuqi Wang, and Jian Zhang. UniProt: the Universal Protein Knowledgebase in 2023. *Nucleic Acids Research*, 51(D1):D523–D531, jan 2023.

[38] Alexandra M. Greer, Zhao Huang, Ashley Oriakhi, Yang Lu, Jun Lou, Kathleen S. Matthews, and Sarah E. Bondos. The drosophila transcription factor ultrabithorax self-assembles into protein-based biomaterials with multiple morphologies. *Biomacromolecules*, 10(4):829–837, apr 2009.

[39] David W. Howell, Shang-Pu Tsai, Kelly Churion, Jan Patterson, Colette Abbey, Joshua T. Atkinson, Dustin Porterpan, Yil-Hwan You, Kenith E.

Meissner, Kayla J. Bayless, and Sarah E. Bondos. Identification of Multiple Dityrosine Bonds in Materials Composed of the Drosophila Protein Ultrabithorax. *Advanced Functional Materials*, 25(37):5988–5998, oct 2015.

[40] Jan L Patterson, Colette A Abbey, Kayla J Bayless, and Sarah E Bondos. Materials composed of the Drosophila melanogaster protein ultrabithorax are cytocompatible. *Journal of Biomedical Materials Research - Part A*, 102(1):97–104, 2014.

[41] Debin Li, Peter M Gannett, and David Lederman. An investigation into the feasibility of myoglobin-based single-electron transistors. *Nanotechnology*, 23(39), 2012.

[42] Karol Szuba-Jablonski. *The Mechanical and Electrical Properties of Ultrabithorax Materials*. Msc thesis, Swansea University, 2020.

[43] A. Bernardus Mostert. The importance of water content on the conductivity of biomaterials and bioelectronic devices, sep 2022.

[44] Karol P. Szuba-Jablonski, Carolyn Greig, Drew Riley, Valeria Italia, Thomas Argue, and Kenith E Meissner. Developing ultrabithorax-based sensing platforms. In Benjamin L. Miller, Sharon M. Weiss, Amos Danielli, Ramesh Raghavachari, and Mikhail Y. Berezin, editors, *Frontiers in Biological Detection: From Nanosensors to Systems XIV*, volume 11979, page 15. SPIE, mar 2022.

[45] Bernard. Valeur and Mário Nuno Berberan-Santos. *Molecular Fluorescence: Principles and Applications*. Wiley-VCH, Weinheim, 2nd ed. edition, 2012.

[46] Joseph R Lakowicz. *Principles of fluorescence spectroscopy*. Springer, New York, NY, United States, 2006.

[47] Jihad René Albani. *Principles and Applications of Fluorescence Spectroscopy*. John Wiley & Sons, Incorporated, Chichester, United Kingdom, 2008.

[48] Nils O Petersen. *Foundations for nanoscience and nanotechnology*. Apple Academic Press Inc., 2017.

[49] Johannes Schindelin, Ignacio Arganda-Carreras, Erwin Frise, Verena Kaynig, Mark Longair, Tobias Pietzsch, Stephan Preibisch, Curtis Rue-

den, Stephan Saalfeld, Benjamin Schmid, Jean-Yves Tinevez, Daniel James White, Volker Hartenstein, Kevin Eliceiri, Pavel Tomancak, and Albert Cardona. Fiji: an open-source platform for biological-image analysis. *Nature Methods*, 9(7):676–682, 2012.

[50] J N Kapur, P K Sahoo, and A K C Wong. A new method for gray-level picture thresholding using the entropy of the histogram. *Computer Vision, Graphics, and Image Processing*, 29(3):273–285, 1985.

[51] Brendan P Cormack, Raphael H Valdivia, and Stanley Falkow. FACS-optimized mutants of the green fluorescent protein (GFP). *Gene*, 173(1):33–38, 1996.

[52] Nathan C Shaner, Robert E Campbell, Paul A Steinbach, Ben N G Giepmans, Amy E Palmer, and Roger Y Tsien. Improved monomeric red, orange and yellow fluorescent proteins derived from Discosoma sp. red fluorescent protein. *Nature Biotechnology*, 22(12):1567–1572, dec 2004.

[53] Ahmed A. Heikal, Samuel T. Hess, and Watt W. Webb. Multiphoton molecular spectroscopy and excited-state dynamics of enhanced green fluorescent protein (EGFP): acid–base specificity. *Chemical Physics*, 274(1):37–55, dec 2001.

[54] Samuel T. Hess, Erin D. Sheets, Alice Wagenknecht-Wiesner, and Ahmed A. Heikal. Quantitative Analysis of the Fluorescence Properties of Intrinsically Fluorescent Proteins in Living Cells. *Biophysical Journal*, 85(4):2566, oct 2003.

[55] Jelle Hendrix, Cristina Flors, Peter Dedecker, Johan Hofkens, and Yves Engelborghs. Dark states in monomeric red fluorescent proteins studied by fluorescence correlation and single molecule spectroscopy. *Biophysical Journal*, 94(10):4103–4113, may 2008.

[56] Bin Wu, Yan Chen, and Joachim D. Müller. Fluorescence fluctuation spectroscopy of mCherry in living cells. *Biophysical Journal*, 96(6):2391–2404, mar 2009.

[57] Talley J Lambert. FPbase: a community-editable fluorescent protein database. *Nature Methods*, 16(4):277–278, 2019.

[58] D A Malencik and S R Anderson. Dityrosine as a product of oxidative stress and fluorescent probe. *Amino acids*, 25(3-4):233–247, dec 2003.

[59] Greg S Harms, Steve W Pauls, John F Hedstrom, and Carey K Johnson. Fluorescence and Rotational Dynamics of Dityrosine. *Journal of Fluorescence*, 7(4):285, 1997.

[60] A. J. Kungl, A. J. Visser, H. F. Kauffmann, and M. Breitenbach. Time-resolved fluorescence studies of dityrosine in the outer layer of intact yeast ascospores. *Biophysical Journal*, 67(1):309–317, 1994.

[61] J W Heinecke, W Li, H L 3rd Daehnke, and J A Goldstein. Dityrosine, a specific marker of oxidation, is synthesized by the myeloperoxidase-hydrogen peroxide system of human neutrophils and macrophages. *The Journal of biological chemistry*, 268(6):4069–4077, feb 1993.

[62] R. M. Hochstrasser and D. K. Negus. Picosecond fluorescence decay of tryptophans in myoglobin. *Proceedings of the National Academy of Sciences of the United States of America*, 81(14):4399, 1984.

[63] S. M. Janes, G. Holtom, P. Ascenzi, M. Brunori, and R. M. Hochstrasser. Fluorescence and energy transfer of tryptophans in Aplysia myoglobin. *Biophysical Journal*, 51(4):653–660, 1987.

[64] Rozhin Penjweini, Alessio Andreoni, Tilman Rosales, Jeonghan Kim, Michael D. Brenner, Dan L. Sackett, Jay H. Chung, and Jay R. Knutson. Intracellular oxygen mapping using a myoglobin-mCherry probe with fluorescence lifetime imaging. *Journal of Biomedical Optics*, 23(10):1, oct 2018.

[65] Rozhin Penjweini, Mateus P. Mori, Paul M. Hwang, Dan L. Sackett, and Jay R. Knutson. Fluorescence lifetime imaging of metMyoglobin formation due to nitric oxide stress. In Ammasi Periasamy, Peter T. So, and Karsten König, editors, *Multiphoton Microscopy in the Biomedical Sciences XXII*, volume 11965, page 47. SPIE, mar 2022.

[66] Jesús Tejero, Sruti Shiva, and Mark T Gladwin. Sources of Vascular Nitric Oxide and Reactive Oxygen Species and Their Regulation. *Physiological reviews*, 99(1):311–379, jan 2019.

[67] Anca Margineanu, Jia Jia Chan, Douglas J Kelly, Sean C Warren, Delphine Flatters, Sunil Kumar, Matilda Katan, Christopher W Dunsby, and Paul M.W. French. Screening for protein-protein interactions using Förster resonance energy transfer (FRET) and fluorescence lifetime imaging microscopy (FLIM). *Scientific Reports*, 6, 2016.

[68] Tanja Kaufmann, Sébastien Herbert, Benjamin Hackl, Johanna Maria Besold, Christopher Schramek, Josef Gotzmann, Kareem Elsayad, and Dea Slade. Direct measurement of protein-protein interactions by FLIM-FRET at UV laser-induced DNA damage sites in living cells. *Nucleic Acids Research*, 48(21):E122–E122, 2020.

[69] Artem Pliss, Lingling Zhao, Tymish Y. Ohulchanskyy, Junle Qu, and Paras N. Prasad. Fluorescence lifetime of fluorescent proteins as an intracellular environment probe sensing the cell cycle progression. *ACS Chemical Biology*, 7(8):1385–1392, aug 2012.

[70] Michael Fritzsche and Carl Fredrik Mandenius. Fluorescent cell-based sensing approaches for toxicity testing. *Analytical and Bioanalytical Chemistry*, 398(1):181–191, sep 2010.

[71] Henk Jan Van Manen, Paul Verkuijlen, Paul Wittendorp, Vinod Subramaniam, Timo K. Van Den Berg, Dirk Roos, and Cees Otto. Refractive Index Sensing of Green Fluorescent Proteins in Living Cells Using Fluorescence Lifetime Imaging Microscopy. *Biophysical Journal*, 94(8):L67–L69, apr 2008.

[72] Alexandros Ch. Lazanas and Mamas I Prodromidis. Electrochemical Impedance SpectroscopyA Tutorial. *ACS Measurement Science Au*, mar 2023.

[73] J. E.B. Randles. Kinetics of rapid electrode reactions. *Faraday Discussions*, 1:11–19, 1947.

[74] D. Marianiová and L. Lapčík. Electrical conductivity measurements of hyaluronic acid and collagen. *Colloid and Polymer Science*, 271(2):143–147, feb 1993.

[75] Bailey Blessing, Cory Trout, Abneris Morales, Karleena Rybacki, Stacy A Love, Guillaume Lamoureux, Sean M. O'Malley, Xiao Hu, and David Salas-

de la Cruz. Morphology and ionic conductivity relationship in silk/cellulose biocomposites. *Polymer International*, 68(9):1580–1590, 2019.

[76] Junyi Cai, Qiusheng Wang, Xiufang Li, Yupin Guan, Liyan He, Shuqin Yan, Renchuan You, and Qiang Zhang. Water-stable natural silk nanofibril composite films for electrical devices. *Materials Today Communications*, 22, mar 2020.

[77] Suvarna C Narayanan, K R Karpagam, and Amitava Bhattacharyya. Nanocomposite coatings on cotton and silk fibers for enhanced electrical conductivity. *Fibers and Polymers*, 16(6):1269–1275, 2015.

[78] Rebecca A. MacDonald, Christopher M. Voge, Mihalis Kariolis, and Jan P. Stegemann. Carbon nanotubes increase the electrical conductivity of fibroblast-seeded collagen hydrogels. *Acta Biomaterialia*, 4(6):1583–1592, nov 2008.

[79] Eden Steven, Jin Gyu Park, Anant Paravastu, Elsa Branco Lopes, James S Brooks, Ongi Englander, Theo Siegrist, Papatya Kaner, and Rufina G Alamo. Physical characterization of functionalized spider silk: Electronic and sensing properties. *Science and Technology of Advanced Materials*, 12(5):55002–55015, 2011.

[80] Anna Baranowska-Korczyc, Alicja Nejman, Marcin Rosowski, and Małgorzata Cieślak. Multifunctional silk textile composites functionalized with silver nanowires. *Journal of Applied Polymer Science*, 140(21), jun 2023.

[81] Ewa Sitkiewicz, Jacek Olędzki, Jarosław Poznański, and Michał Dadlez. Di-Tyrosine Cross-Link Decreases the Collisional Cross-Section of Aβ Peptide Dimers and Trimers in the Gas Phase: An Ion Mobility Study. *PLOS ONE*, 9(6):e100200, jun 2014.

[82] James T. Vivian and Patrik R. Callis. Mechanisms of tryptophan fluorescence shifts in proteins. *Biophysical Journal*, 80(5):2093–2109, 2001.

[83] Buck A. L. New Equations for Computing Vapor Pressure and Enhancement Factor. *Journal of Applied Meteorology*, 20(12):1527–1532, 1981.

[84] The MathWorks Inc. MATLAB version: 9.13.0 (R2022b), 2022.

[85] Tyler W. McCullock, David M. MacLean, and Paul J. Kammermeier. Comparing the performance of mScarlet-I, mRuby3, and mCherry as FRET acceptors for mNeonGreen. *PLOS ONE*, 15(2):e0219886, feb 2020.

[86] Aikaterini G. Mantzila, Vassiliki Maipa, and Mamas I. Prodromidis. Development of a faradic impedimetric immunosensor for the detection of Salmonella typhimurium in milk. *Analytical Chemistry*, 80(4):1169–1175, feb 2008.

[87] H. Jawad, N. N. Ali, A. R. Lyon, Q. Z. Chen, S. E. Harding, and A. R. Boccaccini. Myocardial tissue engineering: A review. *Journal of Tissue Engineering and Regenerative Medicine*, 1(5):327–342, 2007.

[88] Hedeer Jawad, Alex R Lyon, Sian E Harding, Nadire N Ali, and Aldo R Boccaccini. Myocardial tissue engineering, 2008.

[89] Filippo Medeghini, Jajnabalkya Guhathakurta, Giuseppe Tiberti, Sven Simon, Giovanni A. Plizzari, and Peter Mark. Steered fiber orientation: correlating orientation and residual tensile strength parameters of SFRC. *Materials and Structures/Materiaux et Constructions*, 55(10):1–18, dec 2022.

[90] Abbas Mohajerani, Siu Qun Hui, Mehdi Mirzababaei, Arul Arulrajah, Suksun Horpibulsuk, Aeslina Abdul Kadir, Md Tareq Rahman, and Farshid Maghool. Amazing types, properties, and applications of fibres in construction materials, aug 2019.

[91] Malcolm S Loveday, Tom Gray, and Johannes Aegerter. Tensile Testing of Metallic Materials : A Review Tensile Testing of Metallic Materials : A Review . *Sustainable Growth' Programme*, (April 2004):1–171, apr 2002.

[92] A A Griffith. The Phenomena of Rupture and Flow in Solids. *Philosophical Transactions of the Royal Society of London. Series A, Containing Papers of a Mathematical or Physical Character*, 221:163–198, 1921.

[93] John Gosline, Margo Lillie, Emily Carrington, Paul Guerette, Christine Ortlepp, and Ken Savage. Elastic proteins: Biological roles and mechanical properties. *Philosophical Transactions of the Royal Society B: Biological Sciences*, 357(1418):121–132, feb 2002.

[94] Hans Oxlund and Troels T Andreassen. The roles of hyaluronic acid, collagen and elastin in the mechanical properties of connective tissues. *Journal of anatomy*, 131(Pt 4):611–20, 1980.

[95] Peter Fratzl, Klaus Misof, Ivo Zizak, Gert Rapp, Heinz Amenitsch, and Sigrid Bernstorff. Fibrillar structure and mechanical properties of collagen. *Journal of Structural Biology*, 122(1-2):119–122, 1998.

[96] John M Gosline, Paul A Guerette, Christine S Ortlepp, and Ken N Savage. The mechanical design of spider silks: From fibroin sequence to mechanical function. *Journal of Experimental Biology*, 202(23):3295–3303, 1999.

[97] Michael Goldberg, Robert Langer, and Xinqiao Jia. Nanostructured materials for applications in drug delivery and tissue engineering. *Journal of biomaterials science. Polymer edition*, 18(3):241–268, 2007.

[98] Anwarul Hasan, Adnan Memic, Nasim Annabi, Monowar Hossain, Arghya Paul, Mehmet R Dokmeci, Fariba Dehghani, and Ali Khademhosseini. Electrospun scaffolds for tissue engineering of vascular grafts. *Acta Biomaterialia*, 10(1):11–25, jan 2014.

[99] Zhao Huang, Yang Lu, Ravish Majithia, Jaimin Shah, Kenith Meissner, Kathleen S. Matthews, Sarah E. Bondos, and Jun Lou. Size Dictates Mechanical Properties for Protein Fibers Self-Assembled by the Drosophila Hox Transcription Factor Ultrabithorax. *Biomacromolecules*, 11(12):3644–3651, dec 2010.

[100] Ravish Majithia, Jan Patterson, Sarah E Bondos, and Kenith E Meissner. On the design of composite protein-quantum dot biomaterials via self-assembly. *Biomacromolecules*, 12(10):3629–3637, 2011.

[101] Xueran Xiao, Hui Li, Lijian Zhao, Yanfen Zhang, and Zhongcheng Liu. Oligonucleotide aptamers: Recent advances in their screening, molecular conformation and therapeutic applications. *Biomedicine & Pharmacotherapy*, 143:112232, nov 2021.

[102] Cibran Perez-Gonzalez, Daniel A. Lafontaine, and J. Carlos Penedo. Fluorescence-Based Strategies to Investigate the Structure and Dynamics of Aptamer-Ligand Complexes, aug 2016.

[103] Lia S Rotherham, Charlotte Maserumule, Keertan Dheda, Jacques Theron, and Makobetsa Khati. Selection and Application of ssDNA Aptamers to Detect Active TB from Sputum Samples. *PLoS ONE*, 7(10):e46862, oct 2012.

[104] Katrine Kiilerich-Pedersen, Johannes Daprà, Solène Cherré, and Noemi Rozlosnik. High sensitivity point-of-care device for direct virus diagnostics. *Biosensors and Bioelectronics*, 49:374–379, 2013.

[105] Qihong Cai, Lifen Chen, Fang Luo, Bin Qiu, Zhenyu Lin, and Guonan Chen. Determination of cocaine on banknotes through an aptamer-based electrochemiluminescence biosensor. *Analytical and Bioanalytical Chemistry*, 400(1):289–294, 2011.

[106] Y Wang, Y Luo, T Bing, Z Chen, and M Lu. DNA Aptamer Evolved by Cell-SELEX for Recognition of Prostate Cancer. *PLoS ONE*, 9(6):100243, 2014.

[107] Yun Min Chang, Michael J Donovan, and Weihong Tan. Using aptamers for cancer biomarker discovery, 2013.

[108] C Lorenz, T Gesell, B Zimmermann, U Schoeberl, I Bilusic, L Rajkowitsch, C Waldsich, A von Haeseler, and R Schroeder. Genomic SELEX for Hfq-binding RNAs identifies genomic aptamers predominantly in antisense transcripts. *Nucleic Acids Research*, 38(11):3794–3808, 2010.

[109] Nuo Duan, Shijia Wu, Xiujuan Chen, Yukun Huang, and Zhouping Wang. Selection and identification of a DNA aptamer targeted to vibrio parahemolyticus. *Journal of Agricultural and Food Chemistry*, 60(16):4034–4038, 2012.

[110] Hari P. Dwivedi, R. Derike Smiley, and Lee Ann Jaykus. Selection of DNA aptamers for capture and detection of Salmonella Typhimurium using a whole-cell SELEX approach in conjunction with cell sorting. *Applied Microbiology and Biotechnology*, 97(8):3677–3686, apr 2013.

[111] Yeon Seok Kim, Min Young Song, Jongsoo Jurng, and Byoung Chan Kim. Isolation and characterization of DNA aptamers against Escherichia coli using a bacterial cell-systematic evolution of ligands by exponential enrichment approach. *Analytical Biochemistry*, 436(1):22–28, 2013.

[112] Min Young Song, Dung Nguyen, Seok Won Hong, and Byoung Chan Kim. Broadly reactive aptamers targeting bacteria belonging to different genera using a sequential toggle cell-SELEX. *Scientific Reports*, 7, mar 2017.

[113] Soledad Marton, Fernanda Cleto, Marco Aurélio Krieger, and Josiane Cardoso. Isolation of an Aptamer that Binds Specifically to E. coli. *PLoS ONE*, 11(4):1–17, 2016.

[114] Ana Cláudia Graziani, Maria Isabel Stets, Ana Luisa Kalb Lopes, Pedro Henrique Caires Schluga, Soledad Marton, Ieda Mendes Ferreira, Antero Silva Ribeiro De Andrade, Marco Aurélio Krieger, and Josiane Cardoso. High efficiency binding aptamers for a wide range of bacterial sepsis agents. *Journal of Microbiology and Biotechnology*, 27(4):838–843, apr 2017.

[115] Hong Ru Liang, Gui Qiu Hu, Tao Zhang, Yu Jiao Yang, Li Li Zhao, Ying Lin Qi, Hua Lei Wang, Yu Wei Gao, Song Tao Yang, and Xian Zhu Xia. Isolation of ssDNA aptamers that inhibit rabies virus. *International Immunopharmacology*, 14(3):341–347, 2012.

[116] Fan Wu, Su Zhao, Bin Yu, Yan-Mei Chen, Wen Wang, Zhi-Gang Song, Yi Hu, Zhao-Wu Tao, Jun-Hua Tian, Yuan-Yuan Pei, Ming-Li Yuan, Yu-Ling Zhang, Fa-Hui Dai, Yi Liu, Qi-Min Wang, Jiao-Jiao Zheng, Lin Xu, Edward C Holmes, and Yong-Zhen Zhang. A new coronavirus associated with human respiratory disease in China. *Nature*, 579(7798):265–269, 2020.

[117] Yanling Song, Jia Song, Xinyu Wei, Mengjiao Huang, Miao Sun, Lin Zhu, Bingqian Lin, Haicong Shen, Zhi Zhu, and Chaoyong Yang. Discovery of Aptamers Targeting the Receptor-Binding Domain of the SARS-CoV-2 Spike Glycoprotein. *Analytical Chemistry*, 92(14):9895–9900, jul 2020.

[118] Eugene W.M. Ng, David T. Shima, Perry Calias, Emmett T. Cunningham, David R. Guyer, and Anthony P. Adamis. Pegaptanib, a targeted anti-VEGF aptamer for ocular vascular disease. *Nature Reviews Drug Discovery 2006 5:2*, 5(2):123–132, feb 2006.

[119] P.R. Bouchard, R.M. Hutabarat, and K.M. Thompson. Discovery and Development of Therapeutic Aptamers. *Annual Review of Pharmacology and Toxicology*, 50(1):237–257, feb 2010.

[120] Kei Xian Tan, Safina Ujan, Michael K. Danquah, and Sie Yon Lau. Design and characterization of a multi-layered polymeric drug delivery vehicle. *The Canadian Journal of Chemical Engineering*, 97(S1):1243–1252, may 2019.

[121] Maria V Riquelme, Huaning Zhao, Vaishnavi Srinivasaraghavan, Amy Pruden, Peter Vikesland, and Masoud Agah. Optimizing blocking of nonspecific bacterial attachment to impedimetric biosensors. *Sensing and Bio-Sensing Research*, 8:47–54, 2016.

[122] Siranush Babakhanova, Erica E Jung, Kazuhiko Namikawa, Hanbin Zhang, Yangdong Wang, Oksana M. Subach, Dmitry A Korzhenevskiy, Tatiana V Rakitina, Xian Xiao, Wenjing Wang, Jing Shi, Mikhail Drobizhev, Demian Park, Lea Eisenhard, Hongyun Tang, Reinhard W Köster, Fedor V Subach, Edward S Boyden, and Kiryl D Piatkevich. Rapid directed molecular evolution of fluorescent proteins in mammalian cells. *Protein Science*, 31(3):728–751, mar 2022.

[123] Douglas C. Prasher, Virginia K. Eckenrode, William W. Ward, Frank G. Prendergast, and Milton J. Cormier. Primary structure of the Aequorea victoria green-fluorescent protein. *Gene*, 111(2):229–233, feb 1992.

[124] Thermo Fisher Scientific. Texas Red Fluorescence Spectrum, jul 2023.

[125] Prerna Kaur, Yoshiaki Maeda, Andrew C Mutter, Tadashi Matsunaga, Yujia Xu, and Hiroshi Matsui. Three-dimensional directed self-assembly of Peptide nanowires into micrometer-sized crystalline cubes with nanoparticle joints. *Angewandte Chemie (International ed. in English)*, 49(45):8375–8378, nov 2010.

[126] Sabina Burazerovic, Julieta Gradinaru, Julien Pierron, and Thomas R. Ward. Hierarchical self-assembly of one-dimensional streptavidin bundles as a collagen mimetic for the biomineralization of calcite. *Angewandte Chemie - International Edition*, 46(29):5510–5514, jul 2007.

[127] Greeshma Thrivikraman, Poh S. Lee, Ricarda Hess, Vanessa Haenchen, Bikramjit Basu, and Dieter Scharnweber. Interplay of Substrate Conductivity, Cellular Microenvironment, and Pulsatile Electrical Stimulation toward Osteogenesis of Human Mesenchymal Stem Cells in Vitro. *ACS Applied Materials and Interfaces*, 7(41):23015–23028, oct 2015.

[128] Chun-Min Lo, Hong-Bei Wang, Micah Dembo, and Yu-li Wang. Cell movement is guided by the rigidity of the substrate. *Biophysical Journal*, 79(1):144–152, jul 2000.

[129] Jindan Wu, Zhengwei Mao, Huaping Tan, Lulu Han, Tanchen Ren, and Changyou Gao. Gradient biomaterials and their influences on cell migration. *Interface Focus*, 2(3):337–355, 2012.

[130] Kuen Yong Lee and David J Mooney. Alginate: properties and biomedical applications. *Progress in polymer science*, 37(1):106–126, jan 2012.

[131] Jinchen Sun and Huaping Tan. Alginate-Based Biomaterials for Regenerative Medicine Applications. *Materials*, 6(4):1285–1309, mar 2013.

[132] Yiyu Wang, Xinyu Wang, Jian Shi, Rong Zhu, Junhua Zhang, Zongrui Zhang, Daiwei Ma, Yuanjing Hou, Fei Lin, Jing Yang, and Mamoru Mizuno. A Biomimetic Silk Fibroin/Sodium Alginate Composite Scaffold for Soft Tissue Engineering. *Scientific Reports*, 6(1):39477, 2016.

[133] Zita M. Jessop, Ayesha Al-Sabah, Neng Gao, Stuart Kyle, Bethan Thomas, Nafiseh Badiei, Karl Hawkins, and Iain S. Whitaker. Printability of pulp derived crystal, fibril and blend nanocellulose-alginate bioinks for extrusion 3D bioprinting. *Biofabrication*, 11(4):045006, jul 2019.

[134] Margit Mahlapuu, Joakim Håkansson, Lovisa Ringstad, and Camilla Björn. Antimicrobial Peptides: An Emerging Category of Therapeutic Agents. *Frontiers in cellular and infection microbiology*, 6(DEC):194, dec 2016.

[135] Robert E.W. Hancock, Evan F. Haney, and Erin E. Gill. The immunology of host defence peptides: beyond antimicrobial activity. *Nature Reviews Immunology*, 16(5):321–334, may 2016.

[136] David W. Hoskin and Ayyalusamy Ramamoorthy. Studies on anticancer activities of antimicrobial peptides. *Biochimica et Biophysica Acta (BBA) - Biomembranes*, 1778(2):357–375, feb 2008.

[137] Jun Sung Kim, Eunye Kuk, Kyeong Nam Yu, Jong Ho Kim, Sung Jin Park, Hu Jang Lee, So Hyun Kim, Young Kyung Park, Yong Ho Park, Cheol Yong Hwang, Yong Kwon Kim, Yoon Sik Lee, Dae Hong Jeong, and Myung Haing Cho. Antimicrobial effects of silver nanoparticles. *Nanomedicine: Nanotechnology, Biology, and Medicine*, 3(1):95–101, 2007.

[138] Hui Ding, Li Wei Cheng, Ying Ying Ma, Ji Lie Kong, and Huan Ming Xiong. Luminescent carbon quantum dots and their application in cell imaging. *New Journal of Chemistry*, 37(8):2515–2520, 2013.

[139] Meijia Wang, Lianying Wang, Gang Wang, Xiaohui Ji, Yubai Bai, Tiejin Li, Shaoyun Gong, and Jinghong Li. Application of impedance spectroscopy for monitoring colloid Au-enhanced antibody immobilization and antibody-antigen reactions. *Biosensors and Bioelectronics*, 19(6):575–582, 2004.